

High-resolution imaging of transport processes with GPR full-waveform inversion

Peleg Haruzi

Energie & Umwelt / Energy & Environment

Band / Volume 601

ISBN 978-3-95806-678-6

Forschungszentrum Jülich GmbH
Institut für Bio- und Geowissenschaften
Agrosphäre (IBG-3)

High-resolution imaging of transport processes with GPR full-waveform inversion

Peleg Haruzi

Schriften des Forschungszentrums Jülich
Reihe Energie & Umwelt / Energy & Environment

Band / Volume 601

ISSN 1866-1793

ISBN 978-3-95806-678-6

Bibliografische Information der Deutschen Nationalbibliothek.
Die Deutsche Nationalbibliothek verzeichnet diese Publikation in der
Deutschen Nationalbibliografie; detaillierte Bibliografische Daten
sind im Internet über <http://dnb.d-nb.de> abrufbar.

Herausgeber
und Vertrieb: Forschungszentrum Jülich GmbH
Zentralbibliothek, Verlag
52425 Jülich
Tel.: +49 2461 61-5368
Fax: +49 2461 61-6103
zb-publikation@fz-juelich.de
www.fz-juelich.de/zb

Umschlaggestaltung: Grafische Medien, Forschungszentrum Jülich GmbH

Druck: Grafische Medien, Forschungszentrum Jülich GmbH

Copyright: Forschungszentrum Jülich 2022

Schriften des Forschungszentrums Jülich
Reihe Energie & Umwelt / Energy & Environment, Band / Volume 601

D 38 (Diss. Köln, Univ., 2022)

ISSN 1866-1793
ISBN 978-3-95806-678-6

Vollständig frei verfügbar über das Publikationsportal des Forschungszentrums Jülich (JuSER)
unter www.fz-juelich.de/zb/openaccess.



This is an Open Access publication distributed under the terms of the [Creative Commons Attribution License 4.0](https://creativecommons.org/licenses/by/4.0/),
which permits unrestricted use, distribution, and reproduction in any medium, provided the original work is properly cited.

Contents

Abstract	1
List of publications.....	3
Introduction.....	4
1.1 Geophysical properties of subsurface material	6
1.2 Basics of GPR	8
1.3 Objectives and outline	12
Theory	15
2.1 Electromagnetic wave propagation	15
2.2 Geophysical inversion theory	17
2.3 Ray-based method	18
2.4 GPR full-waveform inversion methodology	20
Realistic hydrological aquifer model for tracer modelling	29
3.1 Description of the Krauthausen test site	30
3.2 Stochastic aquifer model setup	32
3.3 Tracer transport simulation	35
3.4 Tracer types and petrophysical relations	37
3.5 Conclusions.....	42
Detection of tracer plumes using full-waveform inversion of time-lapse ground penetrating radar data: a numerical study in a high-resolution aquifer model	43
4.1 GPR FWI modeling.....	44
4.2 GPR FWI results - Background models	44
4.3 Starting model strategies for time-lapse FWI	49
4.4 Recovery of different salt tracer magnitudes and days.....	50
4.5 Recovery of ethanol tracer	54
4.6 Breakthrough curves at single cells.....	57
4.7 Considerations for experimental tracer test.....	58
4.8 Conclusions.....	60
GPR full-waveform inversion monitoring of a salt tracer test	62
5.1 Saline tracer test	62
5.2 Borehole logging	64
5.3 GPR data acquisition.....	66
5.4 GPR data processing	68
5.5 Crosshole ZOP analysis.....	75
5.6 Time-lapse FWI approach	79

5.7 GPR FWI results	81
5.8 Hydrological interpretation with logging data	98
5.9 Discussion	100
5.10 Conclusions	103
Conclusions and Outlook	104
6.1 Conclusions	104
6.2 Outlook	106
Supplements to Chapter 4	108
A.1 Noise in GPR synthetic data	108
A.2 Observed data and FWI data fit	111
A.3 Fit of FWI traces at the presence of salt tracer	112
A.4 Noise level in comparison to the traces amplitude	113
A.5 Observed and modelled FWI traces for background and ethanol scenario	114
A.6 Movie description - comparison of tracer recovery from salt and ethanol tracers	115
A.7 Out of plane effects - 3D versus 2D GPR data	115
B 3D aquifer characterization of the Hermalle-sous-Argenteau test site using crosshole GPR amplitude analysis and full-waveform inversion	118
B.1 Introduction	119
B.2 Field site and GPR measurement setup	121
B.3 GPR amplitude analysis results	126
B.4 Full-waveform inversion results	132
B.5 Petrophysical interpretation	145
B.6 Conclusions	146
C Numerical study for time-lapse GPR full-waveform inversion for salt and heat tracer tests	148
C.1 Introduction	149
C.2 Time-lapse full-waveform inversion strategies	150
C.3 Strategies for time-lapse starting models	150
C.4 Synthetic positive electrical tracer	151
C.5 Conclusions and Outlook	154
Acknowledgments	155
Bibliography	156
List of figures	165
List of tables	167
List of abbreviations	168
curriculum vitae	169
Erklärung zur Dissertation	173

Abstract

Imaging subsurface small-scale features and monitoring transport of tracer plumes at a fine resolution is of interest to characterize transport processes in aquifers. Full-waveform inversion (FWI) of crosshole ground penetrating radar (GPR) measurements enables aquifer characterization at decimeter-scale resolution. GPR FWI provides 2D tomograms of the subsurface properties, the dielectric permittivity (ϵ) and electrical conductivity (σ), which can be correlated with hydrological properties.

In the framework of the thesis, we conducted synthetic and experimental tracer tests that were monitored using time-lapse crosshole GPR full-waveform inversion results, to test the potential and limitation to reconstruct the tracer plume. For the synthetic test, we generated a realistic high resolution aquifer model based on previous hydrological and GPR FWI data from the Krauthausen test site in order to perform a transport simulation that represents reasonable heterogeneity of the tracer concentration. Using petrophysical relations, we converted the concentration distribution to dielectric properties of specific tracers: saltwater (increase σ only), desalinated water (decrease σ only) and ethanol (decrease in both σ and ϵ). One important aspect of the GPR FWI is to investigate an optimal way to define adequate starting models especially for the time-lapse data. Therefore, we investigated three different starting model options in the synthetic test, resulting that ϵ and σ models from the background provide the most accurate FWI of time-lapse data. Hereby, both ϵ and σ FWI results have shown the potential to derive time-lapse changes. The gained insights of the synthetic optimization tests are applied for an experimental test.

To prove the potential of the crosshole GPR FWI also under realistic conditions, we performed an experimental salt tracer experiment at the Krauthausen test site. Thereby, we injected to the sandy aquifer a salt tracer, and monitored the tracer development using crosshole GPR over a timeframe of 14 days within 5 crosshole planes in an area of 11x10 m. These time-lapse data are independently inverted using the background models of each plane as starting models as proposed from the synthetic study to derive the best FWI results. We investigated the consistency of the reconstruction of the plume by temporal and spatial continuity across neighboring planes, by correlating with borehole logging data, and with expectations based on previous tracer experiments from the same site. One challenge arises from the time-lapse GPR data caused by the change of the borehole filling properties over the time and transport of the plume. The salt and freshwater mixture in the tubes couple with the borehole antennae thus influence the GPR data. Fortunately, the processing for the FWI enables accounting this effect by estimating effective source wavelets for each time step and each plane, which compensate for borehole filling effects caused by the salt tracer. If these borehole filling effects would not be considered, errors in the results would occur. Performing the FWI considering the corrected effective source wavelets allows recovery of the aquifer models independently from saltwater-antennae effects. Such effects cannot be incorporated using standard ray-based approaches. In contrast from the synthetic tracer test, investigation of the best starting model for experimental data showed that σ homogenous model rather

than from FWI background provides more accurate results for FWI of time-lapse data. This can be explained that possible errors in the FWI background results caused by measurement or starting model uncertainties, are forcing the FWI with these models to be trapped in a local minimum. The time-lapse GPR FWI has shown a reliable manifestation of a tracer of about 0.2 m resolution, which was not observed before from other geophysical monitoring techniques. These improved and higher resolution images of such a tracer transport can help in future to better constraint hydrological properties of interest for hydrological models. In this thesis, we have shown for the first time the potential of the GPR FWI to characterize and monitor tracer experiments using crosshole GPR data. Especially, the application to salt tracers, which traditionally were investigated with ERT, is now also possible with GPR and higher resolution images of the tracer transport are possible to obtain.

List of publications

At the time of writing this dissertation, parts of the doctoral thesis have been published, submitted, or are in preparation for publication by scientific journals and contributed to scientific meetings as specified below. Chapters 1 – 5 are based on papers numbered 1 – 2, Appendix A is based on paper numbered 1, and Appendices B and C are based on publications numbered 4 and 5, respectively.

Paper numbered 3 is a review about the more general topic of the European research project, which I was taking part in the framework of the ITN "Enigma ITN". Since my contribution to this paper was minor, I did not add this paper to the thesis.

1. **Haruzi, P.**, Schmäck, J., Zhou, Z., van der Kruk, J., Vereecken, H., Vanderborght, J., & Klotzsche, A. (2022). *Detection of tracer plumes using full-waveform inversion of time-lapse ground penetrating radar data: a numerical study in a high-resolution aquifer model*. Water Resources Research, e2021WR030110.
2. **Haruzi, P.**, Schmäck, J., van der Kruk, J., Vereecken, H., Vanderborght, J., & Klotzsche, A. *GPR full-waveform inversion monitoring of a salt tracer test*, in preparation.
3. Hermans, T., Goderniaux, P., Jougnot, D., Fleckenstein, J., Brunner, P., Nguyen, F., ..., **Haruzi, P.**, ... & Le Borgne, T. (2022). *Advancing measurements and representations of subsurface heterogeneity and dynamic processes: towards 4D hydrogeology*. Hydrology and Earth System Sciences Discussions, 1-55.
4. Zhou, Z., Klotzsche, A., Hermans, T., Nguyen, F., Schmäck, J., **Haruzi, P.**, Vereecken, H., and van der Kruk, J. (2020). *3D aquifer characterization of the Hermalle-sous-Argenteau test site using crosshole ground-penetrating radar amplitude analysis and full-waveform inversion GPR amplitude analysis and FWI for 3D imaging*. Geophysics, 85(6), H133-H148.
5. **Haruzi, P.**, Schmäck, J., Zhou, Z., Vanderborght, J., Vereecken, H., van der Kruk, J., and Klotzsche, A. (2020). Numerical study for time-lapse GPR full-waveform inversion for salt and heat tracer tests. That extended abstract was accepted to *18th International Conference on Ground Penetrating Radar*, but eventually was not published because the conference was cancelled due to restrictions of Covid19.

Chapter 1

Introduction

In order to control groundwater quality, monitoring contaminants in the aquifer and prediction of possible ones are essential. Detailed knowledge of the flow and transport processes, which control migration of fluids, particles, and solutes in the subsurface (hereafter tracers), is necessary, e.g., to protect groundwater pumping wells from pollution and operate remediation measures (Maliva, 2016). As groundwater system are sensible, any kind of contamination may lead to geochemical and biological reactions. This may lead to changes in groundwater constituents and to physical changes of the aquifer caused by dissolution and precipitation (Kitanidis and McCarty, 2012), or to groundwater temperature changes (Hermans et al., 2015). Important transport characteristics that need to be known are the tracer velocity, the tracer plume spreading, and the tracer dilution by mixing with groundwater. These transport characteristics depend strongly on the heterogeneity of hydraulic aquifer properties (Bear and Cheng, 2010), which are difficult to observe directly because of the intrinsic inaccessibility of the subsurface. Tracer experiments that monitor tracer plumes in aquifers can be used to determine transport characteristics and infer the underlying hydraulic aquifer properties and their spatial variability (e.g., Vereecken et al., 2000). Therefore, the enhancement of the resolution of time-lapse geophysical transport imaging, is essential to conceptualize the aquifer more precise and for getting predictions with probably less uncertainty (e.g., Scheidt et al., 2018).

Solute particles initially that introduced in the aquifer in a form of a “point-source” (closely spaced particles) will firstly spread out as velocity at the *microscopic* level varies in magnitude and direction from point to point (Bear and Cheng, 2010). Consequently, the shape of the initial point-cloud will gradually change, and so will the fluid volume that occupied by it. At the single tube scale, we observe (Figure 1.1a, top) velocity variations in both magnitude and direction across any pore cross-section. At the *microscopic* scale, the void space can be visualized as an assembly of interconnected tubes with varying diameters (Figure 1.1a, middle). Between flow paths, we observe streamlines deviate from the mean direction of flow. That kind of spreading is called *mechanical dispersion*. As a result, heterogeneous pore system and flow through it generates finger-shape spreading of the tracer particles through fast flow paths, and a tailing part of the tracer particles, which are carried by slower velocities. In addition to the mechanical dispersion, a second dispersion-causing phenomenon that occur at *microscopic* scale is the *molecular diffusion* – random motion of the molecules produces an additional flux of the component’s particles from regions of higher concentrations to those of lower ones. Molecular diffusion fluxes occur intensely at microscopic streamlines transition zones, where high concentrations gradient are created, and tends to equalize the concentration across every microscopic stream tube (Figure 1.1a, bottom). Simultaneously, lateral molecular diffusion across a streamline, which tends to equalize the concentration across pores, are due to a concentration gradient, which is

produced also between adjacent stream-tubes. At the larger scales, the layer meter-scale and the field kilometer-scale (Figure 1.1b, c), the subsurface is highly heterogeneous with respect to their macroscopic coefficients, e.g., porosity and permeability (Bear and Cheng, 2010). Here, mechanical dispersion causes the plume spreading as dispersive fluxes, which result from the variability of the relevant macroscopic quantities. Like in the microscopic scale, the total flux is again the sum of an advective flux and a dispersive one. These larger scales are the ones of interest to monitor when a contamination is introduced to the subsurface.

Traditional techniques for hydrologic characterization, such as pumping tests, provide data on large-scale aquifer hydraulic properties, but with low spatial resolution (e.g., Li et al., 2007, Butler, 2005). Other well-established techniques provide fine-scale information in the vertical direction, such as borehole measurements (Englert, 2003), cone penetration tests (Tillman et al., 2008), and measurements on sediment cores (Vereecken et al., 2000), but cannot characterize spatial variability in the horizontal (flow) direction with high spatial horizontal resolution. Geophysical methods such as electrical resistivity tomography (ERT) and GPR can close this gap in observation capabilities and provide information on an appropriate scale (up to $\sim 5\text{-}100\text{ m}$) and with high spatial resolution in both vertical and horizontal direction, while being minimally invasive (e.g., Looms et al., 2008, Binley et al., 2015). Both methods have the capability to image the subsurface by sensing changes in the physical parameters of a porous medium. In addition, the use of geophysical methods in combination with stochastic subsurface hydrology, data inversion techniques, time-lapse approaches have emerged as tools ("hydrogeophysics") to investigate shallow subsurface heterogeneity, dynamic processes and to link with hydrologically relevant properties (Binley et al., 2015).

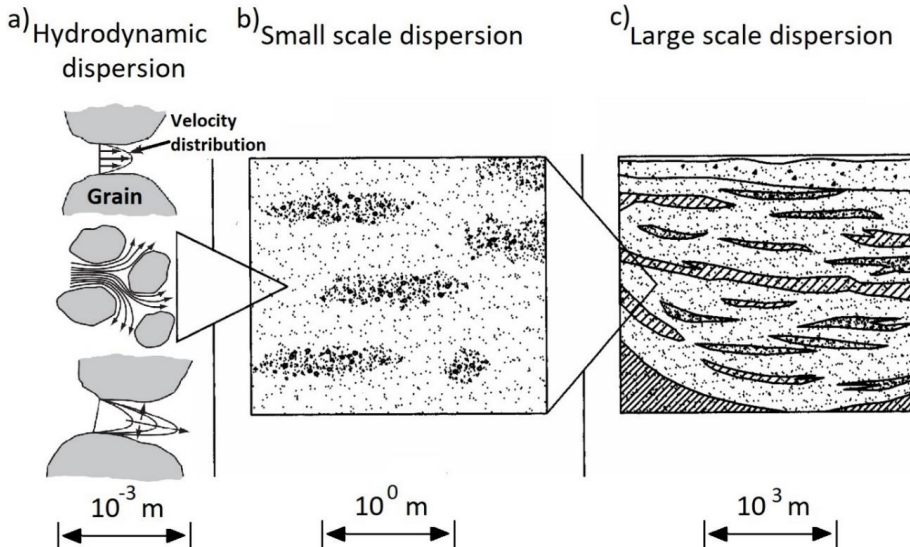


Figure 1.1: Flow in heterogeneities at different scales (adapted from Bear and Cheng, 2010).

Transport processes can be monitored by geophysical observables, when the tracer induces changes in hydrogeological state variables. For example, water saturation is strongly correlated with dielectric permittivity (Topp et al., 1980), salinity is correlated with electrical conductivity (Sreenivas et al., 1995), and temperature is correlated with both of them (Seyfried and Grant, 2007). These changes in the plume can for example be imaged with time-lapse GPR (Klotzsche et al., 2019a, Looms et al., 2008) and ERT (Kemna et al., 2002, Singha et al., 2005, Hermans et al., 2015). As examples, soil water content (Klotzsche et al., 2019a), leaking of industrial fluids (Brewster and Annan, 1994) and saltwater (Giertzuch et al., 2020) were monitored by GPR, while seawater intrusion (Palacios et al., 2020), hot water (Hermans et al., 2015) and saltwater (Müller et al., 2010) were monitored by ERT. The most common used tracer types are salt and therefore ERT, which provides electrical conductivity distribution, is more frequently used rather than GPR. The occurrence of transport in principle can be monitored at the spatio-temporal scale resolution of the geophysical observable. Hydrogeological properties and structures, which control state changes are then derived from the geophysical properties by a given petro-physical model. However, subsurface structures finer than the resolution of the geophysical method, and those affected by constraints of each of the inversion methods in the imaging algorithm may be neglected from the image, or at best, their magnitude will be smoothed and presented over a larger spatial scale.

1.1 Geophysical properties of subsurface material

Subsurface materials are, in large, non-conducting materials that can accommodate a propagating, alternating electromagnetic (EM) field. These class of materials are called *dielectrics* and described by dielectric permittivity (ϵ) and electrical conductivity (σ). Permittivity describes the ability of a material to store and release EM energy in the form of electric charge. In atoms, molecules or crystals contain *bound* electric charges (e.g., in the polar water molecule), which become physically displaced or polarized in relation to their original position. The EM pulse supplies energy to the displaced charges in the form of acceleration which in turn generates small displacement current that produces EM energy with a phase delay with the incident pulse. The total result is slowing down of the propagating wave, thus permittivity is directly linked to propagation velocity. At the atomic/molecular scale, the permittivity of a material depends on its electronic structure and temperature. ϵ of a material is described using the relative permittivity (ϵ_r) to the ϵ_0 value of vacuum $\epsilon_r = \epsilon/\epsilon_0$ with $\epsilon_0 = 8.8542 \cdot 10^{-12}$ F/m. Note that all later mentions of permittivity are reconsidered as relative permittivity. If free charges that increase the electrical conductivity are available, e.g., salt solutes in water, under application of EM field they will flow through the material and produce attenuation and loss of pulse EM energy. Another property is the magnetic permittivity (μ), which describes the ability of a material to involve in magnetic polarization. Generally, the ϵ_r and σ of porous media of an aquifer vary in space and time (Everett, 2013), while the μ is often simplified to the free-space value of $1.257 \cdot 10^{-6}$ H/m.

Above the scale of a single constituent, at the scale relevant for laboratory and field measurements, where multiple material phases exist (e.g., crystal grain, water and air), an averaging and empirical petrophysical models for permittivity (Birchak et al., 1974, Topp, 1980) and electrical conductivity are used (Archie, 1942). On that scale effective properties are called effective permittivity (ϵ) and bulk electrical conductivity (σ_b). For dielectric properties of common subsurface materials, see Table 1.1.

Whereas ERT measurements are made using direct current (i.e., 0 to very low frequencies) and provide the σ (often also expressed by resistivity, which is $1/\sigma$), GPR operates in a high-frequency range between 10-2600 MHz (Daniels, 1996) and uses the propagation of the EM wave in resistive earth materials. GPR utilizes transmission and reflection of propagating waves from subsurface material contrasts, in addition to attenuation of subsurface constituents. In contrast to ERT, GPR can provide both ϵ and σ (Knight, 2001). High-frequency GPR systems allow higher imaging resolution of the subsurface that scales with the wavelength (λ) of the measured signal. For a typical used frequency (f) spectra of 10-200 MHz (the range used in this study) of the EM signal and a ϵ_r of 12-25 of the media, the wavelength scales between 0.3 and 8.5 m ($\lambda(\epsilon_r, f) = (c_0/\sqrt{\epsilon_r})/f$; with $c_0 = 3 \cdot 10^8$ m/s as the EM velocity in air (Annan, 2009).

Table 1.1: Typical values of relative permittivity and electrical conductivity for common subsurface materials at an antenna frequency of 100 MHz (based on Jol, 2008).

Material	Electrical conductivity σ [mS/m]	Relative permittivity ϵ_r [-]
Air	1	1
Clay – dry	1-100	2-20
Clay – wet	100-1000	15-40
Dry sand	0.01	3 – 5
Saturated sand	0.1 – 1	20 – 30
Freshwater	0.1-10	78 (25 °C) – 88 (0 °C)
Freshwater ice	1-0.000001	3
Dry salt	0.001-0.01	6
Seawater	4000	81-88
Gravel, dry?	0.1-100	4-7
Soil – sandy, dry	0.1-100	4-6
Soil – sandy, wet	10-100	15-30
Soil – loamy, dry	0.1-1	4-6
Soil – loamy, wet	10-100	10-20
Soil – clayey, dry	0.1-1	4-6
Soil – clayey, wet	100-1000	10-15
Soil – average	5	16
Limestone	0.5 – 2	6
Granite	0.01-1	6
Ice	0.01	3.18

Next to spatial resolution, another challenge in geophysical imaging is the translation of imaged parameters (dielectric properties ϵ and σ for GPR) to the property of interest, in our case the tracer or substance concentration. To derive soil water content from GPR either empirical- or physical- based models can be used. The most famous ones are Topp's equation (Topp et al., 1980) and the complex refraction mixing model (CRIM, Birchak et al., 1974), respectively. Since the relations between the dielectric properties and the state variable of interest depend on spatially variable aquifer properties like porosity (CRIM model), pore structure (Archie, 1942), and surface charge density of the mineral surfaces (Rhoades et al., 1981), the petrophysical relationships are site dependent and spatially variable (e.g., Müller et al., 2010). The translation of the imaged electric properties to concentration distribution is therefore afflicted by this spatial variability.

1.2 Basics of GPR

The GPR acquisition configuration geometry (Figure 1.2) is chosen depending on the subsurface question under investigation. The most common configurations are the surface-to-surface reflection surveying geometry, with the objective to map subsurface reflectivity versus spatial position (Huisman et al., 2003). In common offset profile (COP) survey from surface, the transmitter and receiver antennas are moved along the Earth's surface with a *constant spacing*. Variations in reflection amplitude and time delay indicate variations in velocity, attenuation, and impedance. In Common-midpoint (CMP) or wide-angle-reflection-refraction (WARR) mode the antenna separation varies the signal path in the ground, while keeping the point of reflection fixed. CMP/WARRs enables to obtain an estimate of the radar signal velocity versus depth in the ground by varying the antenna spacing and measuring the change in the two-way travel time. While the COP method is very fast and easy to apply in the field in transects or grids, a direct conversion from the time to depth axis is often difficult if no hyperboles are present in the data (Huisman et al., 2003). In contrast CMP/WARR are more time consuming, but can provide a detailed description of the velocity distribution in the subsurface, which can be considered for COP data to derive an accurate depth scale.

With the crosshole survey geometry, the transmitter and receiver antenna are placed in two neighboring boreholes and the measurements are performed in trans-illumination mode. In crosshole Zero-offset profiling (ZOP) the transmitting and receiving antenna are simultaneously moved together being at the same depth. ZOP is a quick way to derive a 1D-velocity profile and to locate velocity and attenuation horizontal zones. The second option to measure crosshole data are multi-offset gathers (MOG). Thereby, the transmitter is fixed at a certain location in one borehole, while the receiver (Rx) antennae are lower/rised in the second borehole with a constant spacing. Afterwards, the transmitter (Tx) antennae is moved to a new location in the borehole with a defined offset and the Rx measurements are repeated. After all transmitter positions in one borehole were measured, a semi-reciprocal setup (Klotzsche et al., 2010) can be achieved when the Tx and Rx switch boreholes, and the measurements are repeated. The advantage of this measurement technique is that a large number of angles are passing

through the volume between the boreholes. Because of the high amount of the data with a dense ray-coverage and the known distance between the boreholes, such data are well constrained for inversion approaches (MIP paralyzed code, more details in Klotzsche et al., 2010). Therefore, crosshole MOG data are used in tomography inversion with ray-based and full-waveform methods, to investigate the distribution of subsurface parameters, and allows relatively small acquisition errors (Axtell et al., 2016). Vertical radar profiling (VRP) is a technique in which the receiver antenna is located within a borehole and the transmitter antenna is placed with a certain distance away from the borehole (Tronicke and Hamann, 2013). VRP surveying is used to derive 1D velocity models by inverting the arrival times of direct waves.

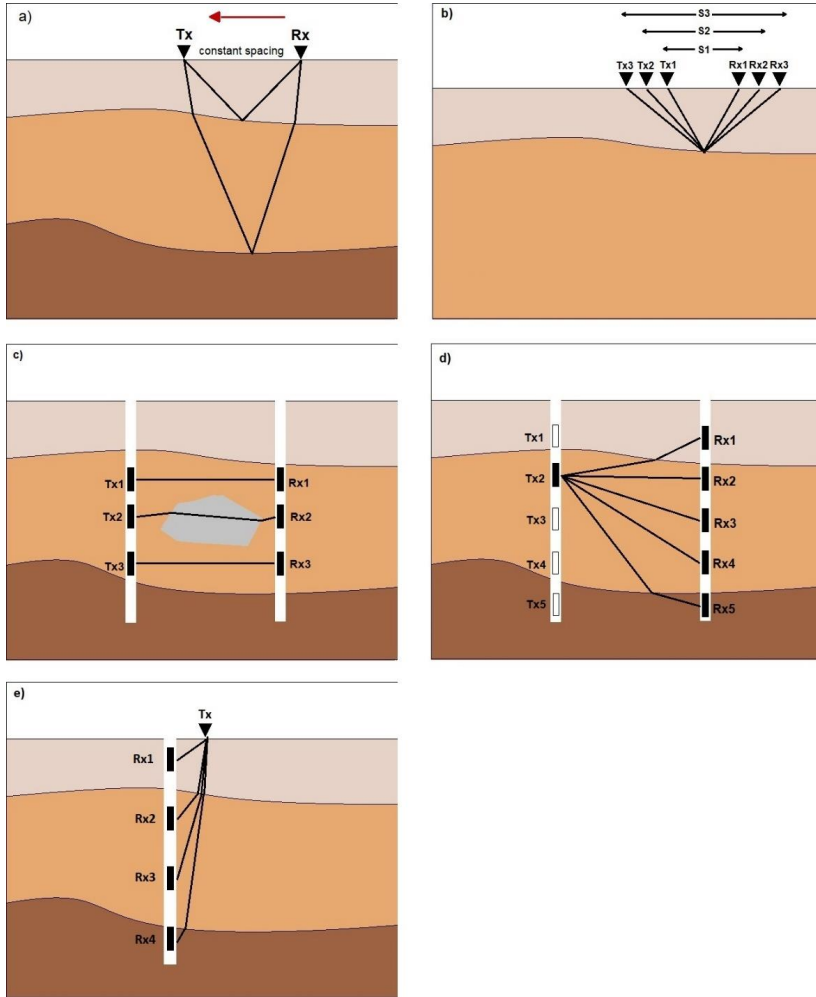


Figure 1.2: Different acquisition geometries for GPR: a) common-offset profile, b) common-midpoint profile, c) crosshole zero-offset profile, d) multi-offset gathers and e) vertical radar profiling survey configurations.

For applications, where quantification is desired, more complex processing procedures such as imaging and/or inversion are necessary. Commonly in crosshole GPR, tomographic inversion is applied which reconstructs medium properties.

The travel-time inversion, which considers the first arrival times of the data, provides information about the EM velocity structure, while first-cycle amplitude inversion, which use the first cycle amplitudes of the measured pulses, about the EM attenuation (Figure 1.3, red and green). They consider a straight or curved-line approximation for the wave propagation, and use smoothing and damping parameters during the inversion (e.g., Holliger et al., 2001). Furthermore, the inversions of travel-times and amplitudes are implemented separately, rather than intermittently update in an iterative process. Moreover, due to inconsistency in travel-time inversion for crosshole GPR, it is a common practice to limit the angular aperture (Peterson, 2001) that affects the resolution of the tomograms. Thereby, the resolution of the ray-based methods is scaled by the first Fresnel zone $\sqrt{\lambda L}$, where L is the total path, and have been found to smooth structures finer than about 1 m (Gueting et al., 2017). With respect to monitoring of plume spread, the relevant scale is the meter scale (Figure 1b). Travel-time inversions have been used to map and characterize the subsurface (e.g., Binley et al., 2002) and to derive flow and transport due to soil water content changes at a meter scale (e.g., Eppstein and Dougherty, 1998, Looms et al., 2008). Specifically, the inversion of amplitudes depend critically on the complex directive properties of the antenna (Holliger et al., 2001). The inversion relies on the assumption that the radiation pattern corresponds to that of an electric dipole in a homogeneous medium (varies symmetrically with the deviation angle from the horizontal). However, the pattern depends on the filling in the borehole (air/water) and on the heterogeneities nearby the antenna as the electric dipole couple with interfaces between electrical material parameters. The effect on ray-based amplitude inversion from systematic radiation pattern error is to shift the inferred attenuation by a constant amount (Holliger et al., 2001). Moreover, the inherently under-deterministic character of the inversion problem does not enable to invert the radiation pattern and the attenuation structure to a unique solution. As a result, inversion of amplitudes is not able to constrain absolute values of attenuation, but it could detect and constrain relative changes in attenuation for locating electrical conductivity contrasts. These challenges inherited in the inversion of amplitudes restricted its use with crosshole GPR data. One of the few studies, used an attenuation feature (difference attenuation) in ray-based tomography inversion was in monitoring of a saline tracer transport through a fracture (Day-Lewis et al., 2003). Due to the limitation to derive quantitative information about amplitude inversion and hence electrical conductivity, GPR has traditionally not applied to monitor salt tracer plumes. Other borehole GPR techniques have been used before for monitoring salt tracer in fractures from time-lapse trace differences (Dorn et al., 2011, Shakas et al., 2016, Giertzuch et al., 2020), but not using tomography.

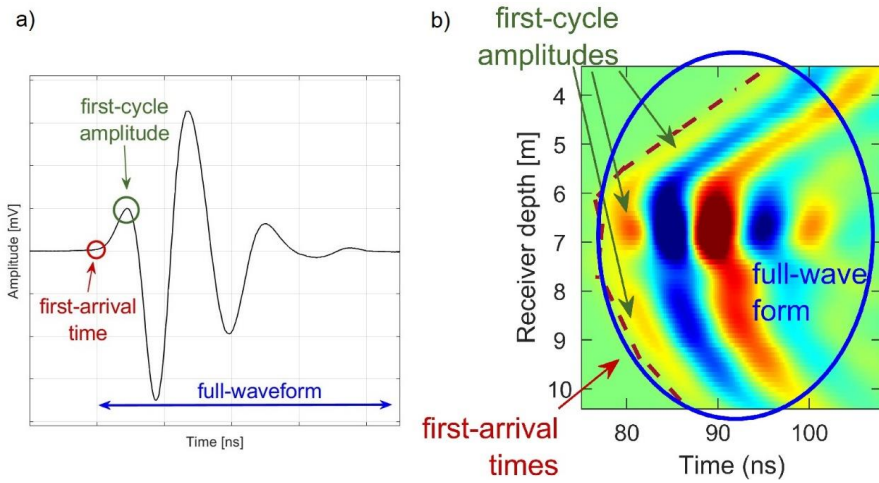


Figure 1.3: Illustration of the difference between ray-based (first arrival in red, first-cycle amplitude in green) and full-waveform (blue). a) Shows an exemplary trace from a single transmitter-receiver combination. b) Image plot of a MOG data set of all receiver traces from a single transmitter. Waveforms between 6.5-7 m depth show a waveguiding behavior caused by a high porosity layer.

In contrast to ray-based approaches, which consider only a limited part of the measured signal, the full-waveform inversion (FWI) uses the entire measured data (Figure 1.3, in blue) to constrain the inversion and is therefore able to obtain higher resolution images (Klotzsche et al., 2019b). Over the recent five decades, significant developments have been made in the field of seismic waveform inversion (e.g., Tarantola, 1984, Pratt and Worthington, 1990, Virieux and Operto, 2009) using time-domain, frequency-domain, and hybrid methods (Sirgue et al., 2008, Agudo et al., 2018). More recent, Ernst et al. (2007) and Meles et al., (2010) developed an algorithm for time-domain crosshole GPR FWI, which was successfully tested in synthetic and experimental studies (overview provided by Klotzsche et al., 2019b). The approach of Meles et al. (2010) was further adapted and tested in the last decade (overview in Klotzsche et al., 2019b). Until now more than 50 different crosshole GPR datasets have been successfully inverted and showed the potential to derive high-resolution images of the permittivity and conductivity. Thereby, they were able to resolve sub-wavelength features in high-resolution (decimeter scale) and could detect high contrast layers. Note that all these studies have been performed in steady state considering no changes over time in the medium properties. In one of these studies, the GPR FWI was performed to improve the characterization of a gravel aquifer (Gueting et al., 2017) and the results could be linked to previously performed tracer experiments from the same test site. Thereby, a hydrogeological facies model that was derived from the FWI models could explain a plume splitting imaged by a previous time-lapse ERT data. Note, that applying the FWI to experimental data requires several pre-processing steps to guarantee reliable inversion results. Klotzsche et al. (2019b) highlights

the challenges, which arise with these steps and provided a guideline how to carefully handle certain problems.

Generally, the time-domain crosshole GPR FWI is an iterative approach that simultaneously estimates ϵ_r and σ by minimizing the misfit function between measured and modeled GPR data with a gradient-type approach. It is considered to be multi-parameter inversion since it enables to update permittivity and conductivity values within the same descent step (Klotzsche et al., 2019b). Thereby, a 2D finite-difference time-domain (FDTD) algorithm solves the full Maxwell equations and allows predicting the EM wave propagation through the heterogeneous medium. To prevent the misfit function from converging to a local minimum, a ϵ_r starting model is required that yields synthetic traces that match all the observed data within less than half of the wavelength to avoid cycle-skipping (Meles et al., 2010). Normally, ray-based inversion results can provide such starting models. In the presence of high contrasts, such as a water table or high permittivity zones, ray-based starting models often need to be updated to meet this criteria (Klotzsche et al., 2012). Local invasion of tracers may generate high contrasts in ϵ_r and σ over short distances, which cannot be resolved by ray-based inversions and could cause problems in the FWI by using ray-based inversions as starting models. So far, most studies analyzed the effect of starting model errors mainly on the ϵ_r model and different methods were suggested, such as the amplitude analysis approach, to guarantee meeting the wavelength criterion (e.g., Klotzsche et al., 2014, Zhou et al., 2020). The definition of the σ starting model is more challenging. In common practice, the first cycle amplitude inversion provides a first guess for a homogenous starting model (e.g., Klotzsche et al., 2010). Note, that all the previous studies on crosshole GPR FWI were performed for steady state conditions, and therefore, how to handle the starting models for time-lapse data is not clear. Next to the stating model criteria, the FWI workflow requires an estimation of the effective source wavelet (ESW) based on the observed waveforms and using a deconvolution approach (Ernst et al., 2007b, Klotzsche et al., 2010). Therefore, inversion of the dielectric models with a priori estimated source wavelet reduces uncertainty in the final models.

1.3 Objectives and outline

The primary objectives of this thesis are to test the potential, to access the limitations, and to apply the crosshole GPR FWI for the first time to time-lapse measured data to characterize and monitor flow and transport processes related to tracer experiments. Note, that in tracer tests commonly, changes in σ monitored from salt (Kemna et al., 2002) and heat (Hermans et al., 2015) tracers in alluvial aquifers are imaged with methods like crosshole ERT. In contrast, ray-based crosshole GPR tomography inversion of amplitudes is not used to image attenuation changes, as errors are added to the attenuation model because the antenna radiation pattern cannot be estimated accurately. However, GPR full-waveform inversion has shown an improved resolution and aquifer characterization and it is able to calibrate simultaneously both the ϵ_r and σ . From here it is straight forward to hypothesize, that as GPR FWI has

shown better subsurface characterization, it will show better time-lapse changes from both ϵ_r and σ models to eventually reconstruct different kind of tracers.

In addition, utilizing high-resolution GPR FWI before tracer injection can be used to reduce the uncertainty in such petrophysical relations. Some petrophysical parameters such as the porosity that is used in the CRIM model and the formation factor used in Archie's Law can be calculated directly for each pixel of the background models that are obtained by FWI of GPR datasets that are acquired before tracer injection. Furthermore, it is expected that these results are significantly better and higher in resolution than traditional time-lapse ray-based inversion approaches.

Following the introductory chapter, Chapter 2 provides a theoretical background of electromagnetic wave propagation, and the crosshole GPR full-waveform inversion. In Chapter 3, we present a derived high-resolution aquifer model, that manifests realistic distribution of hydrological *and* dielectric properties, which are used as the aquifer model before the injection ("background"). The aquifer model is based on past hydrological measurements from the Krauthausen test site (Germany), from which a variogram model (i.e. defining a histogram and correlation lengths) is derived, and then that model is used in a stochastic simulation. The aquifer model is developed to generate a flow and transport model, which realistically mimics a tracer test. The concentration distribution is affected by the heterogeneity of the aquifer model. We present how different types of tracers change the permittivity and conductivity, thus in principle these changes can be monitored from time-lapse measurements. Then, the concentration distribution is assigned to specific tracers: saltwater, desalinated water and ethanol. Adequate petrophysical relations are used to convert the tracer concentration to dielectric properties. In Chapter 4, we acquired time-lapse crosshole GPR data, which are used as input data for FWI. Noise was introduced to the data in order to add a realistic challenge for FWI. We applied different tracer concentration to test the ability of FWI to reconstruct large parameter anomalies and sharp contrasts. Eventually, the fate of the plume was recovered from plume reconstruction that was acquired by converting back the dielectric properties from FWI to tracer concentration. In Chapter 5, the experimental saltwater tracer test in a sandy aquifer is presented. Saltwater was injected through a borehole and monitored on a daily basis by crosshole GPR in five different planes. In this study, the plume reconstruction was derived by subtracting the FWI background conductivity from the time-lapse one. We tested the consistency of the plume reconstruction using neighboring planes, planes on different days and with borehole logging data. In the final Chapter 6 the main findings and results of this thesis are summarized. We draw conclusions and present an outlook for future work.

Appendix A provides detailed extension to topics from Chapter 4. Appendix A is adapted from Supplementary File of publication Haruzi et al. (2022), *WRR*.

Appendix B of thesis includes an additional paper Zhou et al. (2020) that I was involved in my Ph.D. It involves a 3D characterization of a gravel aquifer. The layers mapping explain preferential paths observed from ERT imaging in a previous tracer test. My main contribution was to administrate the

week field trip and its coordination with our hosts in Belgium, taking the responsibility on the GPR acquisition and measure the GPR data and verify its credibility.

Appendix C of the thesis presents an extended abstract accepted to a conference, which shows , to show the potential of reconstruction of the plume in a numerical experiment not only by subtraction of individual time-lapse FWI models, but also using another time-lapse inversion approach which uses the difference between the time-lapse and the background data.

Chapter 2

Theory

In this chapter, the fundamental and theoretical background of the electromagnetic (EM) wave propagation is highlighted. After explaining the ray-based approaches, the details of the GPR FWI are described and discussed including the 3D to 2D conversion and the estimation of the effective source wavelet for experimental data.

2.1 Electromagnetic wave propagation

Maxwell's equations explain the propagation of the electrical and magnetic fields in terms of their sources. Considering Maxwell's equations, GPR waves can be explained and information about the medium through which the waves travelled can be derived. The classical, differential, time-domain, form of Maxwell's equations, in terms of free charges and currents (Griffiths 1981):

$$\nabla \times \mathbf{E} = -\partial \mathbf{B} / \partial t \quad \text{Eq. (2.1)}$$

$$\nabla \times \mathbf{H} = \mathbf{J}_c + \partial \mathbf{D} / \partial t \quad \text{Eq. (2.2)}$$

$$\nabla \cdot \mathbf{D} = \rho_f \quad \text{Eq. (2.3)}$$

$$\nabla \cdot \mathbf{B} = 0, \quad \text{Eq. (2.4)}$$

where \mathbf{E} is the electric field [V/m], \mathbf{H} is the magnetic field [A/m], \mathbf{D} is the electric flux density [C/m²], \mathbf{B} is the magnetic flux density [T], \mathbf{J}_c is the conduction or free current density [A/m²], ρ_f is the volumetric free charge density [C/m³], and t is time [s].

The constitutive relationships describe the material responses to EM fields at macroscopic scale. For earth material, the constitutive parameters are anisotropic, complex and non-linear (Slob et al., 2010). However, for a simplification to modelling it is accepted to regard them linear, isotropic, non-dispersive (Jol ,2009). Thus, the constitutive relationships are:

$$\mathbf{J}_c = \sigma \mathbf{E} \quad \text{Eq. (2.5)}$$

$$\mathbf{D} = \varepsilon \mathbf{E} \quad \text{Eq. (2.6)}$$

$$\mathbf{B} = \mu \mathbf{H}, \quad \text{Eq. (2.7)}$$

where σ is the electrical conductivity [S/m], ε is the dielectric permittivity [F/m], and μ is the magnetic permeability [H/m], and they control the nature of EM wave propagation within a material (see Section 1.1).

The fundamental prerequisite for the successful application of GPR is that EM wave propagation can occur. In such state, the displacement currents ($\mathbf{J}_d = \partial \mathbf{D} / \partial t$), i.e. the energy storage mechanisms

(propagation behavior), dominate over the conduction currents \mathbf{J}_c loss mechanisms (diffusion behavior). That transition from diffusion to propagation is defined by the transition frequency $f_t = \sigma/2\pi\epsilon$. The constitutive relationships are also frequency-dependent, due to irreversible process of the conversion of EM energy into heat through the conduction and relaxation process, which result from the EM interaction with the material. It causes the pulse to change shape and amplitude (in frequency and time domains) with propagation distance. However, for a range of frequencies between 10-2600 MHz and common geological materials an approximation of frequency-independent is adopted for use in GPR applications.

Through substitution of the constitutive parameters (Equations 2.5, 2.6 and 2.7) into Maxwell's Equations (2.1 and 2.2), the EM wave propagation can be described:

$$0 = \nabla^2 \mathbf{E} - \mu\epsilon \cdot \frac{\partial^2 \mathbf{E}}{\partial^2 t} - \mu\sigma \partial \mathbf{E} / \partial t \quad \text{Eq. (2.8)}$$

$$0 = \nabla^2 \mathbf{H} - \mu\epsilon \cdot \frac{\partial^2 \mathbf{H}}{\partial^2 t} - \mu \frac{\sigma \partial \mathbf{H}}{\partial t}. \quad \text{Eq. (2.9)}$$

The solution for a harmonic linear polarized EM plane wave, with $e^{i\omega t}$ dependence (ω is angular frequency), through an electrically conducting dielectric medium of uniform magnetic properties, can be described by the propagation (k), attenuation (α), phase coefficient (β), intrinsic impedance (Z) and velocity (v) in the direction of propagation. For low-loss dielectrically materials, frequency-independent, plane wave travelling in the z-direction the solutions are (Jol, 2008):

$$E^*(z, t) = \mathbf{E}_0 e^{i(\omega t - kz)} \quad \text{Eq. (2.10)}$$

and

$$H^*(z, t) = \mathbf{H}_0 e^{i(\omega t - kz)}, \quad \text{Eq. (2.11)}$$

where \mathbf{E}_0 and \mathbf{H}_0 are the complex amplitudes containing the wave polarization and phase,.

The complex propagation constant k^* , the attenuation coefficient α [Np/m] and the phase coefficient β [rad/m] can be describe with

$$k^* = \alpha + i\beta = \sqrt{(\sigma + i\omega\epsilon)i\omega\mu} \quad \text{Eq. (2.12)}$$

$$\alpha = \omega \left(\frac{\mu\epsilon}{2} \left[\sqrt{1 + \left(\frac{\sigma}{\omega\epsilon} \right)^2} - 1 \right] \right)^{1/2} \quad \text{Eq. (2.13)}$$

$$\beta = \omega \left(\frac{\mu\epsilon}{2} \left[\sqrt{1 + \left(\frac{\sigma}{\omega\epsilon} \right)^2} + 1 \right] \right)^{1/2}, \quad \text{Eq. (2.14)}$$

while the intrinsic impedance of the medium Z [ohms] and the phase velocity v [m/s] is:

$$Z = \sqrt{\frac{j\omega\mu}{\sigma + j\omega\epsilon}} \quad \text{Eq. (2.15)}$$

$$v = \frac{\omega}{\beta}. \quad \text{Eq. (2.16)}$$

The fields may diffuse or propagate as waves, depending on the frequency magnitude and on the relative magnitude of energy loss (associated with conductivity) to energy storage (associated with permittivity and magnetic permeability). GPR is viable when conditions yield a wave-like response and realized in the following conditions:

$$\frac{\sigma}{\omega\epsilon} \ll 1, \quad \text{Eq. (2.17)}$$

under that condition in Equations 2.8 and 2.9 the right-most part becomes negligible, and the solutions in Equations 2.13-2.16 reduce to:

$$\alpha = \frac{1}{2}\sigma\sqrt{\frac{\mu}{\epsilon}} = Z_0 \frac{\sigma}{2\sqrt{\epsilon_r}} \quad \text{Eq. (2.18)}$$

$$v = \frac{1}{\sqrt{\epsilon\mu}} = \frac{c_0}{\sqrt{\epsilon_r}} \quad \text{Eq. (2.19)}$$

$$Z_0 = \sqrt{\frac{\mu_0}{\epsilon_0}} = 377 \, \Omega. \quad \text{Eq. (2.20)}$$

2.2 Geophysical inversion theory

After acquisition (Section 1.2), and after the processing of the GPR data in order to isolate a signal (about processing experimental GPR data we will elaborate on the Section 5.3), in order to convert the data into other quantities more closely related to the physical properties of the target, imaging and inversion techniques are often applied.

The idea of imaging and inversion is to reconstruct a model of the subsurface under investigation (Tarantola, 2005). Geophysical inverse theory assumes that we understand the physics of the problem, such if we knew the physical properties accurately (the model properties $\mathbf{m}(\mathbf{x})$) we could predict the outcome of possible experiments (forward simulation $g(\mathbf{m})$ generates modelled data \mathbf{d}_{mod}) to reconstruct the observation data \mathbf{d}_{obs} . In a mathematical notation, the forward problem can be written as follows:

$$\mathbf{d}_{mod} = g(\mathbf{m}), \quad \text{Eq. (2.21)}$$

where g represents the forward operator that describes the underlying physics and geometry.

The inverse problem can be described by

$$\mathbf{m}_{pred} = g^{-1}(\mathbf{d}_{obs}), \quad \text{Eq. (2.22)}$$

and its solution is to find an appropriate model \mathbf{m}_{pred} , which generates modelled data \mathbf{d}_{mod} that fit well the observed data.

In geophysical tomography, where the model is composed of multiple parameters, there are more unknowns than observations. The inverse problem is then termed underdetermined, and many different models exist that generate a satisfying fit within the uncertainty of the observed data. In most cases in tomography, it is not possible to converge the model for heterogeneous medium without additional damping and regularization, i.e. to reduce the number of possible solutions to find a physically meaningful and realistic model. In addition, the inverse problem of crosshole GPR data for tomography is non-linear, i.e. \mathbf{d}_{mod} is a function of the unknown model parameters, and therefore the problem is needed to be solved iteratively. This optimization in tomography inversion usually uses local search algorithms such as gradient-type (Polak and Ribiere, 1969), which are appropriate for large-scale model-parameter inversion. These algorithms require a starting model that is subsequently refined or updated iteratively in accordance with data misfit between \mathbf{d}_{obs} and \mathbf{d}_{mod} . The big advantage of the local minimization search algorithms is their effectiveness and computational efficiency (Meles et al., 2010). For GPR the inversion method uses the georadar data and a forward model g of the physics of ray/wave propagation (depending on the forward model used). In the inverse problem for GPR tomography, the many parameters that characterize the model *and* the source current density wavelet (or equivalently, the antenna radiation pattern) are unknown. In a first step to reduce the ill-posing of the problem, the effective source wavelet (ESW) is estimated based on information about the antenna (Holliger et al., 2001) or from analysis of the measured waveforms (Klotzsche et al., 2019). Then, once the ESW is specified, the GPR data is used to estimate a subsurface model through inversion.

2.3 Ray-based method

After introducing the ray-based inversion method in Section 1.2, we provide here a more rigorous description of the travel-time and the first-cycle amplitude inversions, which provide information about the EM velocity and attenuation structure of the subsurface. The inversions use a regular grid of points with appropriate spacing, at which the velocities and attenuations are defined, and updated in each iteration.

2.3.1 Travel-time inversion

The method uses the first-arrival travel times in the data to derive a velocity model for the subsurface. In the forward model, ray-paths from the transmitters to the receivers are simulated, using model parameters at equidimensional cells m . Modelled data of first-arrival travel time t that the wave travels along a ray-path S through a 2D isotropic medium is described as follows:

$$t = \int_S u(\mathbf{r}(x, z)) dr, \quad \text{Eq. (2.23)}$$

where $u(\mathbf{r})$ represents the slowness ($u=1/v$) and $\mathbf{r}(x, z)$ indicates the position vector. In the grid representation, the i^{th} travel time of n observations can be expressed by the linear relationship:

$$t_i = \sum_{k=1}^m l_{ik} u_k = \mathbf{L}_i \mathbf{u}, \quad \text{Eq. (2.24)}$$

where the length l_{ik} represents the portion of the ray path i in the k^{th} cell of the model space, and u_k is the slowness in the k^{th} cell. \mathbf{L} should be solved with respect to the slowness field, to provide a curved ray path, which has the earliest travel time among the possible ray paths from a transmitter to a receiver. As a solver of the forward model that calculates \mathbf{L} , the Eikonal equation with finite-difference implementation is preferred for heterogeneous mediums (Vidale, 1990). A travel-time misfit function C_{TT} between the observed and modelled t_{tr}^{mod} data is used until the error is small enough to provide a good model:

$$C_{TT} = \sum_{trn} \sum_{rec} \frac{(t_{obs}^{trn-rec} - t_{mod}^{trn-rec})^2}{n}, \quad \text{Eq. (2.25)}$$

where t and r are transmitter and receiver numbers, respectively, $t_{obs}^{trn-rec}$ and $t_{mod}^{trn-rec}$ are the observed and modelled travel times between a transmitter at location \mathbf{x}_t to receiver at \mathbf{x}_r , and n is the number of data points. For the inverse part in the scheme, the modelled slowness field \mathbf{u} is derived. Commonly for heterogeneous medium addition regularization constraints are needed in the form of smoothing and damping, such Equation 2.24 is written:

$$\begin{bmatrix} t \\ 0 \\ \mathbf{u}_0 \end{bmatrix} = \begin{bmatrix} \mathbf{L} \\ \mathbf{A} \\ \mathbf{I} \end{bmatrix} \mathbf{u}, \quad \text{Eq. (2.26)}$$

where \mathbf{u}_0 is a vector of damping constrains, \mathbf{A} is a smoothing matrix, and \mathbf{I} is the identity matrix. The damping is used to minimize the amount of deviations from the input model \mathbf{u}_0 . The smoothing requests that differences of neighboring model parameters are small, thus makes sure that distinctive features are resolved only if they really present the data. The inversion problem that intends to solve the objective function is non-linear, as the ray-path (controlled by \mathbf{u}) that is represented by \mathbf{L} is unknown, and therefore it needs to be solved iteratively.

2.3.2 First-cycle amplitude inversion

The method uses the first-cycle amplitudes of the data to derive an attenuation model for the subsurface, where the attenuation α is associated with the σ of the medium (Equation 2.18, Davis and Annan, 1989). Thereby, it is assumed that the radiation patterns of the borehole antennas can be described by infinitesimal dipoles (Holliger et al., 2001). The amplitudes of the electrical fields \mathbf{E} in the far-field can be described by:

$$E(r) = \frac{A_0 \exp(-\int_0^r \alpha(s) ds) \theta_{trn}(\varphi_{trn}) \theta_{rec}(\varphi_{rec})}{\int_0^r ds}, \quad \text{Eq. (2.27)}$$

where A_0 is a normalization factor that symbolizes the source strength (i.e., amplitude radiation pattern) and depends on the effect of transmitter and receiver gain and antenna efficiency, and it is generally unknown. r is the distance along the ray, ds is the increment along the ray path; θ_{trn} and θ_{rec} the amplitude radiation pattern of the transmitter and receiver antennas, respectively; and φ is the angle relative to the horizontal. Ray paths are obtained from the first-arrival travel time inversion.

To achieve a linear form of Equation 2.26 (similar to Equation 2.24, but with attenuation α_k in the k^{th} cell instead of slowness u_k), for a discretized model we can write:

$$A'_{ij} = \sum_k \alpha_k \mathbf{L}_{ijk} + A'_0 \quad \text{Eq. (2.28a)}$$

$$A'_{ij} = -\ln \left\{ \frac{E_{ij} \sum_{ijk} \mathbf{L}_{ijk}}{\theta_t(\varphi_{t_i}) \theta_r(\varphi_{r_j})} \right\} \quad \text{Eq. (2.28b)}$$

$$A'_0 = -\ln A_0, \quad \text{Eq. (2.28c)}$$

where E_{ij} and A'_{ij} are the amplitude of the electric field and modified amplitude function, along a grid of k cells from transmitter i to receiver j ; \mathbf{L}_{ijk} represents the segment length through the k^{th} cell; A'_0 is the modified normalization factor.

The system of linear equations to be solved (Equation 2.21) can now be written by the model parameters vector $\mathbf{m} = (A'_0, \alpha_1, \alpha_2, \dots, \alpha_k, \dots)$, which contains the normalization factor A'_0 and the attenuation values α_k . A_0 that symbolizes the source strength is approximated and introduced as a constant to the inversion. However, the uncertainty in A_0 (Equation 2.27) increases the ill-posedness of the problem in comparison to ray-based travel-time inversion (which does not estimate A_0), and causes shifts in the absolute values of the attenuation. To stabilize the inversion, damping and smoothing constraints are included in a similar way to the travel-time inversion.

2.4 GPR full-waveform inversion methodology

GPR full-waveform inversion (FWI) is introduced in Section 1.2, but here the method is presented in more detail. The general workflow of the FWI is shown in Figure 2.1. In Part I, we describe the pre-processing stage. In Part II, the effective source wavelet (ESW) estimation is defined. In Part III, we discuss the inversion algorithm and implementation details. Note that Part I and II are only required for the applications to experimental data. The crosshole GPR FWI is implemented in 2D, therefore Equations 2.1-2.4 determine the propagation of the waves in the x-z plane for the forward model. In crosshole cases the vertical component of the electrical field is obtained by the standard vertical antenna

orientations. Therefore, in the following the transverse electrical mode of the Maxwell Equations is used.

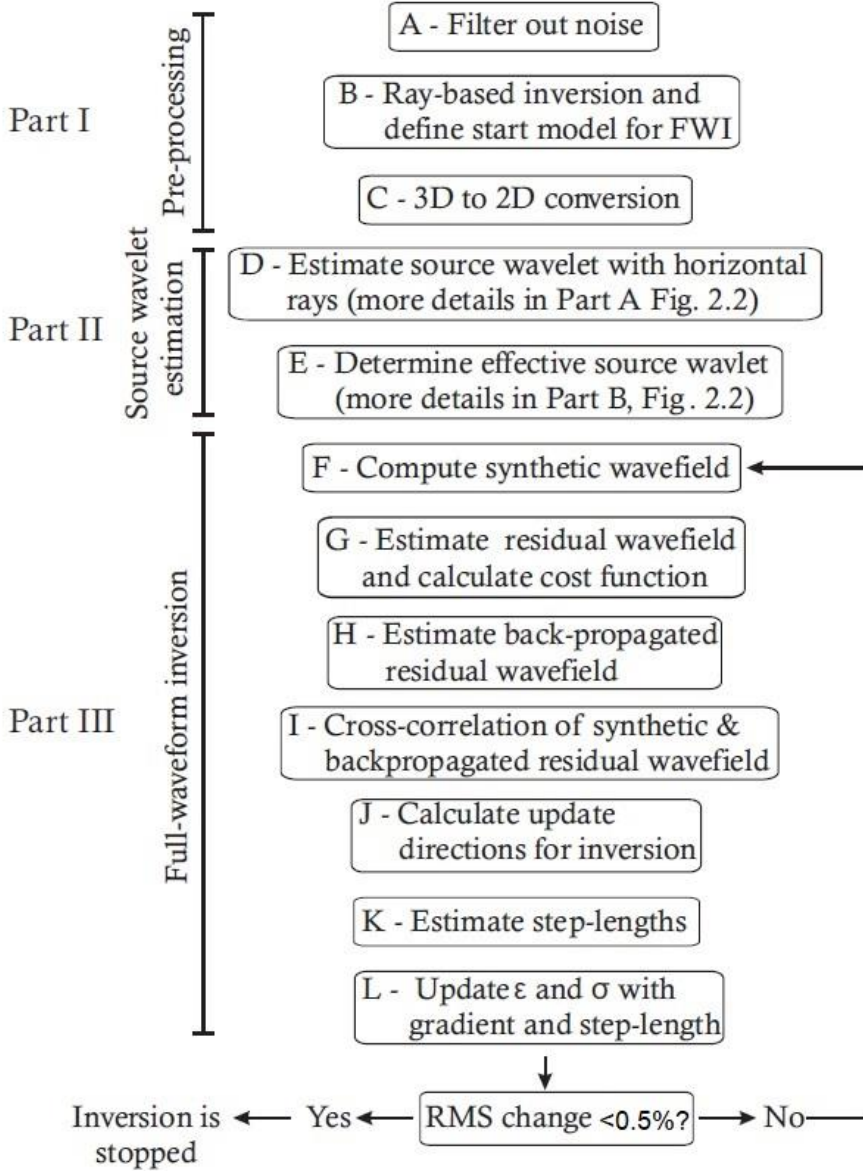


Figure 2.1: Full-waveform inversion workflow showing the three main parts: preprocessing, source wavelet estimation and full-waveform inversion. The arrow indicates that these steps should be repeated until the misfit between the observed and synthetic data between sequenced iterative steps is below 0.5%. (adopted from Klotzsche et al., 2010).

2.4.1 Data pre-processing

The processing part involves three main steps. First noise is removed outside the frequency source spectrum by applying a dewow filter and if necessary a band-pass filtering (Figure 2.1, Step A). Second, the starting model for the FWI is obtained based on ray-based inversions (Figure 2.1, step B) using the first -arrival travel times and first-cycle amplitude inversion, which provide ε_r and σ from Equations 2.18-2.19.

Note that for high contrast changes, especially at the inversion domain boundary often ray-based models do not provide starting models within half a wavelength. Therefore, these models needed either manually updated by testing (Klotszche et al., 2012, 2013) or applying an amplitude analysis approach as introduced by Klotszche et al. (2014). This approach allows detecting and mapping the high contrast zones based on measured data already by checking the data for characteristic wave propagation behaviour, which are related to high contrast zones.

2.4.2 3D to 2D data transformation

The GPR FWI algorithm is implemented in the computationally attractive 2D domain, while the observed data was measured in 3D. Therefore, it is required to account for the 3D radiation characteristics of electromagnetic wave propagation and to adapt the data to the 2D scheme. The geometrical spreading describes the decrease of the energy density along a propagating wave front. The wave front area is widening with increasing travel distance. Consequently, the geometrical spreading is different in 2D and 3D cases, as for the 3D case the wave front propagates spherically and the amplitude A decay is proportional to the travelled distance, while the wave radius r depends on the velocity and time t , where $r = vt$ and $A \propto 1/t$. In 2D, the energy is spread over the perimeter of the circle, which leads to the geometrical amplitude decay of $A \propto 1/\sqrt{r} \propto 1/\sqrt{t}$ (Liner, 2004). Therefore, it is necessary to multiply the 3D data with \sqrt{t} when using a 2D code. Furthermore, in 2D the sources are implicitly considered as infinitive long extended lines of point dipole in the perpendicular direction of the 2D plane. This is not true in reality, thus a phase shift must be introduced.

To compensate for differences in geometrical spreading and pulse shape (Figure 2.1, step C), we apply a 3D to 2D transformation technique (Bleistein, 1986), as proposed in the GPR FWI scheme by Ernst et al. (2007). The transformation uses a phase shift of $\pi/4$ and a scaling factor of $\frac{1}{\sqrt{\omega}}$ in the frequency domain. The corrected data $\hat{\mathbf{E}}^{2D}$ for the transmitter at locations \mathbf{x}_{trn} and receiver \mathbf{x}_{rec} .

$$\hat{\mathbf{E}}^{2D}(\mathbf{x}_{trn}, \mathbf{x}_{rec}, \omega) = \hat{\mathbf{E}}_{obs}(\mathbf{x}_{trn}, \mathbf{x}_{rec}, \omega) \sqrt{\frac{2\pi t(\mathbf{x}_{trn}, \mathbf{x}_{rec})}{-j\omega \varepsilon^{mean} \mu}}, \quad \text{Eq. (2.29)}$$

where ω is the frequency, $\hat{\mathbf{E}}_{obs}$ is the original data, and $t(\mathbf{x}_{trn}, \mathbf{x}_{rec})$ are the travel times (account for 3D to 2D geometrical spreading), ε^{mean} is the mean dielectric permittivity of the media, and \wedge indicates the frequency domain. Note that this assumption is only valid in the far field, which is for most crosshole

applications achieved (Ernst et al., 2007b). Furthermore, the transformation assumes that the highest amplitude is associated with the first arrival time. In cases where this is not fulfilled, like in the presence of high contrast layers, this transformation produces errors in the transformed data, which affect the final permittivity and conductivity tomograms (Mozaffari et al., 2020). In addition, as in crosshole setup the energy is spread in 3D, it is not possible to distinguish between in-plane and out-of-plane events. However, the assumption is that most energy comes from in-plane events, which are linked to the media in the first few cycles of the traces. In a heterogeneous aquifer with presence of a tracer, that imposes large dielectric contrasts over decimeter scale distances this assumption needs to be revalidated.

2.4.3 Full-waveform forward model

As part of the GPR FWI scheme, a forward model that simulates the entire EM fields based on Maxwell Equations (Equations 2.1-2.4) is required. A 2D finite-difference time-domain (FDTD) solution of the Maxwell Equations in Cartesian coordinates is applied to solve the forward problem (for more details and mathematical descriptions see Ernst et al. (2007) and Meles et al., (2010)). The forward model is necessary for the effective source wavelet estimation and the FWI, thus a large amount of computing resources is necessary for the FWI scheme (Figure 2.1).

2.4.4 Source wavelet estimation

The source wavelet is unknown, and is necessary to be estimated (Figure 2.1, Steps D,E) prior to the FWI, to model the entire waveform correctly and to reduce the ill-pose of the FWI problem. The effective source wavelet reflects the current density pattern of the finite length antenna and the antenna coupling conditions, e.g., due to the influence of borehole filling, either air or water. The steps of the effective source wavelet estimation are adopted from Klotzsche et al. (2010) and illustrated in detail in detail in Figure 2.2.

Part A describes the initial source wavelet estimation. There, the shape of the wavelet is determined without considering any amplitude information. Only the horizontal travelling waves are chosen, then they are normalized and aligned to estimate an average pulse (Figure 2.2, step 1). These traces are cross-correlated and as a result, data containing erroneous wave shapes due to for example interfering reflections are identified and excluded. Because the electric field is proportional to the time derivative of the current density source wavelet (Klotzsche et al., 2013b), to obtain the shape of the initial source wavelet, we divide the average Fourier transformed selected electric field pulse by $j\omega$ in the frequency domain (Figure 2.2, step 2). This wavelet is normalized to 1 and the amplitude is optimized in the next step. Part B describes the steps for correction of the first initial source estimation. First, synthetic data is calculated using the 2D FDTD code for each Tx-Rx pair (Figure 2.2, steps 3-4). Therefore, the estimated source wavelet $S_{in}(t)$, and the ray-based permittivity ϵ_{ray} and conductivity σ_{ray} models are utilized. Note that these starting models later also used as starting models for the FWI and if these models are updated also the ESW needs to be updated.

Mathematically, the GPR data $\mathbf{E}_{obs}(t)$ can be seen as the convolution of the source wavelet $\mathbf{S}(t)$ with the impulse response of the earth $\mathbf{G}(t)$ (Green's function) in the time-domain, or equivalently, as the multiplication of the source spectrum $\widehat{\mathbf{S}}(f)$ with the Fourier-transformed Green's function $\widehat{\mathbf{G}}(f)$ in the frequency f domain. Therefore, an effective source wavelet $\widehat{\mathbf{S}}(f)$ can be calculated by deconvolving the data $\widehat{\mathbf{E}}_{obs}(f)$ with an appropriate Green's function $\widehat{\mathbf{G}}(f)$ calculated using the travel time inversion results as input. This is best done using a least-squares approach in the frequency domain (Ernst et al., 2007b; Streich, 2007b). The Green's function $\widehat{\mathbf{G}}(f)$ is calculated by division of $\widehat{\mathbf{E}}_{syn}(f)$ in the frequency domain with the initial wavelet spectra $\widehat{\mathbf{S}}_{k=0}(f)$ (Figure 2.2, step 5). Then we estimate $\widehat{\mathbf{S}}_{k=1}(f)$ by dividing the spectral observed data $\widehat{\mathbf{E}}_{obs}$ by Green's function $\widehat{\mathbf{G}}(f)$ using all traces in a least-squares sense (Figure 2.2, steps 6). We apply the quantities η_D and η_I as pre-whitening factors to stabilize the solution and avoid a division by zero when notches are present in the spectrum of $\widehat{\mathbf{G}}(f)$. Next, the time-domain source wavelet $\mathbf{S}_{k+1}(t)$ is calculated by the inverse Fourier transformation (Figure 2.2, step 7). Steps 3-7 can be repeated until the source wavelet has converged and is stable, where k indicated the iteration (Loop 1), however one correction is usually enough. Note that after this step the phase and the amplitude were updated. Part C (Figure 2.2) describes an additional option to update and refine the source wavelet after a few FWI iterations, when the permittivity ϵ_{k+1} and conductivity σ_{k+1} models have been updated (Loop 2).

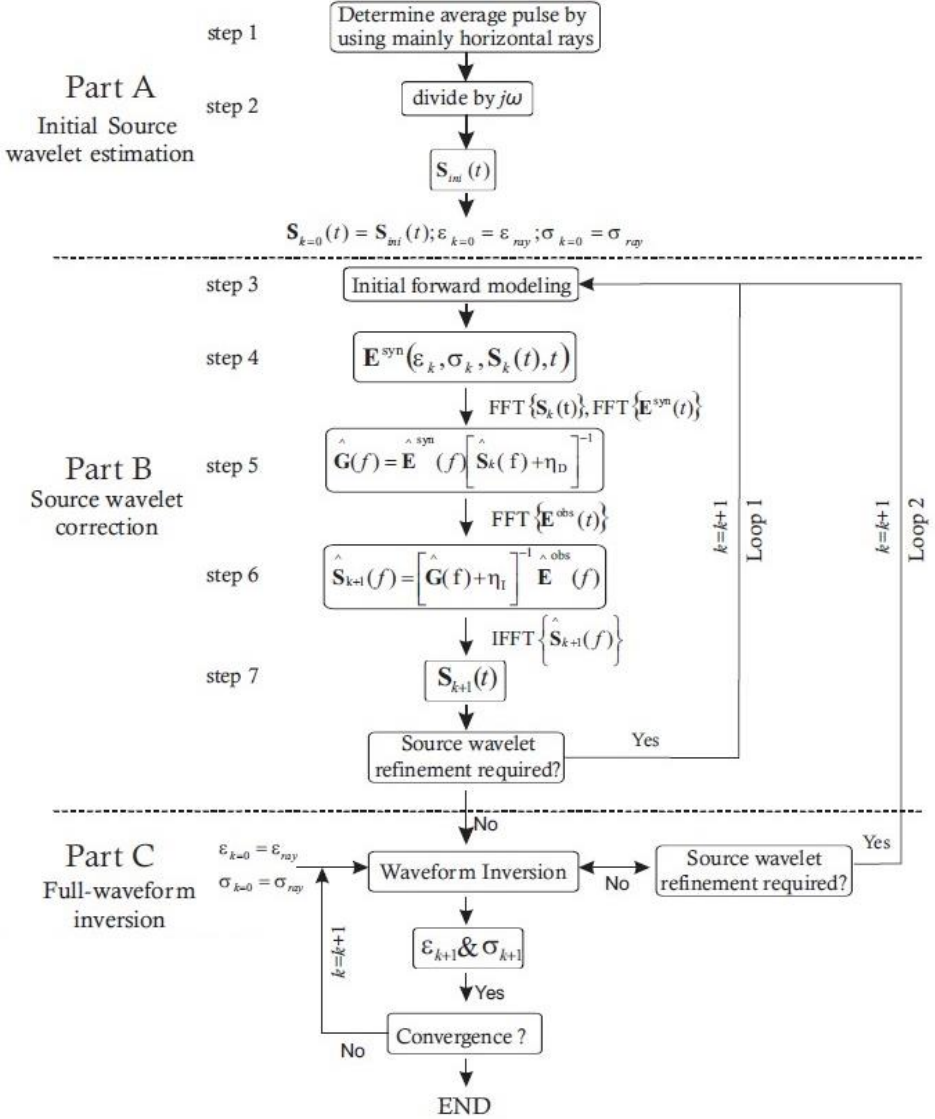


Figure 2.2: Source wavelet estimation flow consisting of three parts: Part A: initial source wavelet estimation using averaged horizontal rays (steps 1 - 2), Part B: the source wavelet correction (steps 3 - 7) with the deconvolution method using all available data (Klotzsche et al., 2019b) and Part C: source wavelet refinement during the full-waveform inversion. The source wavelet estimation is always carried out before starting the full-waveform inversion (loop 1) and can also be performed after several iterations of the full-waveform inversion (loop 2).

2.4.5 FWI inversion scheme

After the initial models and the effective source wavelet are obtained the FWI can be performed. Note that the synthetic data based on the initial models and the effective source wavelet need to be within a half-wavelength with the observed data, in order to avoid cycle-skipping and to update the inversion in the wrong direction.

2.4.5.1 Inverse problem

The full-waveform inversion approach uses conjugate gradient method (Tarantola, 1984) and involves finding the spatial distribution of the permittivity and conductivity models that minimize the squared norm cost (misfit) function $C_{FW}(\varepsilon, \sigma)$ between the modelled \mathbf{E}_{mod} and measured \mathbf{E}_{obs} traces for all transmitter-receiver combinations within a defined time window (Figure 2.1, Part III):

$$C_{FW}(\varepsilon, \sigma) = \frac{1}{2} \sum_{trn} \sum_{rec} \sum_t [\mathbf{E}_{mod}^{trn}(\varepsilon, \sigma) - \mathbf{E}_{obs}^{trn}]_{rec,t}^T \cdot \delta(\mathbf{x}' - \mathbf{x}_{rec}, t' - t) [\mathbf{E}_{mod}^{trn}(\varepsilon, \sigma) - \mathbf{E}_{obs}^{trn}]_{rec,t}, \quad \text{Eq. (2.30)}$$

where E^{trn} stands for the electric field of a particular transmitter and contains the entire space-time domain \mathbf{x}' and t' , superscript T indicates the transposed operator, δ is the delta function, \mathbf{x}_{rec} is the receiver location, and trn , rec , and t indicate sums over transmitters, receivers, and observation times. In the full-waveform inversion C_{FW} the complete traces of the electrical field E^{trn} in time are taken into account, whereas in the travel-time C_{TT} (Equation 2.25) only the first-arrivals are used the misfit function.

We use a gradient type approach that minimizes the cost function. The gradient indicate in which direction the model should be updated to reduce the misfit between the measured and modelled data. In addition, specific step-lengths for each cell need to be determined which indicate the magnitude of the model updates.

2.4.5.2 Gradients of the misfit function

Permittivity and conductivity perturbations $\delta\varepsilon$ and $\delta\sigma$ are used to calculate the modelled electric field \mathbf{E}_{mod}^{trn} due to small changes in ε and σ (Meles et al., 2010). The Maxwell's equations can now be rewritten for small changes in the measured field for a perturbed system, which describes the changes in the measured wavefield due to permittivity and conductivity changes as $\delta\varepsilon$ and $\delta\sigma$ changes:

$$\begin{aligned} \mathbf{E}_{mod}^{trn}(\varepsilon + \delta\varepsilon, \sigma + \delta\sigma) - \mathbf{E}_{mod}^{trn}(\varepsilon, \sigma) &= \hat{G}(\partial_t \mathbf{E}^{trn} \delta\varepsilon + \mathbf{E}^{trn} \delta\sigma) \\ &= [\mathbf{L}_\varepsilon^{trn} \quad \mathbf{L}_\sigma^{trn}] \begin{bmatrix} \delta\varepsilon \\ \delta\sigma \end{bmatrix}. \end{aligned} \quad \text{Eq. (2.31)}$$

The operator \mathbf{L}^{trn} is defined for specific contribution at cell \mathbf{x} of permittivity and conductivity:

$$\mathbf{L}_\varepsilon^{trn}(\mathbf{x}') = \hat{G} \delta(\mathbf{x} - \mathbf{x}') \partial_{trn} \mathbf{E}^{trn} \quad \text{Eq. (2.32)}$$

$$\mathbf{L}_\sigma^{trn}(\mathbf{x}') = \hat{G}\delta(\mathbf{x} - \mathbf{x}')\mathbf{E}^{trn} \quad \text{Eq. (2.33)}$$

The gradients of C_{FW} can now be estimated from the first order approximation of C_{FW} in Equation 2.30:

$$C_{FW}(\varepsilon + \delta\varepsilon, \sigma + \delta\sigma) = C_{FW}(\varepsilon, \sigma) + \nabla C_{FW}^T \begin{bmatrix} \delta\varepsilon \\ \delta\sigma \end{bmatrix} + O(\delta\varepsilon^2, \delta\sigma^2) \quad \text{Eq. (2.34)}$$

To estimate the total gradient ∇C_{FW} , first all the separate contributions for each transmitter, receiver and observation time combination terms of Equation (2.30) are calculated. Next, all these gradients terms are added. The summation of the misfit function over all transmitters t can be written as:

$$\begin{bmatrix} \nabla C_\varepsilon(\mathbf{x}') \\ \nabla C_\sigma(\mathbf{x}') \end{bmatrix} = \sum_t \begin{bmatrix} \delta(\mathbf{x} - \mathbf{x}') \partial_t \mathbf{E}_{mod}^{trn} \\ \delta(\mathbf{x} - \mathbf{x}') \mathbf{E}_{mod}^{trn} \end{bmatrix}^T \hat{G}^T \mathbf{R}^{trn} \quad \text{Eq. (2.35)}$$

where \mathbf{R}^t , is the generalised residual wave field:

$$\mathbf{R}^{trn} = \sum_r \sum_t [\Delta E^{trn}]_{rec,t} \quad \text{Eq. (2.36)}$$

where $\hat{G}^T \mathbf{R}^{trn}$ can be interpreted as the back-propagated residual wavefield in the same medium as E^{trn} . The spatial *delta* function $\delta(\mathbf{x} - \mathbf{x}')$ corresponds to the spatial components of the gradients and reduces the inner product to a zero-lag cross-correlation in time. The residual wavefield $\hat{G}^T \mathbf{R}^{trn}$ is back-propagated from all receivers to the corresponding transmitters through the model, simultaneously (Figure 2.1, step H). Finally, the gradient at each point \mathbf{x} is obtained by a zero-lag cross-correlation of the stored values of E^{trn} with the back-propagated residual wavefield and by summing over all transmitters and times-steps (Figure 2.1, step I, J).

2.4.5.3 Step lengths

FWI requires step-length to identify the magnitude of the ε and σ models update that is necessary for each iteration. We use two individual step-lengths that allows a simultaneously update of the permittivity and conductivity models in each iteration (Meles et al., 2010), while other approaches only consider one step length and a factor for the parameters. The updated ε and σ models can be formulated as:

$$[\varepsilon_{upd}] = [\varepsilon] - \zeta_\varepsilon [\nabla C_\varepsilon], \quad \text{Eq. (2.37)}$$

and

$$[\sigma_{upd}] = [\sigma] - \zeta_\sigma [\nabla C_\sigma], \quad \text{Eq. (2.38)}$$

The step lengths ζ_ε and ζ_σ determine how far we will move alongside the direction indicated by misfit function C , too small ζ_ε and ζ_σ leads to slow convergence while too big cause overshooting of the FWI. Therefore, the step-lengths are adjusted by choosing appropriate perturbation factors κ_ε and κ_σ :

$$\zeta_\varepsilon = \kappa_\varepsilon \frac{\sum_{trn} \sum_{rec} \sum_t [\mathbf{E}_{syn}(\varepsilon + \kappa_\varepsilon \nabla C_\varepsilon, \sigma) - \mathbf{E}_{syn}(\varepsilon, \sigma)]_{rec,t}^T \delta(\mathbf{x} - \mathbf{x}_{rec}, t - t') [\mathbf{E}_{syn}(\varepsilon, \sigma) - \mathbf{E}_{obs}]_{rec,t}}{\sum_{trn} \sum_{rec} \sum_t [\mathbf{E}_{syn}(\varepsilon + \kappa_\varepsilon \nabla C_\varepsilon, \sigma) - \mathbf{E}_{syn}(\varepsilon, \sigma)]_{rec,t}^T \delta(\mathbf{x} - \mathbf{x}_{rec}, t - t') [(\mathbf{E}_{syn}(\varepsilon + \kappa_\varepsilon \nabla C_\varepsilon, \sigma)) - \mathbf{E}_{syn}(\varepsilon, \sigma)]_{rec,t}} \quad \text{Eq. (2.39)}$$

and

$$\zeta_\sigma = \kappa_\sigma \frac{\sum_{trn} \sum_{rec} \sum_t [\mathbf{E}_{syn}(\varepsilon, \sigma + \kappa_\sigma \nabla C_\sigma) - \mathbf{E}_{syn}(\varepsilon, \sigma)]_{rec,t}^T \delta(\mathbf{x} - \mathbf{x}_{rec}, t - t') [\mathbf{E}_{syn}(\varepsilon, \sigma) - \mathbf{E}_{obs}]_{rec,t}}{\sum_{trn} \sum_{rec} \sum_t [\mathbf{E}_{syn}(\varepsilon, \sigma + \kappa_\sigma \nabla C_\sigma) - \mathbf{E}_{syn}(\varepsilon, \sigma)]_{rec,t}^T \delta(\mathbf{x} - \mathbf{x}_{rec}, t - t') [(\mathbf{E}_{syn}(\varepsilon, \sigma + \kappa_\sigma \nabla C_\sigma)) - \mathbf{E}_{syn}(\varepsilon, \sigma)]_{rec,t}}. \quad \text{Eq. (2.40)}$$

To avoid numerical artifacts close to the boreholes, caused by high gradients close to the antenna positions, we use a methodology proposed by van der Kruk et al. (2015). It applies a gradient preconditioning operator \mathbf{P}^k to damp the transmitter and receiver artifacts. For that, the maximum values of the forward-propagated field and the back-propagated residual field are used, with

$$\mathbf{P}^k(\mathbf{x}) = \frac{b(\mathbf{x})}{\max_x b(\mathbf{x})}, \quad \text{Eq. (2.41)}$$

$$b(\mathbf{x}) = \frac{1}{a(\mathbf{x}) + C_{stab} \bar{a}}, \quad \text{Eq. (2.42)}$$

$$a(\mathbf{x}) = \max_t |\mathbf{E}_{syn}| + \max_t |\mathbf{R}^{trn}|, \quad \text{Eq. (2.43)}$$

where C_{stab} represents the stabilization factor that can range between 1 and 100, which needs to be estimated for ε_r and σ gradients. The terms \mathbf{E}_{syn} and \mathbf{R}^{trn} depend on space \mathbf{x} and time t . The term \bar{a} represents the spatial average of $a(\mathbf{x})$. The first term on the right side of equation 2.43 considers the maximum of the synthetic wavefield, and the second term takes the maximum of the residual wavefield into account.

2.4.5.4 FWI convergence criteria

The ε and σ models at each iteration are updated with the obtained gradient and step-length using Equations 2.33 and 2.34 in an iterative process (Figure 2.1, step L) until the following criteria are achieved (Klotzsche et al., 2019b):

- 1) the root-mean-squared error (RMSE) of the observed and modeled data between subsequent iterations changes less than 0.5%,
- 2) decrease of at least 50% in RMSE in contrast to the ray-based inversion starting model,
- 3) absence of the remaining gradients (in the FWI optimization method) for the final models, and
- 4) good fit between the measured and modeled data (direct sample by sample correlation without any shift should be better than 0.8). Note that this value indicates a good trend in the data fit and is based on experimental data experience.

It is important to note that all four points need to be satisfied. For example, if the data fit is less good, although maybe the other three points are satisfied, it indicates that a model was found which is not providing data that fit the entire measured data range (Klotzsche et al., 2014).

Chapter 3

Realistic hydrological aquifer model for tracer modelling ¹

In this chapter, we develop a realistic hydrological model domain of an aquifer in which we simulate flow and transport processes to realistically model time-lapse GPR data and perform the FWI for the different tracer scenarios. This model represents an aquifer with a high spatial resolution considering heterogeneity, which is necessary to demonstrate the potential of the FWI to reconstruct small-scale structures and hence plume spreading. This model is based on an extensive database of different hydrological and geophysical measurements of the Krauthausen test site in Germany. Thereby, we first adopt a 3D hydrological facies model, which was in a second step considered to calculate for each of the facies a histogram and correlation lengths of the hydrological properties (porosity and hydraulic conductivity) and dielectric properties (permittivity and electrical conductivity). Last, we established a stochastic model of the hydrological and dielectric properties for each of the facies. This high-resolution aquifer model is then used to mimic realistic flow and transport scenarios, to generate a plume fate from which different tracer types, magnitudes and distributions are derived, by using adequate petrophysical relations that convert the concentration to dielectric properties. The synthetic tracer fate enables a thoughtful consideration for site-specific design and measurement planning.

¹ Adapted from Haruzi, P., Schmäck, J., Zhou, Z., van der Kruk, J., Vereecken, H., Vanderborght, J., & Klotzsche, A. (2022). Detection of tracer plumes using full-waveform inversion of time-lapse ground penetrating radar data: a numerical study in a high-resolution aquifer model. *Water Resources Research*, e2021WR030110.

3.1 Description of the Krauthausen test site

The Krauthausen test site is located north to Düren and south to Forschungszentrum Jülich, North Rhine-Westphalia, Germany. It is part of the TERENO network and was established 30 years ago. Therefore, long and intensive investigations have been performed in terms of hydrology, hydrogeology and geophysics. The test site extent is 200 x 70 m and has more than 70 wells used for pumping and water sampling which reach to 9 - 12 m depth (Figure 3.1). The site was investigated in multiple studies using hydrogeological characterization by cone penetration test (CPT) (Tillman et al., 2008), tracer tests (Vereecken et al., 2000, Vanderborght and Vereecken, 2001), soil and water sampling (Englert et al., 2000), borehole velocity measurements (Englert, 2003), pumping tests (Li et al., 2008), and geophysical imaging methods of ERT (Kemna et al., 2002, Müller et al., 2010), GPR (Oberröhrmann et al., 2013, Gueting et al., 2015, 2017, Zhou et al., 2020), and spectral induced polarization (Kelter et al., 2018).

The ground water level varies through the year between 1-3 m below surface (Englert, 2003). The Krauthausen aquifer is an alluvial sandy-gravel aquifer with a silt and clay content that varies between 0.5 - 7.5% (Vereecken et al., 2000). The aquifer can be divided into three distinct hydrologic compartments (Figure 3.1b). High K layer from water level down to ~ 4 m of gravel (with large clay extent), lower K from approximately 4-6 m of well-sorted medium size sand, and intermediate K of a sandy gravel layer, with a general trend of increasing gravel extent and K with depth (Gueting et al., 2015). Each layer by itself is heterogeneous, manifested by a recent tracer test and high-resolution characterization of GPR FWI (Gueting et al., 2015, 2107). The groundwater velocity direction distributes spatially and varies between 210°N to 90°N , and the mean flow direction is 340°N (Vereecken et al., 2000), with an overall specific discharge of approximately 1 m/day (Müller et al., 2010). Heterogeneity of K that mostly influences preferential path thickness was derived from $\ln K$ ($\ln \equiv \log_{10}$) histograms with variance of 0.6 and correlation lengths (l) in the vertical and horizontal directions, $l_v=0.18$ m (Englert et al., 2003) and $l_h=1.75$ m (Tillmann et al., 2008), respectively, at the main facies below 6 m. With respect to GPR, the aquifer is well suited due to its low to intermediate bulk electrical conductivity (σ_b) between 5 and 20 mS/m (Zhou et al., 2021).

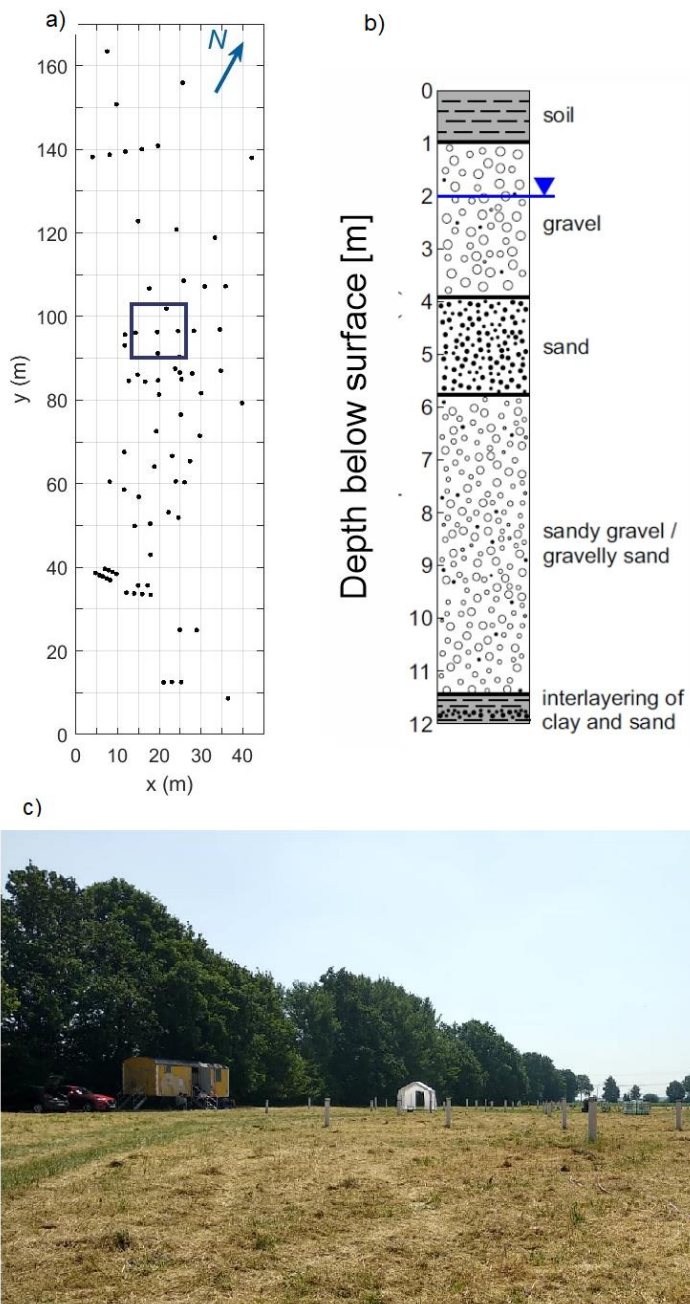


Figure 3.1: Krauthausen test site. a) Locations of the wells. Rectangle represents the area, where the salt tracer is injected and monitored in Chapter 5. b) Cross-section of the uppermost Krauthausen aquifer adapted from Döring (1997) and Tillmann et al. (2008). c) View at the site from the most northern point.

3.2 Stochastic aquifer model setup

We modelled the Krauthausen aquifer using information from past studies. As a first step, we adopted the 3D facies model (Figure 3.2a) from Gueting et al. (2017 and 2018), which was generated based on adjoint tomograms from 2D GPR full-waveform inversions, and subsequently expanded to a 3D cube using multiple-point statistics. This model is composed of three facies: Facies 1 of gravel (mainly above 4 m), Facies 2 of sand (mainly between 4-6 m) and Facies 3 of sandy gravel (mainly below 6 m). The model covers a domain size of 20.07 x 30.15 x 4.68 m, from 3.58 to 8.26 m depth and this is composed of cubic cells with an edge size of 0.09 m. As a second step, based on available data (see Table 3.1), we calculated histograms and correlation lengths to each of the four aquifer parameters (hydraulic conductivity (K), porosity (ϕ), ε_r , σ_b) in the 3 facies. The CPT data provide local measurements with high vertical resolution information about mechanical resistance, natural gamma activity, bulk density, matrix density, water content and electrical resistivity. The CPT measurements were used by multiple regression (Tillman et al., 2008) to estimate local grain size distributions, from which K was calculated using empirical formulas provided in the literature. ϕ in the saturated part of the aquifer is equal to the water content. For our hydrological aquifer model, we considered K and ϕ . For our aquifer model of dielectric properties which will be used later for GPR modelling, ε_r was calculated from ϕ (CRIM model, Birchak et al., 1974) and σ_b from electrical resistivity. As a third step, we generated the distributions of the aquifer parameters (K , ϕ , ε_r , σ_b), in each of the three facies using stochastic Gaussian simulation (SGSIM) based on variogram modeling (SGeMS software, Remy et al., 2009).

For each property and facies (see Figure 3.2b-e, Table 3.1), stochastic simulations were performed over the entire model domain. The resulting models were then integrated into one aquifer model domain (“cookie-cutter”) based on the 3D facies distribution. K and ϕ models were simulated independently with no spatial cross correlation, ε_r was calculated directly from the ϕ model using the CRIM model (Birchak et al., 1974), and σ_b was simulated using sequential Gaussian co-simulation (COSGSIM) based on the ε_r spatial distribution as a secondary information with correlation $r=0.5$ in each facies (Gueting et al., 2015, 2020). For all the stochastic simulations an exponential variogram model was used (Gringarten and Deutsch, 2001).

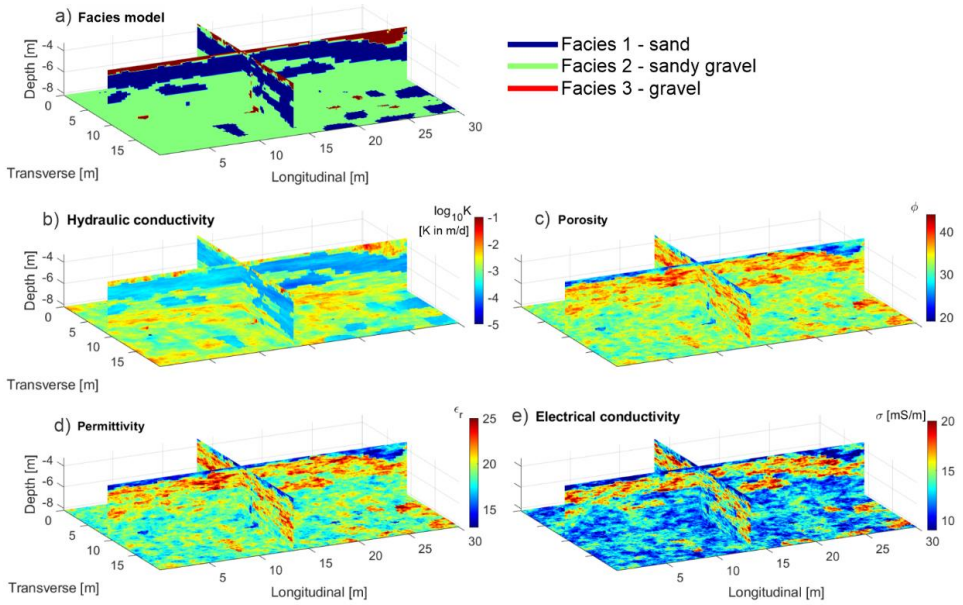


Figure 3.2: Aquifer model domains used for the hydrological flow and transport modelling. (a) Facies model (adopted from Gueting et al. (2018)), (b) log-conductivity, (c) porosity model, (d) background relative permittivity, and (e) electrical conductivity.

Table 3.1: Mean values, variance, horizontal and vertical correlation lengths (I_h , I_v) of aquifer properties: the porosity ϕ , log hydraulic conductivity $\ln K$, relative permittivity ϵ_r and electrical conductivity σ_b of the Krauthausen test site used for stochastic simulation within Facies 1-3.

	ϕ^*	$\ln K^{**}$ [K in m/d]	ϵ_r^{***}	σ_b^{****} [mS/m]
Facies 1 - sand				
Mean	35.8	-7.69	21	17.2
Variance	7.7	0.1	2.94	2
I_v [m]	0.13	0.6	0.13	0.13
I_h [m]	0.56	5	0.56	0.56
Facies 2 - sandy-gravel				
Mean	31.9	-6.4	18.6	12
Variance	3.6	0.6	1.24	1.75
I_v [m]	0.12	0.18	0.12	0.12
I_h [m]	0.39	1.75	0.39	0.39
Facies 3 - gravel				
Mean	25.7	-5.78	15.2	10.3
Variance	6	1	1.97	1.5
I_v [m]	0.12	0.4	0.12	0.13
I_h [m]	0.6	0.3	0.6	0.6

* The mean variance of the porosity was calculated from water content point measurements from neutron logs at CPT locations (Tillmann et al., 2008). The correlation lengths I_h and I_v were calculated (using semi-variogram analysis) after conversion from ϵ_r tomograms at multiple GPR FWI planes (Gueting et al., 2017, Zhou et al., 2021) using the CRIM model.

** Mean value of $\ln K$ was adopted from a K model based on grain size distribution (GSD) (Bialas and Kleczkowski, 1970, Gueting et al., 2017). Variance and I_h of $\ln K$ were calculated based on a dense grid of vertical CPT with ~ 1.5 m horizontal separation distance (Tillmann et al., 2008), using a calibrated correlation between GSD and CPT geophysical properties (mechanical resistance, natural gamma activity and bulk density), where co-located data was available. $I_v=0.18$ m of $\ln K$ in the main Facies 2 of the model (green facie in Figure 3.2a) was adopted from borehole groundwater velocity measurement (Englert, 2003).

*** ϵ_r was calculated directly from the porosity model using CRIM model.

**** Mean value of σ_b and variance, I_h and I_v were calculated from σ_b tomograms at multiple GPR FWI planes (Gueting et al., 2017, Zhou et al., 2021).

3.3 Tracer transport simulation

We used a flow and transport model based on the designed aquifer model domain (Figure 3.2, Table 3.2) to imitate the past positive saline tracer test performed by Müller et al. (2010). The results of Müller et al. (2010) are used in our study as reference for the synthetic plume fate reconstruction. The 3D flow equation was solved using TRACE (Vereecken et al., 1994) and the transport equation was solved using a random-walk particle-tracking algorithm PARTRACE (Bechtold et al., 2011). We simulated a tracer injection for 7 days using a uniform water influx source of 20 m³/day between 3.58 - 8.26 m depth in the borehole, and a particle injection source of $1 \cdot 10^8$ “conservative or non- reactive” particles which were injected uniformly through the injection period, resulting in an injection concentration of $7.15 \cdot 10^5$ particles/m³. We modelled the borehole (diam. 50.8 mm, slots 0.5 mm) by a vertical column of grid cells (cubic, edge of 0.09 m) assigned with $K = 267$ m/d (Klotz, 1990) and a porosity of 1. The borehole was surrounded by a gravel pack that fills the well (diam. 0.328 m), modelled by 8 grid cell columns with $K = 2246$ m/d (Klotz, 1977) and a porosity 0.4. To solve for the total head and velocity distributions in the heterogeneous aquifer, we adopted a natural hydraulic gradient in the aquifer of 0.002 m/m (Vereecken et al., 2000) implemented by pressure head boundary conditions at the up and downstream boundaries, and zero flux conditions at the lateral, top and bottom boundaries. During the injection phase, we used the flow velocity field that was simulated considering the water injection in the well for the transport simulation. After the injection ceased, we simulated the tracer transport using a velocity field that represents the natural hydraulic gradient of the Krauthausen test site. The heterogeneity of the simulated plume was controlled by the stochastically-generated $\ln K$ and porosity (Table 3.1), which generated a variable fluid velocity. To account for the effect of velocity fluctuations on solute transport at the grid-cell scale, we used longitudinal and transverse dispersivities of 0.003 and 0.001 m, respectively.

The high-resolution aquifer model can predict transport processes with high spatial resolution as shown for day 15 after the start of the injection (Figure 3.3). In each plane view, the distribution of mass represents the sum of particle mass along the perpendicular axis to that plane. A substantial part of the plume was transported over a large distance in the lower part of the aquifer (between 7 and 8 m depth), whereas a second part of the plume was moving slower between roughly 5 and 6.5 m depth. The plume is mainly transported in Facies 2, which has a higher hydraulic conductivity than Facies 1, whereas Facies 3 (with the highest conductivity) was barely present within the range of depths where the tracer was injected.

This high-resolution flow and transport model allows us to compare the simulated tracer distribution at monitoring planes with the ERT results from the Krauthausen test site (Figure 3.4). Note that injection well and injection rate in the simulation were the same as the ones of the real tracer experiment for which the ERT images were obtained. For example, 15 days after the injection started, we can observe a splitting of the simulated plume in a transverse view, similar to the ERT images (Figure 3.4b,c). The

general similarity between simulated and ERT observed patterns suggests that the reconstructed facies distribution satisfactorily represents the true distribution. Note that the ERT images did not resolve small-scale tracer concentration variations and the results are more smoothed (Figure 3.4d). The simulated tracer distribution as imaged in longitudinal view (Figure 3.4d) is characterized by thin horizontal lenses of 0.1 m thickness with high concentrations (e.g., at 6.2 m depth), which corresponds with the vertical correlation length of $I_v = 0.18$ m of the hydraulic conductivity in Facies 2.

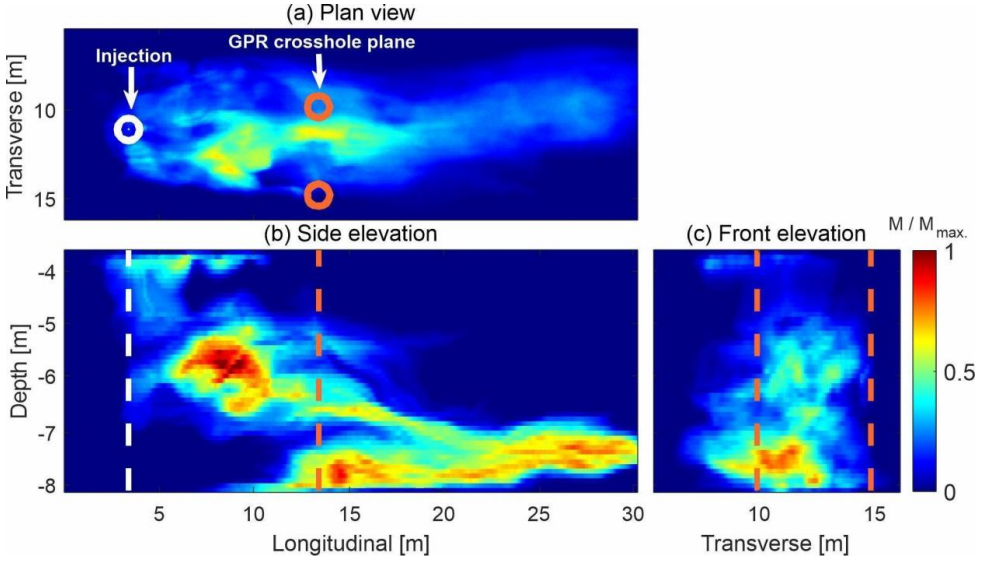


Figure 3.3: Normalized particles mass in plan (a), side (b) and front (c) view at day 15 after beginning of the tracer injection. The mass shown is a sum of mass in a line of cells perpendicular to the view. Color maps are normalized to the maximum mass for each.

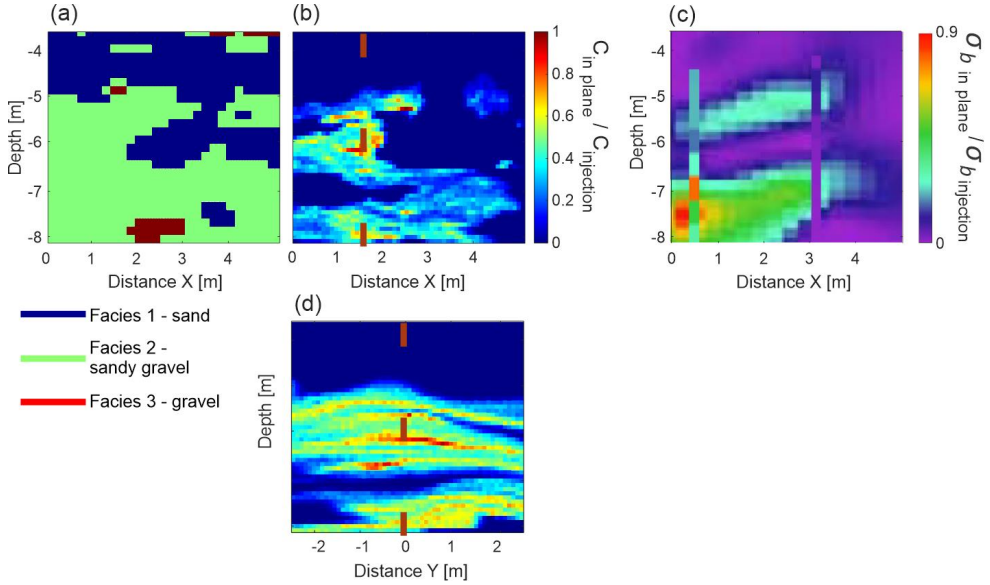


Figure 3.4: Tracer distribution in the monitoring plane. (a) Facies model, (b, d) concentration distribution in transverse and longitudinal directions, and (c) ERT image (modified from Müller et al. (2010), Figure 5) for the domain of the plane between the two GPR monitoring boreholes 10 m downgradient from the injection borehole (see Figure 3.3). The concentration represented the distribution after day 15 from the transport simulation normalized to injected tracer distribution. The red dashed lines in the perpendicular stitching tomograms (b) and (d) represent the stitching location. The electrical conductivity image is derived from the ERT tomogram and borehole loggers from a previous tracer test at day 15 after beginning the injection. Note that the logger data was obtained in two boreholes (seen as vertical anomalies) with vertical intervals of 0.35 m. The color scale represents the bulk electrical conductivity difference.

3.4 Tracer types and petrophysical relations

3.4.1 Change only in electrical conductivity: Salt and desalinated water tracer

The concentration of electrolytes in the groundwater determines the electrical conductivity of the fluid phase, whereas it has only minor influence on the permittivity (Sreenivas et al., 1995, Hagrey and Müller, 2000). For pore fluid conductivities that are smaller than ~ 15 S/m, the fluid electrical conductivity is proportional to the equivalent electrical charge concentration (Sreenivas et al., 1995). Salt tracers with a higher concentration are not often imaged with GPR in transmission mode, because of the high attenuation of the EM wave and the restriction of the ray-based approaches to derive quantitative high-resolution results (exception in Day-Lewis, 2003).

3.4.1.1 Implementation of the salt tracer simulation

We simulated solute transport using particle tracking and one particle was associated with a certain equivalent additional charge compared to the background charge concentration in the groundwater. If a tracer solution with a lower electrical conductivity than the background groundwater conductivity was injected (desalinated water), particles were associated with a ‘negative’ additional charge. Assuming that the electrical conductivity of the injected tracer solution $\sigma_{f_tracer_injection}$ is constant during the injection and that the background fluid conductivity in the aquifer $\sigma_{f_background}$ is constant in space, the electrical conductivity of the fluid at time t in a grid cell centered at a 3D coordinate \mathbf{x} , $\sigma_f(\mathbf{x}, t)$, was related to the number of particles in that grid cell $n_p(\mathbf{x}, t)$ at time t , the volume V_{cell} and porosity $\phi(\mathbf{x})$ in the grid cell, the total number of particles injected $n_{p, injection}$, and the total volume of water that was injected $V_{injection}$ as:

$$\sigma_f(\mathbf{x}, t) = (\sigma_{f_tracer_injection} - \sigma_{f_background}) \cdot C(\mathbf{x}, t) / C_{injection} + \sigma_{f_background} \quad \text{Eq. (3.1)}$$

with

$$C(\mathbf{x}, t) = n_p(\mathbf{x}, t) / (V_{cell} \cdot \phi(\mathbf{x})) \quad \text{and} \quad \text{Eq. (3.2)}$$

$$C_{injection} = n_{p_injection} / V_{injection} . \quad \text{Eq. (3.3)}$$

$C(\mathbf{x}, t)$ and $C_{injection}$ are the particle concentrations in a cell and in the injected tracer solution, respectively. Following Müller et al (2010) we consider a background pore fluid conductivity equal to $\sigma_{f_background} = 93.7$ mS/m. For the electrical conductivity of the injected salt tracer, we considered four cases:

- I. Injection of water with an electrical conductivity smaller than the background (negative tracer, *Desalinated case*, $\sigma_{f_tracer_injection} = 69.6$ mS/m),
- II. Injection with a conductivity slightly higher (positive tracer) than the background (*Low salinity case*: $\sigma_{f_tracer_injection} = 117.8$ mS/m),
- III. Injection with an Intermediate conductivity (*Intermediate salinity case*, $\sigma_{f_tracer_injection} = 610$ mS/m), and
- IV. Injection with a High conductivity (*High salinity case*, $\sigma_{f_tracer_injection} = 1525$ mS/m).

The *Low salinity case* adds the same magnitude of tracer fluid electrical conductivity as the *Desalinated case* subtracts, and the *High salinity case* adds 2.5 times the tracer fluid conductivity of the *Intermediate salinity case*. The background pore water conductivity and the negative and intermediate tracer conductivities were adopted from the tracer experiments carried out by Müller et al. (2010).

3.4.1.2 Salt tracer – electrical conductivity petrophysical relations

The bulk electrical conductivity σ_b is simplified by an adapted Archie's Law which considers a model of two conductors in parallel: the dissolved ions in the water and adsorbed ions on the soil surface as described by Mualem and Friedman (1991):

$$\sigma_b(\mathbf{x},t)=\sigma_f(\mathbf{x},t)/F(\mathbf{x})+ \sigma_{surf}(\mathbf{x}), \quad \text{Eq. (3.4)}$$

where $F(\mathbf{x})$ is the formation factor of saturated soil and $\sigma_{surf}(\mathbf{x})$ is the surface conductivity. $F(\mathbf{x})$ is linked to the complex geometry of the pore channels and is smaller for a larger porosity and smaller tortuosity of the pore network (Archie, 1942; Jackson et al., 1978). $\sigma_{surf}(\mathbf{x})$ is controlled by the specific surface area, surface charge density, and effective ionic mobility in the electrical double layer around the charged surface (Johnson et al., 1986). For low fluid conductivities, σ_{surf} depends in a non-linear way on the fluid conductivity σ_f . But, for sufficiently large σ_f , σ_{surf} reaches a constant value so that the relation between σ_b and σ_f is linear (Friedman, 2005), which we assume further in this study.

For σ_{surf} we based our chosen values on laboratory measurements on soil samples from Krauthausen test site (Müller et al., 2010). Surface conductivities were derived from measurements on sieved material and may therefore be larger than the true values. Therefore, we choose the lowest value observed for the mean σ_{surf} of 1.2 mS/m to better reflect the presence of stony material in the samples on the electrical conductivity with a standard deviation of 0.3 mS/m. Using this information, we generated a random field of $\sigma_{surf}(\mathbf{x})$ using with the same correlation lengths as σ_b (Table 3.1), but with no spatial correlation between σ_{surf} and σ_b (Müller et al., 2010). Then, we calculated $F(\mathbf{x})$ using Equation 3.4 with $\sigma_f(\mathbf{x},t)=\sigma_{f,background}$.

The flowchart in Figure 3.5 illustrates and summarizes the steps to obtain the tracer concentrations from GPR FWI σ_b images. First, $F(\mathbf{x})$ is recovered from background GPR FWI σ_b (Figure 3.5a) using $\sigma_{f,background}$ and assuming a constant σ_{surf} , which represents the average of $\sigma_{surf}(\mathbf{x})$ derived from lab measurements. Second, σ_f is estimated from time-lapse GPR FWI σ_b (Figure 3.5c). Last, the tracer $\sigma_{f,tracer}$ is calculated by subtracting $\sigma_{f,background}$ from σ_f .

3.4.2 Change in permittivity and electrical conductivity: Ethanol tracer

Ethanol is commonly used as an additive in gasoline blends (McDowell et al., 2003, Spalding et al., 2011), and is currently treated as an emerging environmental contaminant (Gomez and Alvarez, 2009). The dielectric properties of ethanol differ from water and these differences can be used to detect ethanol in water-saturated conditions in a sand matrix with GPR (Glaser et al., 2012). Pure ethanol has a relative permittivity of 26.7 at 10 °C and an electrical conductivity of 0.025 mS/m (Petong et al., 2000, Glaser et al., 2012). Note that the properties of the (ground)water at the Krauthausen test site at 10 °C are $\epsilon_r = 84$ (Malmberg and Maryott, 1956) and $\sigma \sim 90$ mS/m (Müller et al., 2010). Water-EtOH mixtures are miscible in all proportions as they are both dipolar liquids (Lide, 2004). Ethanol experiences polarization relaxation at central frequency of about 1 GHz and dispersive behavior becomes effective

from about $f > 200$ MHz, lower than those of water: 25 GHz and 1GHz, respectively (Petong et al., 2000). Thus, dispersive behavior is expected for high GPR frequency ranges, but was not considered in this study using low frequencies between 10-200 MHz with central frequency of 57 MHz. Regarding transport properties, ethanol has a lower density and a higher viscosity than water, and it is microbiologically degraded. However, we neglected density, degradation, and temperature effects on ethanol transport for our study, which focused on the ability to retrieve the distribution of the tracer from time-lapse GPR FWI parameter changes (ϵ_r , σ_b). Therefore, we simulated the ethanol plume migration with the same particle tracking method and using the same transport parameters (velocity, dispersivity) as the ones used for the salt tracer.

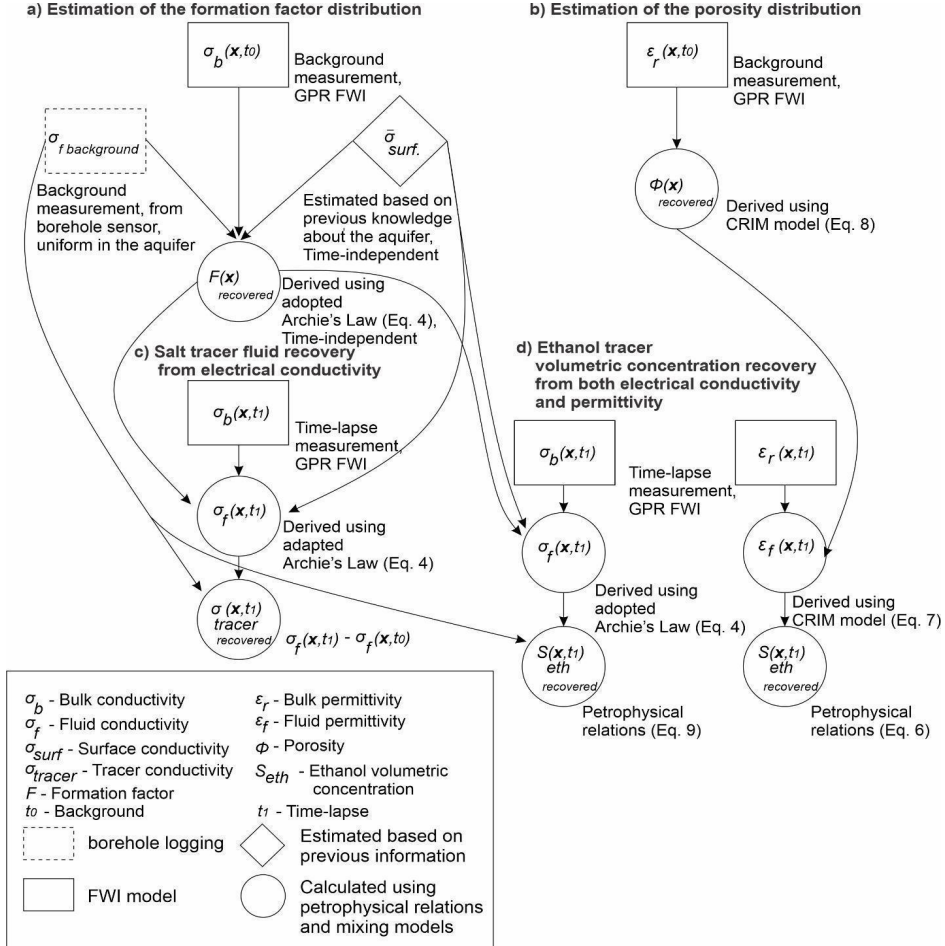


Figure 3.5: Flowchart presenting the recovery of solute (salt and desalinated water) and ethanol tracers. a) Formation factor and b) porosity recovery from background GPR FWI. c) Salt and d) ethanol recovery from time-lapse GPR FWI.

3.4.2.1 Implementation of the ethanol tracer simulation

We produced heterogeneous ethanol plumes that have the same structure as the salt tracer plumes. For the ethanol plume simulations, a particle represents a certain volume of ethanol V_{eth} , and therefore the volumetric concentration of ethanol in a cell $S_{eth}(\mathbf{x}, t)$ is:

$$S_{eth}(\mathbf{x}, t) = S_{eth\ injection} \cdot (n_{p\ injection} / V_{injection})^{-1} \cdot n_p(\mathbf{x}, t) / (V_{cell} \cdot \phi(\mathbf{x})), \quad \text{Eq. (3.5)}$$

where $S_{eth\ injection}$ is the volume concentration of ethanol in the injected solution, which was 0.5. The injection volume $V_{injection}$ and the duration of the injection were identical to those of the saline tracer simulations.

3.4.2.2 Ethanol-permittivity petrophysical relations

We derived an effective mixing model for permittivity of water ethanol mixtures, ϵ_{rf} , at 10°C by fitting a second-order polynomial to experimental data (Wyman, 1931):

$$\epsilon_{rf}(\mathbf{x}, t) = 84.05 - 42.6 \cdot S_{eth}(\mathbf{x}, t) - 15.7 \cdot S_{eth}(\mathbf{x}, t)^2 \quad \text{Eq. (3.6)}$$

To derive the bulk relative permittivity ϵ_r of the mixture-soil system, we used the Complex Refractive Index Model (CRIM) (Birchak et al., 1974)

$$\epsilon_r(\mathbf{x}, t) = (\phi(\mathbf{x}) \sqrt{\epsilon_{rf}(\mathbf{x}, t)} + (1 - \phi(\mathbf{x})) \sqrt{\epsilon_{rs}})^2 \quad \text{Eq. (3.7)}$$

where $\epsilon_{rs} = 4.5$ is the relative permittivity of the solid grains (Carmichael, 1988). In order to retrieve ϵ_{rf} and eventually $S(\mathbf{x}, t)$ from a GPR FWI permittivity model (Figure 3.5d), the porosity must be recovered from ϵ_r background measurements (Figure 3.5b):

$$\phi_{recovered}(\mathbf{x}) = (\sqrt{\epsilon_r(\mathbf{x}, t_0)} - \sqrt{\epsilon_{rs}}) / (\sqrt{\epsilon_{rf}} - \sqrt{\epsilon_{rs}}) \quad \text{Eq. (3.8)}$$

3.4.2.3 Ethanol-conductivity petrophysical relations

We modeled the electrical conductivity of the ethanol-water fluid mixture following Personna et al. (2013):

$$\sigma_f(\mathbf{x}, t) = (S_{eth}(\mathbf{x}, t) \cdot \sigma_{eth}^{\alpha} + (1 - S_{eth}(\mathbf{x}, t)) \cdot \sigma_{f, background}^{\alpha})^{1/\alpha} \quad \text{Eq. (3.9)}$$

Where $\sigma_{eth} = 0.0252$ mS/m is the ethanol electrical conductivity, with $\alpha = 0.3$ for ethanol volumetric concentration $S_{eth} \leq 0.5$.

In order to retrieve $\sigma_f(\mathbf{x}, t)$ and eventually $S_{eth}(\mathbf{x}, t)$ from a GPR FWI bulk electrical conductivity model (Figure 3.5c), the formation factor must be recovered from $\sigma_b(\mathbf{x}, t_0)$ background measurements (Figure 3.5a, Equation 3.2).

3.5 Conclusions

Using the extensive hydrological, hydrogeological, and geophysical dataset from the Krauthausen test site a high resolution and realistic 3D aquifer model was established. This model allows to construct realistic dimensions and heterogeneity of various tracer plumes and the corresponding electrical properties. Using this model we performed several different transport simulations to mimic a real tracer experiment at the entire aquifer dimension. The spatio-temporal field of concentration provides a setup to derive different tracer options and magnitudes that will change the dielectric properties and allow testing the FWI to reconstruct small-scale structures and hence plume spreading. Using this high-resolution aquifer model, it is not only possible to simulate different types of tracers, but also different magnitudes. Specifically, we provided a workflow to implement a recovery of solute and ethanol tracers from time-lapse GPR FWI measurements, which can be adapted to other tracers using the appropriate petrophysical relationships.

Chapter 4

Detection of tracer plumes using full-waveform inversion of time-lapse ground penetrating radar data: a numerical study in a high-resolution aquifer model ²

In this chapter, the potential of time-lapse crosshole GPR FWI for imaging tracer tests in heterogeneous aquifers is analyzed, using a numerical experiment. The setup of the experiment is based on the aquifer model that we generated based on Krauthausen test site, which was described in Chapter 3. Different tracer scenarios are analyzed using a saltwater, desalinated water and an ethanol tracer. Through petrophysical relations the plume concentrations I) of positive/negative salt tracers were converted to increases/decreases in σ_b , and II) of an ethanol tracer to decreases in both σ_b and ϵ_r . Crosshole GPR data were generated before and during the plume intrusion. We test the ability of FWI to recover the tracer distribution for different tracer concentrations that generated different changes and contrasts in ϵ_r and σ_b . To optimize the FWI of time-lapse data, we test different starting models for ϵ_r and σ_b . As the GPR FWI provides 2-D images, we investigated of out-of-plane effect (3D) on crosshole GPR data due to increase heterogeneity and magnitude in dielectric properties which caused by the tracer.

² Adapted from Haruzi, P., Schmäck, J., Zhou, Z., van der Kruk, J., Vereecken, H., Vanderborght, J., & Klotzsche, A. (2022). Detection of tracer plumes using full-waveform inversion of time-lapse ground penetrating radar data: a numerical study in a high-resolution aquifer model. *Water Resources Research*, e2021WR030110.

4.1 GPR FWI modeling

Synthetic GPR data were calculated using the highly resolved parameters of the aquifer model in a crosshole setup at 10 m distance from the injection borehole and perpendicular to the main flow direction (Figure 3.3, Figure 3.4a,b). The distance between the boreholes was 4.95 m. GPR data were derived below the water table (2.4 m depth) between 3.2 - 10 m depth. We added a realistic random instrumental noise level to the synthetic traces to evaluate its effect on the inversion performance (Appendix A.1). To realistically include reflection and refractions of the GPR data, we describe the unsaturated zone above 2.4 m depth with $\epsilon_r = 8$ (in the range of ϵ_r for “soil sandy dry” in Table 4.1 in Daniels (2004)). Similar to previously performed GPR measurements at the Krauthausen test site (Oberröhrmann et al., 2013), we used a semi-reciprocal acquisition setup with 35 transmitters and 69 receivers on each side, spaced with 0.2 and 0.1 m, respectively. With this setup a high ray coverage that enhances the electrical conductivity reconstruction can be obtained (Keskinen et al., 2021). We considered for our modeling a constant source wavelet (SW) with a central frequency of 57 MHz for the background and time-lapse cases (adopted from a previous FWI studies (Gueting et al., 2015, 2020)). It has been shown in experimental studies that for this operating frequency GPR FWI models can be obtained with a vertical resolution as small as 0.2 m (Zhou et al., 2020). Note that changes on the effective wavelet caused by the difference in borehole filling caused by the tracers are not considered in this study, and will be investigated for the experimental data applications.

In this numerical study, we concentrate on modeling and inverting 2D data, because of the high computational demanding 3D environment). For the inversion and forward modeling, we considered a model cell size of 0.09 m and 0.03 m, respectively. Note that the inversion grid has the same cell size as the transport simulation (Figure 3.4b). To avoid numerical artifacts in the crosshole GPR FWI that are caused by high gradients of the ϵ_r and σ_b near the boreholes, we considered the approach based on van der Kruk et al. (2015) that allows an update of the medium properties close to the boreholes by using a gradient preconditioning. The choice for the final iteration and to stop the inversion of the time-lapse datasets were fulfilled based on the FWI convergence criteria (Section 2.4.5.4).

4.2 GPR FWI results - Background models

To evaluate tracer changes over time, we derived FWI results for background data, measured before a tracer injection. The starting models for this FWI were derived from ray-based inversion results (Figure 4.4b,g). For the σ_b starting model, we considered a uniform σ_b of 15 mS/m provided by the mean of the first-cycle amplitude inversion and adaptations of this value based on numerical forward modeling tests (Holliger et al., 2001). In contrast to the ray-based inversion results, the FWI results better reconstruct the medium parameters and resolve finer structures, which the ray-based inversion is not able to detect (Figure 4.1b). Additionally, we performed the FWI for the noise-free and noise-added datasets (Figure 4.1c,d,h,i). Both ϵ_r and σ_b results show the same structures with decimeter-scale resolution for the noise-

free and noise-added datasets. The final RMSE of the noise-added and the reconstruction of the parameters is only slightly less good in comparison to the noise-free data (Table 4.1). The minor differences are caused because the noise-added dataset inversion cannot fit the data below the noise level. Since we have seen that the FWI models of both datasets reconstruct almost identical parameters, hereafter we consider only the more realistic noise-added dataset.

Table 4.1: Performance evaluation of the FWI results of the background data and models.

		Noise-free	Noise
GPR FWI data	Number of FWI iterations	67	59
	RMSE ^a · 10 ⁻⁷	1.26	1.42
	R^2 ^b	0.9986	0.9983
	MAE ^c · 10 ⁻⁷	4.94	5.41
	RMSE ^a · 10 ⁻⁷	1.77	1.96
FWI model ϵ_r	R^2 ^b	0.768	0.742
	MAE ^c	0.659	0.714
	RMSE ^a	0.862	0.936
FWI model σ_b	R^2 ^b	0.648	0.698
	MAE ^c [mS/m]	1.24	1.27
	RMSE ^a [mS/m]	1.64	1.68

^a – Root-mean squared error of the misfit between real and modelled data.

^b – R-squared of the GPR FWI data fit (between 40 and 250 ns).

^c – Mean absolute error

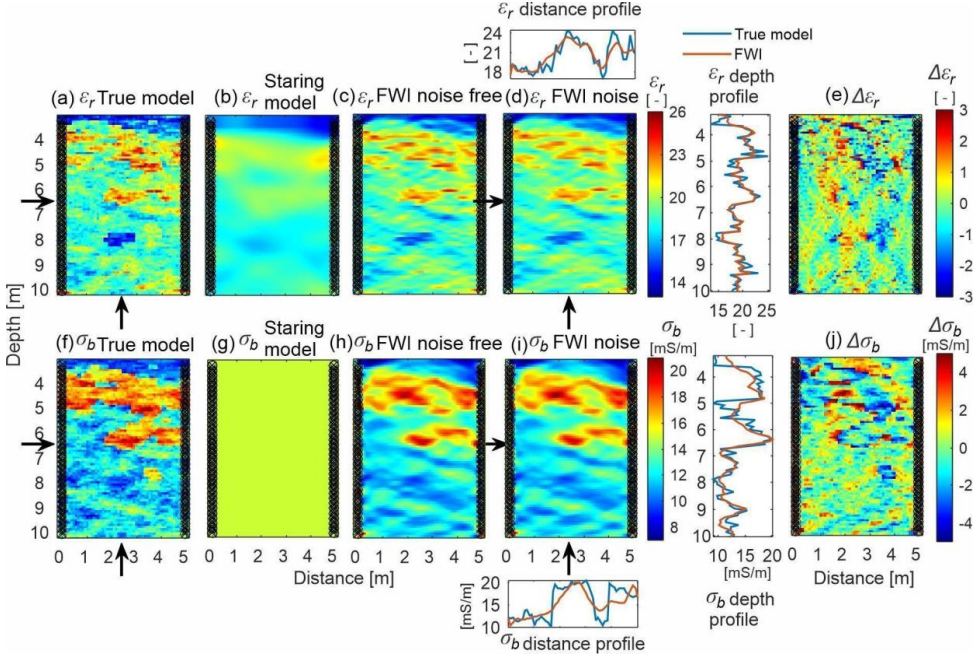


Figure 4.1: Background permittivity (top row) and electrical conductivity (bottom) models. (a, f) real models, (b, g) starting models based on ray-based inversion results, and (c, h) FWI models of the noise free dataset and (d, i) with noise. (e, j) Show the difference between real and FWI models with noise. Transmitter and receiver positions are located on black circles and crosses, respectively near the panel side boundaries. Above and right to (d), plots compare the real (blue) with FWI (orange) permittivity models (a, d) along vertical profile at 2.5 m distance and horizontal profile along 6.5 m depth (indicated by arrows). Below and right to (i), plots compare the real (blue) with FWI (orange) electrical conductivity models (f, i).

Generally, the reconstruction of the permittivity and conductivity is very good by the FWI, which is also indicated by the lower RMSE of the modeled data, the FWI data correlation coefficient of almost 1, and the low FWI ϵ_r and σ_b model errors compared to the real models (Figure 4.1e,j; Table 4.1). It can be noticed that the model errors are larger at locations of high contrasts. The RMSE of the background models are 0.86 for ϵ_r and 1.64 mS/m for σ_b . The ϵ_r FWI models resolved the fine features better than the FWI σ_b models, as indicated in horizontal and vertical 1D profiles and by spectral analysis (Figure 4.2, (Van der Schaaf and van Hateren, 1998). The illumination of the domain using crosshole acquisition results in a better resolution of the vertical than the horizontal structures (Meles et al., 2010). In the vertical direction, the ratio of the spectral densities of the FWI to the real model starts decreasing for wavenumbers larger than $\nu = 3 \text{ m}^{-1}$ and $\nu = 1.13 \text{ m}^{-1}$ (equiv. to wavelength λ of 0.33 m and 0.88 m, $\lambda = 1/\nu$) for ϵ_r and σ_b , respectively. In the horizontal direction, this ratio starts decreasing for wavenumbers larger than $\nu = 0.77 \text{ m}^{-1}$ ($\lambda = 1.3 \text{ m}$) and $\nu = 0.51 \text{ m}^{-1}$ ($\lambda = 2 \text{ m}$) for ϵ_r and σ_b , respectively.

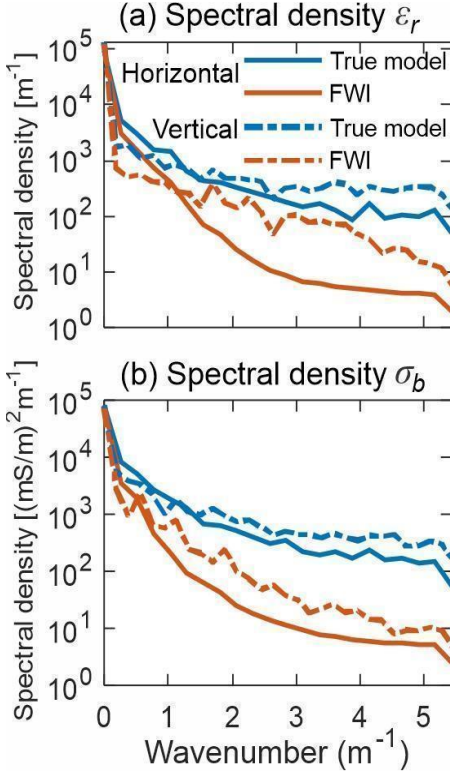


Figure 4.2: Spectral density of (a) permittivity and (b) electrical conductivity. Curves compare between the real models (RM, blue) and reconstructed FWI (orange) models for horizontal (solid line) and vertical (dashed line) directions.

Calculating the porosity $\phi_{recovered}$ and the formation factor $F_{recovered}$ distributions using Equations 3.4 and 3.8 (Figure 3.5) for both background ray-based and FWI results (Figure 4.1 b,d,i), we can see clearly that FWI better reconstructs the parameters than the ray-based inversion. The $\phi_{recovered}$ calculated from ray-based shows smoothed and dampened structures, while the FWI $\phi_{recovered}$ structures show more details and are closer to the true model ϕ_{RM} (Figures 4.3a-c). The $F_{recovered}$ calculated from the ray-based (attenuation) inversion recovered an erroneously lower value and a smaller variance than in FWI (Figures 4.3e-g). Thus, FWI provides a more accurate recovery than the ray-based inversion of these parameters, which in turn, through the use of petrophysical relations, reduces the uncertainty of the tracer recovery. $\phi_{recovered}$ shows a better correlation with ϕ_{RM} than $F_{recovered}$ with the true model F_{RM} . The mismatch for both parameters is related to the unresolved structures and deviations between FWI and real ϵ_r and σ_b models (Table 4.1, Figure 4.1e,j). Low values of $\phi_{recovered}$ (<0.28) overestimate ϕ_{RM} , while high values of $\phi_{recovered}$ underestimate ϕ_{RM} (Figure 4.3c), which is a bias originating from FWI results. We derived F_{RM} using the $\sigma_{b,background}$ from a previous study by Gueting et al. (2015, 2020). Note that this F is larger than the point measurements of Müller et al. (2010), where the soil was sieved and only

soil grains smaller than 20 mm were considered. For higher values of $F_{\text{recovered}}$ (>10) we can notice larger scatter. Locations with a high F correspond with locations where $\sigma_{b,\text{background}}$ is low. Errors in the recovered $\sigma_{b,\text{background}}$ and deviations between the local σ_{surf} and the mean σ_{surf} , which is used to recover F , lead to a larger scatter for high values of $F_{\text{recovered}}$.

Analyzing the correlation plots between the true and the FWI recovered distribution of $F(\mathbf{x})$ shows a range from 4.5 to 14.5. F is bimodally distributed (Figure 4.3h), reflecting the two main Facies 1 and 2 (Figure 4.2a, whereas the contribution of Facies 3 is minor). The sand Facies 1 has a mean porosity of $\phi_{1,\text{mean}}=0.36$ and a mean $F(\mathbf{x})$ of approximately 6. The sandy gravel Facies 2 shows a mean porosity $\phi_{2,\text{mean}}=0.31$ and a mean formation factor of 8.5. The gravel Facies 3 has a mean porosity $\phi_{3,\text{mean}}=0.25$ and a mean $F(\mathbf{x})$ value is about 11, which is larger than the laboratory measured value for the disturbed samples of Müller et al. (2010) of 4.56 to 6.63, which excluded larger stones.

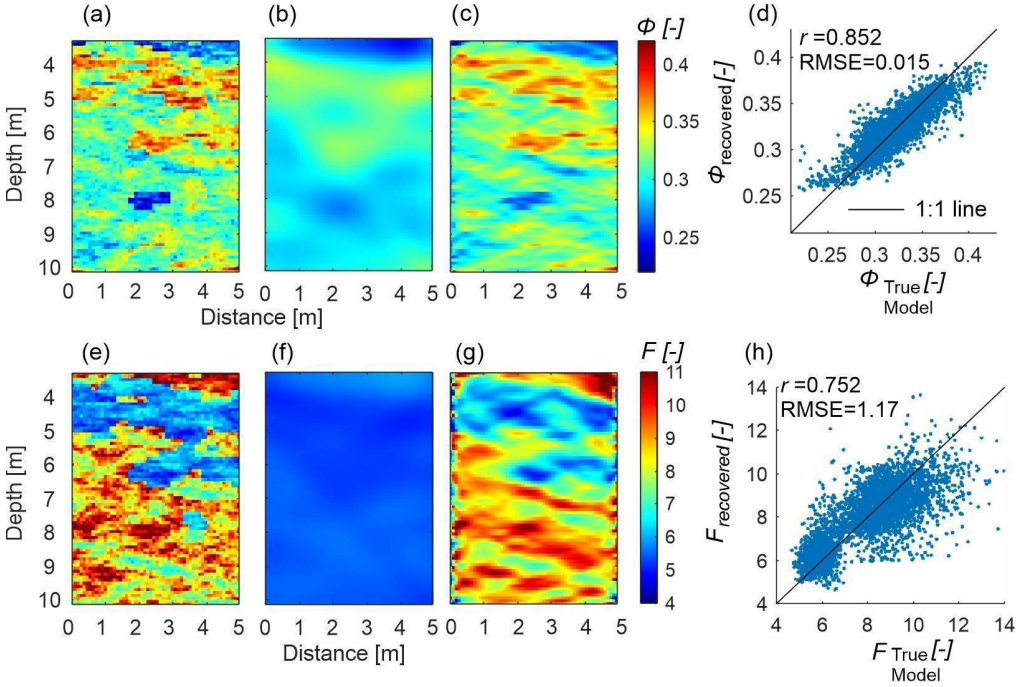


Figure 4.3: Porosity (top row) and formation factor (bottom row) distribution calculated from permittivity and electrical conductivity models, respectively: a) and e) show the true models, b) and f) are calculated from the ray-based models, and c) and g) from the FWI models. (d, h) Correlation plots between the true and FWI recovered d) porosity and h) formations factors.

4.3 Starting model strategies for time-lapse FWI

As mentioned before, for the FWI of time-lapse data it is highly important to guarantee that the starting models of the different time steps hold the half wavelength criterion. Because of the extensive knowledge that is already existing on how to optimize the ϵ_r starting model (e.g., Keskinen et al., 2021), we will concentrate on defining the best strategy for time-lapse σ_b starting models, which to our knowledge has not been investigated before.

Therefore, we first tested four different FWI starting model strategies for the salt tracer time-lapse GPR data. Note that we used for all the strategies the FWI ϵ_r background model \mathbf{m}_{t0} as permittivity starting model, while for the σ_b starting model different options were tested: using a uniform σ_b value (FWI1), the background model \mathbf{m}_{t0} (FWI2) and the previous day model \mathbf{m}_{t-1} (FWI3, FWI4). For FWI3 the \mathbf{m}_{t-1} model was calculated from the day-by-day sequential FWI inversions starting with the background, while in FWI4 \mathbf{m}_{t-1} was calculated using a single FWI inversion with starting model \mathbf{m}_{t0} . Note that we also tested different standard ray-based starting model approaches for the permittivity, which resulted in less good results and reconstructions of the tomograms, and we therefore do not present them.

For all the tests, the real permittivity models are unchanged (Sreenivas et al., 1995) in the salt tracer test and therefore only the σ_b real models are investigated.

For the FWI starting model tests (Figure 4.4), the time-lapse GPR data are derived for day 15 after the salt tracer injection based on the σ_b distribution shown in Figure 4.4a. Overall, all the 4 FWI recovered the main structures of the true model. While FWI1 shows fewer features of the tracer anomaly, FWI2 provided more accurate structures and performs better based on R^2 between the true and FWI model and the RMSE of the difference between the two ($R^2 = 0.64, 0.66, 0.58, 0.69$; $RMSE$ [mS/m] = 5.8, 5.6, 6.5, 5.4 for FWI strategies 1-4, respectively). Although FWI3 provides a more detailed σ_b structure, the R^2 and the $RMSE$ of FWI3 compared to the true model resulted in a worse performance than of FWI1 and FWI2. Analyzing the spectral density in the recovered FWI σ_b models (Figure 4.5), FWI3 provides the most information. These results of FWI3 are explained on the one hand by a better resolution of small-scale structures due to the better σ_b starting model from the previous day \mathbf{m}_{t-1} , but on the other hand there is a lower accuracy due to model overfitting, most likely caused by accumulation of errors in recovered FWI models which are then used as starting models for the following day.

The structure of FWI4 is similar to FWI2 but does not show as many details as FWI3. The best results of the four different starting models are obtained with FWI4, while the spectral analysis information is between FWI3 and FWI2. Overall, FWI2 shows robust results and in addition can be applied fast, because as a starting model it requires the FWI background and not any following day.

Thus, all FWI from here (for both salt and ethanol tracer tests) will use FWI2 starting model strategy.

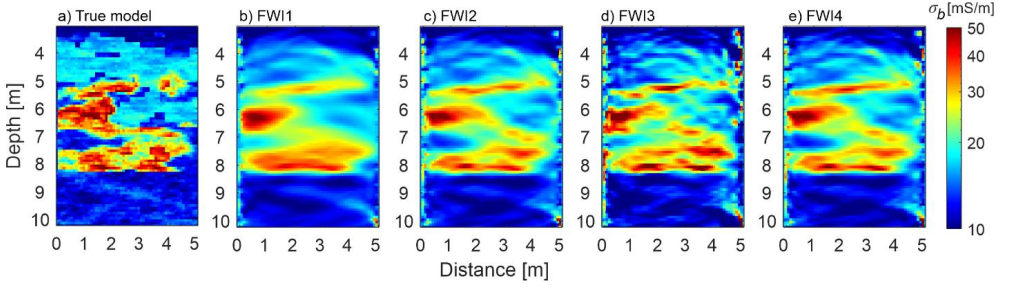


Figure 4.4: FWI σ_b results for the salt tracer using different starting model strategies. (a) σ_b true model at day 15. (b-e) FWI σ_b models from using starting models' strategies FWI 1-4, as explained in the text.

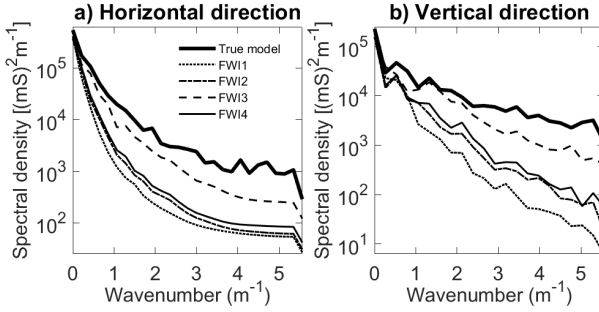


Figure 4.5: Spectral density of recovered FWI σ_b using different starting model strategies. The spectral information of the true model is shown by a thick line, and of the FWI from different starting model strategies by thinner curves. FWI 1-4 are presented in Section 4.3. (a,b) Spectral density in horizontal (solid line) and vertical (dashed line) directions, respectively.

4.4 Recovery of different salt tracer magnitudes and days

After we defined an appropriate starting model strategy, we now apply this to four different salt tracer scenarios with different σ_b changes at day 15 after injection. Similar to the tests before, the real permittivity models are unchanged for all scenarios and only the σ_b models are analyzed (Figure 4.6).

For injections with *Intermediate* and *High* salinity tracers, the σ_b distribution is predominantly determined by the distribution of the saline tracers, which generate larger variations in σ_b than the spatial variations of $\sigma_{b_background}$ (Figure 4.6d-e). For the *Desalinated* (negative) and *Low salinity* (positive) tracers, the changes in σ_b are in the same order of magnitude as the spatial variation in $\sigma_{b_background}$. (Figure 4.6a-c). The FWI σ_b models show a recovery of the structures for all cases, but the *High-salinity* case shows a worse recovery, for example at $z=6.5$ m, $x=1$ m it misses a main anomaly, probably due to the high attenuation of the signal.

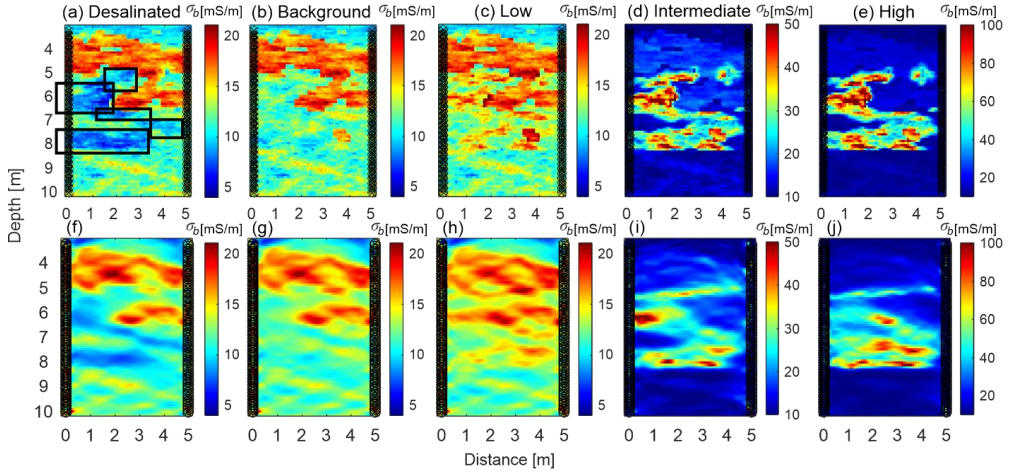


Figure 4.6: Bulk electrical conductivity FWI recovery from the synthetic salt tracer. Input (top) and recovered (bottom) models in the monitoring plane for different cases of injected salt tracer salinities: (a,f) Desalinated water, (b,g) Background, (c,h) Low, (d,i) Intermediate and, (e,j) High. The intrusion is shown for 15 days after the injection, and the main location of the tracer intrusion are emphasized by rectangles in (a). Note that panels (a-c, f-h) have the same colorbar scale, and (d-e, i-j) have different ones. Transmitter and receiver positions are located on black circles and crosses, respectively near the panel side boundaries.

Investigating the data fit between the simulated and FWI modeled traces between 4 to 8 m (Figure 4.7, Figure A.2 for *Desalinated* and *High* salinity cases) for the different salinity cases of day 15 (Figure 4.6), we generally notice a good overlap of the traces and that FWI traces can recover most details of the traces. A higher σ_b entails lower amplitudes causing gradually decreased amplitudes from Background to *Intermediate* salinity cases (Figure 4.6a-c, compare the *Observed* data for the transmitter shot gathers at 6 m of different cases – note for the amplitude scale). We observed a gradual decrease in R^2 between the true and modeled traces from Background to *Intermediate* salinity cases. The FWI traces seem to have difficulties to fit the signal amplitude and phase at regions where the tracer intrudes in comparison to where there is no intrusion (e.g., between transmitter at 6 m and 9.6 m in *Intermediate* salinity case). This is even more pronounced for the *High* salinity case (Figure A.2b). At the central part of the plume, the *High* salinity FWI traces at 6 and 7 m show a bad fit (Figure A.3f,h), with erroneous amplitudes and phase shifts.

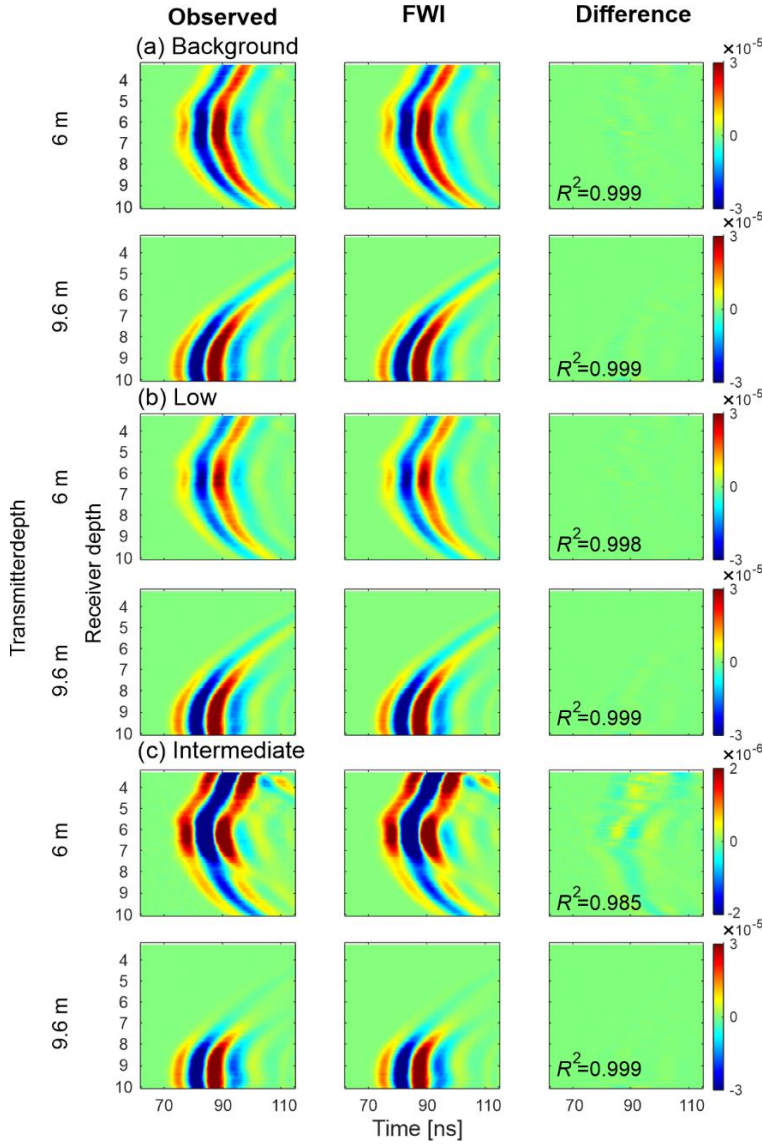


Figure 4.7: Observed (real data noise-added), FWI inverted and the difference between inverted and observed data for transmitters at the depth of major tracer intrusion (6 m) and at depth, where no intrusion occurs (9.6 m). GPR Data is presented for the (a) background (tracer case in Figure 4.6b) and (b,c) Low and Intermediate (tracer case in Figure 4.6c-d) salinity tracer cases. Note that for the Intermediate salinity case in (c) for the transmitter at 6 m depth panel where the signal is weaker because the wave travels through the increased σ of the tracer, the color scale is 15 times smaller. R^2 quantifies the correlation between FWI inverted and the observed data. The standard deviation of the Gaussian random noise was $4.6 \cdot 10^{-8}$ in all cases. Desalinated and High salinity cases are shown in Figure A.2.

Note, at high salinities the amplitudes of traces that cross regions with tracer intrusion are much lower than those of traces that cross regions without tracer intrusion and can be even lower than the instrumental noise level (Figure A.4b). No weighting on the data is applied to enhance the small residuals and for all data the squared differences between the measured and modeled traces are minimized. As a consequence, a poor match is obtained between the measured and FWI modeled traces for the high salinity data having much lower amplitude (Figure A.3f,h). The higher conductivity changes result in an increased non-linearity of the FWI, which is more difficult to invert and needs more sophisticated FWI techniques using progressively expanded bandwidths of the data and effective source wavelet (Zhou et al., 2021), which are beyond the scope of this paper.

To evaluate the possibility to monitor the σ_f tracer movement and transport over time, we performed an intense study by inverting 50 sequential days for the *Intermediate-salinity* case (Figure 4.8, 8 days chosen from day 6 until day 30). At all days the structures of the plume could be recovered and resolved to about 0.2 m scale, thus showing the potential of time-lapse monitoring.

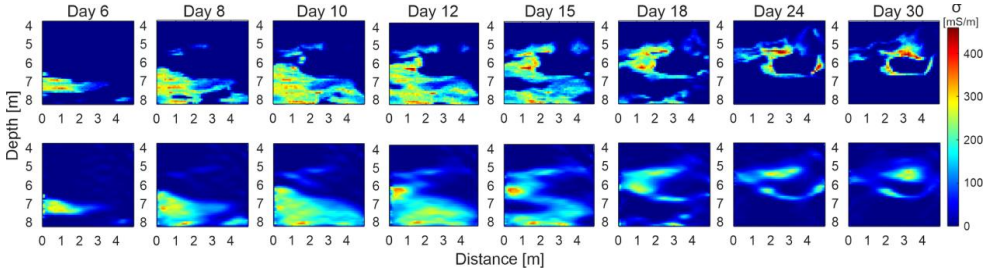


Figure 4.8: Salt tracer conductivity σ_f recovered on different days. Top row: real σ_f from transport simulation. Bottom row: recovered σ_f from GPR FWI bulk conductivity. Only the depths within the transport model domain are shown, from 3.67 to 8.26 m.

4.5 Recovery of ethanol tracer

As described in Section 3.4.2, we derived GPR data for a synthetic ethanol tracer experiment. Similar to the saline tracer tests, we considered the distribution of the tracer at day 15 after the tracer injection and applied for the σ_b starting model the optimal strategy by considering the background FWI results. To define the optimal ε_r starting model for this time-lapse data, we performed different tests by considering the travel time inversion (not shown) and the FWI results of the background data. As expected, the background FWI model provided the best results, therefore we choose this strategy for the following steps and do not show the FWI results for other tests.

The true models of ε_r and σ_b in the monitoring plane 15 days after the ethanol tracer injection show a decrease in both ε_r and σ_b (Figure 4.9a,b) compared with the background (Figure 4.1a,e), with maximum changes of $\Delta\varepsilon_r = -3.35$ and $\Delta\sigma_b = -11.95$ mS/m at $Z = 6.3$ m, $X = 1$ m. This corresponds to the GPR traces with increased amplitude, and which are shifted to earlier times by about 1-1.5 ns (examples of ethanol FWI and corresponding real traces at the main intrusion depth are shown in Figure A.5). We used the FWI results of the background as a starting model (Starting model strategy FWI2). Overall, both medium parameters are resolved well, and the main features are detected within high resolution. Especially permittivity changes caused by the ethanol tracers around 8 m depth are well reconstructed. The final FWI σ_b recovery is more smoothed than the ε_r recovery (Figure 4.9c,d), as was also observed for the FWI background models (Figure 4.1). This phenomenon is related to a higher sensitivity in ε_r in fitting the phase than in fitting the amplitude of the signal in natural media (Lavoué et al., 2015). Modeled FWI traces (blue dashed lines in Figure A.5) for the ethanol case show a good fit to the observed traces.

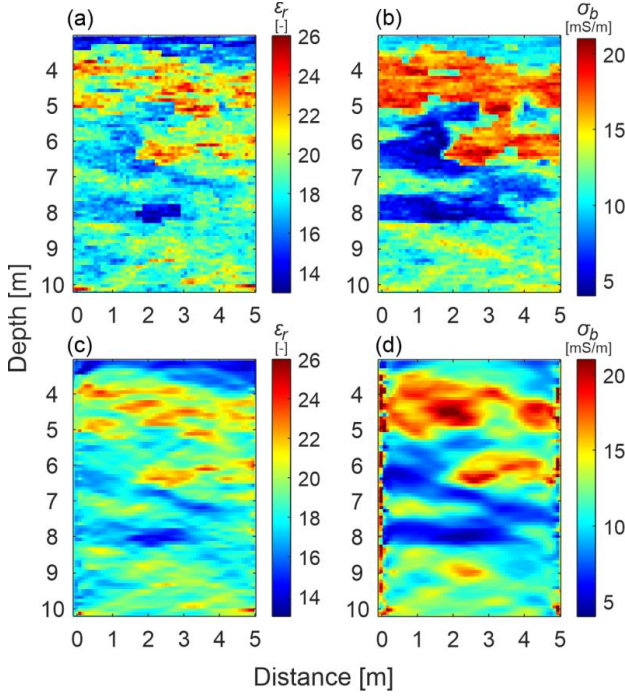


Figure 4.9: Permittivity and bulk electrical conductivity FWI recoveries from the synthetic ethanol tracer for 15 days after the injection. Real models are shown in (a) permittivity and (b) electrical conductivity, while (c) and (d) show the corresponding FWI results.

Also, for the ethanol tracer, we performed a similar study as for the *Intermediate* salinity case and calculated for 50 consecutive days the FWI results using starting model strategy FWI2 (Figure 4.10). For these days, we recovered the volumetric concentration of ethanol S_{eth} distributions from time-lapse FWI ϵ_r and σ_b models. For both cases, the S_{eth} distributions show a good correspondence to the true time-lapse distributions for all days. Because of the better recovery of FWI ϵ_r (see also Figure 4.9), a more accurate recovery of S_{eth} distribution is derived from ϵ_r than from σ_b , which is also caused by higher uncertainty in $\sigma_{surf}(x)$ that propagates in the derivation of S_{eth} from σ_b . In addition, since the uncertainty of $\phi_{recovered}$ is smaller than that of $F_{recovered}$ (Figure 4.3), less errors propagate in the recovery of S_{eth} from ϵ_r than from σ_b .

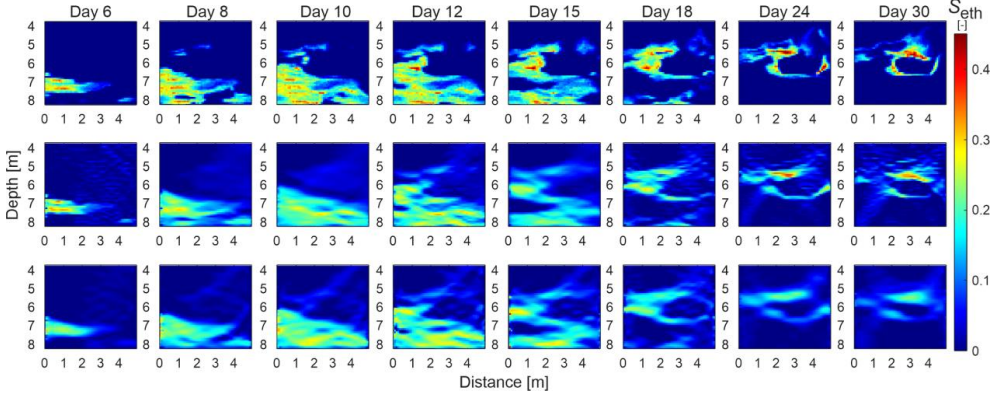


Figure 4.10: Volumetric concentration of ethanol S_{eth} recovered on different days. Top row: real S_{eth} derived from transport simulation. Middle and bottom rows: recovered S_{eth} from GPR FWI permittivity and conductivity, respectively.

Further, subtracting ϵ_r at day 13 from that in day 15 (Figure 4.11a,b) shows that time-lapse GPR FWI can image tracer changes based on time lapse ϵ_r images with about 0.2 m resolution, and better than from time lapse σ_b images (Figure 4.11c,d).

Note that a movie that shows the tracer reconstruction and developments over time for both ethanol and salt tracers can be found in (link and description is provided in Appendix A.6).

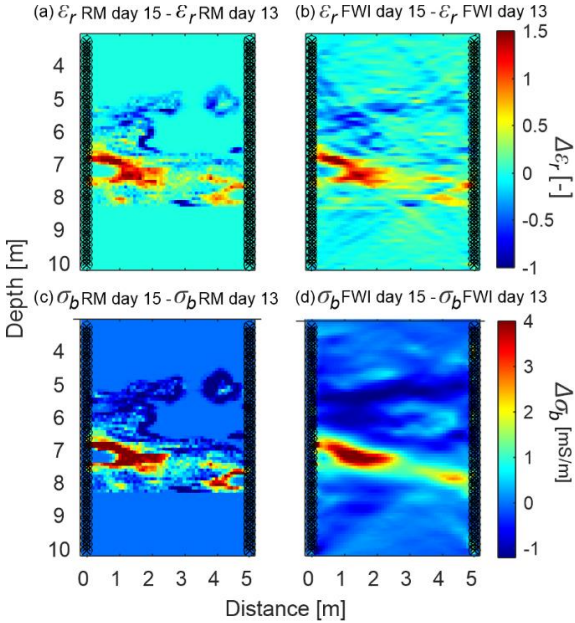


Figure 4.11: Tracer distribution changes between day 15 and day 13 based on permittivity: a) Real and b) FWI recovered models and based on bulk conductivity: c) Real and d) FWI recovered models.

4.6 Breakthrough curves at single cells

The day-by-day tracer FWI recovery results of the *Intermediate-salinity* and the ethanol tracer allowed to calculate the breakthrough curves (BTC) at each single cell (0.09 m) in the crosshole tomogram. From these results three FWI parameters can be considered: σ_b from salt tracer (Figure 4.12a), and ε_r and σ_b from ethanol tracer (Figure 4.12b). The true tracer properties (σ_f or S_{eth}), which were derived using petrophysical relations from the same synthetic transport simulation, were normalized to the highest values, to allow a better comparison. From observing BTCs at 4 random locations (Figure 4.12a,b) we identify that the shapes of the FWI breakthrough curves are in general recovered. However, for the majority of the recovered BTCs the first arrival is too early, the tail is too long, and the breakthrough peak is in general too low, but sometimes also too high. That inaccuracy is partly because for the given acquisition settings the receiver antenna records a signal which represents roughly the volume of the wave path with an effective cross-section of the size of Fresnel zone and with a diameter of about 1.25 m (in Section 4.6.1).

To assess which tracer test and which FWI parameter recovered BTCs the most accurately, we used the RMSE of the BTCs at all cells to calculate the cumulative distribution function (CDF, Figure 4.12c). Low values of RMSE and a similar CDF are observed for normalized σ_f (salt) derived from σ_b and for normalized S_{eth} (ethanol) from ε_r , while for S_{eth} (ethanol) derived from σ_b RMSE is higher. The larger normalized error of σ_b -derived S_{eth} (ethanol) than the normalized error of the salt tracer is due to the larger change in σ_b caused by the *Intermediate* salinity tracer than by the ethanol tracer.

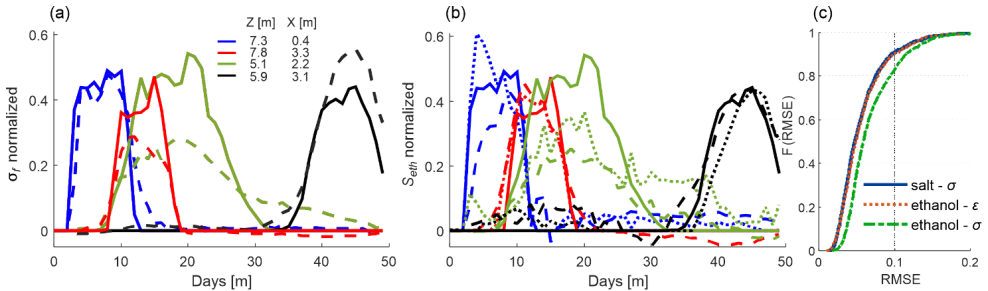


Figure 4.12: Recovered tracer breakthrough curves at single cells from FWI parameters. Breakthrough curves for days 0-49 drawn at 4 locations in the crosshole plane (see legend) in the plane for the salt (a) and ethanol (b) tracers. The breakthrough curves are normalized to the maximal true σ_f (salt test) and S_{eth} (ethanol test) in the entire aquifer volume, respectively. The true tracer, and the tracer recovered from permittivity and conductivity are presented by continuous, dotted and dashed lines, respectively. (c) Cumulative distribution function (cdf) from all-cells of RMSE of the breakthrough curves, for the recovered tracer that was derived from salt (from σ_b) and from ethanol (from ε_r and from σ_b). 2444 breakthrough curve locations cells were used for the cumulative distribution function.

4.7 Considerations for experimental tracer test

Overall, we have demonstrated a high potential of the FWI to recover tracer from time-lapse crosshole GPR data. Especially in contrast to the ray-based results, the FWI can reconstruct the medium parameters with high resolution resolving small-scale structures within the decimeter-scale and allows detecting tracers that mainly affect the electrical conductivity. Nevertheless, for the application to experimental data, several issues and challenges should be considered.

4.7.1 3D versus 2D GPR wave behavior

The crosshole GPR FWI is currently mainly applied in 2D due to computational limitations for 3D approaches. Therefore, diffracted energy from out-of-plane scatters, and specifically in the case of heterogeneous tracer concentration, cannot be considered. Applying a 2D FWI to 3D measured/simulated data, can cause several issues that should be considered in the results evaluation of experimental data. Two main problems arise by inverting 3D data with a 2D inversion. First is the out-of-plane effect on the GPR signals, which is not simulated with a 2D forward model. Second is the errors introduced by the 3D to 2D transformation of measured GPR data for experimental data application (e.g., Klotzsche et al. (2019b)). Note that for our presented synthetic study both effects are not incorporated.

To investigate out-of-plane effects on the 3D and 2D data, we can apply two approaches. One way is to estimate the zone of influence on the GPR data. The Fresnel zone of the used GPR signals indicates the sampling zone for the cross-borehole signals. The Fresnel zone can be described by a 3D ellipsoid volume (Fresnel volume), which depends on the distance between the antennas, the center frequency of the signals, and permittivity of the medium. Generally, the radius of the first Fresnel zone R_{FR} is approximated for a monochromatic wavelength λ (Schuster, 1996):

$$R_{FR} = \sqrt{\frac{\lambda \cdot x_0}{2}}, \quad \text{Eq. (4.10)}$$

where x_0 is half the crosshole distance [L], and λ [L] is depending on ε_r and f . To evaluate the effect of the Fresnel zone in a tracer experiment due to out-of-plane effects, we compare R_{FR} with the horizontal correlation length (I_h) of $\ln K$, which dominates the distribution of the plume in the flow direction. For the aquifer conditions and acquisition setup in this study, the minimum, average and maximum of ε_r result in R_{FR} of 0.96, 1.23 and 1.83 m, respectively. Thus, in the main Facies 2 the R_{FR} for the average ε_r is smaller than the horizontal correlation length $I_h=1.75$ m and, larger than the vertical $I_v=0.18$ m. Therefore, for the size of R_{FR} , there are small spatial variations in out-of-plane direction, but large spatial model variations in the in-plane vertical direction. As a result, out-of-plane effects in these crosshole measurements have a relatively low weight in the overall signal. Using FWI with 2D data and for an R_{FR} of 1.23 m, features with a size of about 0.2 m could be resolved in the vertical direction (Figure 4.6), and also at a decimeter scale for a real GPR data (in 3D) in Krauthausen aquifer (e.g., Gueting et

al., 2017). This shows that FWI of an extensive and dense dataset can get better model resolution than expected from the magnitude of the Fresnel zone.

Additionally, we performed some modeling tests and compared 3D, 2.5D and 2D GPR data of an exemplary day after a salt tracer injection to investigate the effect of plume heterogeneity on the data itself. A detailed description can be found in the Appendix A.7. Our tests, which considered a day with a strong out-of-plane σ contrast, indicate that in 3D and 2.5D data only minor differences are shown in the phase and amplitude, mainly where off-plane scatterers are present. Overall, the out-of-plane effects on the GPR data seem to be minor (comparing 2.5D and 3D data), and probably related to the zone of influence on the signal. It is expected that they will not change the inversion results significantly, since the phase and amplitude differences will probably not change gradient directions because the out-of-plane travel paths cannot be explained by the travel paths in-plane that are used by the FWI.

A larger effect and hence influence on the final 2D FWI tomograms is associated with the 3D to 2D transformation filter of the GPR data to allow a 2D FWI (Bleistein, 1986). We performed for our 3D data a 3D-to-2D conversion, resulting in “semi 2D” GPR data (Figure A.6b-d). Mozaffari et al. (2020) demonstrated that this transformation mainly affects late arrival amplitudes of the measured data in the presence of high contrast layers, which results in a difference of approximately 2% between 2.5D and 2D FWI results for both ϵ_r and σ_b . A similar behavior can be seen in our tests. Especially in the zone where the tracer is present, which causes a high contrast (Figure A.6a, right), late arrival data is affected and a mismatch between the 2D and “semi 2D” is present. These errors are introduced by the Bleistein filter, because one assumption of the filter is that the highest amplitude of the data is associated with the first arrival times. But in the presence of high contrast zones, which can cause wave interferences, this assumption is not always valid and hence the amplitudes are not accurately correct towards 2D. Note that the Bleistein filter for data outside the tracer region performs well and a good fit between the 2D and “semi 2D” can be observed (Figure A.6d, receiver at 5.5 m). As expected the “semi 2D” data in the presence of the high contrast tracer show some errors in the amplitude of the wavelets (Figure A.6d, receiver at 6.58 m, 7.66 m) and hence will affect the electrical conductivity results.

Overall, it seems that the out-of-plane effects on the GPR data are minor and the errors introduced by the 3D to 2D conversion are probably larger. As a result, only 3D GPR FWI and to a lesser extent 2.5D, which consider the 3D medium and plume heterogeneity, can minimize such errors. Although a 2.5D FWI method in the time domain exists (Mozaffari et al, 2020), to analyze a high number of datasets is currently not feasible due to the high computation costs, as just for a single forward run it is 10 times larger than for a 2D forward run.

4.7.2 Time-lapse data acquisition

To improve the quantitative values mainly of the σ_b FWI results and decrease the uncertainties of the results, Oberrohrmann et al. (2013) and Keskinen et al. (2021) indicated that a dense transmitter and receiver spacing during the acquisition should be used. Such acquisitions are time consuming and should not be applied during a tracer experiment, where shorter temporal changes are expected. Therefore, we propose to measure a dense background dataset that is able to reconstruct the medium with a good accuracy, which is then used as a starting model for the time-lapse data that is sampled with a larger spacing. To improve the σ_b results in the region of the expected tracer, a denser transmitter sampling could be used for a limited domain. For large contrasts in permittivity due to tracer changes, cycle-skipping between the starting model's background and time-lapse data should be carefully checked to set the wavelength criteria. In case that criterion is not met, another approach should be adopted, e.g., ray-based permittivity inversion from that time-lapse data.

4.7.3 Temporal tracer changes during crosshole GPR data collection

In our studies, we assumed quasi-static conditions for each FWI and time-step. For experimental data acquisition this is of course not the case and if the GPR data collection is slower than the dynamic process of tracer transport, this could cause changes in the aquifer for GPR measurements during the survey period. From our experience in crosshole GPR field measurements, for the amount of data considered in this study (7 m depth interval in both boreholes using a transmitter and receiver spacing 0.2 and 0.1 m, respectively), data collection takes about 3 hours. From the transport modeling results (Figure 4.8, top row) under realistic aquifer conditions the plume's leading front and center is transported at about 3 m/day and 1 m/day, respectively. This results in approximately 0.375 m and 0.125 m transport distance in 3 hours. These transport distances are shorter than the Fresnel Zone. Thus, transport changes in the aquifer during GPR measurements occur across distances shorter than the GPR sampling zone, and therefore are not resolved by GPR. Overall, the effect for the Krauthausen test site is expected to be minor under the mentioned conditions, but this should be judged independently for different aquifers having a higher flow velocity. One approach to reduce the error introduced by data-collection time for crosshole GPR was performed using space-time parameterization and regularization of two sequential datasets (Day-Lewis et al., 2002, 2003), and principally could be applied also to the FWI scheme.

4.8 Conclusions

In this study, we tested the reconstruction of tracer plumes with crosshole GPR FWI in a numerical experiment. We tested the GPR FWI to reconstruct the plume for a saline and desalinated tracers, which changed σ_b , and an ethanol tracer, which changed both ε_r and σ_b , and found that the resolution obtained with FWI was much higher than ray-based inversion. To mimic field conditions, we added random instrumental noise to the synthetic data and found that FWI fitted the data successfully, except for when

the tracer attenuated the signal too much. Similar aquifer structures and only a minor statistical degrade in comparison to FWI noise-free data was obtained due to instrumental noise. We showed that as long as the data amplitude is higher than the level of the random noise, and not attenuated too much due to the presence of the tracer, the FWI reconstructs the plume successfully.

Since all previous crosshole GPR FWI studies were applied under steady state conditions, we tested four different strategies to define the optimal starting model of the time-lapse data. Thereby it was shown that using the FWI of the previous day (strategy III), the FWI images contain more spectral information in comparison to the background starting model, however the tomograms showed a lower model accuracy. One reason for this could be that numerical model errors are accumulated in the recovered FWI models, which are then sequentially further propagated in the following inversion resulting in overfitting causing more numerical artifacts. Therefore, using FWI background (strategy II) is found as a robust and practical FWI starting model strategy for time-lapse data, adequate for all tracer experiments. FWI Recovery of both permittivity and electrical conductivity distributions resolved structures of about 0.2 m. While the electrical conductivity structures are more smoothed and the anomalies in the model are more dampened, the permittivity model is able to reconstruct more details. Therefore, the reconstruction of the plume from GPR time-lapse datasets and using petrophysical relations which depend both on porosity (from FWI permittivity background) and formation factor (from FWI electrical conductivity background), provided better reconstruction of permittivity changes. The high-resolved reconstructed distribution of the tracer allowed us to calculate breakthrough curves which successfully recovered the true ones, at each cell in the cross-borehole plane.

We showed by estimating the approximated first Fresnel volume (zone which affects the GPR traveling wave) and by performing 3D modeling, that out-of-plane effects which include the heterogeneity of the elongated plume, do not significantly affect the signal. Because the horizontal distribution of the plume is relatively uniform within the Fresnel zone radius, for synthetic 2D data that is generated in a crosshole plane perpendicular to the flow direction, out-of-plane effects of the heterogeneity of the plume will not dominate the recorded signals. Thus, for the realistic tracer transport heterogeneity, investigating GPR FWI with 2D data is acceptable, and saves computation time in comparison to simulating 3D data for multiple days in a tracer test. In addition, changes in concentrations during acquisition time were small and it was acceptable to neglect these changes. However, in aquifers with a fast transport velocity, this assumption would require further testing.

To summarize, the ability to monitor and locate environmental tracers using two GPR FWI parameters at a high-resolution, shows the potential of time-lapse GPR FWI in practical applications, e.g., to locate and monitor pollutants and remediation injection liquids.

Chapter 5

GPR full-waveform inversion monitoring of a salt tracer test ³

In this chapter, for the first time we apply the GPR time-lapse FWI to an experimental dataset acquired during a salt tracer experiment. Thereby, we investigate the potential and challenges for time-lapse GPR data and discuss several processing steps to derive reliable FWI results for each data set measured during the experiment. As already discussed in Chapter 4, important aspects are to have a robust starting model strategy and the estimation of the effective source wavelets are carefully investigated. We investigated the consistency of the reconstruction of the plume by analyzing the temporal and spatial continuity across neighboring GPR FWI planes, by correlating with borehole logging data, by comparing to time-lapse ZOP analysis and with expectations based on past tracer tests in the aquifer.

5.1 Saline tracer test

For our experimental study, we acquired data at the Krauthausen test site, as described in Section 3.1. In April 2019, 4000 L of salt tracer was injected to the sandy aquifer. The tracer was prepared by mixing dry CaCl_2 salt with pumped groundwater at the site and stored in one-cubic-meter containers. The electrical conductivity (σ) in each container was approximately 1200 mS/m (13 times more than groundwater of ~ 92 mS/m), which regard to density it is equivalent to about 0.7% denser tracer than the groundwater at the injection borehole. The tracer and the groundwater temperature were about 10°C with negligible changes with time. The tracer was pumped into the aquifer through borehole B29 (Figure 5.1a) using an injection pipe at a depth of 5 m and a mechanical pump at a constant rate of 2100 L/hour (Figure 5.1b). Borehole B29 is screened from 3.1 to 11.1 m below surface and therefore allows a direct flow of the tracer into the aquifer along the entire water filled borehole. During the pumping, we carefully checked that no rise of the water table height in the borehole occurred to avoid infiltration from the unsaturated zone of the aquifer. The tracer was transported from the injection well in the aquifer with the natural groundwater velocity.

Additionally to the GPR measurements, the tracer was monitored at the boreholes in the expected tracer transport path using electrical conductivity borehole sensors (CTD-Diver DI27, vanEssen Instruments). These tools provided σ and temperature depth profiles, and were measured at the injection borehole B29, and at the monitoring boreholes B32, B31 and B34, during the first two weeks after the injection once or twice a day, and later every 2-4 days. Borehole B38 has no slots in the tube, is not connected to the aquifer and was therefore not measured. The temperature is measured using a semiconductor sensor.

³ adapted from Haruzi, P., J. Schmäck, J. van der Kruk, H. Vereecken, J. Vanderborght and A. Klotzsche, 2022. GPR full-waveform inversion monitoring of a salt tracer test, Water Resources Research, in preparation.

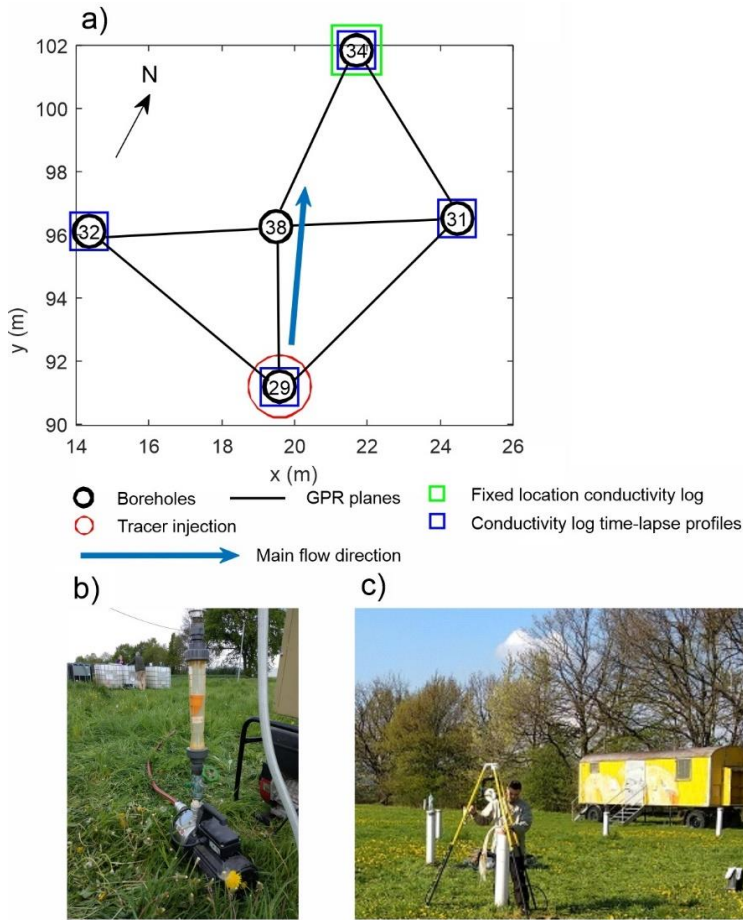


Figure 5.1: Setup of the salt tracer test scenario at the Krauthausen test site a) Schematic setup of the used boreholes for the injection (red circle) and the crosshole GPR measurements. Note that the setup is embedded in Figure 3.1b. The seven crosshole GPR planes are indicated with the black lines. The green and blue squares indicated the location of the fixed and time-lapse conductivity logs, respectively. For a larger view on the test site see Figure 3.1a. b) Picture of the injection pump and salt tracer containers. c) Example of a crosshole GPR measurement performed during the tracer test.

The conductivity in the water is measured using a 4-electrode measuring cell (vanEssen product manual Diver®). The temperature measurements at each location were used to standardize the corresponding σ measurement to σ at 25 °C (see e.g., Hermans et al., 2015). The depth is measured as a sum of the water level from the surface, calculated using a water level indicator (dipmeter), and the water column (WC) from the pressure measurements. The Diver measures the absolute pressure (p_{Diver}), i.e. the sum of the water pressure and the atmospheric pressure (p_{Baro}) pushing on the water. The WC can be expressed as:

$$WC = 9806.65 \cdot \frac{p_{Diver} - p_{Baro}}{\rho \cdot g}, \quad \text{Eq. (5.1)}$$

where WC is measured in meters, p is the pressure in cmH₂O, ρ is density of the water (1000 kg·m⁻³), and g is the acceleration due to gravity with 9.81 m·s⁻². A slow move-down of the measuring sensor and a sampling rate of 1 second produced high-resolution depth profiles within centimeter scale. However, the daily GPR measurements with borehole antennae along the water column unavoidably mixed the water. As a result of the mixing, the conductivity profile was smoothed. We measured each day with the Diver in the morning before the GPR measurements, and after the measurements.

5.2 Borehole logging

Thirty minutes after the injection was terminated, we can observe a slightly lower σ in B29 of about 1180 mS/m than the σ of the injected tracer of 1200 mS/m (Figure 5.2a). Additionally, distinct differences of ~30 mS/m can be observed in the σ depth profile. Above 4 m, the lower σ is related to dilution in the borehole due to high velocity in that region, in agreement to the gravel facie (Figure 3.1b) of high hydraulic conductivity (K). Between 4-5.9 m, high σ values relate to a lower dilution in the sand facie, which has a smaller K . Between 6-7.5 m and 8.3-10 m, the low σ correspond with high velocity, whereas the high σ between 7.6-8.3 m corresponds to a small K layer. The aquifer facie between 6-10 m was interpreted as a sandy gravel facie (Guetting et al., 2015); however, the slow flow velocity layer at 7.6-8.3 m was not observed in previous measurements that were measured at different locations at the site, thus suggesting also horizontal variability. Inside that facie, the vertical variability of the velocity magnitude inside is in general agreement with stratification (Döring, 1997), with well water velocities from dilution tests (Englert, 2003), and grain size distribution along the profile (Guetting et al., 2015). σ abrupt changes of 0.1 m width scale are observed at 7 and 9 m depths, suggesting narrow flow paths. High σ below 10 m is due to less dilution, which may be related to a layer of a lower K , due to an increase in clay fraction (Tillmann et al., 2008), or also due to sinking of the dense plume to the bottom of the well.

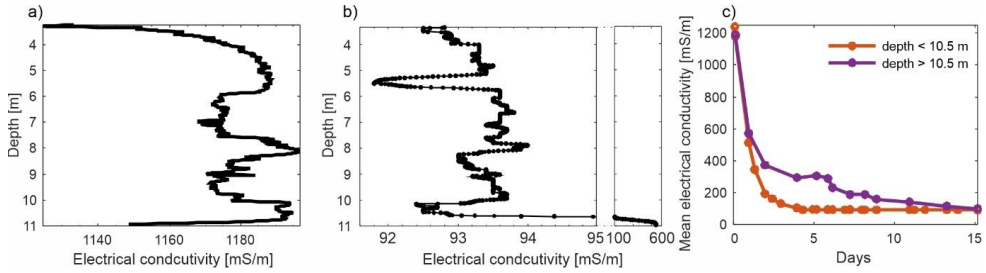


Figure 5.2: Electrical conductivity measurements in the injection borehole B29. a,b) Electrical conductivity depth profile a) 30 minutes and b) 7 days after the end of injection. C) Mean electrical conductivity at depths below and above 10.5 m over a time of 15 days. The injection conductivity was 1200 mS/m.

Figure 5.2b shows that on Day 7 the σ above 10.5 m is back to the values of the groundwater and ranges only within 2 mS/m. In general, for all following days after the injection in B29 (σ logging depth profiles on Days 1-6, not shown here), we observed a decrease in σ , but because of unavoidable mixing of the water by the moving of the GPR antennae, clear variability was not observed above 10.5 m depth. Below 10.5 m σ was high (up to ~ 500 mS/m) due to tracer density effects. Therefore, for all time-lapse logging measurements we averaged the σ for the regions above and below 10.5 m (Figure 5.2c). The upper part shows an exponential-like decay with σ back to normal groundwater values at about Day 4, and the lower part shows normal groundwater values after 15 days.

In the monitoring boreholes B32 and B31 (5 m at the sides to the main flow path, Figure 5.1a) on Day 7, we observe σ variability of about 1 mS/m (Figure 5.3a,b), but it is too small for interpretation for velocity variability. We averaged the σ depth profile across the water column. Mean σ changes were too small to show a trend (Figure 5.3d), thus we cannot imply that a change is due to a tracer migration at these boreholes, and it is indicating that the plume is narrow. B34 at the main flow path on Day 7 shows variability of σ with depth (Figure 5.3c). On 6 m depth, low σ is probably related to high velocity, which causes dilution, but not to migration of tracer due its lower values. In addition, the daily vertical mixing by GPR antenna complicates the quantitative interpretation of σ . Still, we recognize three distinct layers in the profiles at all days: above 8 m (L1), between 8 and 10.5 m (L2), and below 10.5 m depth (L3). Similar layers were derived from the grain size analysis from Gueting et al., (2015). First arrival of the plume at B34 (10.8 m distance) can be observed after 3 days. For the top two layers, the curve breakthroughs after 8 days, and the σ increase from the background with respect to the injection σ are 3.5% and 5.8% for L1 and L2, respectively. At bottom part L3 breakthroughs after 18 days with 22.7% difference to the injection σ , probably related to the dense injection salt water that sunk at B29 and migrated on the bottom of the aquifer.

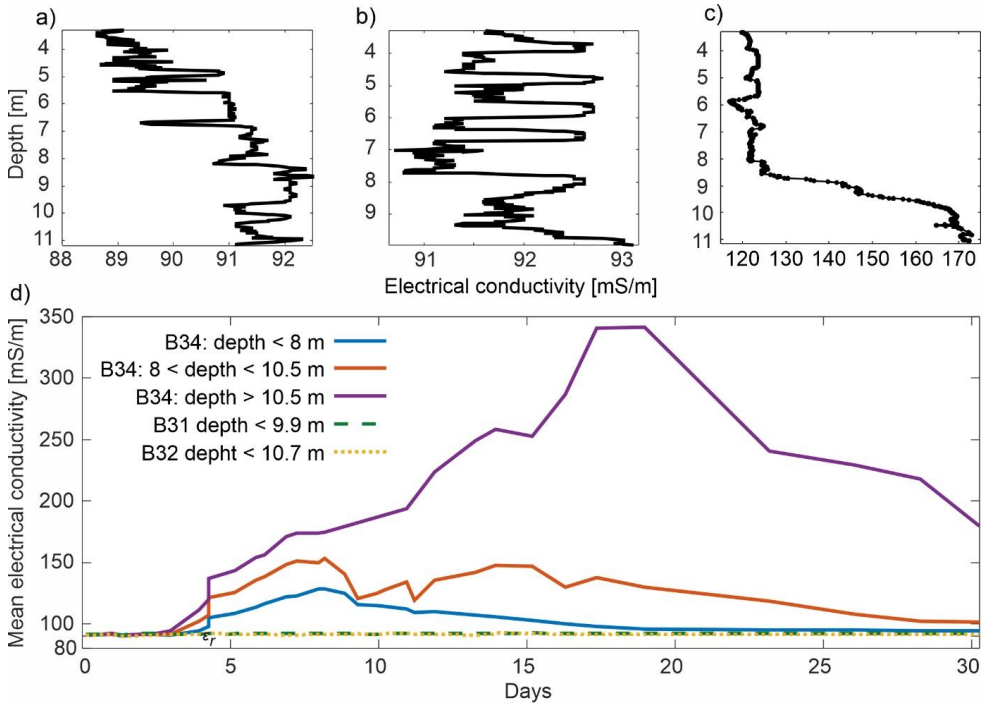


Figure 5.3: Electrical conductivity logs in monitoring boreholes B34, B32 and B31. a-c) Electrical conductivity depth profile 7 days after the end of injection, in borehole B34, B32 and B31, respectively. d) Mean electrical conductivity from depth profiles over a time of 30 days.

5.3 GPR data acquisition

We measured five crosshole GPR planes with distances between 5 and 6 m with the 200 MHz antennae, while for larger borehole distances we utilized the 100 MHz antennae of the Sensors and Software (Canada) pulseEKKO Pro system. Note that in this study, we only investigated in detail the 200 MHz data.

Table 5.1: Detailed overview of the acquisition days and when each crosshole plane was measured, and the number of transmitters and receivers used in the acquisition.

Plane	Back-ground	1	2	3	4	5	6	7	8	9	10	11	12	13	14
3831	✓		✓	✓	✓	✓	✓	✓	✓		✓				
trn.	62		32	44	49	48	49	49	49		49				
rec.	126		126	125	125	125	125	125	125		125				
3238	✓		✓	✓	✓	✓	✓	✓	✓		✓				
trn.	43		43		31	42	50	50	50	50	50				
rec.	135		135		132	132	132	132	132	132	132				
2938	✓	✓	✓	✓	✓			✓		✓		✓			✓
trn.	47	44	33	44	56			46		62		62			62
rec.	142	114	131	129	139			138		137		137			137
3834	✓							✓		✓		✓			✓
trn.	47							46		61		63			52
rec.	142							139		137		137			137
3134	✓									✓					
trn.	55									61					
rec.	144									137					

In crosshole data there is no air wave, hence calibrations measurements are needed to estimate the time-zero of the GPR data. Therefore, we performed WARR measurements in air, which were repeated several times during the acquisition of one crosshole plane to capture time dependent variation on the signals (about 3-4 times per plane). In WARR mode, one borehole antenna is held fixed, while the other antenna is moved from a starting antenna offset of 0.5 with a 0.1 m spacing to the end of a 6 m long profile. ZOP data were measured for the same planes, where MOG data was measured at the same day. ZOP data was acquired with a vertical spatial sampling of 0.1 m and temporal sampling of 0.2 ns. Considering a water table height of approximately 2.5 m, the ZOP data have 65-80 traces per plane depending on the depth of the boreholes.

Per day, we normally measured between 1-4 crosshole MOG planes using a semi-reciprocal setup (Section 1.2). For both background and time-lapse datasets, we always used receiver spacing every 0.1 m. As shown by Oberröhrmann et al. (2013), a denser transmitter and receiver spacing is providing better FWI models as a more spares one. Moreover, the synthetic study showed that starting models for time-lapse data, which are closer to the reality of the subsurface provide more accurate FWI results (Figure 4.4). Therefore, the background GPR data were measured with a denser transmitter spacing of 0.2 m than the time-lapse data that were measure with 0.4 m transmitter spacing. For the time-lapse data a compromise between spacing and measurement time needed to be found to allow to measure as

many MOG planes as possible per day. Note that in the processing of some of the background datasets (2938, 3238 and 3834) inconsistencies were observed, which required to use background datasets from another tracer experiment performed some months later (Tx spacing 0.4 m).

The acquisition time of one crosshole plane depends on the amount of data, and for trained persons the time was approximately 1-2 hours. Measurements were conducted from 0.5 m below the water table, until the maximal depth of available deviation data at 9 - 10.5 m depth. Borehole deviation data were used to correct for the lateral antenna location, which are necessary to avoid inversion artifacts.

5.4 GPR data processing

Before the inversion of the crosshole GPR data, the following pre-processing steps were performed: dewow filtering, time-zero correction, deviation correction of the tubes and first arrival time picking to obtain a ray-based start model for the FWI.

5.4.1 Dewow filter

In raw GPR data, a low-frequency wow is present (Huisman et al., 2003), which can be removed with the so called dewow filter. In the frequency domain, this wow is present for low frequencies (Figure 5.4a), resulting in the time domain with long wavelength and static amplitude offset (Figure 5.4b) that interfere the actual signal of interest. Additionally, the dewow filter shifts all the traces to zero amplitude at time $t=0$. Figure 5.4c shows a raw data image scan with shot gathers from WARR, ZOP and part of the MOGs that were measured at the beginning of the measurement in an exemplary plane. The dewowed data image scan shows that the wow is removed (Figure 5.4d). Overall, the noise level in crosshole GPR data is low, therefore no additional filters are applied.

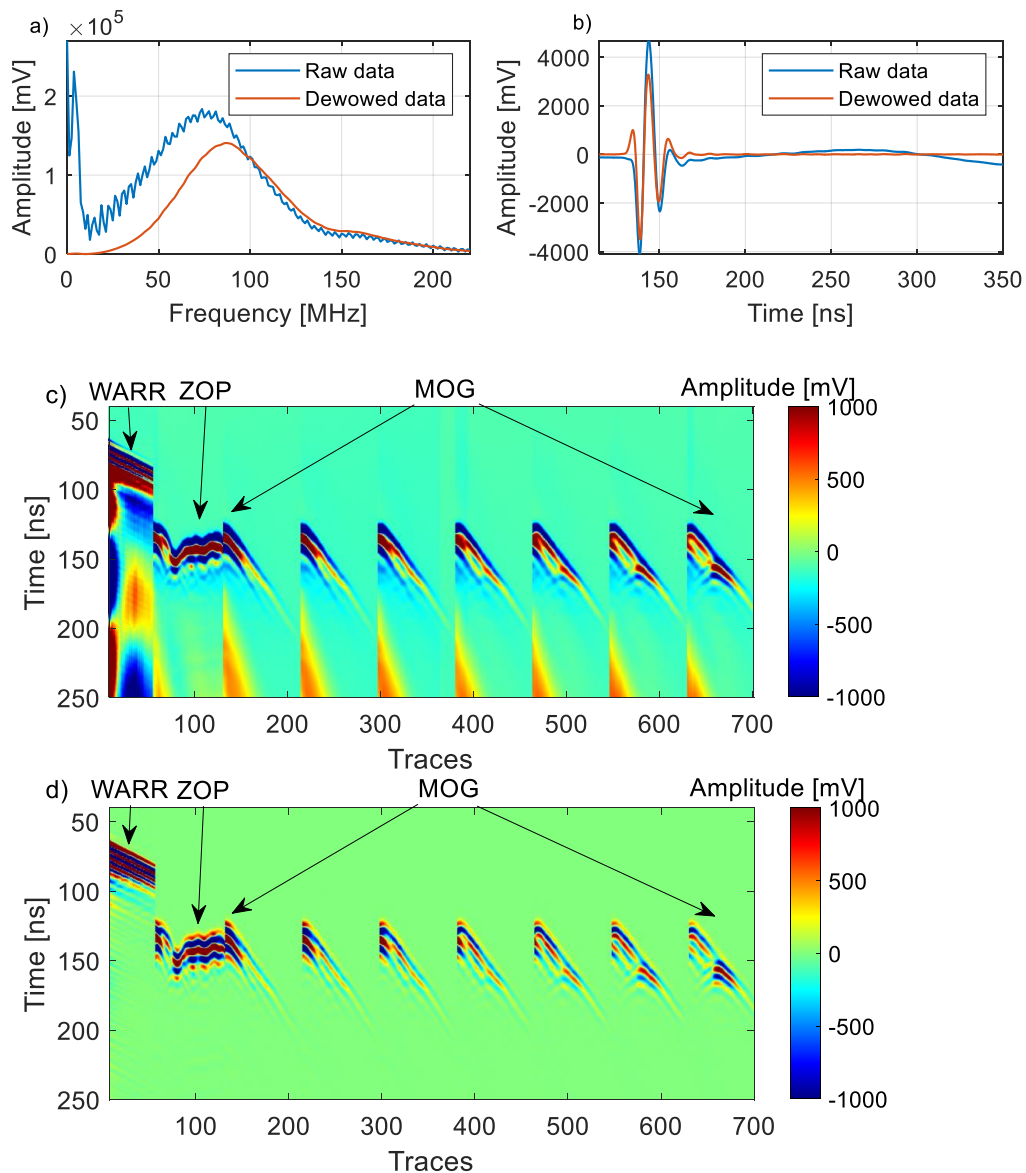


Figure 5.4: Example of the procedure of the dewow filter. a) Frequency spectra and b) time-domain plot of an exemplary raw and dewowed trace. c) Raw and d) dewowed data from WARR, ZOP and MOG shot gathers as indicated in the figure.

5.4.2 Time-zero correction

The pulse time that is measured at the receiver depends on the subsurface properties where it is travelling, and also on the time when the pulse enters the medium (commonly called 'time zero'). This starting time is generally unknown, system dependent and time varying, therefore it needs to be defined and corrected for each data set (Klotzsche et al., 2019b). Differences in this time zero point can be caused by thermal drifts, cable length differences, electronic instability, and variations in antenna air gap. Especially for crosshole applications, where no air wave is present in the data, additionally calibration measurements need to be performed. Commonly, calibration measurements in air are applied, by either measuring the air wave at a fixed offset using Tx and Rx antennas, or by performing WARR/CMP measurements at defined profiles. Since the known velocity of the wave in air and the known offset, the time zero t_0 can be calculated. Because t_0 can change during the measurements (Klotzsche et al., 2019), WARR calibrations were acquired approximately every one hour.

From WARR acquisition on the surface, where the signal is measured from direct air wave, t_0 is calculated from subtracting the expected arrival time of the pulse in air from the actual first arrival time t_{fa} :

$$t_0 = t_{fa} - \left(\frac{|\mathbf{x}_t - \mathbf{x}_r|}{c_0} \right), \quad \text{Eq. (5.2)}$$

where \mathbf{x}_t (fixed) and \mathbf{x}_r (moving) are the positions of transmitter and receiver antenna, and c_0 is the velocity in air. These calibrations measurements are in the best case performed several times during the measuring time of the crosshole plane. Using this approach, t_0 of the WARR measurements is calculated from the intercept of the linear regression line with the vertical axis. WARR acquisitions are performed at the beginning and at the end of each plane, and the t_0 of each individual MOG (or ZOP) in between is estimated over time between the exact defined calibration time zeros by a linear interpolation from assuming that the t_0 shift is linear (example in Figure 5.5a). However, time zero shift can vary during the measurement time, and because the FWI is sensitive to small time zero errors, this approach is sometimes not sensitive enough. to capture also small-time changes.

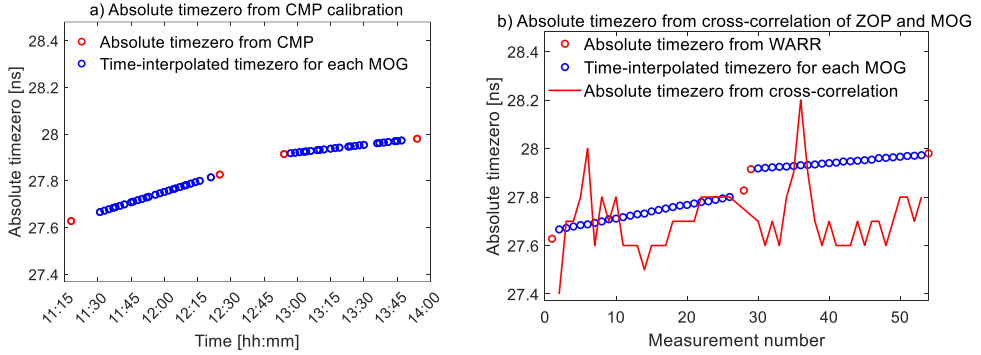


Figure 5.5: a) Zero time from WARR calibration. b) Absolute zero time derived from ZOP cross-correlation (a, red line), with blue and red circles from WARR calibration.

Oberhörmann et al. (2013) introduced a new improved time-zero correction method, which uses ZOP measurements and one subsequent WARR measurement. This method cross-correlates each ZOP trace with the corresponding trace of each MOG, which has travelled the same path between the same transmitter and receiver positions (Figure 5.6a,b). Note that the ZOP traces first need to be time corrected using the WARR measurement, which is recorded in a short time interval before or afterwards. From the highest cross-correlation of the two ZOP and MOG traces shows the time shift that occurs over time (Figure 5.4), caused by the time zero changes. This time difference between the ZOP and MOG traces (Figure 5.6c) is used to correct the time zero of the single MOG shot data (Figure 5.5b).

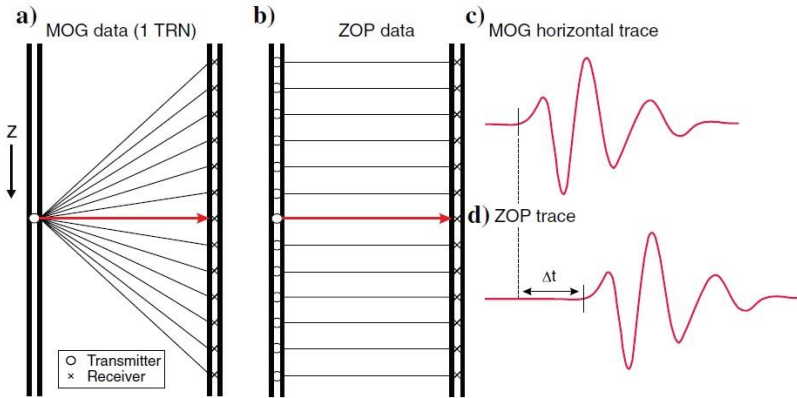


Figure 5.6: Time zero correction for MOG data based on ZOP and MOG traces cross-correlation. (a) The setup of one MOG data set for one transmitter (TRN) position and (b) the ZOP data set. This method cross-correlates each ZOP trace with one trace of every MOG, which has traveled the same path between the same transmitter and receiver positions (red lines in a and b). The corresponding red traces of (a and b) are shown in (c and d), respectively. The time zero is the time shift Δt , which needs to be applied to correct the MOG data (Reprinted from Klotzsche et al., 2019b).

5.4.3 Borehole geometry

In reality, boreholes deviate from straight vertical lines, which influence the distance between transmitter and receiver, hence can influence the travel times and the obtained soil properties. Therefore, accurate deviation coordinates of each borehole were determined using the QL40, DEV Borehole Deviation Probe (*ALT*, Mount Sopris Instrument). Using this logging tool, the azimuth and the magnetic inclination for each antennae position in the borehole is measured and the true coordinates for each measurement point can be obtained (Figure 5.7). Additionally, the depth of the measurement is correct to the surface by subtracting the height of the tubes and to an overall maximum height of the test site.

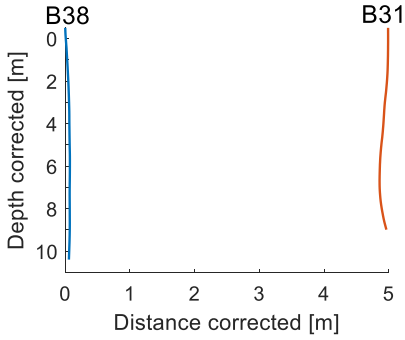


Figure 5.7: Exemplary borehole depth and lateral distance projected to the crosshole plane of two boreholes.

5.4.4 Picking of first arrival time of ZOP and MOG traces

Although the full-waveform approach uses the entire trace information, the first arrival time of each MOG trace (Figure 5.8) is needed as input data to constrain the ray-based inversion to derive the background starting models for the FWI. To avoid manual picking of thousands of traces, an automatic picking routine is used, which requires only picking of some reference traces (Klotzsche et al., 2019c). This routine requires for each data type a constant between the first break and the first maxima position of the traces. These constants are picked for some exemplary traces and applied with the automatic picking routine to all the data. Note that these constants are defined for each crosshole plane dataset. In a second step, data that have a high noise level or small amplitudes (normally high angle data) are excluded to avoid errors in the ray-based inversion.

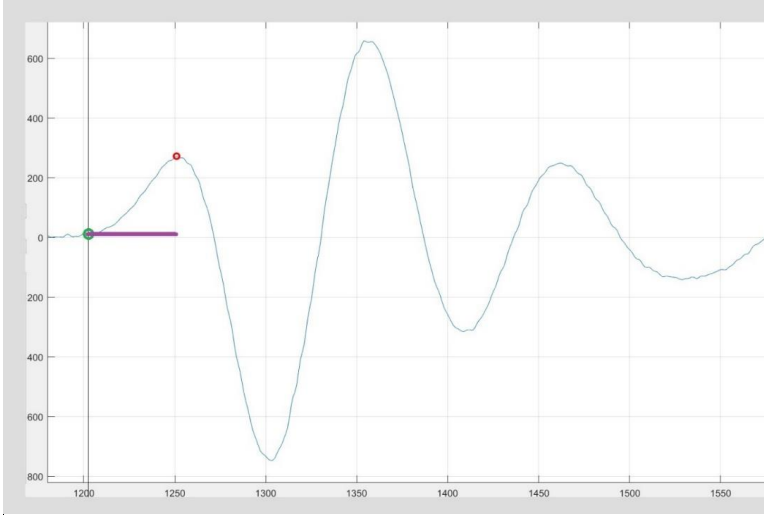


Figure 5.8: Exemplary first arrival time picking of one MOG trace. Green circle represents the first arrival-time, red circle represents the first maxima. The time difference (here in samples) indicated by the purple line is the defined constant used in the automatic picking routine.

5.4.5 Investigation of data consistency

A GPR signal emitted from a source in a water-filled borehole is coupled with high electrical conductivity of salt solutes in water (Liu et al., 1998) which causes frequency-dependent attenuation. In a crosshole survey during a salt tracer migration each antennae is located at boreholes with different salt concentration, and later the Tx and Rx switch locations. We introduce a new data validation approach to investigate the borehole filling effect on the data. In each semi-reciprocal data set, data pairs are considered, which have the same Tx-Rx and Rx-Tx locations (Figure 5.9). We tested this approach for two planes, one which only has a minor effect and one which has a large effect by the temporal σ changes. Plane 3831 is perpendicular to the flow direction, therefore the σ temporal changes in B31 are minor, while in B38 water σ is not affected by the tracer (not connected to the aquifer, sealed tube). For the plane 2938 significant differences are expected due to that this plane is parallel to the flow direction and B29 is the injection borehole. For each plane, we plot the semi-reciprocal traces for two locations where the tracer is expected to travel (8.3-10.2 m): one horizontal pair of Tx-Rx and one pair with a 20° angle (Figure 5.9).

All the results show visually and mathematically by calculating correlation coefficient R^2 between both reciprocal traces, and root mean square error $NRMSE$ ($RMSE / (A_{max}^{obs} - A_{min}^{obs})$), that the semi-reciprocal traces are almost identical. The good alignment of traces regardless whether the transmitter (or receiver) was located in a high or low conductivity borehole suggests that the total effect of the

borehole water on the signal is an integration of the borehole effect on both the transmitter and the receiver. These findings underline that the contribution of the Tx and the Rx on the GPR data are same.

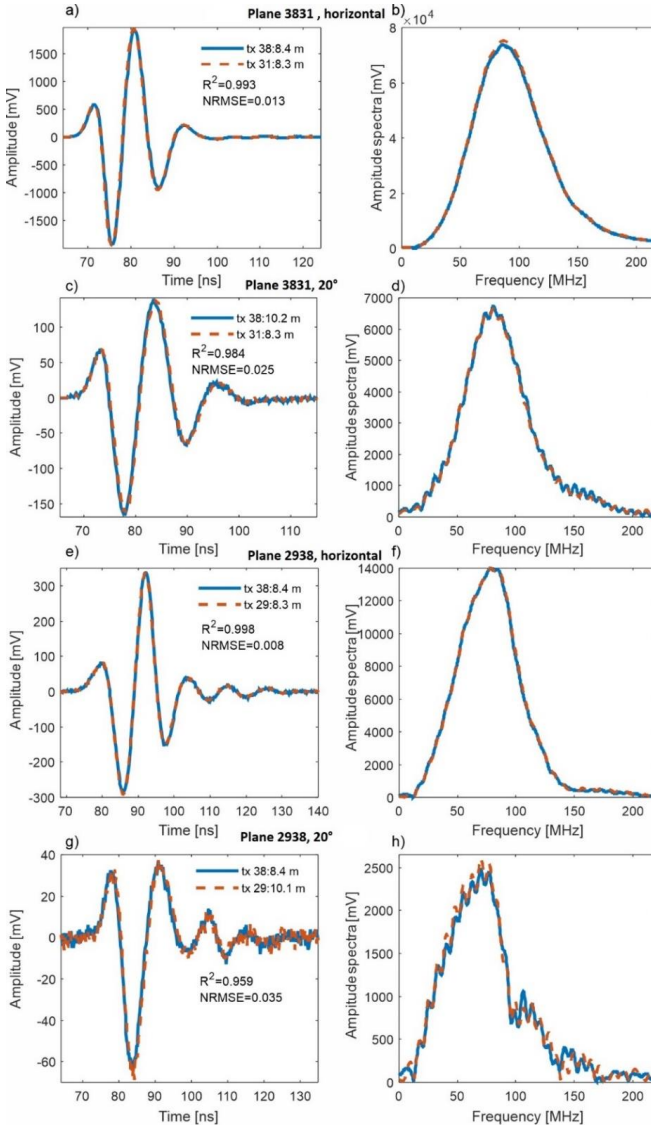


Figure 5.9: Data quality check for the time-lapse crosshole GPR data. Exemplary GPR traces from reciprocal locations of transmitter and receiver antennae during the tracer transport, at time and location which the tracer is present at the plane. Left and right columns show the traces in time and frequency domain, respectively. R^2 and NRMSE between the traces are shown to estimate the alignment of the reciprocal traces. a,b) Plane 3831, horizontal direction. c,d) Plane 3831, 20° to the horizontal. e,f) Plane 2938, horizontal direction. g,h) Plane 2938, 20° to the horizontal. In planes 3831 and 2938 the data are from days 4 and 3, respectively (see Table 5.1 for more details).

5.5 Crosshole ZOP analysis

The time-lapse ZOP data with relation to the background ZOP data are used to produce 1D-depth profiles of the permittivity and attenuation. With the final ZOP results, we investigate the effect on the permittivity and attenuation over time by calculation of the permittivity differences $\Delta\epsilon_r$ using

$$\epsilon_r = (c_0 / (\Delta x / t_{arrival-time}))^2 \quad \text{Eq. (5.3a)}$$

and

$$\Delta\epsilon_r = \epsilon_r(\text{Day } t) - \epsilon_r(\text{Day } 0), \quad \text{Eq. (5.3b)}$$

where Δx is the Euclidean distance between the transmitter and receiver position, and $t_{arrival-time}$ is the wave traveling time between transmitter and receiver (see Section 5.3.2).

From the ZOP data, we can also derive the differences of the attenuations of each ZOP. The difference attenuation $d\alpha$ (calculated in dB) between data measured in time-lapse to background data for a single trace comparison is calculated for the respective transmitter and receiver locations (Day-Lewis et al., 2003):

$$d\alpha = 10 \cdot \log_{10} \left[\frac{\sum_{i=1}^n (A_i^0)^2}{\sum_{i=1}^n (A_i^t)^2} \right], \quad \text{Eq. (5.4)}$$

where n is the number of samples in a single trace, and A_i^0 and A_i^t are the amplitudes of samples in the background and time-lapse data, respectively.

ϵ_r depth profile of all days, and $\Delta\epsilon_r$ time interpolation using a color scale, are presented for all ZOP depth measurements (Figure 5.10).

The results of plane 2938 show increased permittivity until $\Delta\epsilon_r=3$ on days 1-3, days when high σ were still observed in the borehole (Figure 5.2c), and no changes on later days. This effect could maybe be caused by the correlation between high σ and an effect of the borehole filling (i.e. high σ in boreholes because of the salt tracer) and the resulted of delay in time on the data. In the planes 3238, 3831 and 3834 we observe time-lapse $\Delta\epsilon_r$ -1.5 and 1.5, but with no clear explanation for depth or correlation to other data. In general, no changes in permittivity are expected caused by the salt tracer changes. A possible explanation for these observed differences could be explained by acquisition errors (position of the antennas in the boreholes) or picking errors.

Trace energy depth profile of all days, and difference attenuation $d\alpha$ time interpolation using a color scale, are presented for all ZOP depth measurements (Figure 5.11). We note that the measurements and interpolation for plane 2938 (B29 is the injection borehole) after Day 1 present a decay shape of $d\alpha$, which were caused by the salt tracer. Before the first time-lapse measurement at Day 1, however, the results erroneously show an increase in $d\alpha$. On Day 0 the background was measured with no tracer and thus resulted in low attenuation. After the injection was terminated (after 0.1 day) and until Day 1 data was not measured. Therefore, the expected high σ in borehole B29 until Day 1 are not shown in

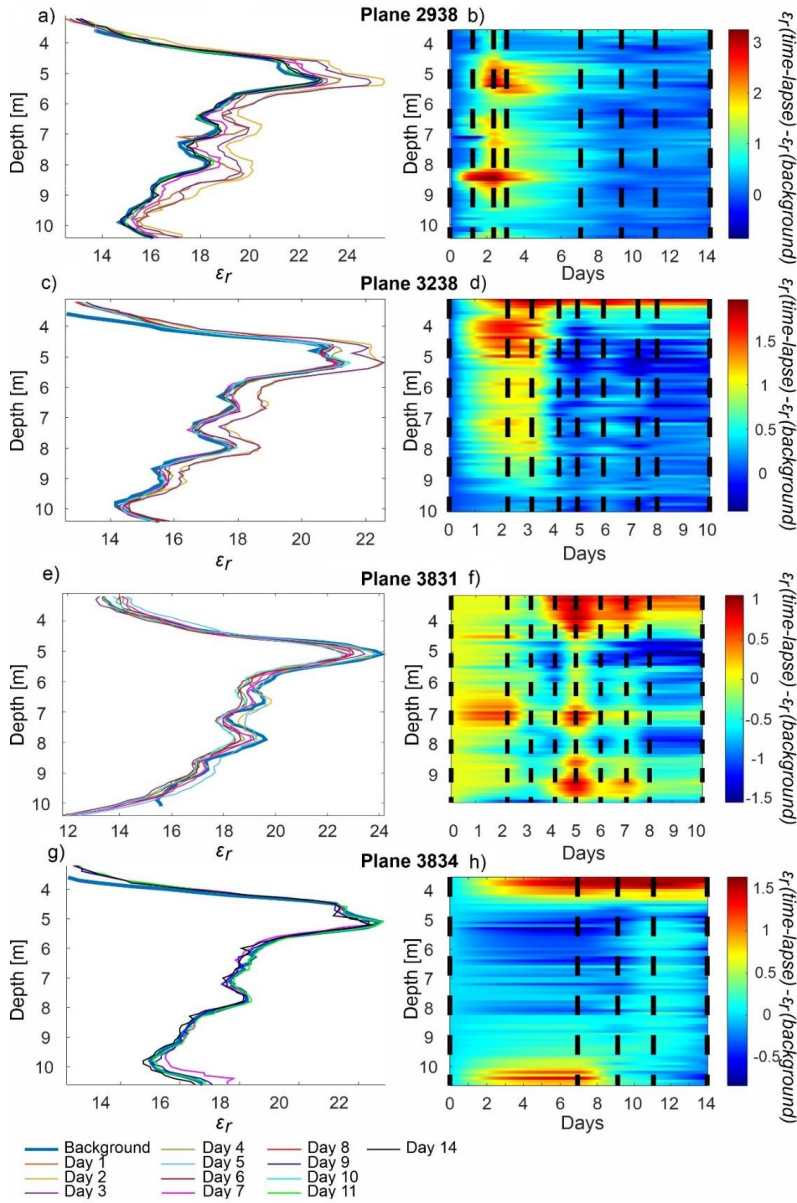


Figure 5.10: Analysis of the time-lapse ZOP relative permittivity data. Top two planes (3831 and 3238) were measured perpendicular to flow direction, while the bottom two planes (2938 and 3834) were measured in flow direction. a,c,e,g) Depth profiles for the single ZOPs. The colors of the different measurement days for a,c,e,g are shown at the bottom of the figure. b,d,f,h) Interpolated relative permittivity difference (difference to base line data). The measurement days are indicated with the black lines.

interpolation curve. Thus, for plane 2938, for the times between 0 and 1 day, we should assume trace difference attenuation at values close to those measured at Day 1.

Figure 5.11b,d,f,h shows da time interpolation for all time-lapse ZOP measurements. For the planes in the flow direction that include boreholes B29 and B34, we expect a significant σ effect caused by an energy loss due to the presence of the tracer. For the plane 2938 (Figure 5.11a), which is located at 0-5 m distance in flow direction, the trace energy difference da is visible at all depths, especially for the measurements of Day 1-3. The high da on these days is related to the tracer in the plane, and to the tracer in borehole B29 which was shown to be high on days 1-3 (Figure 5.2c). On the following days, of measurements 7,9,11 and 14 the effect of the tracer that remained in B29 was removed. Then, at depths, and on days in which da decays, (Figure 5.11a) the tracer has already effectively finished passing through the plane, which generally implies on the hydraulic conductivity of the layer in that depth. For example, the main parts of the plume travel at ~9 and 10.5 m depth and leave the plane 2938 after about 9 days (Figure 5.11b), whereas between 4-5.5 m depth of the tracer did not leave the plane at 14 days after the injection, correlating with previous knowledge of the sand facie with a lower K (Gueting et al., 2017). In the results of the parallel plane 3834 (Figure 5.11h) of 5-11 m distance in flow direction, we observe on Day 7,9,11 (the first 3 time-lapse measurement for this plane) the plume is at all depths below 7.5 m. The main plume at 9-10 m depth had left the plane after 14 days, and between 7.5-8.5 m and below 10.5 m the tracer didn't leave the plane after 14 days. This stratification is in agreement with the σ dilution results at the injection borehole (Figure 5.2a). At Day 14, we observe an increase in attenuation between 5.5-7.5 m depth, suggesting that this is a layer with lower hydraulic conductivity than the layers below 7.5 m.

For the planes perpendicular to the flow direction 3238 and 3831 (Figure 5.11c-f), we see especially for depths below 7.5 m that the da increases after a few days, reaching the maxima of this depth, and then decreased in a breakthrough-like curve shape. Above ~7.5 m depth the energy is very similar for all time-lapse measurements indicating that tracer transport cannot be deduced confidentially in this region. Plane 3831 show 3 compartments: 7.5–8.2 m, 8.2-9.5 m and below 9.5 m, and the interpolation suggests arrival times after 5, 3 and 1 days, respectively. Based on this, we can assume that the main plume traveled below 9.5 m. The results for plane 3238 shows only the two bottom compartments. Larger trace difference attenuation at plane 3831 than 3238 suggest that more tracer mass flows thorough 3831, in accordance with the previous knowledge on the flow direction (Figure 1a, Vereecken et al., 2000).

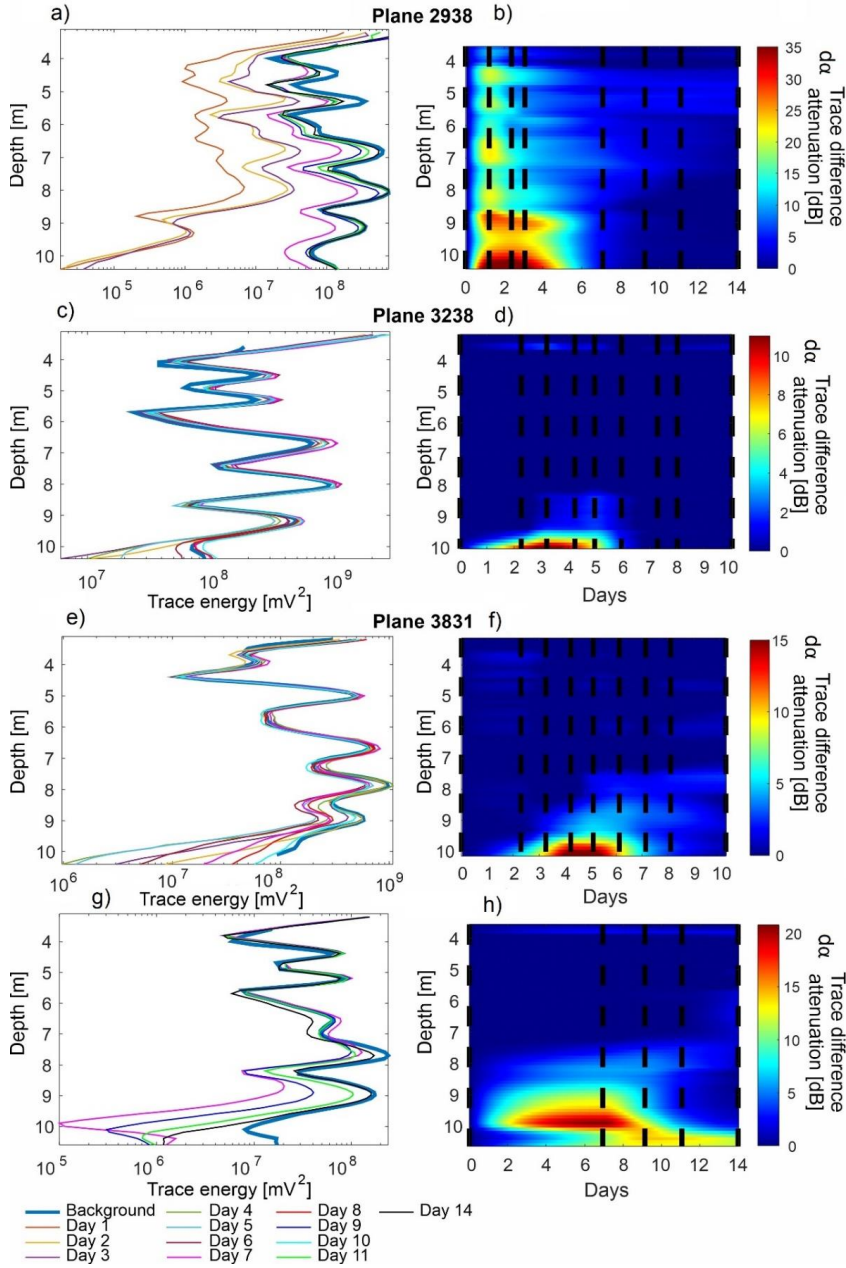


Figure 5.11: Time-lapse ZOP trace energy data. Top two planes (3831 and 3238) were measured perpendicular to flow direction, while the bottom two planes (2938 and 3834) were measured in flow direction. a,c,e,g). Depth profiles for the single ZOPs. The colors of the different measurement days for a,c,e,g are shown at the bottom of the figure. b,d,f,h) Interpolated trace difference attenuation (difference to base line data). The measurement days are indicated with the black lines.

Note, that erroneous results with higher energy for time-lapse days than the background are observed, but they are small and probably related to acquisition errors (e.g., antenna positioning).

To sum up and conclude, the ZOP results provide a first insight into the flow patterns of the salt tracer. However, the borehole filling effects and changing salt concentrations in the boreholes over time prevents the ZOP analysis, which is based on ray-based assumptions, to provide a reliable and quantitative reconstruction of the permittivity and conductivity.

5.6 Time-lapse FWI approach

As mentioned in Section 2.4, to apply the FWI to experimental data requires several pre-processing steps including the definition of the starting models and the estimation of the effective source wavelet (ESW). We have seen in the numerical study that special care needs to be taken to find an adequate starting model strategy for inverting the time-lapse data with FWI. To enable the use of measured 3D GPR data in the 2D forward simulation as part of the full-waveform inversion scheme, we applied the 3D to 2D conversion to all data sets (Equation 2.29). Similar to the synthetic studies, first, the FWI was applied to the background datasets for all the planes. Thereby, the ray-based inversion results of the travel time inversion are used as starting models for ϵ_r . For σ a homogeneous starting model based on extensive previous studies was applied (e.g., Zhou et al., 2020). We normalized the background data to the maximal amplitude in that dataset, which is not affecting the resulting conductivity results but minimizes the computational burdens. Note that the time-lapse data is normalized not to its maximal amplitude, but to the *background* maximal amplitude of the same plane. By that, we assume that for each crosshole plane the actual transmitter antenna was identical at all days.

Based on the starting models, the ESWs are estimated using the two steps deconvolution approach (See Section 2.4.4). An accurate estimation of the source wavelet is important for accurate FWI results and especially for the background data, which in turn is crucial when it is used as starting model for the FWI of time-lapse datasets. To improve the ESW correction, the FWI loop can be stopped, and the source wavelet can be updated again using the last FWI models (Klotzsche et al., 2019). Since the ESW estimation is depending on the starting models, we decided to keep the conductivity starting model's constant over all time steps and background. Similar to the synthetic study (Section 4.3) we study the effect of using different starting model strategies based on the time-lapse FWI (Figure 5.12). Strategy S1 applies the same starting model approach described for the background data, i.e. ϵ_r from ray-based and σ homogenous of the time-lapse data. Strategy S2 uses the FWI background ϵ_r and a homogenous σ as starting models. Strategy S3 uses both the FWI background ϵ_r and background σ as starting models. To estimate the ESW (Figure 5.12) we also used the two steps deconvolution approach (Section 2.4.4). However, for the first step, while S1 is based on the horizontal rays of the time-lapse data, S2 and S3 the ESW is adopting the ESW of the FWI background. The second step uses the deconvolution approach for all three strategies.

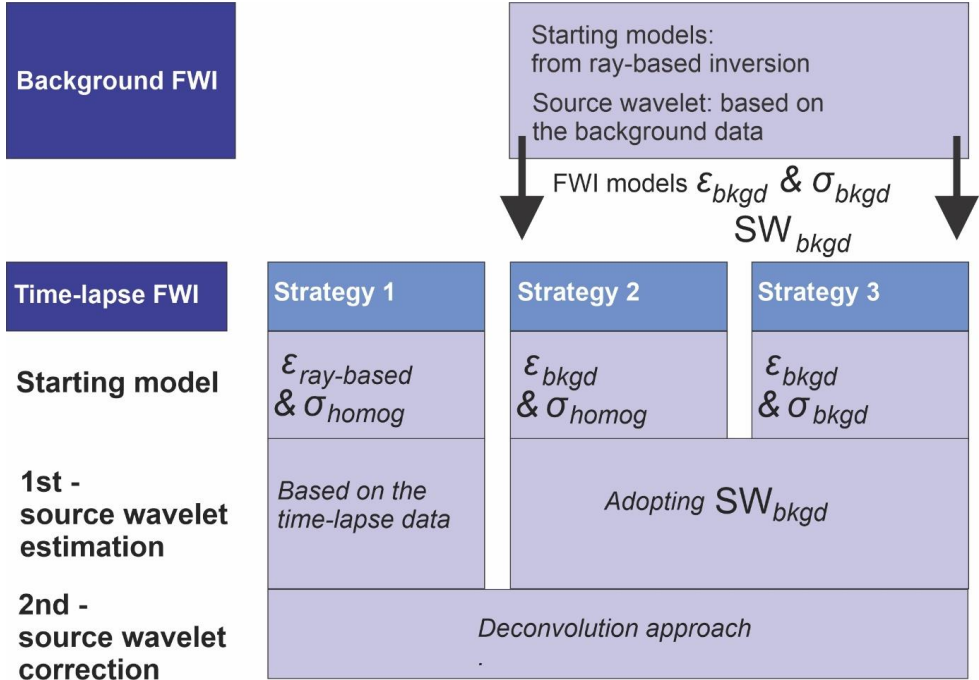


Figure 5.12: Sketch of the different starting model strategies tested for FWI of time-lapse data. SW – source wavelet; $Bkgd$ – background; $homog$ – homogeneous;

For the forward modeling and inversion of the FWI, we considered a model cell size of 0.03 m and 0.09 m, respectively. To realistically include reflections and refractions of the GPR data, we describe the unsaturated zone with $\epsilon_r = 8$ (in the range of ϵ_r for “soil sandy dry” in Table 4.1 in Daniels (2004)) above the water table. As Klotzsche et al. (2019b) showed, it is necessary to adjust four inversion parameters to tune the FWI. Therefore, we adjusted the ϵ_r and σ perturbation factors (Equations 2.39-2.40) that provided the best inversion update and minimized the cost function best. For most of the background, and the saltwater intruded time-lapse datasets, the perturbation factors of 10^{-3} and 10^0 for ϵ_r and σ , respectively, provided the best solution. For days and planes where more tracer was present in the planes (e.g., Day 1 of plane 2938), the conductivity perturbation was changed to 10^1 . In order to avoid numerical artifacts close to the boreholes, we applied the gradient normalizations which allows a medium parameter to be updated in the entire inversion domain with a value of 50 for both parameters (Equations 2.41-2.43). According to Section 2.4.5.4, we applied the proposed criteria to define the best FWI. Note that for all the following presented results these criteria were fulfilled.

5.7 GPR FWI results

To reconstruct the plume from σ time-lapse changes, we inverted crosshole GPR data from 5 crosshole planes (Figure 5.1a): 5 background and 29 time-lapse datasets from Day 1 until Day 14. To characterize the saltwater tracer σ from the σ FWI models, which represent the bulk conductivity, we derive the plume reconstruction from electrical conductivity difference to the background (rather from petrophysical relations, Chapter 4).

5.7.1 FWI of the background data

In a first step all the background datasets were inverted using the FWI (exemplary shown for Plane 3831 in Figure 5.13a,b). To check the robustness of the FWI results, we compare the new background results from plane 3831 with a previous study (Figure 5.13c,d) described by Zhou et al., (2020). Note that the previous dataset was measured in 2012, while our dataset was acquired 7 years later. The final FWI permittivity and electrical conductivity tomograms show very similar structures and values. Small local changes are present, which can be explained by the different transmitter and receiver spacing in the two data sets. While in the previous study the transmitter and receiver spacings were 0.5 m and 0.1m, respectively, we have in the current study 2.5 times more data with transmitter and receiver spacing of 0.2 m and 0.1m, respectively, which better constrain our FWI results. As Oberbröhrmann et al. (2013) showed, especially the conductivity results improve with a higher spatial sampling, concluding that the new conductivity results are quantitatively better. Nevertheless, the very similar results show a great repeatability of the FWI and the results of the test site.

5.7.2 Starting model strategy for time-lapse GPR FWI

To make sure we find an optimal strategy for all planes, we investigate the effect of the three starting model strategies as described in Section 5.6 for two planes in detail. We first consider plane 3831 perpendicular to flow direction (Figure 5.16). Although the plume reconstruction in the salt tracer is derived from σ changes, to obtain a reliable σ recovery it is required that the ϵ_r time-lapse model is accurate (Klotzsche et al., 2019b). As expected, since the salt tracer should only affect ϵ_r very minorly (Hagrey and Müller, 2000), the structure of the FWI ϵ_r models in plane 3831 of the background and strategies S1-S3 for time-lapse data are very similar (Figure 5.16i-l). As expected, the magnitude of FWI ϵ_r results from S2 and S3 is similar to the ϵ_r background. However, the magnitude of FWI ϵ_r from S1 is lower, because it used as starting model from ϵ_r from that day ray-based inversion which is different than ϵ_r background for S2 and S3. The ϵ_r final gradient of S2 is the lowest amongst the three strategies (Figure 5.14m-p, Table 5.2). In contrast to the background conductivity model, the final time-lapse FWI σ models show a large similar increase at 9-10.5 m depth for all three strategies S1-S3 (Figure 5.14q-t). However, strategy S2 shows the lowest σ final gradient (Figure 5.14u-x, Table 5.2). Note that all three inversion strategies resulted in a decay *RMSE* behavior with proceeding iterations and showed

generally a good data fit (not shown). Summarizing the S2 shows also the best $RMSE$ and R^2 of the data, in addition to the other criteria.

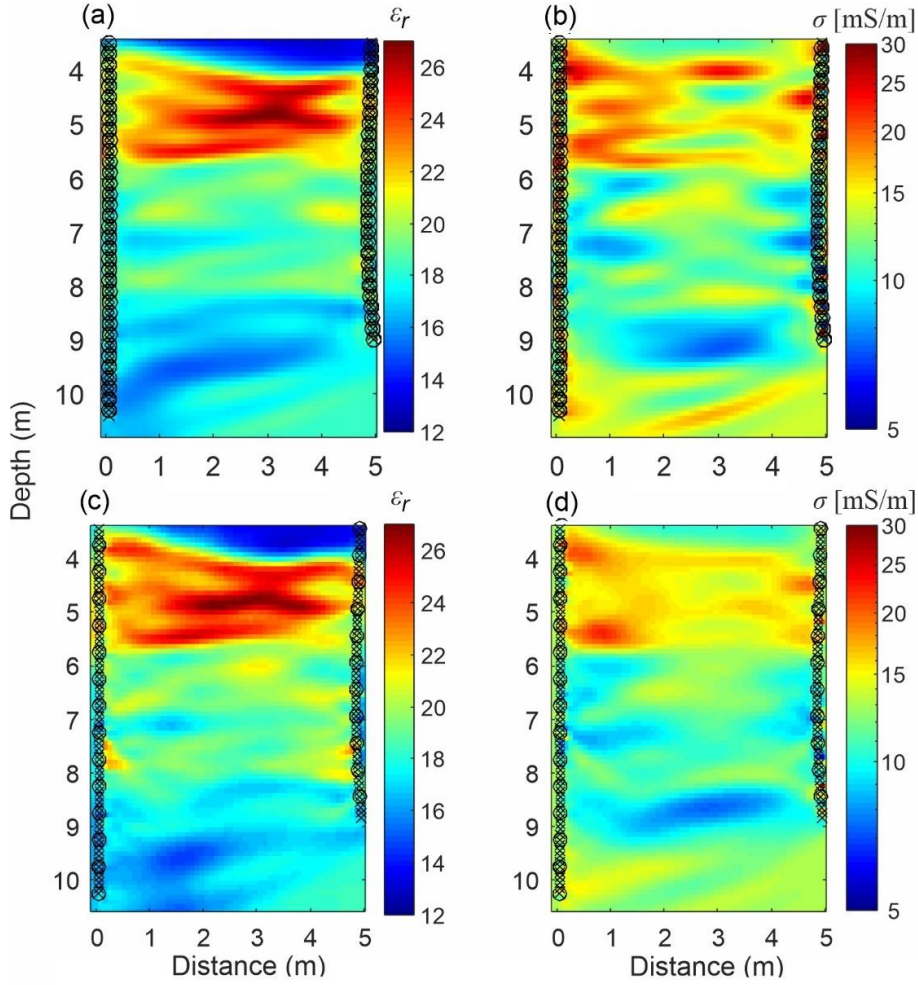


Figure 5.13: Comparison of the FWI background results of plane 3831 from two different acquisitions. (a,b) permittivity and electrical conductivity in the current study, and (c,d) from previous study (Zhou et al., 2021). Transmitter and receiver locations are indicated by circles and crosses, respectively. Note that the conductivity models are plotted with a logarithmic scale.

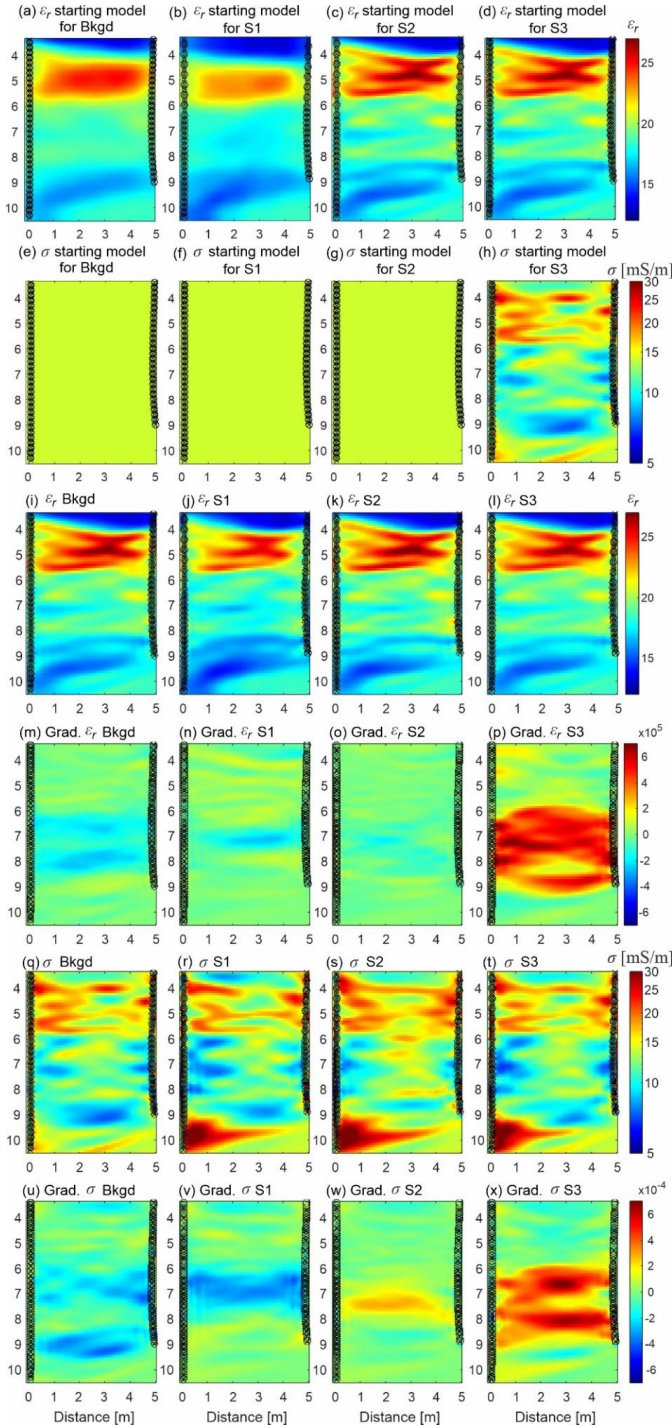


Figure 5.14: FWI results for the background and the three starting model strategies for plane 3831 (perpendicular to flow direction), at Day 4. B38 is the left and B31 is the right borehole. a-d) ϵ_r starting models for the different starting model strategies and e-h) corresponding σ starting models. i-l) Final FWI ϵ_r models and corresponding m-p) ϵ_r gradients. q-t) Final σ FWI models and u-x) corresponding Final σ gradient. Circles and crosses, respectively indicate transmitter and receiver locations.

Following the processing flow (Figure 5.12), for each of the strategies an own ESW was defined and considered for the FWI in Figure 5.14. Comparing the ESW (Figures 5.15), we can observe that when the same starting models were used, also similar ESW and corresponding frequency spectra were obtained (background and S1). Similarly, when the FWI background ε_r starting model used (S2 and S3, Figure 5.14c,d), the ESW phase is similar, but in 2 ns phase delay in comparison to the Background and S1 (Figure 5.15a, yellow and green). The central frequency of these wavelets are not much affected (Figure 5.15b). The amplitude of the ESW in S3, which used the FWI background σ as starting model is lower than the amplitude in S2, which in turn affects the FWI σ model from S2 to have higher values than FWI σ model from S3 (Figure 5.14s,t, e.g., red/yellow spots at 6-6.5 m, and at 8 m, in FWI σ from S2 and S3, respectively).

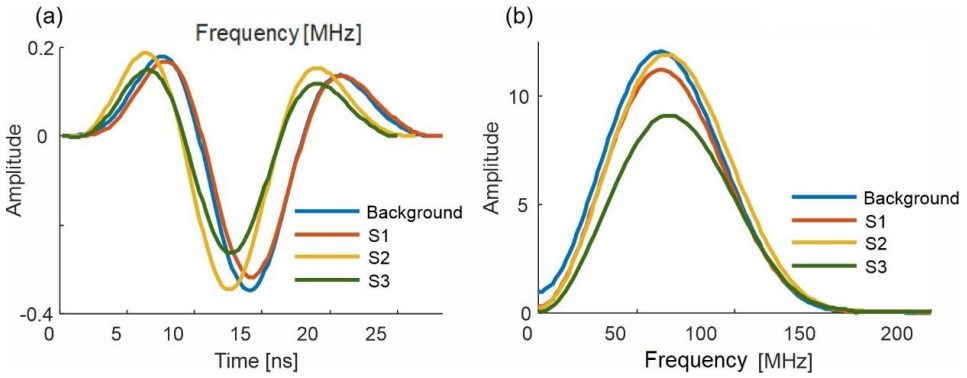


Figure 5.15: (a) Source wavelet and corresponding (b) frequency spectra of the final corrected source wavelet of the background and three starting model strategies S1-S3, at Day 4 for plane 3831.

Similar to the results of plane 3831, the final FWI permittivity models for all strategies S1-S3 and the background for plane 2938 are relatively similar (Figure 5.16i-l). The ε_r final gradient of S1 is the lowest (Figure 5.16m-p, Table 5.2) in contrast to S2 and S3. For this crosshole plane the σ FWI models from S1 and S2 (Figure 5.16r,s) that used the same homogenous σ starting model (Figure 5.16f,g) are relatively similar, although they started with a different ε_r starting model (Figure 5.16b,c). That similarity from S1 and S2 is a sign for the reliability of these FWI σ models. Interestingly to notice is that using the background σ starting model in S3, the FWI σ differs in terms of structures and values especially in the region where the tracer is expected (Figure 5.16h). The final σ gradients (Figure 5.16u-x), the *RMSE* and the R^2 of the data (Table 5.2) indicate that strategy S2 shows the best results.

The magnitude of the final gradients in both ε_r and σ in plane 2938 (Figure 5.16 i-l,q-t) is lower than in plane 3831 (Figure 5.14 i-l,q-t), because the amplitude in 2938 is lower due to the higher attenuation. However, the final gradients in both ε_r and σ in plane 2938 show larger contrasts than in plane 3831, because of the higher contrasts in σ that the tracer imposes. In addition, the ε_r is less good, because of the multi-parameter inversion. Similar to other studies (e.g., Klotzsche et al., 2010), we conclude that to derive the most robust and reliable FWI results for the conductivity, it is best to start with a homogeneous model rather than a model that contains already certain structures. If the changes in medium properties are too large between two time steps of the infiltration, the FWI is trapped within a local minimum and is not able to converge towards the global minimum. Based on the results of these FWI starting model tests for the planes 3831 and 2938, we choose strategy S2 as optimal strategy and apply it to all the time-lapse GPR datasets.

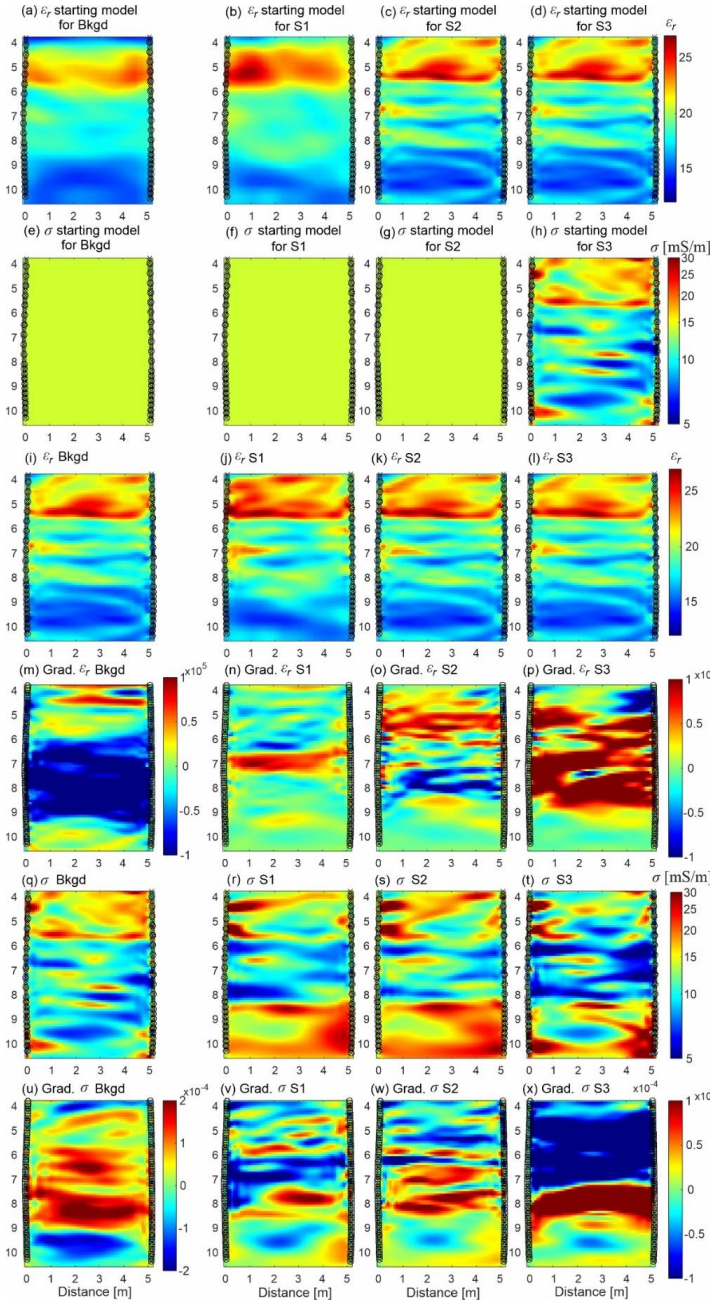


Figure 5.16: FWI results for the background and the three starting model strategies for plane 2938 (in flow direction), at Day 3. B29 is the left and B38 is the right borehole. a-d) Permittivity starting models. e-h) Electrical conductivity starting models. i-l) FWI permittivity models. m-p) Final permittivity gradient. q-t) FWI electrical conductivity models. u-x) Final electrical conductivity gradient. Transmitter and receiver locations are indicated by circles and crosses, respectively.

Table 5.2: Performance evaluation of the FWI results for the different starting model strategies S1-S3 of the GPR data of Day 4 of the plane 3831, and of Day 3 of plane 2938. Iteration num. indicated the number iterations required for the inversion, RMSE stands for the root-mean-square error, R^2 is the correlation coefficient between the measured and FWI modeled data, and the last two columns indicate the mean value of the final gradient for the permittivity and the conductivity.

3831	Iteration num.	Final RMSE ($\cdot 10^{-7}$) *	R^2 *	Grad. ε mean ($\cdot 10^5$) **	Grad. σ mean ($\cdot 10^{-4}$) **
S1	34	6.76	0.986	0.44	0.85
S2	31	6.54	0.987	0.33	0.61
S3	12	7.51	0.983	2	1.61

2938	Iteration num.	Final RMS ($\cdot 10^{-7}$) *	R^2 *	Grad. ε mean ($\cdot 10^5$) **	Grad. σ mean ($\cdot 10^{-6}$) **
S1	23	2.194	0.934	1.68	2.99
S2	17	2.09	0.945	2.77	2.95
S3	16	2.166	0.936	5.77	9.95

* Between real and FWI modelled data.

** The mean over the model, of the absolute of the remaining ε and σ gradients.

For the plane 2938 of Day 3 with large tracer mass in the plane, the the central frequency of the ESW is shifted from 60 to 53-55 MHz in contrast to the background data (Figure 5.17b). This shift is then causing an *apparent* time delay shift of 2.5-4 ns behind the background (Figure 5.17a). S1-S3 also show much lower amplitude than the background. S2 and S3, which use the same ε_r starting model, have 0.5 ns phase shift (while for S2 and S3 in plane 3831 there was no phase shift). Overall, the effects of the salt tracer on the ESW are phase shift to smaller center frequency and reduced amplitude.

We see an uncertainty in the source corrections for S1-S3, which use the same observed data, but involve different starting model pairs of ε_r and σ in the deconvolution at the pre-processing FWI scheme (Figure 2.2, step 6). Thus, choosing a starting model, which is able to explain the measured data best, results in a more accurate ESW, which in turn reduces errors from the FWI models.

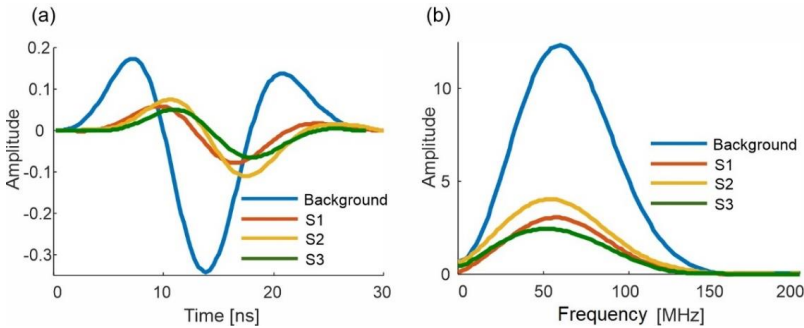


Figure 5.17: (a) Effective source wavelet and (b) spectra of the final corrected source of the background and three starting model strategies, at Day 3 for plane 2938.

5.7.3 Time-lapse FWI results

After we defined the optimal starting model strategies, we inverted all the time-lapse data sets. First, we investigate for some exemplary planes and days the actual data fit of the observed and FWI modelled data (Figures 5.20, 5.22). Overall, the data fit is good and only minor differences are present. However, we can observe for plane 2938, where the tracer mass is large on Day 2 (Figure 5.18b,e), that the FWI data fit the measured data less good than at Background and Day 14, seen by a higher ratio between difference data to the signal. For a transmitter (in B38) at 5.2 m depth, the data is decreased on Day 2 (note the colorbar is about 5 times lower than Background and Day 14), and on Day 14 the data suggest a full recovery. For a transmitter at 9.6 m depth, we also see a decrease of the amplitudes on Day 2 (the colorbar is about 3 times lower than Background and Day 14), which is fully recovery on Day 14. The decrease in amplitude is especially pronounced below 8 m, where most of the tracer mass is transported. A trend of decreased FWI convergence evaluation (i.e., increase in $RMSE-normalized$ and decrease in R^2) is in correlation with increased σ at the borehole and in the plane due to the tracer (Table 5.3, see the statistics trend for plane 2938 from Day 1 to Day 14). A close observation on Day 2 (Figure 5.19) shows there is about 3 ns apparent arrival-time delay in comparison to the background and Day 14 datasets. This apparent delay in phase correlates with higher saltwater concentration in the injection borehole B29 (Figure 5.2c).

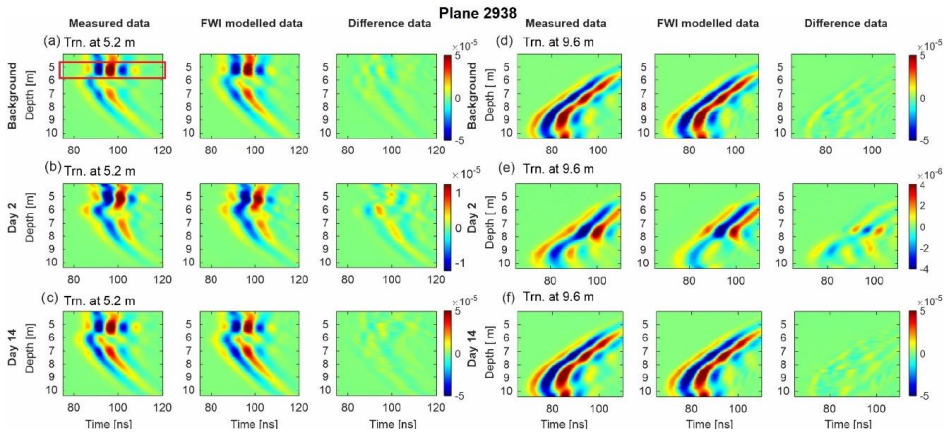


Figure 5.18: Exemplary GPR data for different time-lapse days for plane 2938 (in flow direction). Measured, FWI modelled data and the difference data are shown for two different antenna locations (left (a-c) at 5.2 m, right (d-f) 9.6 m) before the tracer injection (Background, top row), short time after the injection (Day 2, middle) and at the last day of monitoring (Day 14, bottom). Red rectangle emphasizes the high porosity waveguide. Note the different colorbars for Day 2. Transmitter is located at B38, receiver at B29.

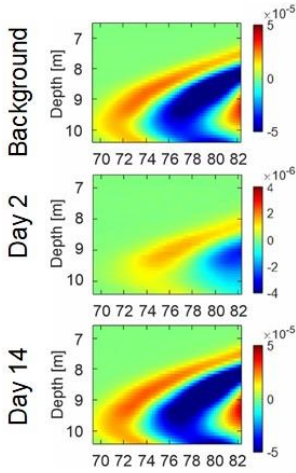


Figure 5.19: High borehole saltwater effect on the data. GPR measured data for different time-lapse days for plane 2938 (in flow direction) with transmitter at 9.6 m depth (zoom-in of Figure 5.18d-f).

Transmitter is located at B38, receiver at B29.

In the data difference of plane 3831 we can observe only small residuals. To view the effect of the tracer, the black ellipses emphasize small changes in the measured data between the different days. No change is observed between Day 4 and the background, while Day 10 shows a decrease in amplitude compared to Background and Day 4. This suggests that at 5.3 m depth (Figure 5.20a-c) the tracer did not arrive plane 3831 at 5 m down gradient after 4 days, and that after 10 days the aquifer had not been yet recovered. This relates to sand facie (Figure 3.1b) of low K and slow velocities. However, these small nuances in the data are not preserved that clearly in the FWI modelled data. Similar data plots are shown for the transmitter at 9.3 m (Figure 5.20, right). The data fit of the FWI to the measured data is good. Rectangles in the measured data emphasize the high amplitudes in background, the lowest amplitudes at Day 4 and then increased at Day 10, but not to a full recovery. This early breakthrough and fast recovery relates to sandy gravel facie (Figure 3.1b) with average K of 1 m/day (Vereecken et al., 2000).

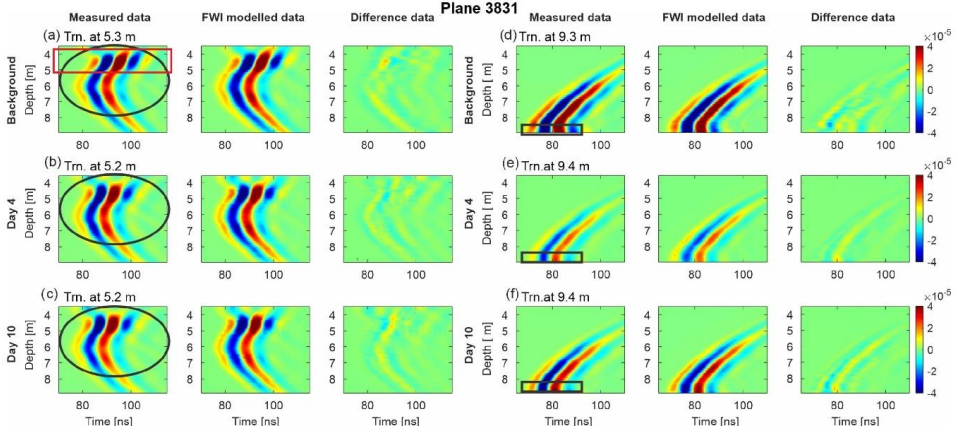


Figure 5.20: Exemplary GPR data for different time-lapse days for plane 3831 (perpendicular to flow direction). Measured, FWI modelled and difference data are shown for two different transmitter locations (left (a-c) at 5.3 m, right (d-f) 9.3 m) before the tracer injection (Background, top row), short time after the injection (Day 4, middle) and at the last day of monitoring (Day 10, bottom). Black ellipse and rectangle emphasize locations of time-lapse changes in the data. Red rectangle emphasizes the high porosity waveguide. Transmitter is located in B38, receivers in B31. The colorbar is for all images the same.

After we obtained all the time-lapse GPR FWI results, we calculate based on Equation 5.3a the differences of each time step to the background FWI results. For example, for the plane 2938 for Day 3 the difference between the FWI results (Figure 5.18k,s) to the background (Figure 5.18i,q) shows that at locations, where σ increases also ε_r increases (Figure 5.21a,b). That is mainly related to the multi-parameter inversion, which updated both ε_r and σ parameters simultaneously and hence tries to compensate the amplitude fit with changes in the phase hence the permittivity is erroneously updated (Klotzsche et al., 2019b). In the $\Delta\sigma$ plot, we identify the main flow paths. At depths 4.2-4.6 m and at 5.1-5.6 m the tracer velocity is slow and $\Delta\sigma$ is high due to small dispersion in the sand facie. At depths 6.5-6.9 m in the sandy gravel facie, we identify higher velocity and lower $\Delta\sigma$ more due to larger dispersion. At depths 8-10.5 m in that facie, where the grain size is larger (Gueting et al., 2017) the velocity is the highest and $\Delta\sigma$ is the lowest due to dispersion in the vertical direction seen by vertical smearing of the plume.

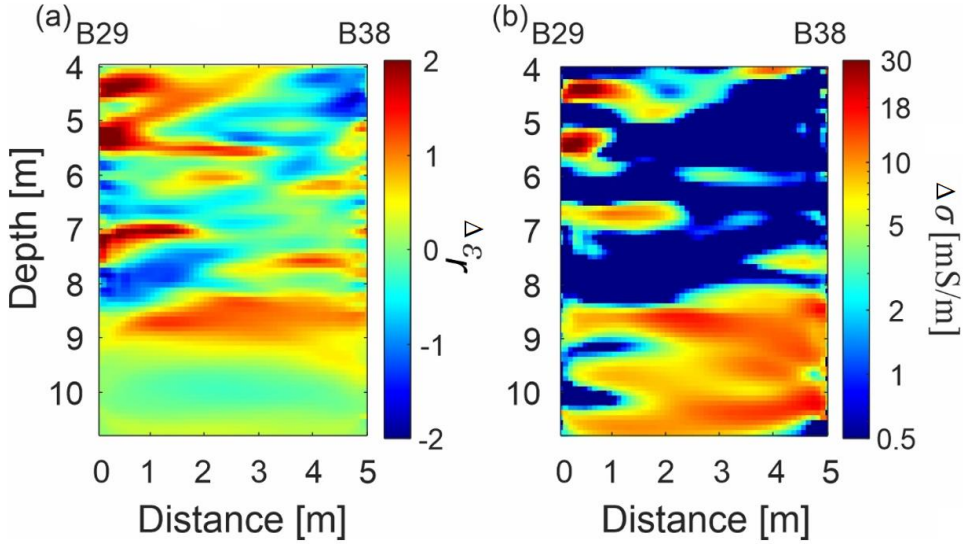


Figure 5.21: FWI difference models for a) permittivity and b) electrical conductivity for plane 2938 on Day 3. B29 is the injection borehole and B38 is on the main flow direction.

As a final step, we stitch all the obtained difference images of the conductivity models for all the planes together to construct the plume transport over time (different viewing angles on Figure 5.22a,b, and corresponding animation of these images can be found [in this link](#)). Note that all the inversions are performed in 2D and are performed independently. As a reliability measure for the plume reconstruction, we check for a spatial continuity of the tracer in given days, and by continuity in time that meets with the expected groundwater velocity and tracer spreading and dilution. In addition, we summarize the FWI convergence statistics from all datasets in Table 5.3. In the table, note that *RMSE* of the FWI models is normalized to the *RMSE* of the starting model, where for the FWI background the starting model is the ray-based model (Figure 5.18a,e), and for the FWI time-lapse the starting model is the FWI background model (Figure 5.18c,g). The *RMSE* magnitude is also affected by the amplitude of the data, therefore in datasets where the attenuation is high because of the influence by the tracer *RMSE* may be low. R-squared (R^2) in most of the datasets is above 0.95, where the lowest R^2 are calculated for Plane 2938 at days 1-3 (0.885, 0.907, 0.945) were also above the accepted threshold of 0.8 (Section 5.4.2.4), when large mass of the tracer was observed both in B29 and in the crosshole plane, causing lower signal-to-noise ratio and large σ contrasts. Therefore, we find R^2 as an acceptable measure to assess the quality of the inversion and compare between different datasets.

For plane 2938, close observation on Days 1-4 consistently show infiltration from the injection borehole B29 to the aquifer through main trajectories at two facies: i) the *sand facie* at depths 4.2-4.6 m and 5.1-5.6 m. ii) the *sandy gravel facie* 6.5-6.9 m; and iii) at the deeper part of the *sandy gravel facie* where a trend of increasing grain size with depth occurs (Tillmann et al., 2008), infiltration is observed at depths

8.3-8.9 m, 9.4-9.7 m, and 10.3-10.8 m. High tracer velocities and tracer dilution are observed below 8 m depth, and also elongating of the plume (longitudinal dispersion) and vertical (transversal) dispersion are observed. A continuous plume structure from 9-10.8 with a narrow horizontal barrier at about 9.9 m depth is observed for all days with good spatial continuity between planes 3238 and 3831, and also to Planes 2938, 3834 and the side diagonal Plane 3134 (on Day 9 only). However, at some days and planes the magnitude of $\Delta\sigma$ shows inconsistency, e.g., at both sides of borehole B38 on Day 5. The errors originate either from the background or time-lapse FWI results. However, we could not identify the reasons and neither improve the results with adjustment of FWI controlling parameters and processing steps.

In describing the plume fate from the FWI plume reconstruction, the most mass of the tracer is transported below 8 m. This facie is also the fastest as on Day 14 it has almost completely passed B34 (at 11 m distance), where tracer is mainly viewed below 10.5 m of probably tracer that sunk and transported at the aquifer surface. Between 5-8 m depth, the anomalies are lower in magnitude and sparse, with less continuity within a plane. That can be explained by the low magnitude, which increases the uncertainty in $\Delta\sigma$. Between 4-5 m there is an anomaly that dilutes and disperses (seen at plane 2938) and transports slowly from B29 towards B38. It is still seen with high $\Delta\sigma$ on Day 14, and by that day it is not seen at plane 3834. The weak dispersion is explained by that this facie is composed of sorted sand and has slow flow velocity. The flow direction on that layer was found to be NW (Vereecken et al., 2000), while plane 2938 direction is NNW, and plane 3834 is N, which may explain why the plume is not seen in 3834.

We define errors as $\Delta\sigma$ anomalies at unrealistic location at the aquifer, and uncertainties where the plume is sparse and not continuous. We observe errors, e.g., in plane 2938 on Day 1, where anomalies are imaged nearby B38 (i.e. 5 m travel distance over one day) at 5.5-9 m depth. On Day 1, when the fit was the lowest of all datasets ($R^2=0.88$) due to the strong attenuation, we interpret these anomalies as errors and not as a part of the plume. Also, high anomalies nearby boreholes B31 and B32 seem less likely, because σ borehole water measurements showed an increase up to only 2 mS/m (Figure 5.3d), suggesting a narrow plume travelling mainly nearby the axes of boreholes 29-38-34.

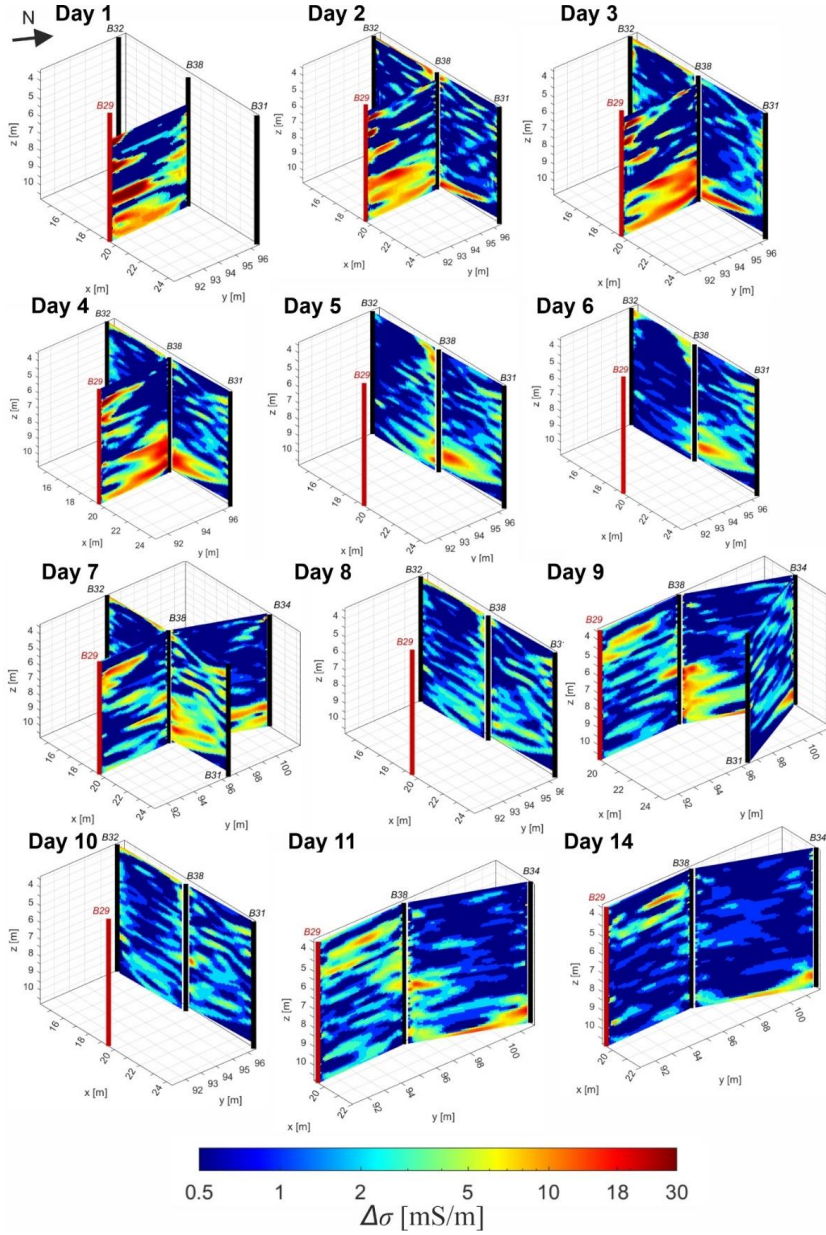


Figure 5.22a: Difference of electrical conductivity FWI results between time-lapse and background FWI models, from Day 1 until Day 14. Borehole injection B29 is indicated in red. The conductivity differences are plotted on a logarithmic scale. For visualization purposes, the same plume reconstruction is shown from two different angles in Figure 5.22 a) and b).

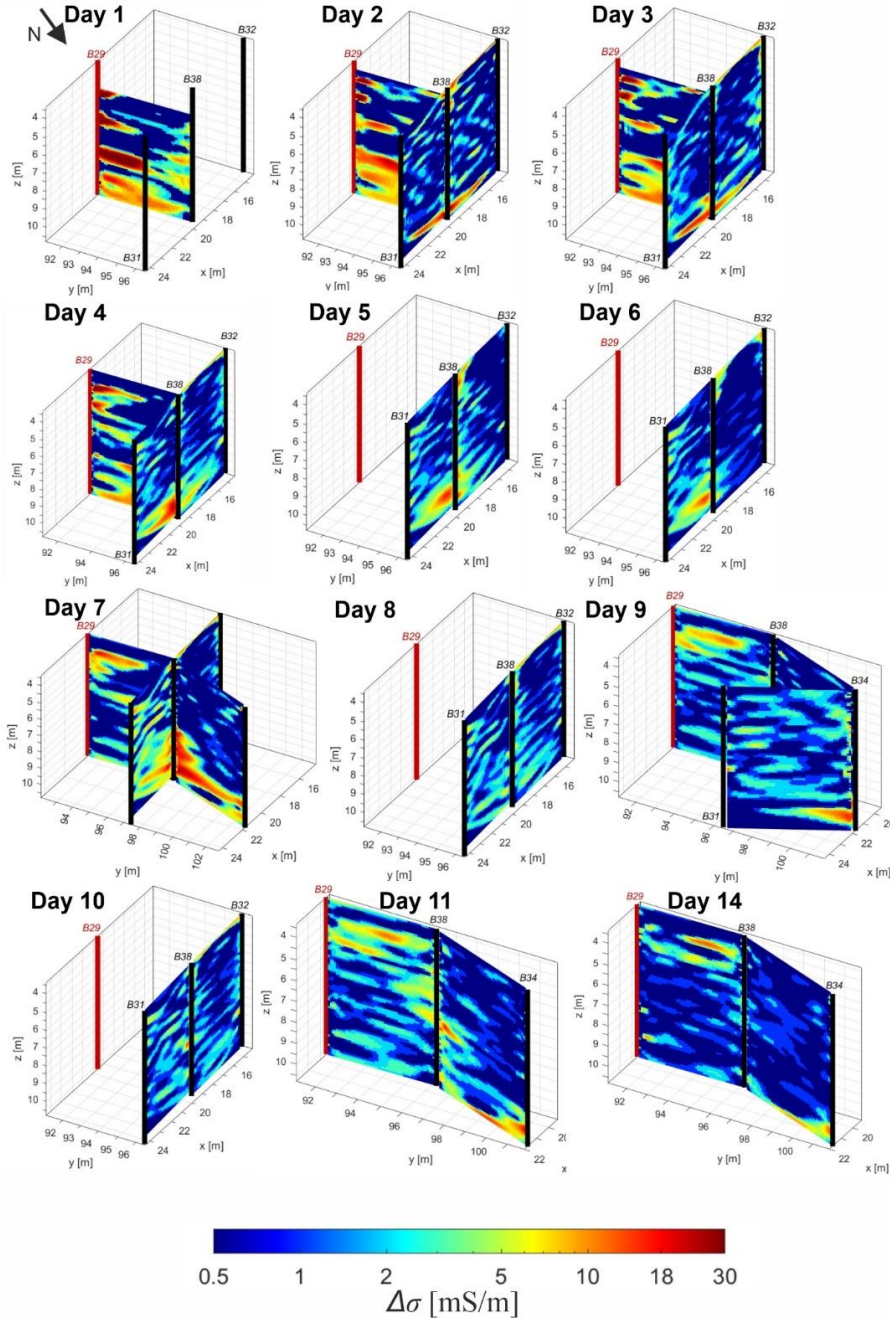


Figure 5.22b: Difference of electrical conductivity FWI results between time-lapse and background FWI models, from Day 1 until Day 14. Borehole injection B29 is indicated in red. The conductivity differences are plotted on a logarithmic scale. For visualization purposes, the same plume reconstruction is shown from two different angles in Figure 5.22 a) and b).

Table 5.3: Performance evaluation of FWI convergence using strategy S2 for all inverted planes. RMSE stands for the root-mean-square error between the FWI modelled data to the observed data, RMSE norm (%) is the RMSE with relation to the RMSE between the starting model modelled data to the observed data. R^2 is the correlation coefficient between the measured and FWI modeled data. Iter. num. indicates the number iterations required for the inversion.

		Bkgd	1	2	3	4	5	6	7	8	9	10	11	14
3831	RMSE ($\cdot 10^{-7}$)	7.21	-	5.91	6.33	6.54	7.32	6.71	6.18	5.66	-	6.78	-	-
	RMSE norm.(%)	31	-	31.5	35.4	36.9	48.9	46.8	37.6	27.3	-	42.3	-	-
	R^2	0.972	-	0.978	0.974	0.974	0.956	0.962	0.972	0.978	-	0.968	-	-
	Iter. num	23	-	35	30	31	12	13	20	34	-	16	-	-
3238	RMSE ($\cdot 10^{-7}$)	4.5	-	6.27	6.51	7.18	7.49	8.32	7.17	6.82	-	7.09	-	-
	RMSE norm.(%)	32	-	34.1	37.1	41.5	31.5	45.7	39.7	39.9	-	39.8	-	-
	R^2	0.965	-	0.972	0.969	0.966	0.961	0.959	0.969	0.97	-	0.968	-	-
	Iter. num	42	-	24	25	15	28	16	23	21	-	22	-	-
2938	RMSE ($\cdot 10^{-7}$)	8.73	1.16	2.39	2.09	2.33	-	-	3.87	-	5.17	-	5.62	9.02
	RMSE norm.(%)	29	41	48	41	39	-	-	34	-	31	-	29	29
	R^2	0.952	0.885	0.907	0.945	0.954	-	-	0.966	-	0.968	-	0.971	0.965
	Iter. num	40	23	22	17	30	-	-	30	-	17	-	26	25
3834	RMSE ($\cdot 10^{-7}$)	6.3	-	-	-	-	-	-	4.17	-	4.28	-	5.03	4.57
	RMSE norm.(%)	24	-	-	-	-	-	-	30	-	31	-	32	26
	R^2	0.971	-	-	-	-	-	-	0.975	-	0.977	-	0.974	0.978
	Iter. num	39	-	-	-	-	-	-	30	-	31	-	30	27
3134	RMSE ($\cdot 10^{-7}$)	8.09	-	-	-	-	-	-	-	-	5.45	-	-	-
	RMSE norm.(%)	38.9	-	-	-	-	-	-	-	-	35	-	-	-
	R^2	0.936	-	-	-	-	-	-	-	-	0.974	-	-	-
	Iter. num	22	-	-	-	-	-	-	-	-	30	-	-	-

One very important aspect for all of these FWI time-lapse results is to analyze the ESW of the planes over time and how they develop (Figure 5.23). In plane 3831, the ESW phase of Days 4,6,7,8 and 10 are 1-2 ns earlier than of the Background, Day 2,3 and 5 (Figure 5.23a). The ESW amplitude of the frequency spectra (Figure 5.23e) of Days 2,5,6 and 10 are lower than the background, while for Days 3,4 and 8 the amplitude is similar to the background, and of Day 7 is erroneously higher than the

background. We did not notice an increase in $\Delta\sigma$ at water borehole B31 (Figure 5.23d), and B38 in not connected to the aquifer, therefore we do not expect an effect on the ESW. We suggest that these changes were caused during the experiment due to water filling that we did in B38, which lost water when the GPR antenna was moved down and up and so forth multiple times during the measurements. We filled borehole B38 almost daily (about 1 m of the 8 m water column) either with desalinated or tap water, which are lower in σ than groundwater, and then the water column was mixed. We observe too high $\Delta\sigma$ magnitudes in Day 7 and too low in Days 5 and 6, to which we did not find an explanation. However, in general, we do suggest that the deconvolution approach separates between the ESW which composes all the effects that happen in the borehole, to the crosshole plane FWI model.

In plane 3238 the background ESW has the lowest amplitude and the central frequency of 54 MHz comparing to all other days which are consistent with of 56 MHz (Figure 5.23f). The ESW of the background is compensating due to a cause unknown to us. Note that this background dataset was used in replacement of the original dataset measured some months before (for planes 3238, 2938 and 3834, see section 5.3). Days 2,3 and 6 have an apparent phase delay of 1-2.5 ns in the ESW comparing to Days 4,5,7,8 and 10, which show in contrast almost consistent ESW (Figure 5.23b).

In plane 2938, where high σ were measured at the injection borehole B29 on Days 1-4 (Figure 5.2c), we identify an apparent phase delay of the ESW (Figure 5.23c), which increases with σ of the borehole water (except of Day 1) until 4.5 ns apparent phase delay on Day 2 (On Day 2 this apparent phase delay was also observed in the data (Figure 5.20)). Correlative trend is also observed for increased σ at B29, as the central frequency (from 60 MHz at Day 14 to 44 MHz at Day 1) and the frequency spectra amplitude were both decreased. Again, the background amplitude is lower than Day 14 amplitude. In plane 3834, which was measured on Days 7,9,11 and 14, when σ at borehole B34 is higher than groundwater, but lower than Days 1-4 at B29, we see very small difference in the apparent phase of the ESW (Figure 5.23d), very similar central frequencies (~ 63 MHz), and similar amplitudes for all the time-lapse days, which are lower than that of the background (Figure 5.23h).

We clearly noticed that effective source wavelet is compensating for all possible borehole filling effects and allows a reliable reconstruction of the permittivity and electrical conductivity using the FWI. If this would not be the case, the borehole filling effect would propagate into the FWI results and hence erroneous reconstructions would be present.

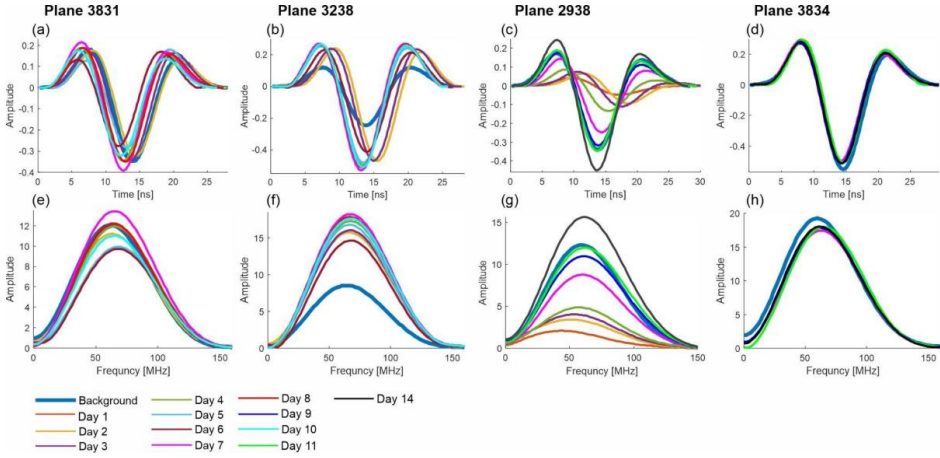


Figure 5.23: Effective source wavelets and corresponding frequency spectra used in all the time-lapse FWI for planes 3831, 3238, 2938 and 3834. The different colors indicate different measurement days.

5.7.4 Cell-wise breakthrough curves

Since we have a plume reconstruction in each cell between the boreholes using the conductivity results, we can calculate breakthrough curves for each cell. As an example, we generated such breakthrough curves from the results of plane 3831 perpendicular to the flow direction (Figure 5.24). Generally, a clear trend for each cell can be observed, however interrupted with differences up to 3 mS/m in $\Delta\sigma$. A high heterogeneity in the flow paths can be observed, e.g., for the nearby cells at 4.9 and 5.4 m depth (Figure 5.24a,b), on Day 10 they show a $\Delta\sigma$ recovery trend and an increase trend in $\Delta\sigma$, respectively. At depth below 9.3 m $\Delta\sigma$ was higher and (Figure 5.24e,f) and the breakthrough curve at 5 m distance was 4-5 days.

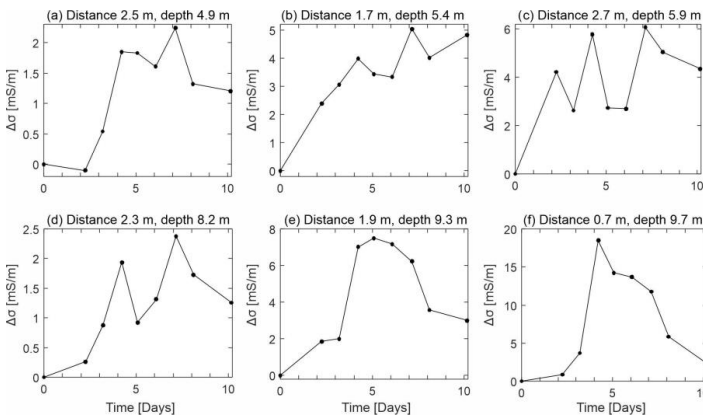


Figure 5.24: Difference of electrical conductivity between FWI time-lapse and background models at specific locations in plane 3831. The title of each subplot relates to the distance from borehole B38, and the depth from the surface. Note the different scale at the vertical axis.

5.8 Hydrological interpretation with logging data

We interpret the logging results (Section 5.2) while acknowledging the daily borehole mixing in the borehole, which occurred due to move of GPR antenna. Measurements of water σ at injection borehole B29 above the σ groundwater, at depths below 10.5 m along 13 days after the injection (Figure 5.2c) imply that a portion of the tracer mass, which was 0.7% denser tracer than the groundwater, sunk to the bottom of the injection well. An indication is seen by higher σ at borehole B34, 10.8 m downstream from the injection borehole (Figure 5.3c,d), at depths below 10.5 m for longer periods than above 10.5 m. In addition, there was a significantly higher concentration at depths between 8-10.5 m than above 8 m in B34. Regarding a transverse spreading of the plume, the tracer hardly reached the boreholes at 5 m aside (B31 and B32), suggesting that it was migrated through a narrow path.

We also test whether the tracer mass that arrived to B34 is in agreement with the transport expectations using convection-dispersion equation (CDE). We use the CDE equation in the form of an equivalent *homogeneous* medium for a mean flow in the horizontal direction (Kemna et al., 2002):

$$c_{rel}(x', y', z', t) = \frac{1}{8} \left[erf \left(\frac{x' + L_{x'} - u_{x'} t}{\sqrt{4u_{x'} \lambda_L t}} \right) - erf \left(\frac{x' - L_{x'} - u_{x'} t}{\sqrt{4u_{x'} \lambda_L t}} \right) \right] \quad \text{Eq. (5.5)}$$

$$\times \left[erf \left(\frac{y' + L_{y'}}{\sqrt{4u_{x'} \lambda_{TH} t}} \right) - erf \left(\frac{y' - L_{y'}}{\sqrt{4u_{x'} \lambda_{TH} t}} \right) \right]$$

$$\times \left[erf \left(\frac{z' + L_{z'}}{\sqrt{4u_{x'} \lambda_{TV} t}} \right) - erf \left(\frac{z' - L_{z'}}{\sqrt{4u_{x'} \lambda_{TV} t}} \right) \right],$$

where c_{rel} is the relative concentration $(c - c_{GW})/(c_0 - c_{GW})$, c is the concentration varies in time and space, c_{GW} and c_0 are the background groundwater and the injection concentration, respectively, erf is error function. The rest of the variables are described in Table 5.4.

We use the dispersivities derived by Kemna et al. (2002) from their tracer test in Krauthausen aquifer, and the setup parameters of our tracer experiment (Table 5.4), to calculate the breakthrough concentration at B34 at 10.8 m distance in the main flow direction. The result from the model is that in the breakthrough time after 10.8 days, 4.8% of the injection concentration is expected, while in our experiment test the breakthrough occurred after 8 days with 3.5% and 5.8% for L1 and L2 (Section 5.2), respectively. The results show that in general the input parameters and the results from our tracer test agree.

Table 5.4: Input parameters and tracer injection properties used for CDE equation in the form of an equivalent homogeneous medium.

Input parameter	Value
Distance and position (x', y', z')	(10.8, 0, 0) m
Groundwater flow velocity ($v_{x'}$)	1 m/sec
Time (t)	10.8 days
Porosity	0.3 -
Volume of water infiltrated	4 m ³
Plume horizontal traverse size ($2 \times L_{x'}$)	1.29 m
Plume longitudinal size ($2 \times L_{y'}$)	1.29 m
Depth of borehole infiltration ($2 \times L_{z'}$)	8 m
Longitudinal dispersivity (λ_L)	0.36 m
Traverse horizontal dispersivity (λ_{TH})	0.18 m
Traverse vertical dispersivity (λ_{TV})	0.048 m

5.9 Discussion

5.9.1 Comparison of tracer monitoring by time-lapse GPR FWI with other data

Time-lapse GPR FWI monitoring was shown to be successful in a synthetic study by comparing to the real models (Chapter 4). In a field experiment, we compare the obtained results with other available data. First, the background results are in agreement with previous results (Zhou et al., 2021) in an exemplary Plane 3831 (Figure 5.15). Also for time-lapse data the FWI convergence criteria (Table 5.3) show satisfying results, and the FWI data fit well the measured data (Figures 5.18, 5.20)., The salt tracer is visible from the difference in time-lapse FWI conductivity models, while there is no effect on the permittivity models, as expected (Hagrey and Müller, 2000).

In plane 2938, where the tracer first infiltrates the aquifer, preferential paths identified from GPR FWI at a few depth locations (Figure 5.21b, 5.22a,b) are correlated with depth locations of high attenuation from ZOP measurements (Figure 5.11b). In addition, borehole σ results measured in the injection borehole shortly after the injection (Figure 5.2a) present a good correlation with the infiltration paths from the injection borehole B29 to Plane 2938. For Plane 3831 (Figure 5.11f) below 7.5 m the ZOP indicates that the tracer is still observed at Day 10, but above 7.5 m ZOP does not show the tracer while the FWI does. Since the ZOP data uses less data and an approximate model, whereas the FWI uses more data and a detailed physical model, we expect that the FWI results are more reliable.

The ZOP in plane 3238 (Figure 5.11d) implies that the tracer has left the bottom part of the plane already on Day 7, while the FWI suggests it is still in the plane on Day 10. We suggest that the time-lapse attenuation results in plane 3238 are underestimated, based on the low amplitude of the ESW in the background of that plane. Low ESW amplitude relates to low signal amplitude. However, we cannot confidently explain the reason for the lower amplitudes in background 3238. High attenuation from ZOP in plane 3834 (Figure 5.11h) are consistent with the FWI results by that most of the tracer mass below 8 m had already passed B34. However, logging data in B34 at 8-10.5 m depth still shows high σ results on Day 14 (Figure 5.3d).

We observe from the measured data in plane 2938 at 4.8-5.6 m depth (Figure 5.18a-c), and in plane 3831 at 4.2-5 m (Figure 5.20a-c) in a red rectangle a high-porosity waveguide layer (Klotzsche et al., 2012, Appendix A.3). The FWI shows infiltration through plane 2938 at 4.2-4.5 m and at 5.1-5.5, m depths (Figure 5.21b, 22a), to be in general agreement with the information derived from the waveguide layer. The flow in this sand layer is slow comparing to the sandy gravel below 8 m depth because K is lower (Tillmann et al., 2008). Still, within the sand facie (4-6 m) the GPR waveguide correlates with a preferential flow path, as also shown by Zhou et al. (2020) at a different sandy aquifer (Appendix B.4.3). Plume reconstruction from $\Delta\sigma$ shows preferential paths, which some are not visible in the ZOP results, because here a simplified approximate model is used. At 3.5-4 m depth nearby B38 on Days 2-4 a connected plume reconstruction is viewed from all 3 planes, which are connected to it: 2938, 3238 and

3831 (Figure 5.22a). The good connectivity in time and space strengthen its reliability. This part of the aquifer is composed by gravel, which is characterized by high K (Tillmann et al., 2008).

Amongst two previous salt tracer tests monitored by time-lapse borehole ERT, we will compare our results with those from Müller et al. (2010), who injected the tracer across an entire borehole, and not from Kemna et al. 2002 who injected the tracer to the aquifer through the borehole in a 1 m width packer. Note, that the injection borehole in our study is different than in Müller et al. (2010) and located 15 m away from the one in Müller et al. (2010), who measured ERT in two planes at 10 and 20 m distance down gradient (Figure 5.25a,c). We chose an injection borehole, which allows reducing significantly the tracer water volume (4 vs. 140 cubic liters), while still using a borehole setup for monitoring with ~ 5 m crosshole distances in both parallel and perpendicular direction to flow. Therefore, we make the comparison between the tracer recoveries not for testing repeatability but to see if the tracer follows similar layers and the for the how good the tracer is resolved. Müller et al. (2010) detected a plume splitting between 6-7.5 m, with a fast layer at 7.5-10 m and a slower between 5-6 m. This splitting was not complemented by the data from their borehole loggers, but in a later crosshole GPR survey splitting was explained by high-resolution FWI in correlation with grain size data (Gueting et al., 2017), providing fine hydraulic characterization. In our tracer monitoring by FWI, we show tracer recovery from the neighboring Planes 3238 and 3831 perpendicular to the flow direction at 5 m down flow distance (Figure 5.1) on Days 4 and 8 (Figure 5.25b,d), presenting tracer connectivity in the neighboring planes and repeating location of the tracer at different days. Our FWI results suggest more splitting layers than in Müller et al. (2010), including one at 6-7 m depth in agreement with the previous study. High $\Delta\sigma$ at depths 8.5-10 m agrees in both of the tracer and monitoring tests. GPR FWI provides a higher resolution than ERT and recovers flow path in width of 0.18 m (size of two model cells). This size scale in $\Delta\sigma$ is at least as fine as the one retrieved from FWI background σ (e.g. Figure 15.5b), possibly because for time-lapse data with changes only in σ , FWI with ε_r starting model from the background allows the optimization to update mainly in σ . Moreover, recovery of $\Delta\sigma$ seems to be only slightly more smoothed than recovery of ε_r (Figure 15.5a), where in general in FWI the ε_r resolution is better than σ .

Overall, the consistency in spatial connectivity of the plume between neighboring planes and the repeatability of tracer location on different days, indicate about the reliability of these high-resolution tracer-monitoring images.

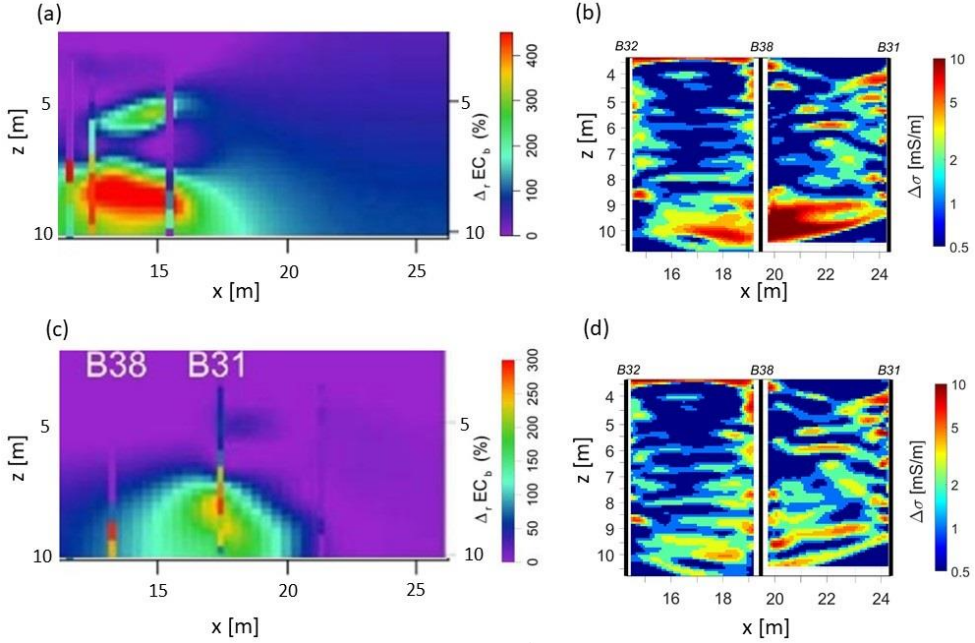


Figure 5.25: Comparison of the resolution of plume reconstruction between previous salt tracer test measured with borehole ERT (Müller et al., 2010) and the salt tracer test measured with crosshole GPR FWI. a,c) Snapshots at a transect 10 m distance downstream on Day 15, and at 20 m distance (the transect parallel of Plane 3831) downstream on Day 22, respectively. b,d) Plume reconstruction from time-lapse GPR FWI on Days 4 and 8, respectively. In a) and c) vertical lines represent electrical conductivity measured in the boreholes by sensors. Note, that in the two tracer tests the tracer was not injected from the same borehole. Also, note that c) shows the same transect as in b) and d), while a) shows a transect parallel to it but different.

5.9.2 Saltwater effect on the effective source wavelet

High electrical conductivity surrounding the borehole antenna have shown to affect the ESW, especially in plane 2938 (Figure 5.23c,g), where the largest tracer mass is travelling (Figure 5.2c). We observed a trend of increased saltwater in borehole together with i) ESW central frequency shift to lower frequencies ESW; ii) an apparent phase delay, and iii) a decrease in ESW amplitude. This is a dispersive attenuation response because of a coupling effect between the borehole antenna and the high σ at the borehole. This coupling effect which affected the source wavelet was observed also in a borehole antenna GPR survey at boreholes partly filled with water and air (Klotzsche et al., 2019a), and for surface antenna, when they were located on soils with different permittivity and conductivity (Busch et al., 2014). Permittivity difference from ZOP (Figure 5.10b) also show an increase of $\Delta\epsilon_r=0.5-3$ on Days 1-3. GPR FWI corrects the ESW in a FWI pre-processing step. The ESW contains the optimal wavelet

that is able to describe the measurements with the full-waveform. In the ideal case one could also include the borehole and filling such that reality is even better approximated (Mozaffari et al., 2021). Hence, the FWI tomograms are independent from borehole filling effect except for the lower frequency content. Without this separation, like in ZOP basic processing and ray-based inversions, an erroneous apparent phase shift and attenuation will be estimated. These results also stress that for each dataset an ESW correction is required using its deconvolution process. The use of the same ESW from the background in the FWI for time-lapse data can lead to erroneous result of the FWI inversion model.

5.10 Conclusions

We conducted a saltwater tracer test in a sandy aquifer in order to test the potential of high-resolution imaging of time-lapse crosshole 2D GPR full-waveform inversion to monitor the tracer fate for 14 days after the tracer injection over an 11 m X 10 m area. The plume reconstruction was obtained by subtracting the FWI background σ model from the time-lapse σ . The imaged plume from FWI was compared with σ sensors at the boreholes, ZOP data, and by spatial continuity at neighboring planes. Imaging of the tracer at the same location on different days implies on repeatability. Moreover, trend of an increase followed by a decrease trend in $\Delta\sigma$ is observed, which implies on the plume velocity. Dispersion is implied from an increase in size of $\Delta\sigma$ anomalies and smoothing in vertical transverse horizontal and longitudinal horizontal direction (e.g. in Figure 5.22a Plane 2938 follow the development of the plume below 8 m depth). Flow paths and splitting layers were resolved in thickness of about 18 cm (2 model cells), which is in improvement compared with FWI background σ , and seems to be only slightly more smoothed than ϵ_r recovery.

The starting model for time-lapse data that provided the best FWI results was the one using the FWI background permittivity and a homogenous conductivity. That was observed for experimental data, in different to the synthetic data results, which suggested the background conductivity (Chapter 4). In experimental data, when a starting model uses the FWI background conductivity for the time-lapse data, it incorporates errors in the starting model, which probably cause the time-lapse inversion to converge to a local minima. The possible errors in the FWI background are due to propagated errors from the effective source wavelet and antenna location errors. The effect of salt water on the antenna source wavelet was detected from GPR measurements on days when significant σ were measured in the borehole. Effective source wavelet corrections calculated using a deconvolution approach showed that for increased σ in the borehole there is a trend of an increased dispersive attenuation of the source wavelet, which results in a larger center frequency shift towards lower frequencies, and an increased apparent time delay. The effective source wavelet is compensating for all possible borehole filling effects and allows a reliable reconstruction of the permittivity and electrical conductivity from FWI. These borehole filling effects cannot be compensated in ZOP and ray-based imaging. The high-resolution reconstruction of a salt tracer using time-lapse GPR FWI imaging can provide vast and continuous data to constraint hydrological models.

Chapter 6

Conclusions and Outlook

During this thesis, we conducted synthetically and experimentally tracer tests that were monitored by time-lapse crosshole GPR full-waveform inversion, in order to test the ability, to reconstruct the tracer plume in higher resolutions compared to other conventional methods and approaches. I found that the tracer plume was reconstructed successfully from tracers which change either permittivity or electrical conductivity or both.

6.1 Conclusions

First, we generated a realistic gravel aquifer model based on previous hydrological and FWI data in order to produce realistic heterogeneity of tracer transport and changes in dielectric properties. Then, we tested for a starting model to the FWI of time-lapse data. As for the permittivity starting model, the FWI background model was found the best. For the conductivity, the synthetic study showed that the FWI background model is the best whereas the experimental study suggested that a homogenous conductivity is the actually better. We explain this inconsistency because of errors that were added to FWI background results, which are then used as starting models for the time-lapse data. In the experimental FWI, these errors were propagated from errors in the effective source wavelet correction, whereas in the synthetics the source wavelet was known a priori. The FWI conductivity model shows low flexibility to modify erroneous anomalies that are introduced by the starting model. Moreover, time-lapse permittivity changes were more accurate than conductivity changes.

The magnitude changes over a large range introduced by the tracer, in both permittivity and conductivity, were possible to recover. In conductivity the range goes from negative conductivity change to the background (desalinated water) to positive change (saltwater). However, we found that when an electrical conductivity increase introduced by the tracer exceeds a threshold, the attenuation affects some of the signals to be lower than the noise. Thus, some of the modelled traces cannot fit the observed traces, what eventually causes errors in both FWI models. In the practical implementation of the FWI in a case where there is a large conductivity change, I found that for a better FWI convergence it is needed to increase the parameter that controls the conductivity step length (a single-scale increase provided better FWI convergence criteria). For the permittivity changes by a tracer, I tested in the synthetic study only a decreasing permittivity (ethanol) which replaces or mixes with higher water permittivity and the FWI recovery was good. The phase shift from the initial traces modelled through the FWI background to the observed data were not as large to cause a cycle-skipping, thus for expected permittivity changes from a tracer the use of the background FWI model as a starting model is appropriate.

While in the synthetic study the fate of the true plume and the heterogeneity of the dielectric properties were known and used for validation, in the experimental tracer test complementary data are used to check the consistency with the time-lapse FWI results. First, the background FWI models were similar to FWI from previous data of a recent study. To investigate the consistency we used the borehole logging data, the temporal continuity of the plume reconstruction, i.e. between sequential measurements, and the spatial continuity, i.e. between neighboring planes. In addition, analysis on time-lapse ZOP data, which provided a simpler model of difference attenuation 1D depth-profile, observed that the plume is transported at the same depth and time that the FWI imaged. Note however, that no other method can really validate these results, because GPR FWI images are currently the best one can get. Overall, we found consistency in the recovery of transport anomalies which were introduced by the tracer through preferential paths as narrow as 0.2 m. This resolution in tracer recovery was not observed before in other geophysical monitoring techniques. With 29 time-lapse FWI models in 5 planes over a span of 14 days, we could calculate breakthrough curves of the plume, through the size of tomogram cells (0.09 X 0.09 m), which provides high-resolution quantified information of the plume temporal-spatial heterogeneity. The tracer fate we monitored was in agreement with past tracer tests at the same test site.

In the experimental pre-processing step, we calculated the effective source wavelet for each dataset. For a given plane in time-lapse days, the sources were similar but not identical. We suggest it is a result of changes in the saltwater concentration in the antenna borehole and incomplete repeatability in acquisition. In addition, differences in the corrected source wavelet were observed for a given time-lapse dataset when different starting models were used. This shows the uncertainty that exists in estimating of the source wavelet, where the starting model is also a factor that affects it. Overall, the error in the source propagates to an error in the FWI model.

We found a trend of increased saltwater in the borehole with central frequency shift to lower frequencies of the effective source wavelet, an apparent phase delay and a decrease in the effective source wavelet amplitude. This is a dispersive attenuation response, which occurred due to the coupling of the antenna with electrical conductivity contrasts near the antenna. Different from FWI, ray-based approaches assume that wave propagation occurs only over a ray path, whereas in reality this is not the case. Full-waveform modeling includes all the physics occurring in reality. With the FWI where an effective wavelet is used, the wave propagation through the medium is accurately modelled. Since coupling effects close to the source and receiver antennas require a refined grid (Diamanti and Giannopoulos) to include in the modelling and accordingly increased computing power, the effective source wavelet estimation enables a simplified description of the transmitter and receiver antennas in combination with an effective wavelet. In FWI practice, from the deconvolution approach in which the effective source wavelet is corrected, all the effects on the antenna in the borehole are added to the source. Consequently, the FWI run which uses the corrected source wavelet provides a more accurate FWI model. If this would

not be the case, the borehole filling effect would propagate into the FWI results and hence erroneous reconstructions would be present. Therefore, the characteristic of source wavelet correction in GPR FWI workflow shows its advantage over ray-based methods and fast ZOP data analysis, for recovering more accurate models and especially when the borehole water has high salinity, e.g. in saltwater tracer tests.

To summarize, time-lapse GPR FWI has enabled a reliable imaging of a tracer at decimeter scale (0.2 m) which has not observed before from geophysical monitoring. It provides data which can be used for better constraining hydrological properties of interest from hydrological models. For reducing errors in the FWI results and thus in the plume reconstruction, we would like to stress the importance of the acquisition repeatability in producing GPR time-lapse data: in the antenna location, in the GPR system and its preparation for operation, in the FWI input parameters, and put a special importance on the background acquisition and inversion. More experience in time-lapse data acquisition and FWI of newly acquired data will probably improve the technique and will make it more robust.

6.2 Outlook

There are two main points on which further investigations could be based: theoretical algorithm developments and application of the full-waveform inversion.

6.2.1 Theoretical development

Tracers introduce high dielectric contrasts in the aquifer over short distances. In order to recover the conductivity better a 2.5D FWI is beneficial (Mozaffari et al., 2020), as we also showed (Appendix A.7) that 2.5D is better than 2D in approximating the 3D data. Mozaffari et al. (2020) showed in a synthetic study that the average relative error over the model drops in ϵ_r from 2.5% in 2D FWI to 0.18% in 2.5D FWI, and σ drops from 2.8% in 2D to 0.5% in 2.5D. As we showed the importance of reducing the error in the effective source wavelet from 2D data on the recovery of the 2D FWI models, a test for optimizing the source wavelet estimation from 2.5D experimental data is required. Overall, FWI of time-lapse 2.5D data is expected to show another improvement in the imaging recovery of tracer.

6.2.2 Application of the full-waveform inversion

I derived time-lapse differences based on the inversion of individual datasets. Then, the difference in geophysical property can be derived (like in the experimental study), or the tracer concentration from additional petrophysical relation adequate for the tracer. Double-difference inversion (Asnaashari et al., 2015), an inversion of the difference data starting from the recovered baseline model, has shown an improved inversion FWI results for seismic synthetic data. This approach can be applied to time-lapse GPR data. To implement experimental data in double difference FWI, also the source have to be identical as possible. Therefore, the approach can be used only when the boreholes antenna are located at boreholes which are not affected by the tracer saltwater.

6.2.3 Acquisition improving

In this study, for the given aquifer we showed that the GPR data collection is slower than the dynamic process of tracer transport, thus an assumption of quasi-static conditions is viable (Section 4.7.3). In addition, we showed that out-of-plane effects due to the presence of a tracer in 2D FWI are not affecting the data significantly and thus not on the FWI models (Section 4.7.1), and we discussed GPR acquisition regarding antenna spacing to best retrieve the tracer (Section 4.7.2) and implemented it in the experimental tracer test monitoring (Section 5.7.1). More experience is needed regarding the starting model and the acquisition of the data. Since this is the first high resolution GPR FWI of time-lapse data, experience need to be build up to optimize the acquisition setup and also the inversion setup.

Appendix A

Supplements to Chapter 4 ⁴

A.1 Noise in GPR synthetic data

GPR data are contaminated with random instrumental noise that originated from the electronics of the transmitter, receiver and cables (Annan, 2009). In order for events in the data to be detectable, the power at the receiver must be in excess of the noise level at the receiver. At the presence of a salt tracer, the signal power at the receiver will lose energy, and events in the data may be overshadowed by the random noise. Eventually, this will lead to a lower signal-to-noise ratio. This noise could cause errors in FWI in cases when the attenuating effect of the tracer will be in the range of the error level. Other sources of uncertainty in the reconstructed FWI models that originated from the instrument time drift, antennae spatial positioning (Axtell et al., 2016), the effect of the effective source wavelet (Belina et al., 2012) and data processing (Peterson, 2001) are neglected in this study. Nevertheless, in GPR datasets the quality of recorded data and the acquisition setup differ and each of the sources of errors may be the one of the largest impact on the quality of the reconstructed model, in this study we concentrate on the effect of the random instrumental noise.

We added a realistic random instrumental noise level to the synthetic waveforms to evaluate its effect on the inversion performance. We assumed that the random noise level (of the trace before the first rise) is independent of the conductivity of the tracer. This then leads to a different *signal* to noise ratio for different configurations. We obtained these noise levels from real GPR traces that were acquired from the Krauthausen site using the same cross borehole distance (Gueting et al., 2015). Based on this data, we calculated a relative random noise level with:

$$\text{Ambient noise ratio min. [\%]} = \frac{\text{std.}(\text{noise recorded traces})}{\text{max.}|A(\text{recorded traces})|} \cdot 100\%, \quad \text{Eq. (A.1)}$$

where *std. (noise recorded traces)* is the standard deviation of the random noise in recorded traces, which was calculated from amplitudes at the time range before the wave first arrival time, and *max. |A(recorded traces in entire dataset)|* is the maximum absolute amplitude of the recorded traces over the entire dataset.

From Equation A.1, the minimal random noise ratio is 0.062%. For short distances (4.95 m, parallel ray path) the signal dominates over the noise (Figure A.1a,c), with typical noise level ~ 0.2%. For a typical wide-angle long-distance ray path trace (8.4 m, 54°) the noise has a larger footprint in the recorded trace (Figure A.1e,g) with noise level ~ 3%.

⁴ Adapted from Haruzi, P., Schmäck, J., Zhou, Z., van der Kruk, J., Vereecken, H., Vanderborght, J., & Klotzsche, A. (2022). Detection of tracer plumes using full-waveform inversion of time-lapse ground penetrating radar data: a numerical study in a high-resolution aquifer model. *Water Resources Research*, e2021WR030110.

Then, we generated the absolute random noise as Gaussian random error $G(0, std.^2_{noise\ in\ synthetics})$ with a standard deviation based on the *Ambient noise ratio min*.

$$std.\ noise\ in\ synthetic\ traces = \frac{max.\ |A(noise\ free\ simulated\ traces)| \cdot Ambient\ noise\ ratio\ min}{100\%} \quad \text{Eq. (A.2)}$$

where $max.\ |A(noise\ free\ simulated\ traces)|$ is the maximum absolute amplitude of the simulated traces over the entire dataset before adding noise. Finally, we added the same absolute random noise to the synthetic simulated waveforms of the background, salt and ethanol tracer cases:

$$data(noisy\ added\ simulated\ traces) = data(noise\ free\ simulated\ traces) + G(0, std.^2_{noise\ in\ synthetics}) \quad \text{Eq. (A.3)}$$

The noise-added traces (in blue) eventually show a similar random noise level to the real traces for short and long ray paths (see Figure A.1).

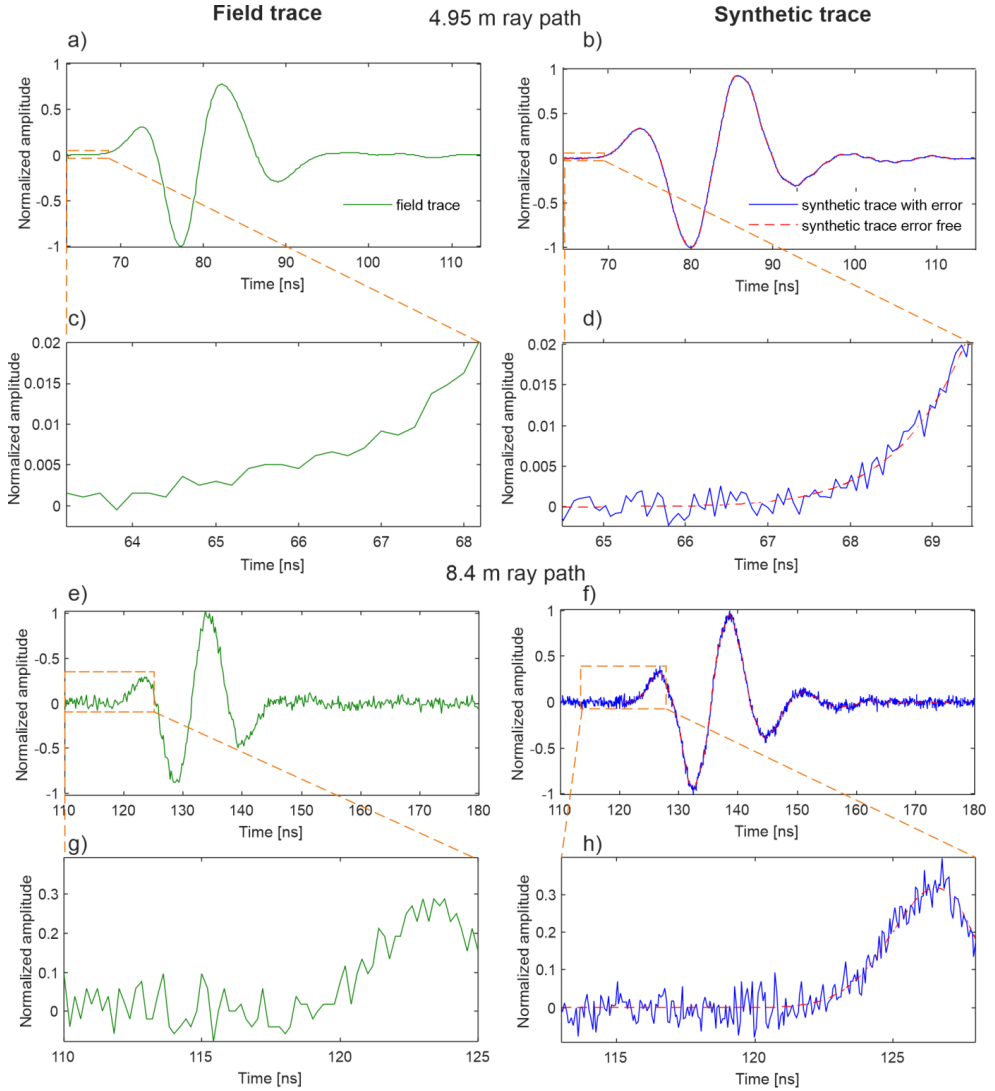


Figure A.1: Realistic noise added to synthetic waveforms based on random instrumental noise from experimental data. Examples for two different waveforms: a-d) the shortest ray path of 4.95 m and e-h) 54° wide-angle ray path of 8.4 m. Panels c, d, g, h zoom in to view the noise. Scale is a normalized amplitude to the maximal absolute amplitude of the same trace. Sampling rate of the experimental GPR data is 0.2 ns, whereas the sampling rate of the synthetic data is 0.063 ns.

A.2 Observed data and FWI data fit

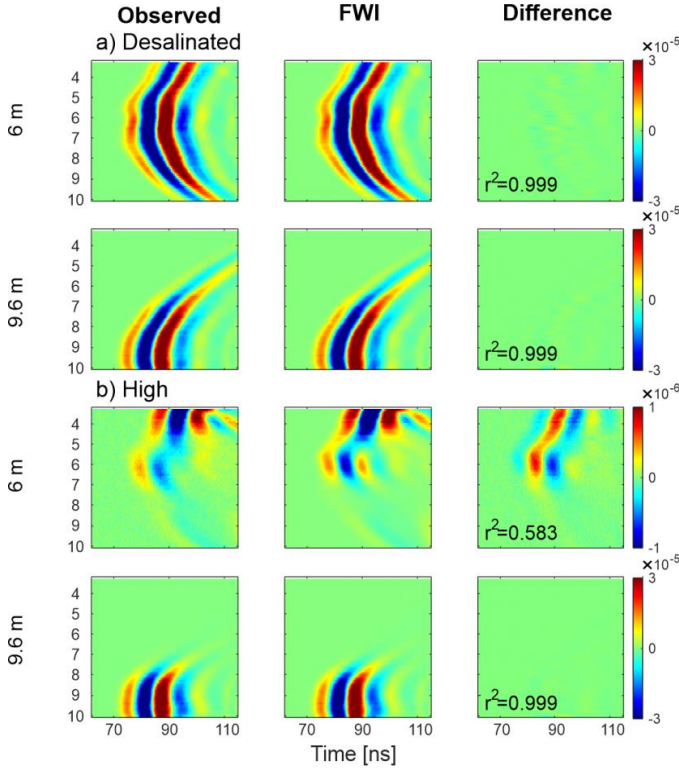


Figure A.2: Observed (real data noise-added), FWI inverted and the difference between inverted and observed data for transmitters at the depth of major tracer intrusion (6 m) and at depth where no intrusion occurs (9.6 m). This figure is complementary to Figure 4.9 in the paper. Data is presented for the (a) Desalinated salinity (tracer case in Figure 4.6 (a)) and (b) High salinity (tracer case in Figure 4.6 (e)) tracer cases. Note that for the High salinity for the transmitter at 6 m depth panel where the signal is weaker because the wave travels through the increased σ of the tracer, the color scale is 30 times smaller. R^2 quantifies the correlation between FWI inverted and the observed data. The standard deviation of the Gaussian ambient noise was $4.6 \cdot 10^{-8}$ in all cases.

A.3 Fit of FWI traces at the presence of salt tracer

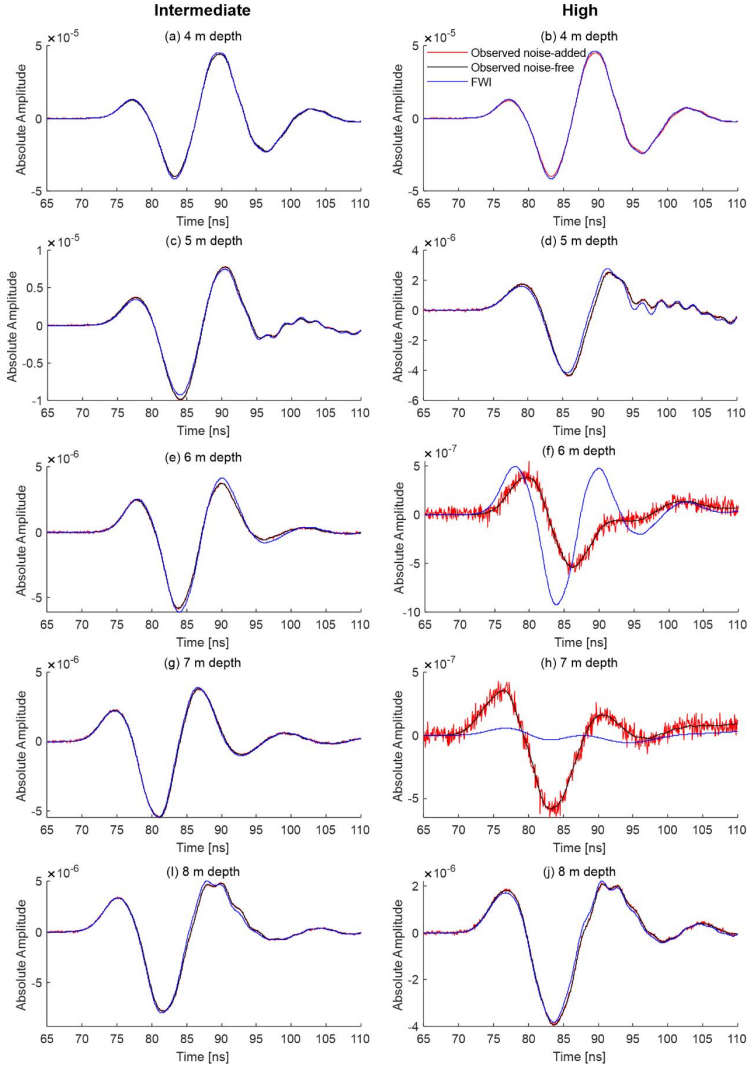


Figure A.3: Fit of FWI traces. Traces of Intermediate (left) and High salinity cases (right) for ray paths travelling parallel to surface at depths, where the plume intrudes in the crosshole plane. Note for the different amplitude scales in the plots.

A.4 Noise level in comparison to the traces amplitude

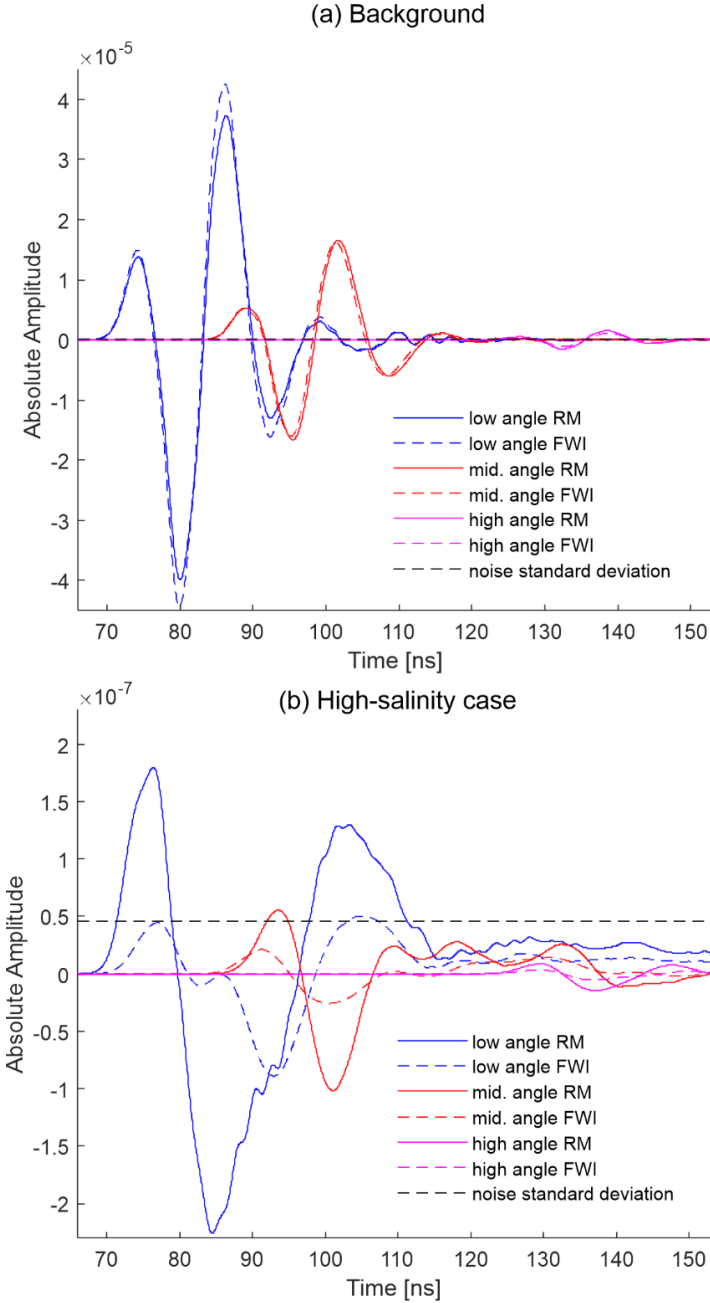


Figure A.4: Noise level in comparison to the traces amplitude. (a) Background and (b) High salinity case real data and FWI for low, middle, and high angle traces (0° , 32° and 54°). Note the higher amplitude scale in the background than in High salinity case.

A.5 Observed and modelled FWI traces for background and ethanol scenario

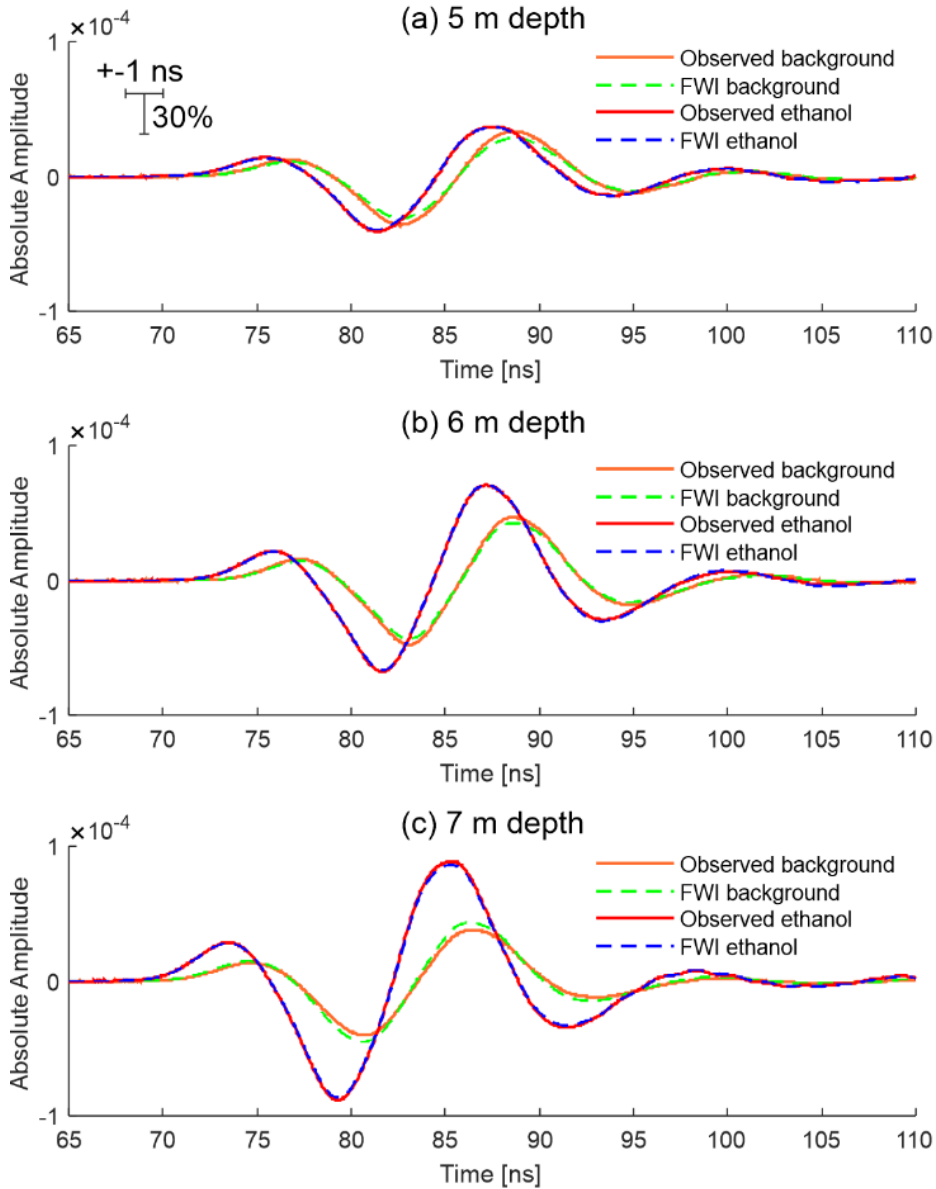


Figure A.5: Observed and modelled FWI traces for background and ethanol scenario for day 15 after infiltration (using starting model from day 13) models at the main intrusion (a) 5 m, (b) 6 m and (c) 7 m.

A.6 Description of the movie - comparison of tracer recovery from salt and ethanol tracers

The movie shows *normalized* tracer distribution evolution of the first 49 days of the concentration from the true transport model (top left), salt tracer conductivity from FWI σ model (top right), ethanol volumetric concentration from FWI ϵ model (bottom left), and ethanol volumetric concentration from FWI σ model (bottom right). Because the conductivity/concentration of both salt tracer conductivity and ethanol are derived from the same concentration field from the transport model, the tracer distributions can be compared by normalization. For each of the four subplots (of different derived-tracer parameters), each spatio-temporal (i.e. in each day) field in the 2D crosshole plane was normalized by dividing the *true* maximal conductivity/concentration over all the spatio-temporal field volume domain (i.e. all days in the 3D domain). Thus, the colors range in each of the subplot is [0,1].

A.7 Out of plane effects - 3D versus 2D GPR data

For the modeling of out-of-plane effects, we considered the subsurface model of Day 8 after the salt tracer injection to investigate the effect of the plume heterogeneity on the data (Figure A.6a,b). This day was chosen, because the mass of the tracer in the crosshole plane location is lower (tracer mass in an increased trend) than in locations closer to the center of the plume. Thereby, in investigating the out-of-plane effects, we considered significant σ heterogeneity (and especially from outside the crosshole plane) and only minor ϵ_r aquifer heterogeneity. An investigation of significant heterogeneity in ϵ_r was discussed by Mozaffari et al. (2020).

For the 3D forward modeling, we employed the 3D FDTD solver gprMax (Warren et al., 2016) with the model dimensions 10.44 x 8.1 x 5.49 m and a cell size of 0.09 m. We truncated the computational domain with 30 cells of perfectly matched layer (PML) at each boundary (Berenger, 1994, Giannopoulos, 2011). Because of the large computational time of the 3D forward simulation, the model cell length is 3 times longer than the one used in the forward runs in the 2D FWI (0.03 m). For the 2D model, the 3D model was sliced at the crosshole location (Figure A.6a, right) with the model dimensions 10.44 x 8.1 x 0.09 m. In addition, the 2D was extended to 3D model (“2.5D”), by extending the 2D model in the perpendicular direction to the plane, to the same model dimensions as the 3D model. For 3D, 2.5D and 2D forward model simulations, we used two transmitters, at a location where the tracer is present at 7 m and is not present at 5.85 m depth, with 31 receivers. We used the same source wavelet described in section 4.1.

The computational time for a simulation of a heterogeneous model (which uses multiple discrete materials) in gprMax is influenced mainly by reading in the properties of the multiple cells and building the model (Warren et al., 2016). The 3D simulation was composed of 102480 different materials and the model building lasted 1:03 hours, while the forward run for each transmitter lasted only 15 seconds.

The 2.5D was composed of 1680 materials, with model building lasting 24 seconds, while the forward run for each transmitter lasted 8 seconds. The 2D was composed of 1680 materials, with model building lasting 3 seconds, while the forward run for each transmitter lasted only 0.5 seconds. The simulations ran on a computer with 16 GB installed RAM. Although the larger cell size, the numerical dispersion is low, as the dominant wavelength is still more than 10 times larger than the cell size.

To evaluate the effect on the 2D FWI similar to experimental data applications, we transformed the 3D GPR data using the standard 3D to 2D conversion with the Bleistein approach (e.g., Klotzsche et al, 2019) and estimated “semi 2D” data, which would be used for the 2D GPR FWI. By comparing the 3D, 2.5D, “semi 2D” and 2D GPR data (Figure 4.S6b,c), generally a similar trend along the receiver depths can be observed. A decrease of amplitudes for both transmitters are observed at 7-8.2 m depths due to the presence of the tracer. The amplitudes at 5.85 m are about 10 times higher than in 7 m, where the salt tracer is present.

The arrival times of the 3D and 2.5D data are about 2 ns earlier than the semi 2D and 2D data (estimated at the first maxima). This difference can be explained by the differences in the line source for 2D and a point source for 3D and corresponding 2D and 3D wave propagation (Mozaffari et al., 2020). Therefore, we only compare the 3D and 2.5D data to each other, and the semi-2D and the 2D data, whether out-of-plane reflections can be identified in the 3D and semi-2D data. To investigate these results in more detail, we investigated individual traces for the transmitter at 5.85 m depth with no σ complexity (not shown). Both 3D and 2.5D, and semi 2D and 2D fit each other for the phase with little difference in amplitude, as expected from an environment with small changes in ϵ_r and in σ (Mozaffari et al., 2020). The traces from three individual traces from the transmitter at 7 m depth are shown in Figure A.6d. The comparison of 3D to 2.5D, and of semi 2D and 2D data show for receivers at 5.5 a similar shape, and only small differences in the amplitude can be observed. For the 6.58 m and mainly for 7.66 m receivers larger differences can be observed. We interpret these differences as *minor* out of plane reflections, probably due to the relatively moderate localized heterogeneities that are present out of plane compared to the whole Fresnel volume through which the waves are traveling through.

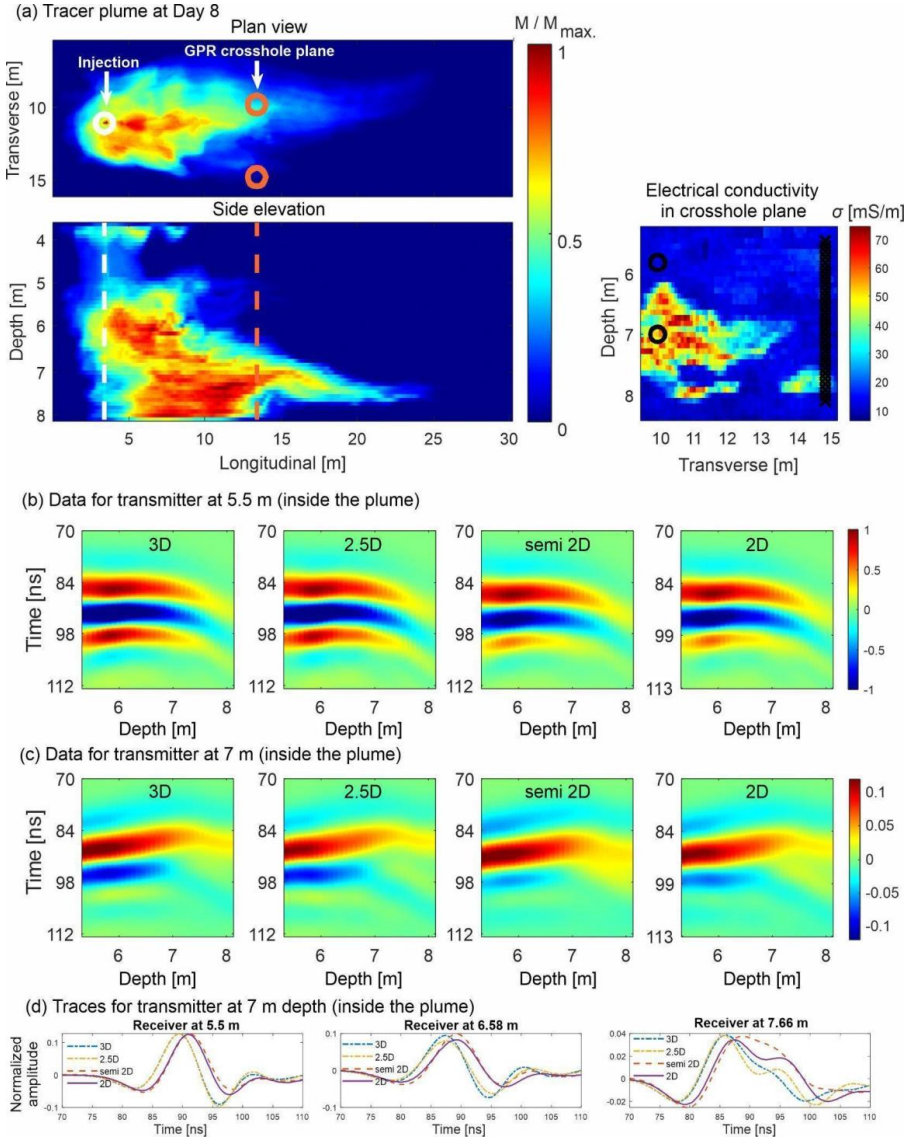


Figure A.6: Investigation of the tracer's out of plane on the GPR data. a) At Day 8: plan and side elevation views of the plume (left), and the bulk electrical conductivity in the crosshole plane (right). Black circles and crosses refer to two transmitter and 31 receiver locations, respectively. b) GPR data for transmitter at 5.85 m which is outside the plume, using 3D, 2.5D and 2D simulations, and semi 2D. c) Same as (b) for the transmitter at 7 m which is inside the plume. Note that the amplitudes for c) are lower than in b), because of the higher σ in c). d) Individual traces from the transmitter inside the plume using 3D, 2.5D and 2D simulations, and semi 2D. For (b)-(d), the amplitudes of the data for each 3D, 2.5D, 2D and semi 2D datasets are normalized to the maximum amplitude of each dataset.

Appendix B

B 3D aquifer characterization of the Hermalle-sous-Argenteau test site using crosshole GPR amplitude analysis and full-waveform inversion⁵

To improve the understanding of flow and transport processes in the critical zone, high resolution and accurate estimation of the small-scale heterogeneity is essential. Preferential flow paths related to high porosity layers and clay lenses in gravel aquifers greatly affect flow and transport processes in the subsurface, and their high-electrical contrast to their surrounding matrix and limited extent can act as low-velocity electromagnetic waveguides. In the last decade, time-domain full-waveform inversion (FWI) of crosshole ground penetrating radar (GPR) data has shown to provide 2D decimeter-scale resolution images of relative permittivity and electrical conductivity of the subsurface, which can be related to porosity and soil texture. Most studies using crosshole GPR FWI resolved high porosity zones that were identified by an amplitude analysis approach. But clay lenses or zones with higher electrical conductivity that act as low-velocity waveguides are hard to distinguish in the measured data and amplitude analysis because of the absence of characteristic wave-propagation features. We investigate a set of nine crosshole GPR datasets from a test site in Hermalle-sous-Argenteau near the Meuse River in Belgium to characterize the aquifer within a decimeter-scale resolution and to improve the understanding of a previously performed heat tracer experiment. Thereby, we extend the amplitude analysis to identify two different types of low-velocity waveguides either caused by an increased porosity or a higher electrical conductivity (and higher porosity). Combining the GPR amplitude analysis for low-velocity waveguide zones with the standard FWI results provided information on waveguide zones which modified the starting models and further improved the FWI results. Moreover, an updated effective source wavelet is estimated based on the updated permittivity starting models. In comparison with the traditional FWI results, the updated FWI results present smaller gradient of the medium properties and smaller root-mean-squared error values in the final inversion results. The nine crosshole sections are used to generate a 3D image of the aquifer and allowed a detailed analysis of the porosity distribution along the different sections. Consistent structures of the permittivity and electrical conductivity show the robustness of the updated FWI results. The aquifer structures obtained by the FWI results agree with those results of the heat tracer experiment.

⁵ Adapted from Zhou, Z., Klotzsche, A., Hermans, T., Nguyen, F., Schmäck, J., Haruzi, P., Vereecken, H., and van der Kruk, J. (2020). 3D aquifer characterization of the Hermalle-sous-Argenteau test site using crosshole GPR amplitude analysis and full-waveform inversion. *Geophysics*, 85(6), H133-H148.

B.1 Introduction

Detailed characterization of the critical zone and aquifers is important to understand the influence of small-scale heterogeneities on the prediction of flow and (reactive/solute) transport processes. Traditional methods to obtain aquifer characteristics either have small spatial sampling with a poor lateral resolution (e.g., coring), or they capture an average response over a large volume (e.g., pumping test, remote sensing methods) which typically treats the volume as homogeneous, and lacks detailed characterization at smaller scale. In the last decades, crosshole geophysical methods, such as seismics (e.g., Doetsch et al., 2010), electrical resistivity tomography (ERT; e.g., Coscia et al., 2012) and ground penetrating radar (GPR; e.g., Klotzsche et al., 2018) have been increasingly used to provide detailed models of the near surface and the critical zone (overview provided by Binley et al., 2015). Compared to other imaging methods, GPR provides the highest possible resolution due to the usage of high frequencies. GPR is sensitive to electromagnetic wave velocity and attenuation of the subsurface, which can be used to estimate relative permittivity ϵ_r and electrical conductivity σ , respectively. Due to the large difference between the relative dielectric permittivity of air $\epsilon_r = 1$ and water $\epsilon_r = 80$, relative permittivity can directly be linked to porosity and soil water content of the subsurface using appropriate petrophysical models (Steelman and Endres, 2011) or empirical relationships (e.g., Topp et al., 1980) and is therefore effective to characterize aquifers.

Crosshole applications of GPR are well suited to characterize the shallow subsurface and monitor aquifers (e.g., Paz et al., 2017). Because of the known distance between the antennae, a good subsurface illumination with dense ray-coverage and relatively small acquisition errors, they are well suited for inversion schemes (e.g., Axtell et al., 2016; Klotzsche et al., 2019b). To investigate flow and transport processes, time-lapse GPR measurements with a high spatial and temporal resolution can be linked to soil hydrological parameters such as hydraulic conductivity. For example, the zero-offset profiling (ZOP) approach for GPR, which is a quick and simple survey method by simultaneously moving the transmitter and receiver antennae, can detect velocity anomalies and attenuation zones (e.g., Gilson et al., 1996; Binley et al., 2001). A more advanced measurement technique is the collection of multi-offset-gathers (MOG), in which the transmitter is fixed at a certain location in one borehole and the receiver antenna is continuously lowered with a constant offset in a second borehole. By repeating this measurement at a variety of different transmitter positions and by interchanging the transmitter and receiver borehole, a dense ray-coverage between the two boreholes can be obtained (Klotzsche et al., 2018). Traditional tomography inversion methods for crosshole GPR data are based on geometrical ray theory (e.g., Irving et al., 2007; Dafflon et al., 2011, 2012). The ray-based inversion methods only exploit the first-arrival times and the first-cycle amplitudes of the measured GPR data, and, damping and smoothing constraints are necessary to stabilize the inversion (e.g., Holliger et al., 2001; Maurer & Musil, 2004). The main drawback of these methods is that features smaller than the dominant wavelength cannot be resolved (resolution scales approximately with the diameter of the first Fresnel

zone). Other aspects such as recording geometry and positioning errors can have significant effects on the resolution of the ray-based result (e.g., Oberröhrmann et al., 2013; Axtell et al., 2016). Furthermore, ray-based approaches only consider data until a certain angle to avoid an increasing apparent-velocity for increasing ray path angles (Peterson, 2001), therefore only a limited angular coverage of the target is available.

In comparison to the ray-based approaches, full-waveform inversion (FWI) can significantly improve the resolution to the sub-wavelength scale by using the entire waveform information in the inversion process including secondary events of the data. FWI approaches were first developed and applied in the seismic community (e.g., Tarantola, 1984, 2005; Shin & Cha, 2008; Virieux & Operto, 2009). In the last decade the first adaptations for GPR data were developed (e.g., Kuroda et al., 2007; Ernst et al., 2007a). The time domain approach of Ernst et al. (2007a; b) was further developed by Meles et al. (2010) and has been applied with slight modifications to more than 30 different datasets to characterize aquifers within decimeter-scale resolution. Klotzsche et al. (2019b) provides an overview about the developments, applications, and corresponding challenges. All these applications show a great potential of the GPR FWI to characterize aquifers with higher resolution than ray-based approaches and to obtain decimeter-scale high resolution images of permittivity and electrical conductivity at the same time. The GPR FWI permittivity image can be converted to porosity using petrophysical models such as the CRIM model (Birchak et al., 1974). To validate the FWI results, the tomograms can be compared to available ground truth data, logging data, or to co-located cone penetration tests (e.g., Gueting et al., 2015; Keskinen et al., 2017). The insights into aquifers that are gained using the FWI results helped to enhance and improve the understanding of hydrological relevant processes such as porosity changes in an aquifer that could be correlated to preferential flow paths (Klotzsche et al., 2013).

One important criterion to successfully perform the FWI is to estimate starting models that yield synthetic data within half of a wavelength of the measured data in the entire inversion domain to avoid cycle-skipping (Virieux and Operto, 2009; Meles et al., 2012; Lopez-Alvis et al., 2019). Normally, ray-based inversion results fulfill this criterion for the starting models, but in the presence of high contrast layers (e.g., water table) adaptations are necessary (e.g., Klotzsche et al., 2012). To improve the starting model definition, especially for the permittivity, and thereby to avoid cycle-skipping, Klotzsche et al. (2014) introduce an amplitude analysis approach that identifies and maps the boundaries of sub-wavelength high contrast zones that show a lower velocity than the surrounding medium in the measured data. Such thin layers act as low-velocity waveguides for the GPR data causing characteristic wave propagation behavior like late arrival high amplitude events and are caused by an increase in permittivity/porosity in the saturated zone. This approach has not been used to identify clay lenses or zones with higher permittivity and higher electrical conductivity in experimental data so far.

To improve the characterization of hydrogeological parameters (e.g., hydraulic conductivity or dispersivity), time-lapse tracer experiments can be applied (e.g., Linde et al., 2006; Saar, 2011; Hermans

et al., 2015a). Commonly applied tracers are salt or heat tracers, which can be monitored with ERT (e.g., LaBrecque et al., 1996b; Hermans et al., 2012b) or GPR traveltime data (Kowalsky et al., 2004). Müller et al. (2010) apply a negative and positive salt tracer at the Krauthausen test site and monitored the time-lapse changes with crosshole ERT to characterize flow and transport processes. They observed a plume splitting that could not be explained with standard inversion methods. Gueting et al. (2017) use GPR FWI results to generate a facies model of the Krauthausen site, which was able to explain the plume splitting in the salt tracer test. This application showed the potential of the GPR FWI to obtain high resolution images of aquifers that can help to explain behaviors of tracers in aquifers. Hermans et al. (2015a) investigate the ability of crosshole ERT to monitor a heat tracing experiment in a complex heterogeneous alluvial aquifer at the Hermalle-sous-Argenteau test site near Liege (Belgium) and observe the splitting of the heat plume between the injection well and the monitoring plane. Direct measurements using piezometers (Wildemeersch et al., 2014) confirmed the ERT results and showed the ability of crosshole ERT to qualitatively monitor temperature variations in the aquifer.

In this study, we apply the crosshole GPR FWI to characterize the aquifer at the Hermalle-sous-Argenteau site with decimeter-scale resolution to identify the structures that cause the heat plume transport behavior. We investigate three important new aspects for this site and the GPR FWI performance. Firstly, we want to demonstrate the potential of the FWI to resolve small-scale structures and relate them to previously detected plume transport. Secondly, we extend the amplitude analysis to identify high porosity and high electrical conductivity zones, which we then include in the FWI processing. Thirdly, we investigate how reliable FWI results between boreholes with a small offset are and how such results can be improved.

B.2 Field site and GPR measurement setup

The study site is located on the alluvial plain of the Meuse River at Hermalle-sous-Argenteau near the city of Liege, Belgium (Figure B.1a). In the saturated zone, between 3.0 m and 10.0 m depth, the aquifer is composed of gravel and pebbles in a sandy matrix (Hermans et al., 2015a; Lesparre et al., 2019). This layer can be divided in two main units: the upper aquifer from 3.0 m to 6.0 m depth, consisting of sandy gravels and the lower aquifer between 6.0 m and 10.0 m depth, which is characterized by coarser and cleaner gravels. The water table lies at approximately 3.2 m depth. Below 10.0 m depth, the aquitard consists of folded shales and sandstones. According to Hermans et al. (2015a), we can expect an electrical conductivity change of 5 mS/m to 10 mS/m between boreholes Pz13 and Pz17 (see Figure B.1c). The heated water experiment of Hermans et al. (2015a), hot water was injected from Pz09 (red triangle in Figure B.1b). The ERT results revealed the ability of the time-lapse ERT to monitor the variations of temperature in the aquifer as shown exemplary for an ERT plane after 30 hours of injection in Figure B.1d, where the temperature variations clearly display two anomalies as a result of a heterogeneous flow field (Klepikova et al., 2016; Hoffmann et al., 2019).

Crosshole GPR measurements were performed at nine cross-sections at the same investigation area as the ERT monitoring (different color lines in Figure B.1b) using 200 MHz PulseEKKO borehole antennae (Sensors & Software Inc.) in September 2018. A semi-reciprocal MOG acquisition setup was used with transmitter and receiver spacings of 0.2 m and 0.1 m, respectively, as proposed by Klotzsche et al. (2010, 2019b). We chose as 0.0 m depth the casing of borehole Pz09 similar to Hermans et al. (2015a). To avoid critical angle reflections and refractions of the GPR waves from the interface between the saturated domain and the groundwater table, the first antenna position was located at least 0.4 m deeper than the water table (Klotzsche et al., 2019a). Up to 60 transmitters and 120 receivers positions were used for each plane (see Table B.1 for detailed information). Note that the plane between the boreholes Pz10-Pz17 was measured two months later than the others. One critical step in the FWI data pre-processing is the estimation of an accurate time zero of the signal (see Klotzsche et al., 2019b for more details). To reduce travel time errors, time-zero was determined using a cross-correlation between MOG and zero-offset (ZOP) data as proposed by Oberröhrmann et al. (2013). Firstly, wide-angle reflection and refraction (WARR) measurements in air before and after the multiple-offset (MOG) measurements are acquired. Secondly, a ZOP measurement is performed before the last WARR measurement (used for correcting the ZOP data); the individual time shifts of each MOG are obtained by cross correlating the ZOP traces with the corresponding horizontally travelled rays within the MOGs traces. To reduce borehole geometry errors in the measurements, borehole dip and azimuth deviation data were collected using a magnetic inclinometer tool (QL40-DEV from Mount Sopris Instrument Co.).

Table B.1: A comparison of FWI results between the traditional FWI and the updated FWI. Percentages in parentheses indicate the ratio of the updated FWI final RMS to the traditional FWI RMS

Different boreholes	Pz10-Pz13	Pz11-Pz15	Pz12-Pz17	Pz15-Pz19	Pz09-Pz11	Pz10-Pz14	Pz12-Pz13	Pz10-Pz17	Pz12-Pz16
	Traditional FWI								
Iterations	26	30	24	30	27	27	30	30	30
Mean abs. Gradient (ϵ_r) (10^5)	2.08	0.88	1.52	1.77	0.94	0.90	0.72	1.82	0.54
Mean abs. Gradient (σ) (10^{-4})	1.58	1.21	2.38	1.95	1.55	2.02	0.99	2.12	1.38
R for observed and modeled data	0.9652	0.9618	0.9774	0.9478	0.9761	0.9669	0.9702	0.9726	0.9677
RMS (10^{-6})	1.11	1.06	1.23	1.47	0.91	1.02	0.90	1.45	1.17

	Updated FWI									
Iterations	29	26	30	27	30	30	29	30	28	
Mean abs. Gradient (ε_r) (10^5)	0.28	0.31	0.55	0.66	0.87	1.08	1.21	0.59	0.52	
Mean abs. Gradient (σ) (10^{-4})	0.88	1.15	1.46	1.22	0.96	1.45	1.87	0.80	1.25	
R for observed and modeled data	0.9768	0.9660	0.9798	0.9593	0.9763	0.9743	0.9749	0.9729	0.9695	
RMS (10^{-6})	0.90 (81.1%)	0.99 (93.4%)	1.16 (94.3%)	1.28 (87.1%)	0.91 (100%)	0.89 (87.3%)	1.39 (95.9%)	0.86 (95.6%)	1.13 (96.6%)	

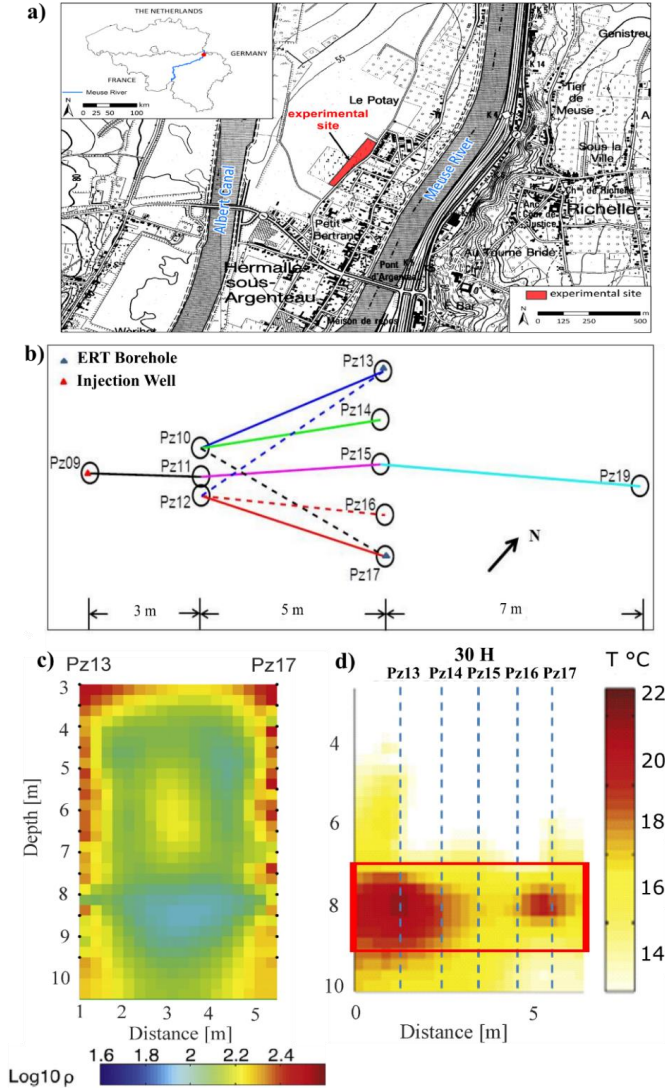


Figure B.1: a) The site of Hermalle-sous-Argenteau is located at the northern part of the Meuse River in Belgium (modified from Hermans et al., 2015a). The red area indicates the experimental site. b) Schematic setup of the Hermalle-sous-Argenteau test site in Belgium indicating the boreholes used for the crosshole GPR measurements with Pz-numbers. The colored lines indicate the nine GPR cross-sections (modified from Klepikova et al., 2016). c) Background inverted ERT section showing the resistivity values between the boreholes Pz13-Pz17 (indicated by blue triangles in Figure B.1b). d) ERT-estimated temperature between Pz13-Pz17 30 hours following hot water injection from Pz09 (modified from Hermans et al., 2015a). The location of the heat plume intrusion is indicated with a red rectangle.

B.3 GPR amplitude analysis results

B.3.1 Amplitude analysis approach

Guided electromagnetic waves can be formed in the near surface when a low-velocity layer with a thickness smaller than the electromagnetic wavelength is embedded between higher velocity layers (van der Kruk et al., 2009). Such small-scale high contrast layers can often be linked to high porosity layers because they have a lower velocity (high permittivity) than the surrounding medium. Such so-called waveguides cause most of the energy of the emitted wave to be trapped within the low-velocity layer if the propagating wave angle at the interface is larger than or close to the Snell critical angle. Klotzsche et al. (2014) observe that when a transmitter in a crosshole setup is located within such a waveguide zone, multiple internal reflections interfere constructively, causing late arrival high amplitudes in the observed GPR data. Furthermore, for transmitter positions outside the waveguide zone, a clear diminished amplitude gap could be observed close to the boundary of the waveguide zone. Using these characteristic wave-propagation features, they proposed an amplitude analysis approach that can detect low-velocity waveguides from the measured data. This amplitude analysis approach detects local maxima and minima positions within the trace energy (squared amplitude of the trace) spectra of each transmitter to first detect and second map low-velocity waveguides, respectively. In the first step, clear maxima positions (at least one order of magnitude higher) in the trace energy spectra are picked to identify a low-velocity waveguide. Secondly, in the trace energy spectra for transmitter which do not show maxima, local minima positions close to the previously found maxima position are estimated. Finally, the estimated maxima and minima picks are plotted against receiver depth to indicate the dimensions of the waveguide zone. Note that the maxima positions can only be observed if the electrical conductivity of the high contrast layers is not too large, which is the case for example for thin higher porosity layers. Until now this approach was only applied to experimental data to detect small-scale high contrast zones related to higher porosity layers. To distinguish between waveguides caused by porosity and clay content changes, the image plots of measured GPR data should be carefully analyzed for elongated wave trains and amplitude gaps in the data. If only amplitude gaps and significant minima positions are present in the GPR data, this could be an indicator for a low-velocity waveguide caused by an increase of electrical conductivity caused e.g., by a higher amount of clay. To sum up, we propose to distinguish in the first step on visual inspection of the data between two types of waveguides that could be identified with the amplitude analysis approach:

- Waveguide type I (WGT I): High permittivity and low/intermediate electrical conductivity that could be related to high porosity zones. Elongated wave trains and zones with diminished amplitudes can be found in the GPR data.
- Waveguide type II (WGT II): High permittivity and high electrical conductivity that could be related to layers with high clay content. No elongated wave trains can be detected due to higher attenuation

of the electromagnetic wave in the waveguide zone, but zones with diminished amplitudes are present.

By combining the amplitude analysis with FWI results and independently measured logging data, the origin of such zones could be validated.

B.3.2 Detailed analysis for crosshole plane Pz10-Pz13

We applied the amplitude analysis to the measured GPR data from the Hermalle-sous-Argenteau site. We will explain the associated steps and the results in detail for the plane Pz10-Pz13 and we will summarize the finding for all planes. Plane Pz10-Pz13 was considered as a representative example because both waveguide types can be identified in this dataset with a sound explanation. In the first step, we analyze the measured data for the characteristic wave propagation features that could indicate waveguide zones (Figure B.2). For transmitter locations at 8.09 m and 9.09 m in borehole Pz10 (Tx nr. 23 and 28), and, at 7.73 m and 9.13 m in borehole Pz13 (Tx nr. 20 and 27) between 7.7 m and 9.2 m depth in both boreholes very clear elongated wave trains can be observed (red circles). Therefore, we see indicators for at least two low-velocity waveguides with a higher permittivity and lower electrical conductivity (WGT I). Interestingly around the two elongated wave train features, zones with diminished amplitudes can be observed probably related to the other waveguides (see green circles with numbers in Figure B.2e - 2h). Transmitter locations around 6.5 m depths (Tx nr. 15 in Pz10; Tx nr. 14 in Pz13) in both boreholes show no significant features in the data. Some minor diminished amplitude changes could be sensed at 4.0 m, 6.0 m, and 7.0 m depth for transmitter at 6.5 m in Pz13 (blue and light blue circles Figure B.2d). For the transmitter positions at 3.9 m depth (Tx Pz13=1) in borehole Pz13 a zone at around 4.0 m can be observed, which shows diminished amplitudes in contrast to the surrounding. Such features with no clear elongated wave trains close by could be an indicator for a low-velocity waveguide with a higher permittivity and a higher electrical conductivity (WGT II).

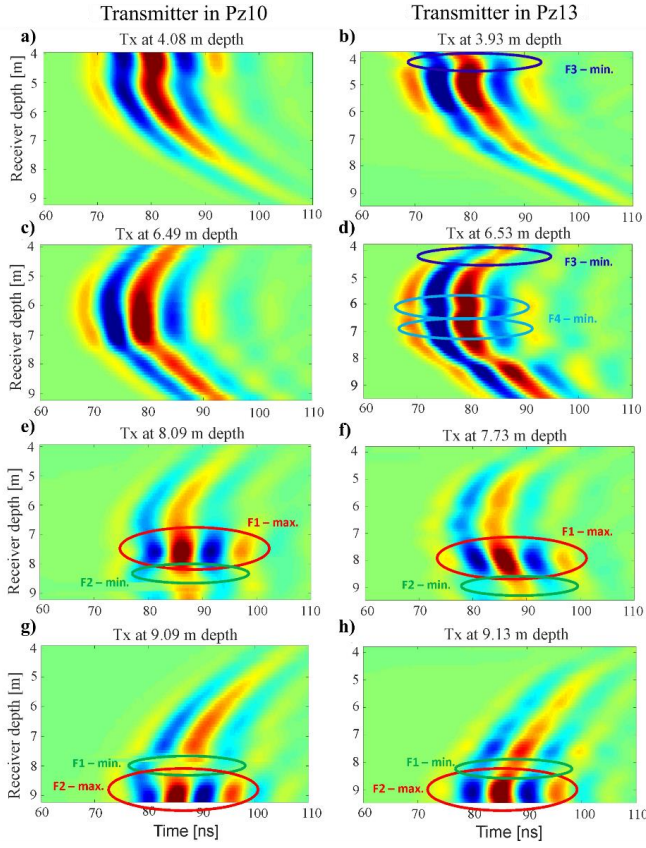


Figure B. 2: Image plots of the measured data of the cross section Pz10-Pz13 for different transmitter (Tx) locations in both boreholes. Different waveguide features are indicated with F1-F4, while WGT I features are marked with red and green circles and WGT II features with blue and light blue circles. Amplitudes of each image plot are normalized to the maximum value of the amplitudes for the cross section and range from -7×10^{-1} to 7×10^{-1} .

In the second step, we calculate the energy spectra for each transmitter gather and plot them against receiver depth. First, spectra that show clear maxima beyond a certain threshold (1.1×10^{-7} for transmitter in Pz10 and 1.5×10^{-7} for transmitter in Pz13) are identified for both boreholes (Figure B.3a and 3b). We used the logarithmic scale along the energy direction to better show the energy changes. The peak of the maximum is picked (red crosses) for each transmitter position that is used to identify a low-velocity waveguide. For the borehole pairs Pz10 and Pz13 two waveguide zones of the WGT I can be identified. Second, all remaining spectra are plotted (Figure B.3c and 3d) and distinct local minimum are picked with green crosses around the previously found maxima positions. Note that in the plots that shows the maxima in the spectra also the minima of the other features can be observed (not shown). Next to the two defined waveguide structures below 7.5 m depth, a very clear zone with minima (blue crosses in

Figure B.3d) can be observed at around 4.0 m depth for the transmitter in Pz13. Since no elongated wave trains (Figure B.2b) and no maxima at this location can be observed, these minima could be an indicator for a zone with a higher permittivity and conductivity of a WGT II. Between 6.0 m and 7.0 m depth in Pz13 two zones with minor minima positions can be identified. These minima structures are only observed in one borehole, which indicates that the detected structures are not continues between the boreholes as demonstrated by Klotzsche et al. (2014). The obtained positions of maxima and minima are plotted against receiver depth to estimate the dimension of the different waveguide zones (Figure B.3e and 3f). Note that only the boundaries of the waveguides close to the borehole can be obtained.

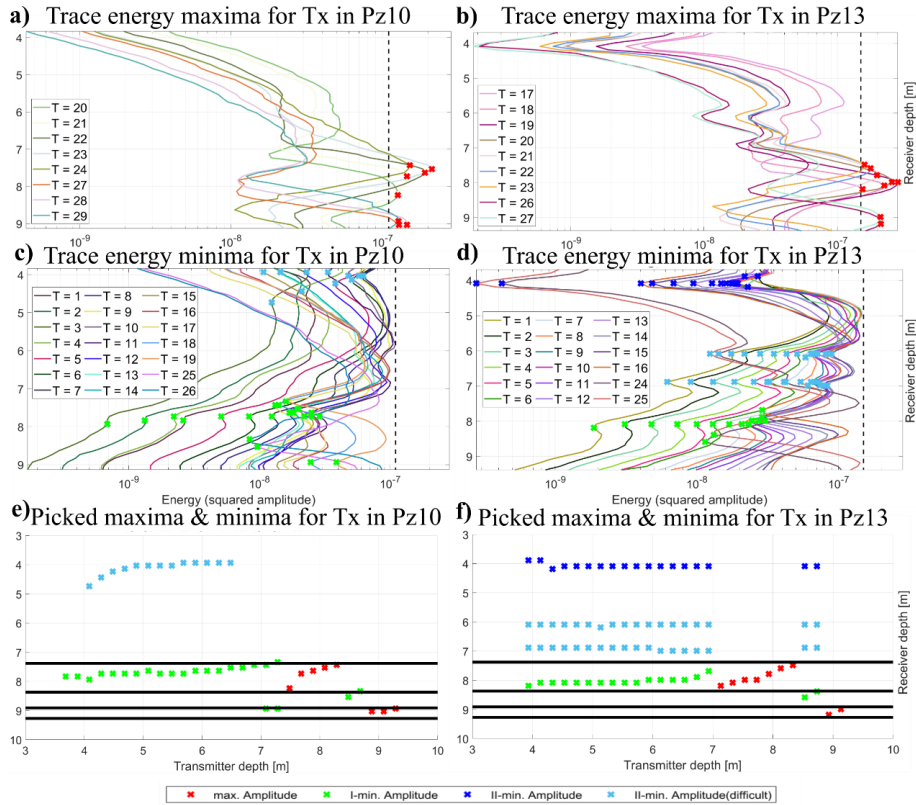


Figure B.3: Trace energy profiles of the measured data of Pz10 and Pz13 that show clear a) - b) maxima and c) - d) minima. Each transmitter has a certain color affiliation in a) - d) and the vertical dashed lines represent the selected energy thresholds. Picked positions of the trace energy spectra for the Tx data in e) Pz10 and f) Pz13. The red and green crosses indicate the position of the maxima and local minima of the energy caused by waveguides WGT I. The blue (and light blue) crosses represent the local minima energy locations caused by possible WGT II. The black solid lines indicate the boundaries of waveguide structures of WGT I using amplitude analysis.

B.3.3 Amplitude analysis for all measurement planes

Similar to the amplitude analysis for boreholes Pz10-Pz13, the amplitude analysis was employed to the other crosshole planes to define the approximate locations and dimensions of the low-velocity waveguides of both types WGT I and II. Thereby, each plane is separately analyzed and the different types of waveguides are identified. In Figure B.4, we present the waveguide locations of WGT I marked by red and brown boxes. Blue and light blue boxes represent the approximate locations of WGT II with both high permittivity and high conductivity clay layers. Different colors mean waveguide structures at different depths that might be discontinuous. In general, the locations of WGT I are present for all boreholes between 7.3 m to 9.1 m. Furthermore, indicators of WGT II can be found nearby 4.0 m depth at most of the boreholes. In addition, in the vicinity of 6.0 m, 7.0 m and 9.0 m depths, there are some discontinuous features that could be related to events caused by WGT II. Next, we will use the obtained information to modify the permittivity starting models of the updated FWI, and with this, we will verify the location of the waveguiding structures.

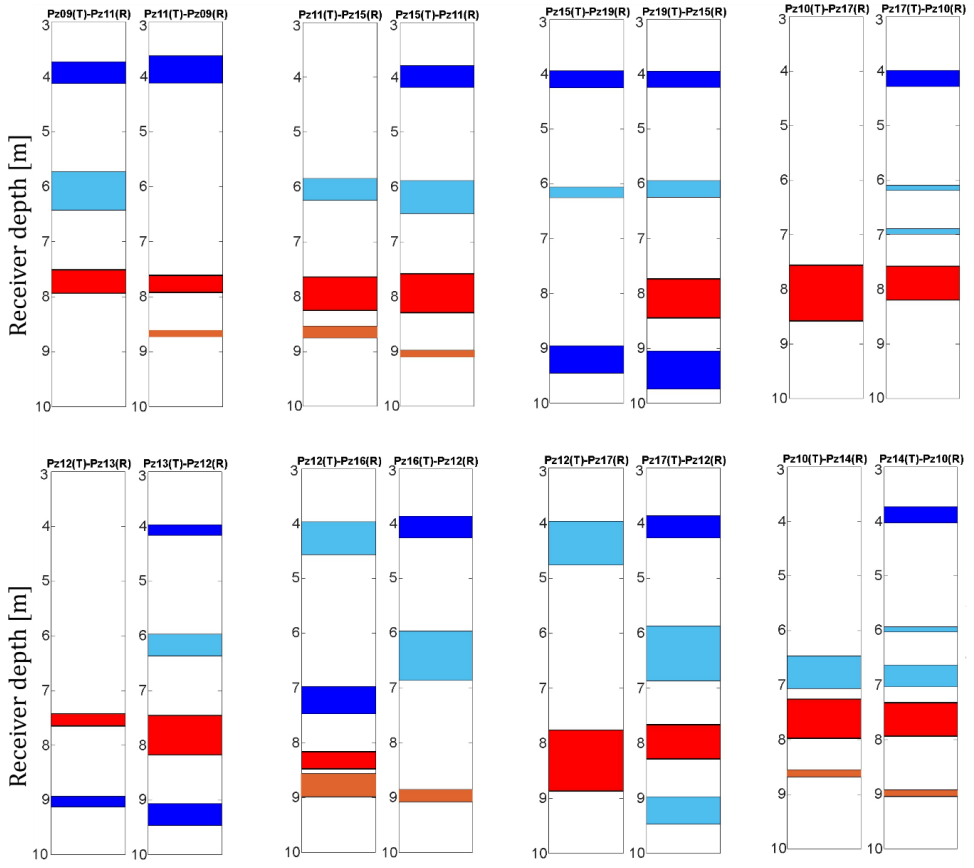


Figure B.4: Approximate waveguide structures based on the amplitude analysis for the eight cross sections. Red zones indicate possible waveguide locations caused by WGT I, while brown color express waveguide locations caused by WGT I that are difficult to pick. Blue and light blue (difficult picking) layers indicate possible waveguide locations caused by WGT II. The depths of different color shades indicate possible discontinuous waveguide structures.

B.4 Full-waveform inversion results

B.4.1 Full-waveform inversion method

To make it much more likely to converge with a reliable and stable crosshole GPR FWI, several pre-processing steps need to be carefully applied to the GPR data. In this study, we will only focus on one major criterion: the estimation of the starting models. For more information about additional pre-processing steps we refer to Klotzsche et al. (2019b). The starting models for the FWI should return synthetic data that are within half a wavelength ($\lambda/2$) of the measured traces in the entire inversion domain to avoid cycle clipping and trapping of the inversion in a local minimum of the misfit function (Meles et al., 2012). For the Hermalle-sous-Argenteau test site considering an average velocity of the aquifer of 0.08 m/ns and a center frequency of the data of 67 MHz this results in a maximum time offset of approximately 7.5 ns (with a $\lambda/2 \approx 0.6$ m). It is highly important that the starting models are sufficiently accurate and full-fill the half wavelength criterion, because they are also considered in the following processing steps of the FWI such as the 3D to 2D conversion and the effective source wavelet estimation. In most of the applications of the GPR FWI, the ray-based inversion results of the measured data provide sufficient good starting models. But, in high-contrast scenarios such as the water table the ray-based models need to be modified to fit the half wavelength criteria (see Klotzsche et al., 2012).

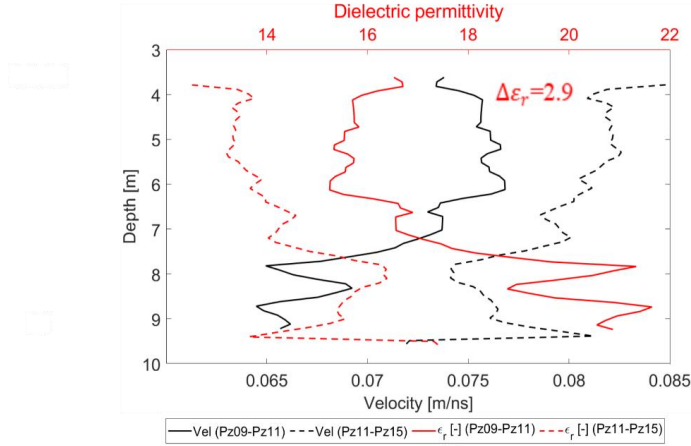
The FWI forward modeling is based on a 2D finite-difference time-domain (FDTD) solutions of Maxwell's equations. Therefore, after estimating the starting models, the 3D GPR data are transformed to 2D and the effective source wavelet is obtained. The FWI is iteratively solved using a gradient-type inversion scheme that simultaneously updates the permittivity and the conductivity in the time domain to minimize the cost function (Meles et al., 2010). The misfit function can be described as L2 norm of the difference between synthetic and observed GPR data. To find the update directions, we use a zero-lag cross-correlation of the synthetic data with the residual data. Normally, the FWI algorithm is stopped when the RMS error changes less than 0.5% between two subsequent iterations to avoid overfitting of the observed data (Klotzsche et al., 2019b). Furthermore, we investigate the behavior of the remaining gradient values of ϵ_r and σ . In the framework of this study, we applied a mute zone around the boreholes to avoid the effect of nested wells in the vicinity of GPR boreholes (Klepikova et al., 2016). Note that gradient normalization as proposed by van der Kruk et al. (2015) leads to artifacts close to the boreholes due to the presence of more than one PVC tubes in some of the boreholes. Each plane was independently analyzed and inverted with the FWI following the guidelines of Klotzsche et al. (2019b).

B.4.2 Short distance boreholes

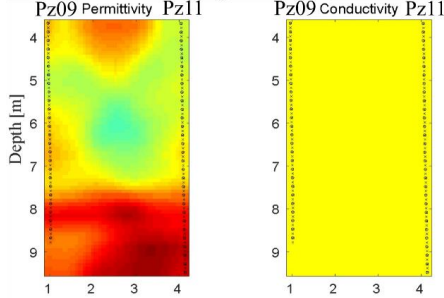
During this study, we note that the ray-based results of short distance boreholes (approximate 3.0 m) provided ϵ_r starting models that were not within half a wavelength of the measured data. Such borehole pairs are probably affected by the presences of the 10 cm diameter water-filled boreholes and could create 3D effects. Generally, the permittivity values are overestimated in comparison to neighboring

planes with larger offsets (Peterson, 2001). Reducing the angle of the measurements did not improve the results. To solve this problem, we combined the results of the short distance boreholes with close larger distance boreholes, and then compared the mean velocity based on both ZOP data sets. We assume that the aquifer is isotropic and that the mean velocity should not change much between neighboring boreholes. For example, the plane between Pz09-Pz11 has a width of 3.02 m and the close by plane Pz11-Pz15 has an offset of 4.88 m. In Figure B.5a, the calculated mean velocities (black lines) and relative permittivity (red lines) based on the ZOP data for cross-section Pz09-Pz11 (solid lines) and Pz11-Pz15 (dashed lines) show a clear difference of about 2 - 4 in ϵ_r . Pz09-Pz11 shows lower mean velocity (higher mean ϵ_r) along the vertical depth axis. If we assume that in the horizontal direction the medium behaves similarly and therefore the mean velocities should be in the same range, we can speculate that the lower velocity for short distance borehole pairs is caused by the increased proportion of the borehole fillings compared to the whole measured distance, an effect that should be corrected. Considering the boreholes distance between Pz09 and Pz11 is 3.02 m, we calculated a delay time of approximately 3.3 ns ($\Delta\epsilon_r = 2.9$) for the short distance boreholes ($3.3 = \frac{3.02}{\bar{V}_{Pz09-11}} - \frac{3.02}{\bar{V}_{Pz11-15}}$). Using this delay time, we corrected the picked first arrival times of the MOG data for the short plane and performed a new ray-based inversion. For the unsaturated zone above the water table, we modeled a homogeneous layer with a relative permittivity of $\epsilon_r = 4.4$ (not shown, same for all following inversions) and for the σ starting model, we selected a homogeneous model of 13 mS/m (mean of the first cycle amplitude inversion results). By comparing the FWI results of both uncorrected and corrected ray-based starting models for the FWI, we note that the corrected FWI results of Pz09-Pz11 show generally lower permittivity results than the uncorrected data (Figure B.5). This is also in agreement with the ZOP results of the neighboring borehole pair with the larger offset. Although the final RMS error is similar for both inversions, the data fit and the remaining gradient were better for the corrected data.

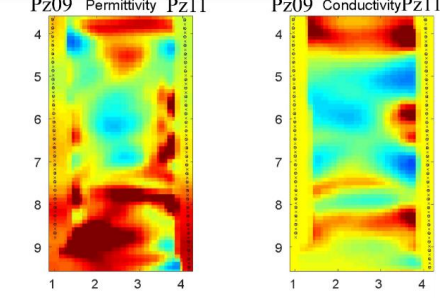
a) ZOP profiles of Pz09-Pz11 and Pz11-Pz15



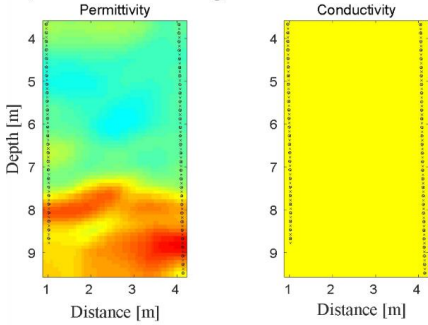
b) Ray-based starting models



c) FWI results (RMS= 1.00×10^{-6})



d) Corrected starting models



e) Corrected FWI results (RMS= 0.91×10^{-6})

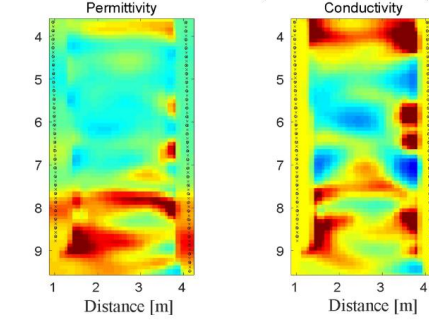


Figure B.5: a) Velocity (black lines) and ϵ_r (red lines) comparison over depth based on the ZOP data for boreholes Pz09-Pz11 (solid lines) and Pz11-Pz15 (dashed lines). b) and d) indicate the ray-based ϵ_r results and the updated starting models based on the ZOP analysis, respectively. Conductivity starting model is homogeneous with 13 mS/m. c) and e) show the corresponding FWI results based on the ray-based starting models and the updated starting models, respectively. The RMS value is indicating the root-mean-square error between the measured and model GPR data.

B.4.3 Starting model test for waveguide zones

From the amplitude analysis we know the approximate locations of possible waveguide structures. Instead of adding homogeneous layers at the expected locations of the waveguide zones as shown by Klotzsche et al. (2012), we investigate another strategy that considers different stages/iterations of the traditional FWI. Details are investigated for the crosshole plane Pz10-Pz13 and will then be applied to the other planes. First, we perform the standard FWI using the ray-based starting models including the water table contrast (Figure B.6a and 6b). The obtained FWI results show higher resolution images than the ray-based results, and the FWI modeled and measured data are in a good agreement in phase and amplitude (not shown), and, show only minor differences also indicated by a correlation coefficient of 0.9652 (Table B.1). Analyzing the results in more detail, we note that the permittivity results with only ten iterations provide clear indications of the waveguide locations, which were consistent with the amplitude analysis results. Therefore, we used the permittivity result of the tenth iteration as a new starting model (Figure B.6c) and updated the effective source wavelet (the red one of intersect in Figure B.6c). Note that standard applications of the crosshole GPR FWI normally consider the ray-based results also with updated effective source wavelets. Here, we apply results of a previous FWI iteration as an updated permittivity starting model and a corresponding updated effective source wavelet. The updated FWI results based on this new effective source wavelet and updated starting model show clearer structures with more details and provide a lower RMS in the final iteration ($\text{RMS}=0.90 \times 10^{-6}$ instead of $\text{RMS}=1.11 \times 10^{-6}$ for the traditional FWI). The green boxes in Figure B.6d indicate the waveguide structures that are probably caused by high porosity waveguides (WGT I), while the blue boxes indicate waveguide zones that could be caused by a higher clay content yielding a higher electrical conductivity (WGT II). Generally, we see a good correlation between the waveguide zones identified with the amplitude analysis and the final FWI inversion results. Similar to previous studies (e.g., Klotzsche et al., 2014), the WGT I structure below 7.0 m depth shows a higher permittivity than the surrounding media indicating an increase in porosity. This is consistent with the heat tracer was flowing preferentially at the bottom of the aquifer, which has a larger hydraulic conductivity. Furthermore, the FWI confirmed the hypothesis that the WGT II structures are caused by an increase of electrical conductivity that could be caused by an increase in clay content. To further confirm the updated FWI results, we present image plots of the FWI modeled data for boreholes Pz10-Pz13 in Figure B.7, which can be compared to the measured data in Figure B.2. The modeled data show a good fit to the measured data in the entire aquifer domain indicating that the FWI solution explains the measured data well. The features that were identified and marked as possible WGT I (red and green circles) and WGT II (dark and light blue) features in the measured data correspond to the features observed in the FWI result.

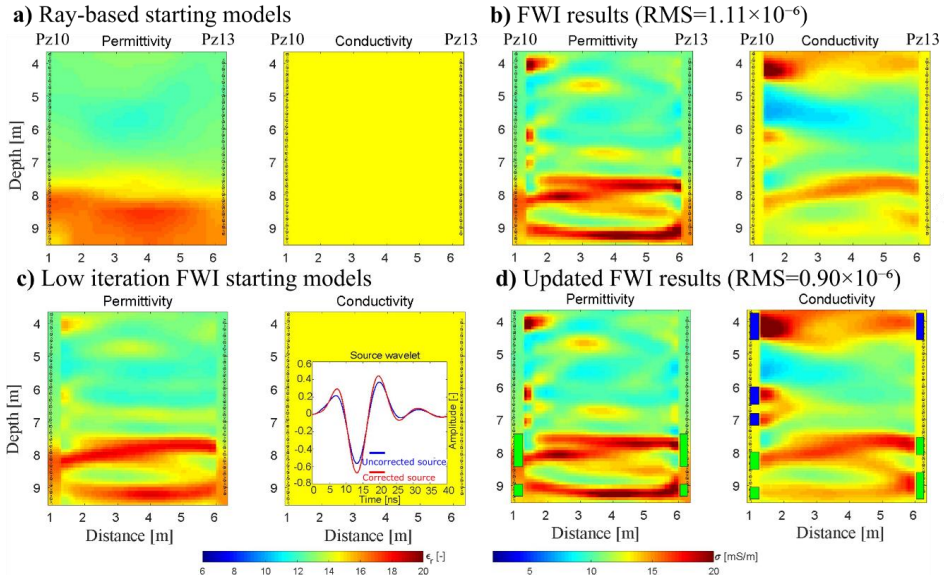


Figure B.6: a) Ray-based starting models and b) corresponding FWI results for cross section Pz10-Pz13. c) Updated starting models based on a lower iteration number result of b) and d) corresponding FWI results. Inset in Figure B.6 c) shows the estimated effective source wavelets based on different starting models. The green and blue boxes in d) indicate the locations of waveguides of WGT I and II, respectively.

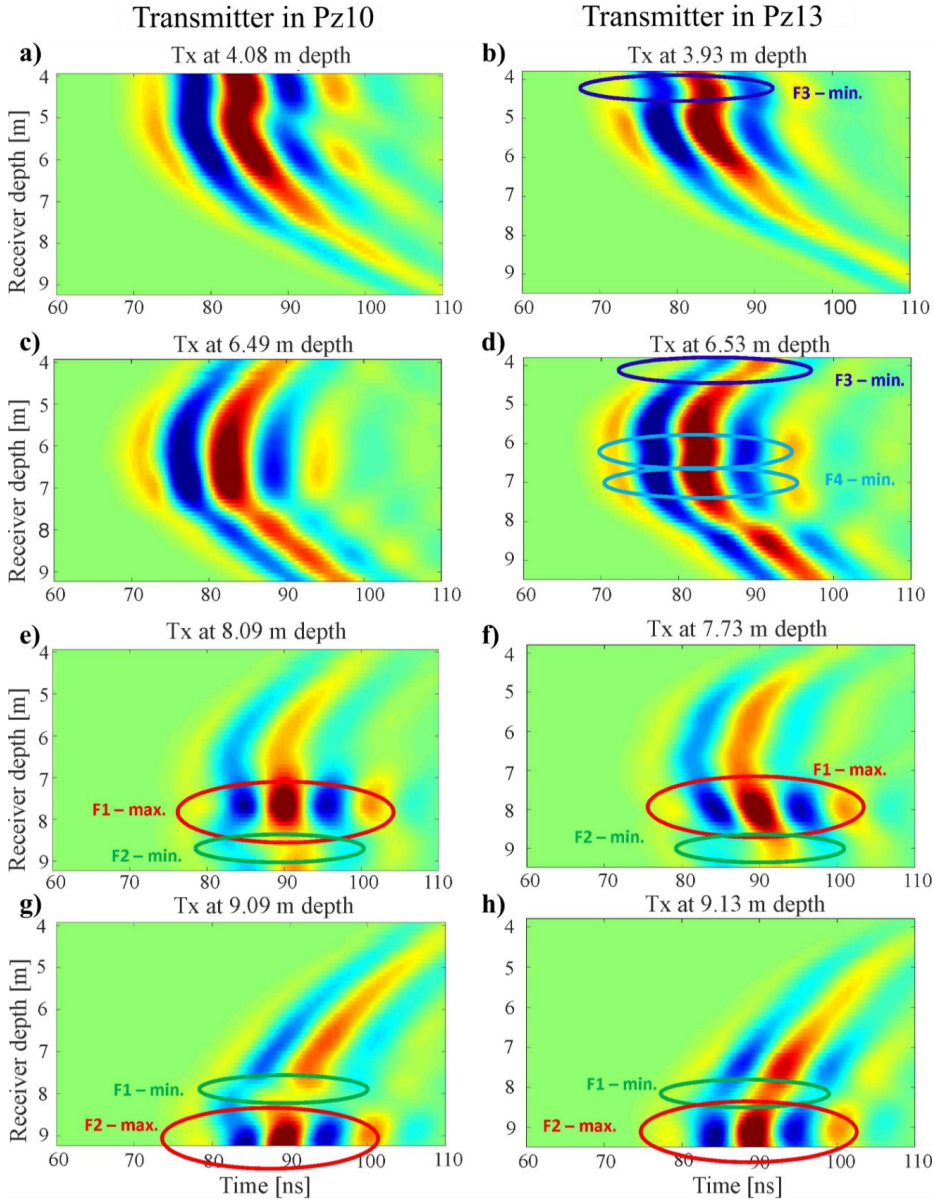


Figure B.7: Image plots of the modeled data based on updated FWI results for the cross section Pz10-Pz13 (Figure B.6d). Different waveguide features are indicated with F1-F4, while WGT I features are marked with red and green and WGT II features with blue and light blue, respectively. Note that we have normalized the amplitudes values to the maximum value of amplitudes for the cross section (range from -7×10^{-1} to 7×10^{-1}).

An erroneous permittivity starting model also affects the high electrical conductivity zone and vice versa. If the permittivity estimate is inaccurate and the modeled data cannot fit the shape of the traces, the conductivity model tries to compensate for this and yields erroneous structures. Therefore, it is highly important to confirm that the inverted permittivity results are reliable. Numerous studies show that it is necessary that first the permittivity (shape of traces) are updated before the conductivity (amplitude of the traces) can be optimized in more detail (Klotzsche et al., 2019a). In previous studies, higher homogenous permittivity layers were added into the permittivity starting model (Klotzsche et al., 2014) to ensure that the starting models fulfill the half-wavelength criteria.

To verify the higher permittivity and conductivity zone near 4.0 m close to Pz10, we performed additional starting model tests. In these tests, we investigate the possibility that the high electrical conductivity zone is caused by an erroneous permittivity starting model and the possibility that the waveguide is caused by an increased permittivity instead of conductivity. Note that due to a reduced ray coverage in the upper part of the investigation domain, it is possible that the permittivity starting model based on the ray-based approach does not fulfil the half-wavelength criterion. In such a case, it can happen that the electrical conductivity results compensate for an erroneous permittivity model. As proposed by Klotzsche et al. (2014), we added different scenarios of a higher homogeneous ϵ_r layer ($\epsilon_r=16$) in the ray-based ϵ_r model (Figures 8a-d) and repeated the FWI analysis. We kept the effective source wavelet and the conductivity starting model unchanged. All results of the different starting model tests confirmed the previously obtained structure, but some discontinuity in the inversion results is visible indicating difficulties of the inversion to find the global minimum. Therefore, we can assume that our FWI results based on the updated permittivity starting model (Figure B.6c) without the homogeneous layers produced reliable results and that the FWI indicates that the minimum locations in the amplitude analysis approach are caused by an increased electrical conductivity (Figure B.8, WGT II).

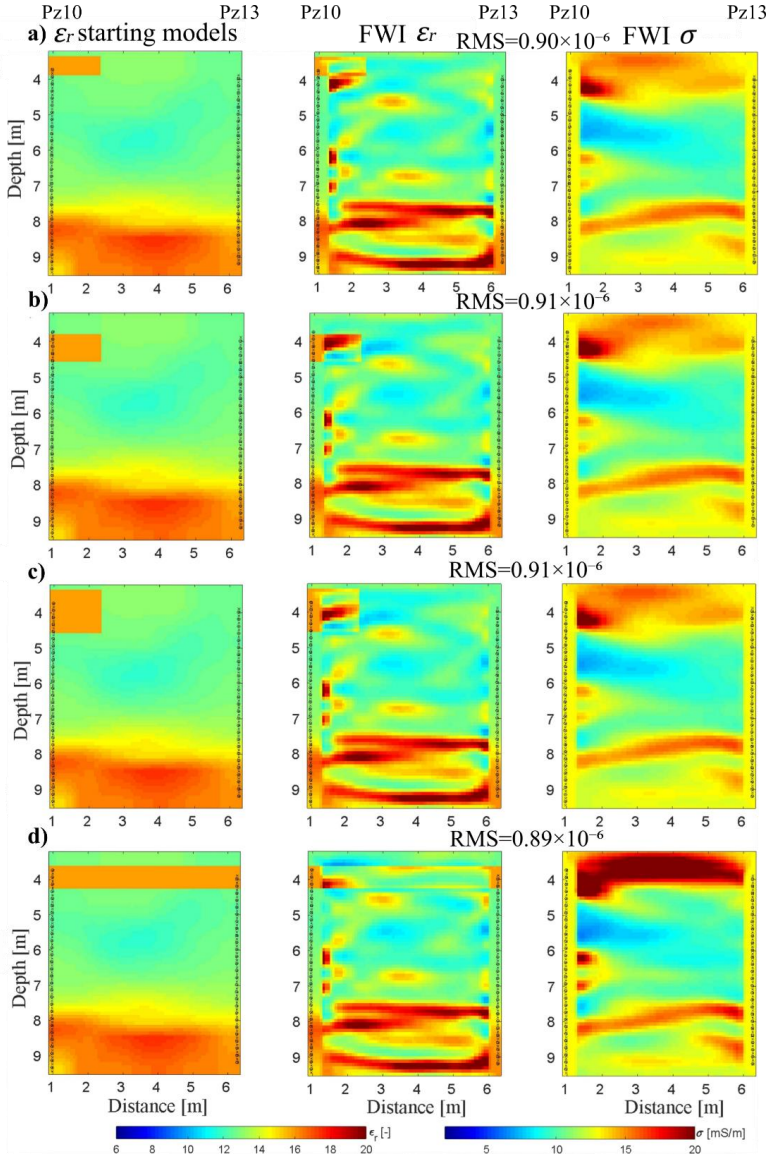


Figure B.8: Starting model tests for ϵ_r are to determine the FWI σ reliability. The first column shows the ray-based starting models of ϵ_r with an added high ϵ_r value zones ($\epsilon_r = 16$). Conductivity starting models are homogenous with 13 mS/m (not shown). The second and third columns show the corresponding FWI ϵ_r and σ results, respectively. Note the effective source wavelet in Figure B.6c (red) is used to perform the FWIs.

B.4.4 Combined FWI results of the Hermalle-sous-Argenteau

For the other crosshole planes, we followed the same approach and updated the effective source wavelets based on the iteration ten FWI ε_r field. The effective source wavelet of a cross-section is depending on the borehole fillings and couplings, and anything is not included in the forward model (e.g., finite length antennae). The obtained updated effective source wavelets are also depending on the borehole distance as shown in Figure B.9. The crosshole pair with the largest distance shows the highest amplitude in time and frequency domain. Furthermore, we observe a shift in center frequency from a higher center frequency for small distance pairs towards a lower center frequency for larger offset combinations (Figure B.9b). Note that boreholes Pz09-Pz11 and Pz15-Pz19 show the largest ($f_c = 80$ MHz) and the smallest ($f_c = 57$ MHz) center frequency, respectively. Except for the effect in amplitude values, similar shapes are observed for all cross-sections using the 200 MHz antennae. The effective center frequency is significantly lower than the nominal center frequency of the antennae in air (200 MHz). This is caused by the fact that the antennae are electrically longer in high-permittivity media and emit lower frequencies than in air (e.g., Klotzsche et al., 2013). Therefore, considering that the signals travel longer in the subsurface for larger offset datasets, the center frequency of effective source wavelet decreases with increasing distance.

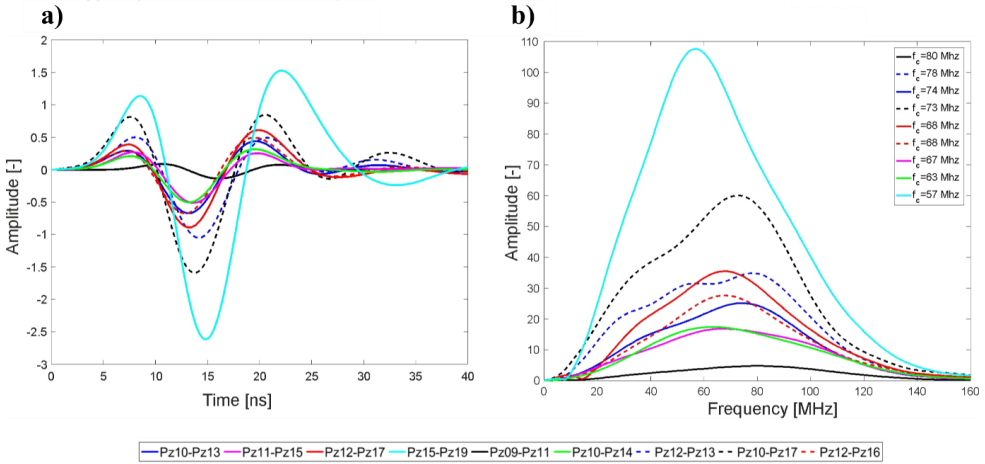


Figure B.9: a) Estimated effective source wavelets for the nine cross-sections in time domain using the updated low iteration FWI results as starting models. b) Corresponding frequency spectra of the nine different effective source wavelets. Each color represents a different plane. The legend values in b) indicate these effective center frequencies for different planes.

The ray-based permittivity results and the final FWI results of the nine crosshole planes combined together to generate a 3D image of the aquifer (Figure B.10). The ray-based results show generally a three-layer model with lower and intermediate permittivity values above 7.5 m depth and higher permittivity values between 7.5 m to 9.5 m depth. In contrast, the FWI results show higher resolution images for both permittivity and conductivity and more structures can be observed. Although the inversions are performed independently, consistent structures at the borehole locations are observed. For simplification, the locations of waveguides with high porosity from amplitude analysis are marked at the cross-sections of Pz09-Pz11, Pz11-Pz15 and Pz15-Pz19 using green boxes (WGT I). Additionally, the waveguides caused by WGT II are indicated with blue boxes in the conductivity image. In the FWI ϵ_r results, the higher permittivity values located from 7.5 m to 9.5 m comprise waveguide structures of WGT I and a higher continuous conductivity zone is clearly shown in the FWI σ results around 4.0 m depth.

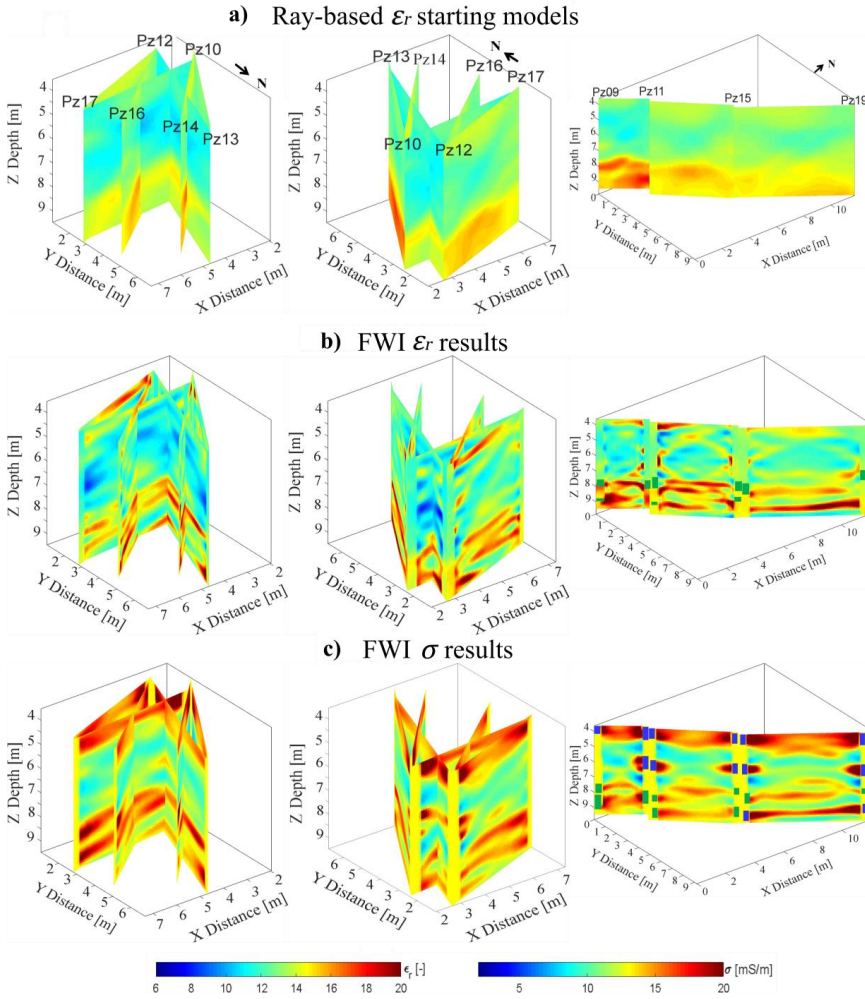


Figure B.10: a) Ray-based results of ϵ_r for all crosssections for different viewing angles. b) and c) FWI ϵ_r and σ results, respectively, using the traditional low (ten) iteration FWI results as starting models and a homogenous model with 13 mS/m for the σ (not shown). Green and blue boxes next to the cross sections image boundaries along Pz09 to Pz19 indicate the boundaries of the waveguide structures of WGT I and II obtained from the amplitude analysis, respectively.

For all inversion planes a good fit between the measured and modeled data was found (not shown). Table B.1 shows a comprehensive comparison between the traditional and the updated FWI for all planes. The final RMS, the absolute mean gradient (AMG) values for permittivity and conductivity, and the correlation coefficients (R) between observed and modeled data indicate that the updated FWI results are better than the traditional FWI results.

The updated FWI results show a good consistency at the different borehole cross-sections as indicated by the R at the intersections of 15 cross-sections (Table B.2). For all cross-sections, we used the mean of two inversion cells to compute R values (Klotzsche et al., 2013). For the planes that have a separation of approximately 5.0 m the R for ϵ_r shows values from 0.52 to 0.89. Note that the cross-sections Pz09-Pz11 (3.02 m) and Pz15-Pz19 (7.07 m) are different from others. Further, a lower R of 0.26 for the permittivity intersection between Pz09-Pz11 and Pz11-Pz15 is calculated, which shows the FWI results are not very consistent at the borehole Pz11. Similarly, Pz15 shows a weak correlation of the intersections. The R for ϵ_r between Pz10-Pz13 and Pz10-Pz17 is 0.24, and R for ϵ_r between Pz10-Pz14 and Pz10-Pz17 is 0.35. The reason for this weak correlation could be that the plane between the borehole Pz10 and Pz17 was measured two months later than the other crosshole sections and seasonal fluctuations could have caused this effect in the permittivity. Comparing these values with the $R (\epsilon_r)$ values derived from the crossing point of non-borehole (Pz10-Pz17) zones, which are 0.69, 0.89 and 0.90, we believe the later measured GPR cross-section is affected by the vicinity of borehole Pz10. Note, that there is a second well very close by to Pz10, which could affect the results of the planes connected to this borehole. Finally, although a lower mean $R (\epsilon_r)$ was achieved for some locations, for most cases an acceptable value above 0.61 for permittivity and 0.85 for conductivity indicate consistent and reliable results.

Table B.2: Correlations coefficient R for the updated full-waveform inversion permittivity and conductivity results at the ten boreholes. The mean values of R for the permittivity and conductivity planes were 0.61 and 0.85, respectively.

Borehole(Pz)	10	11	12	13	15	17	The crossing of diagonal (intersecting) planes								
Planes	10-13	10-14	09-11	12-16	12-16	12-13	10-13	11-15	12-16	11-15	10-17*	10-14			
	10-14	10-17*	10-17*	11-15	12-13	12-17	12-13	15-19	10-17*	12-13	12-13	12-13			
	0.52	0.24	0.35	0.26	0.67	0.89	0.75	0.74	0.38	0.69	0.89	0.58	0.90	0.62	
$R(\sigma)$	0.79	0.93	0.75	0.70	0.88	0.89	0.90	0.92	0.87	0.91	0.85	0.78	0.81	0.88	0.83

Pz10-Pz17* was measured later than other boreholes and close by to Pz10 is a second well installed which is water filled.

B.5 Petrophysical interpretation

To improve the understanding and to explain the heat tracer experiment of Hermans et al. (2015a), which described quantitative temperature monitoring at the Hermalle-sous-Argenteau field site, we analyzed the porosity of the saturated zone based on the new GPR FWI ε_r results using the complex refractive index model (CRIM) similar to Gueting et al. (2015):

$$\phi = \frac{\sqrt{\varepsilon_r} - \sqrt{\varepsilon_s}}{\sqrt{\varepsilon_f} - \sqrt{\varepsilon_s}} \quad \text{Eq. (B.1)}$$

for the fluid permittivity ε_f we considered 84 for a water temperature of 10 °C and for the solid permittivity ε_s we used 4.5 based on literature values of quartz (e.g., Birchak et al., 1974; Eisenberg and Kauzmann, 2005; Carmichael, 2017). To evaluate the porosity values between Pz13 and Pz17 (ERT cross-section in Figure B.1d), we considered five cross-section porosity results in Figure B.11a (3D) and Figure B.11b (2D). Higher permittivity zones of the FWI results (Figure B.10) result in higher porosity values (Figure B.11). Porosity values reach 30-35% in the high porosity zones between 7.0 m to 9.0 m depth. The higher porosity at these depths is consistent with the classification from ERT and borehole log results (Hermans, 2014; Hermans et al., 2015a, b, 2017) with coarse gravel at the bottom and gravel in a sandy matrix on the top. The gravel at the bottom is very coarse (pebbles) with almost no matrix, and is referred to as the swimming pool due to its large hydraulic conductivity. In addition, the coarse gravel has a lower resistivity compared to the sandy gravel due to a larger water content. The high porosity layers are more continuous between the boreholes P10-Pz13 and Pz10-Pz14, while for P12-Pz16 and Pz12-Pz17 more discontinuous structures can be observed, which is consistent with the splitting of the thermal plume (Figure B.1d). By analyzing the mean porosity close to the boreholes crossing the intersection of Pz13 and Pz17 between 7.0 m and 9.5 m depth (dashed rectangles in Figure B.11b), we see that the mean porosity values in the selected 2D zones become smaller from Pz13 towards Pz17 (Figure B.11c). Such a behavior of the porosity structures could explain the heat tracer distribution observed by Hermans et al. (2015a). Zones with a higher porosity and continuous structures such as observed close to Pz13 and Pz14 could also cause preferential flow paths for heat when hot water was injected from borehole Pz09.

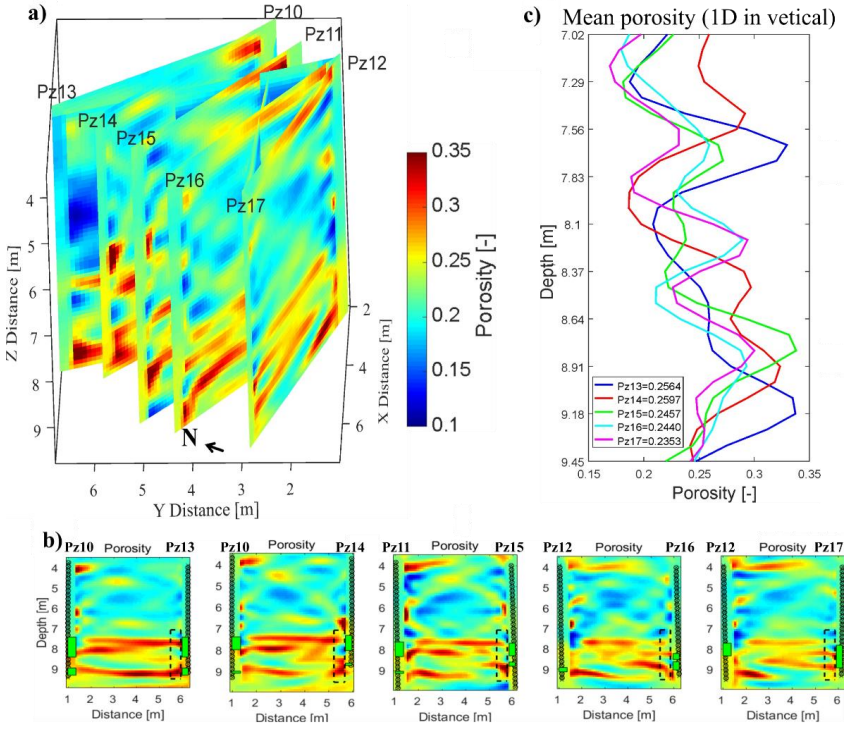


Figure B.11: a) Estimated porosity distributions in 3D based on CRIM to relate to the ERT measured profile Pz13-Pz17 (Figure B.1). b) Detailed porosity distribution of the five relevant crosshole sections. The green boxes close to antennas indicate the boundaries of the wave-guiding structures WGT I obtained from the amplitude analysis. Dashed black rectangles indicate the zones close to boreholes to compute the mean porosity profiles in c) along the vertical direction.

B.6 Conclusions

We applied an extended amplitude analysis approach and the crosshole GPR FWI to the Hermalle-sous-Argenteau test site located in the alluvial aquifer of the Meuse River in Belgium. The results of the GPR FWI provided high-resolution images of the aquifer within decimeter-scale resolution and allowed a detailed characterization of the porosity structures. The amplitude analysis, which can be used to identify low-velocity guided wave structures, is extended to detect two waveguide types (WGT) with different origins. To further improve traditional FWI results, the estimation of different starting models for permittivity was proposed. First, for short distance cross-sections, zero-offset profile data were used to correct the travel-time inversion results and to update the starting model of the permittivity. Second, the FWI results were updated by using low iteration number traditional FWI results as starting models and performing new effective source wavelet corrections. Comparisons of the RMS, the mean remaining gradients for ϵ_r and σ , and correlation R of the measured and the final FWI data, indicated

an improvement of the FWI results using these low iteration starting models in contrast to the traditional results.

By using the amplitude analysis, the approximate locations of WGT I caused by higher permittivity (porosity) and low/intermediate electrical conductivity that produced elongated wave trains in the measured GPR data were detected and confirmed by FWI. For the first time, WGT II structures that are caused by an increase in permittivity and electrical conductivity were identified in the measured data using the amplitude analysis approach. Such waveguides are difficult to detect from the measured data and the amplitude analysis due to the absences of the elongated wave trains (higher wave attenuation in the waveguide zone). The FWI inversion results of the WGT II zones confirmed the existence of these structures probably caused by an increase of clay content.

For the 3D characterization of the alluvial aquifers, nine 2D intersecting GPR planes were separately inverted. We evaluated the updated 2D FWI results by computing correlation coefficient (R) for consistent structures, where acquisition planes intersect. In most of the cases, the FWI results in combination with the amplitude analysis presented consistent structures between the intersections for both permittivity and conductivity images. From the 3D FWI image, high-permittivity layers between 7.5 m to 9.5 m depth for all cross-sections were observed (WGT I). Further, continuous higher conductivity zones above 4.0 m are detected in all cross-sections that aligned with the WGT II features. Compared with ERT tomography results, the updated GPR FWI results confirmed the presence of a high hydraulic conductivity zone with high porosity, but provided higher resolution images of the subsurface and much more details about the lateral heterogeneity. This refined description of the heterogeneity allows a better explanation of the spatial distribution (plume splitting) of the heat tracer test performed on the experimental site. Further research will investigate the potential to use the FWI results to construct a full 3D aquifer model including small-scale heterogeneity and to discriminate geological scenarios as a basis for starting models. In addition, the approach of source-independent time-domain waveform inversion of cross-hole GPR data will be considered in future studies.

Appendix C

C Numerical study for time-lapse GPR full-waveform inversion for salt and heat tracer tests⁶

Crosshole GPR full-waveform inversion has proven to be a powerful tool to characterize aquifers within a high resolution. Until now, studies have only been performed in a steady state and correlations to flow and transport processes have been difficult. In this study we investigate how the crosshole GPR FWI can be used to map and quantify different tracers, that not only affect the permittivity of the subsurface but also the electrical conductivity. Thereby, our main focus is to investigate the effect of a salt and heat tracer using a realistic aquifer flow and transport model. Synthetic time-lapse GPR data is used to analyze different full-waveform inversion and starting model strategies to find the method that reconstructs the tracer movement best.

⁶ Adapted from Haruzi, P., Schmäck, J., Zhou, Z., Vanderborght, J., Vereecken, H., van der Kruk, J., and Klotzsche, A. (2020). Numerical study for time-lapse GPR full-waveform inversion for salt and heat tracer tests. That extended abstract was accepted to *18th International Conference on Ground Penetrating Radar*, but eventually was not published because the conference was cancelled due to restrictions of Covid19.

C.1 Introduction

A detailed understanding of flow and transport processes in aquifers is necessary to protect or remediate groundwater that is endangered by anthropogenic pollution or seawater intrusion. To infer channelized transport properties time-lapse geophysical imaging of tracer tests can be used. Among the geophysical methods, ground-penetrating radar (GPR) has shown a high potential to detect contaminant plumes in the subsurface (e.g. Knight, 2001). So far, GPR time-lapse studies only investigated changes in permittivity (e.g. Binley, 2002), and did not consider the use of salt and heat tracer which mainly affects the electrical conductivity of the media. Crosshole GPR full-waveform inversion (FWI) is able to characterize the critical zone with a decimeter-scale resolution, which allows the consideration of small-scale heterogeneities that influence flow and transport significantly. GPR FWI tomograms provide at the same time high resolution images of the electromagnetic soil properties relative dielectric permittivity ϵ_r and electrical conductivity σ , which can be linked to soil water content/ porosity, and, soil texture, clay content, respectively. A detailed overview of the theoretical developments and applications of the crosshole GPR FWI is provided by Klotzsche et al. (2019).

This study investigates the potential of time-lapse GPR FWI to map and monitor tracer plumes during time-lapse experiments for changes mainly in electrical conductivity (e.g., salt tracer). Therefore, a numerical study, which mimics the travel of tracers through a realistic sandy aquifer based on the Krauthausen test site in Germany, was used to generate GPR permittivity and electrical conductivity images for different time steps. FWI starting model (SM) strategies are tested for the different tracer scenarios and the independent time-lapse FWI is compared to the double-difference time-lapse FWI strategy that Asnaashari (2015) used to obtain robust time-lapse seismic velocity changes.

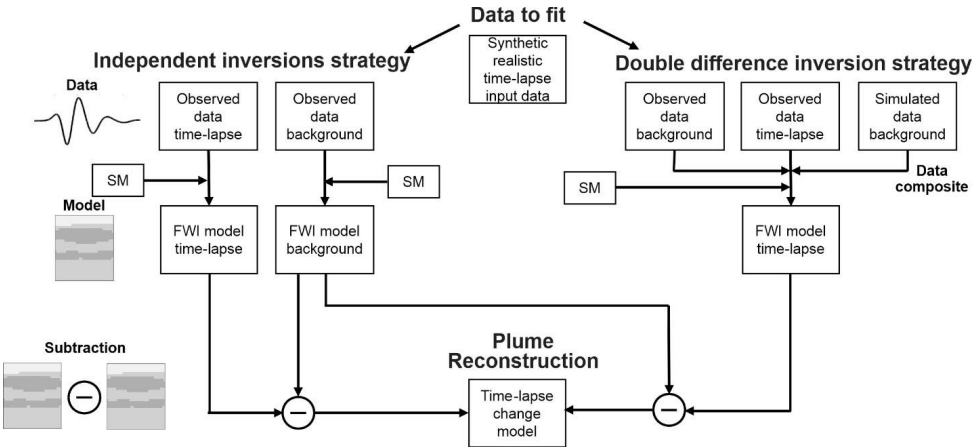


Figure C.1: Flow chart of different time-lapse inversion strategies. Independent and double-difference strategy are shown on the left and right branches, respectively.

C.2 Time-lapse full-waveform inversion strategies

In this study, images of permittivity and conductivity from time-lapse (TL) datasets are obtained using the standard GPR FWI procedure and the double-difference strategy. While the standard procedure inverts the wave fields independently for each dataset (Figure C.1, left side), the double-difference strategy inverts the difference in wave fields between TL and background (BG) datasets, caused by TL variations. In other words, by iteratively updating the GPR model parameters, the inversion minimizes the misfit function Δd between the differences in observed ($\mathbf{E}_{TL}^{obs} - \mathbf{E}_{BG}^{obs}$) and synthetic time-lapse modeled ($(\mathbf{E}_{TL}^{syn} - \mathbf{E}_{BG}^{syn})$) and BG wave fields (Figure C.1, right side).

It implies that the inverted TL model \mathbf{m}_{TL}^{syn} is affected by TL changes in the observed data and on synthetic background modeled data. The main benefit of the double-difference strategy is that as long unexplained features in the BG and TL data remain the same, the difference will be free of them and will not produce time-lapse artifacts. In addition, accurate \mathbf{E}_{BG}^{syn} synthetic wavefields of the background is required. In contrast, independently inverted datasets may contain unexplained events (Asnaashari et al., 2015). In order to enable a robust TL model using the double-difference FWI, acquisition errors need to be minimized, antennae positions and source wavelets must be consistent in all TL measurements (Asnaashari et al., 2015, Klotzsche et al., 2019). In this synthetic study perfectly consistent transmitter and receiver positions will be used in BG and TL acquisition, and the data will be free of noise. For detailed discussion on the difference between the strategies see Asnaashari et al. (2015).

C.3 Strategies for time-lapse starting models

The full-waveform inversion requires a good starting model (SM), such that the modeled data calculated from it overlaps the observed data in at least half a wavelength in the entire investigation domain. This avoids cycle-skipping artifacts during the inversion, which might result in convergence towards local minima (Virieux and Operto, 2009). An inversion that uses a closer and more accurate starting model with relation to the real model (RM) will result in a more accurate FWI result. Commonly, ray-based inversion models are used as SM for both GPR parameters (Klotzsche et al., 2019). However, for TL investigations the use of the BG FWI results as SM might even increase the data fit as long the half-wavelength criteria is still fulfilled. In this study, three SM combinations of ε_r and σ are tested. These combinations consist of the independent ray-based inversion results (which in this synthetic case is a smoothed RM) and the background FWI results. The SM strategies are summarized in Table C.1, and used for both independent difference and double-difference FWI strategies.

Table C.1: Starting model strategies for time-lapse GPR Full-waveform inversion. SM, RM and BG stand for starting model, real model and background.

	SM 1	SM 2	SM 3
ϵ_r	Smoothed RM	BG FWI	BG FWI
σ	Averaged uniform value of RM	Averaged uniform value of RM	BG FWI

C.4 Synthetic positive electrical tracer

To predict flow and transport in an aquifer, a realistic synthetic 3D flow and transport simulation has been performed (Bechtold, 2011) to generate a plume fate for synthetic GPR data. Therefore, the large database of the Krauthausen test site in Germany was used to build up a synthetic aquifer model.

The aquifer model is based on the data provided by Gueting et al. (2018) and generated stochastically using sequential gaussian simulation (Remy et al., 2009), incorporating log-conductivity histogram and correlation lengths to manifest realistic preferential paths. The time-lapse GPR data was calculated for a positive electrical tracer with a maximum contrast of 25 mS/m to the background dataset simulated in a 2D crosshole plane with an offset of 5 m.

First, the standard independent crosshole GPR FWI was performed and the different FWI starting model strategies (Table C.1) for time-lapse data were tested to find the most accurate plume reconstruction. The FWI results of the background GPR data (without electrical conductivity change, permittivity constant) reveal most of the heterogenous structures of the input models and a good data fit or rather a good reconstruction of the medium properties was obtained (Figure C.2, third column). SM strategy 1, which is normally applied in standard FWI applications and considers the ray-based inversion results, was able to reconstruct most of the important features of the input models and detected the plume location and dimensions. However, the contrast of the electrical conductivity plume is not fully reproduced. SM 2 and SM 3 show similar time-lapse FWI results for permittivity and perform better in the reconstruction of the electrical conductivity plume. SM 3, which is using the background FWI results of ϵ_r and σ as starting models, produces the most accurate plume reconstruction in terms of plume location, dimension and contrast.

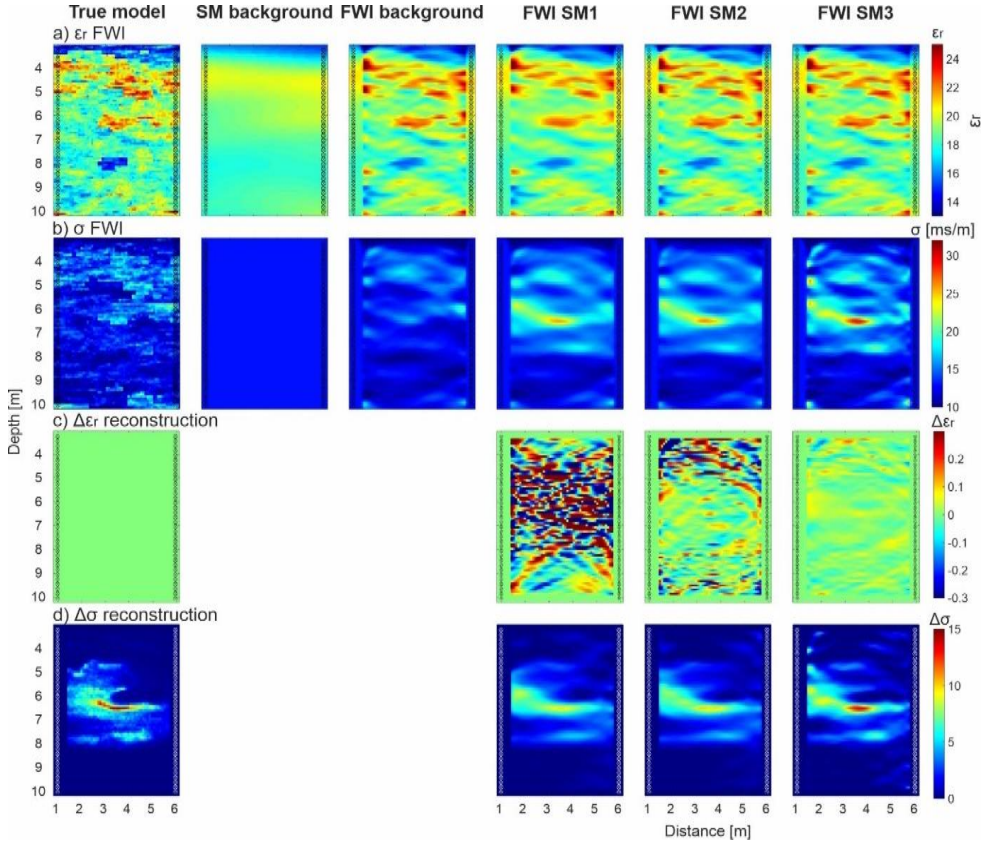


Figure C.2: Plume reconstruction from independent FWI of a positive electrical tracer with maximum contrast of 25 mS/m for starting model strategies 1-3. a,b) FWI models of permittivity and electrical conductivity, respectively. c,d) changes from background to time-lapse FWI models for permittivity and electrical conductivity, respectively.

Second, the double-difference FWI strategy was performed to resolve the time-lapse GPR data using the same starting model strategies (see Table C.1) than for the standard FWI. Similar to the independent FWI results, the final permittivity images only show minor differences, although SM1 performs a little bit less good. In contrast to SM 2, SM1 and SM3 show a relatively good reconstruction of the electrical conductivity changes of the plume. While SM1 shows a slightly better reconstruction of the dimension and location, SM3 reproduces the maximum change inside the plume better. Generally, the numerical artifacts outside of the plume location are less than for the standard FWI procedure (close to inversion boundaries). Note that for all FWI inversion results the standard criteria that indicate a good inversion result are fulfilled (see Klotzsche et al., 2019b).

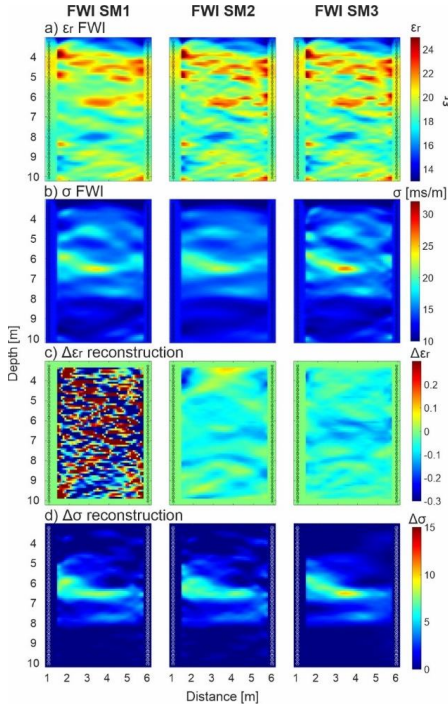


Figure C.3: Plume reconstruction from double-difference FWI of a positive electrical tracer with maximum contrast of 25 mS/m for starting model strategies 1-3. a,b) FWI models of permittivity and electrical conductivity, respectively. c,d) changes from background to time-lapse FWI models for permittivity and electrical conductivity, respectively.

Comparing the best results of the standard and the double-difference approach, we can conclude that the standard approach using SM3 performs best when we are only interested in the σ reconstruction of the plume dimension, location and difference. Considering the entire inversion domain the double-difference approach produces slightly better results. In time-lapse seismic velocity changes study (Asnaashari et al., 2015) the plume reconstruction from double-difference approach performed better than the standard, in contrast to our study. The reasons may be related to deficient accuracy in the background synthetic wavefields \mathbf{E}_{BG}^{syn} which are used in double-difference approach. Whereas in the seismic case the attenuation parameter was kept fixed, for the radar data in addition to the velocity update, the input conductivity distribution was not fixed and was updated too, introducing more degrees of freedom in the inversion resulting in larger misfit in \mathbf{E}_{BG}^{syn} .

C.5 Conclusions and Outlook

This study highlights the potential of time-lapse GPR full-waveform inversion as high resolution imaging technique that is able to monitor tracer movement in the subsurface. While ray-based analyses of crosshole GPR data are not able to reconstruct the tracer behaviour (especially not electrical conductivity changes) because small heterogeneities are smoothed, the FWI improves the quantification of tracer plumes. The comparison of different starting model and time-lapse FWI strategies showed that by starting with the background FWI results and using the independent FWI method the best reconstruction of the tracer plume could be achieved. Note that the changes applied to the time-lapse GPR data were within-half the wavelength criteria of the FWI. In the future, the results of this synthetic study will be used to analyze a salt and a heat tracer test, which were conducted at the Krauthausen test site in Germany. Thereby, we will also investigate the effect of the effective source wavelet estimation for different borehole fillings for the different starting model strategies. For experimental time-lapse data applications the double-difference approach will not be considered.

Acknowledgments

Here, I want to express my gratitude to

- Prof. Dr. Anja Klotzsche for the supervision of the work, on the theoretical part, the GPR FWI data processing guidance, teaching me the GPR field work and help me with preparation, implementation of the tracer tests, and working with me on the papers and thesis.
- Prof. Dr. Jan van der Kruk for providing me the chance to participate in the PhD project, and helping with paper revision and prepare my required deliverables.
- Prof. Dr. Bülent Tezkan who accepted me to submit my dissertation to the Faculty of Mathematics and Natural Sciences at the University of Cologne and to be my second supervisor.
- Rainer Harms for preparing the tracer experiments and the equipment, and for leading the injection.
- Dr. Richard Hoffmann, for planning, coordinating, and implementing with me the heat tracer experiment, and also helping me with the GPR measurements.
- Prof. Dr. Jan Vanderborght for his advices about the tracer test experiments and monitoring, taking a major part in as co-author in my papers, and also for encouraging me by always seeing the bright side from where I can proceed.
- Prof. Dr. Harry Vereecken, for advising me on my work, for seeing the whole picture of a PhD student in a foreign land, and for always encouraging me.
- Jessica Schmäck, for helping me with everything about GPR FWI: field work, equipment and data processing.
- Zhen Zhou for helping me the FWI processing.
- Guillaume De Schepper from AQUALE company for sending us the CTD Diver for borehole logging monitoring.
- Yu Yi, Lena Lärm, Katalin Havas, Nasim Nassar, Nicole Höring, Tobias Ganther, Emil Shahnazaryan, Louisa Hain, Sofie Raemdonck, for helping me with GPR measurements and data processing.
- I thank the Jülich Supercomputing Center (JSC) for providing access to the JURECA high performance cluster. This study is part the Enigma ITN program (European training Network for in situ imaGing of dynaMic processes in heterogeneous subsurfAce environments). This project has received funding from the European Union's Horizon 2020 research and innovation program under the Marie Skłodowska-Curie Grant Agreement No 722028.
- This study is part of the Enigma ITN program (European training Network for in situ imaGing of dynaMic processes in heterogeneous subsurfAce environments). This project has received funding from the European Union's Horizon 2020 research and innovation programme under the Marie Skłodowska-Curie Grant Agreement No 722028.

Bibliography

- Agudo, Ò. C., da Silva, N. V., Warner, M., & Morgan, J. (2018). Acoustic full-waveform inversion in an elastic world Acoustic FWI in an elastic world. *Geophysics*, 83(3), R257-R271.
- Annan, A. P. (2009). Electromagnetic principles of ground penetrating radar. *Ground penetrating radar: theory and applications*, 1, 1-37.
- Archie, G. E. (1942). The electrical resistivity log as an aid in determining some reservoir characteristics. *Transactions of the AIME*, 146(01), 54-62.
- Asnaashari, A., Brossier, R., Garambois, S., Audebert, F., Thore, P., & Virieux, J. (2015). Time-lapse seismic imaging using regularized full-waveform inversion with a prior model: which strategy?. *Geophysical prospecting*, 63(1), 78-98.
- Axtell, C., Murray, T., Kulesa, B., Clark, R. A., & Gusmeroli, A. (2016). Improved accuracy of cross-borehole radar velocity models for ice property analysis. *Geophysics*, 81(1), WA203-WA212.
- Bechtold, M., Vanderborght, J., Ippisch, O., & Vereecken, H. (2011). Efficient random walk particle tracking algorithm for advective-dispersive transport in media with discontinuous dispersion coefficients and water contents. *Water Resources Research*, 47(10).
- Belina, F. (2011). *Source Wavelet Estimation for Waveform Inversion of Crosshole Georadar Data* (Doctoral dissertation, éditeur non identifié).
- Belina, F., Irving, J., Ernst, J., & Holliger, K. (2012). Analysis of an iterative deconvolution approach for estimating the source wavelet during waveform inversion of crosshole georadar data. *Journal of applied geophysics*, 78, 20-30.
- Bear, J., & Cheng, A. H. D. (2010). *Modeling groundwater flow and contaminant transport* (Vol. 23, p. 834). Dordrecht: Springer.
- Berenger, J. P. (1994). A perfectly matched layer for the absorption of electromagnetic waves. *Journal of computational physics*, 114(2), 185-200.
- Bialas, Z., and A. Kleczkowski (1970), Über den praktischen Gebrauch von einigen empirischen Formeln zur Berechnung des Durchlässigkeitskoeffizienten, K. Archivum Hydrotechniki, Warschau.
- Binley, A., Winship, P., Middleton, R., Pokar, M., & West, J. (2001). High-resolution characterization of vadose zone dynamics using cross-borehole radar. *Water Resources Research*, 37(11), 2639-2652.
- Binley, A., Cassiani, G., Middleton, R., & Winship, P. (2002). Vadose zone flow model parameterisation using cross-borehole radar and resistivity imaging. *Journal of Hydrology*, 267(3-4), 147-159.

- Binley, A., Hubbard, S. S., Huisman, J. A., Revil, A., Robinson, D. A., Singha, K., & Slater, L. D. (2015). The emergence of hydrogeophysics for improved understanding of subsurface processes over multiple scales. *Water resources research*, 51(6), 3837-3866.
- Birchak, J. R., Gardner, C. G., Hipp, J. E., & Victor, J. M. (1974). High dielectric constant microwave probes for sensing soil moisture. *Proceedings of the IEEE*, 62(1), 93-98.
- Bleistein, N. (1986). Two-and-one-half dimensional in-plane wave propagation. *Geophysical Prospecting*, 34(5), 686-703.
- Bradford, J. H. (2007). Frequency-dependent attenuation analysis of ground-penetrating radar data. *Geophysics*, 72(3), J7-J16.
- Brewster, M. L., & Annan, A. P. (1994). Ground-penetrating radar monitoring of a controlled DNAPL release: 200 MHz radar. *Geophysics*, 59(8), 1211-1221.
- Buselli, G., Davis, G. B., Barber, C., Height, M. I., & Howard, S. H. D. (1992). The application of electromagnetic and electrical methods to groundwater problems in urban environments. *Exploration Geophysics*, 23(4), 543-555.
- Butler, J. J. (2005). Hydrogeological methods for estimation of spatial variations in hydraulic conductivity. In *Hydrogeophysics* (pp. 23-58). Springer, Dordrecht.
- Carmichael, R. S. (2017). *Practical handbook of physical properties of rocks and minerals (1988)*. CRC press.
- Coscia, I., Linde, N., Greenhalgh, S., Vogt, T., & Green, A. (2012). Estimating traveltimes and groundwater flow patterns using 3D time-lapse crosshole ERT imaging of electrical resistivity fluctuations induced by infiltrating river water. *Geophysics*, 77(4), E239-E250.
- Dafflon, B., Irving, J., & Barrash, W. (2011). Inversion of multiple intersecting high-resolution crosshole GPR profiles for hydrological characterization at the Boise Hydrogeophysical Research Site. *Journal of Applied Geophysics*, 73(4), 305-314.
- Dafflon, B., & Barrash, W. (2012). Three-dimensional stochastic estimation of porosity distribution: benefits of using ground-penetrating radar velocity tomograms in simulated-annealing-based or Bayesian sequential simulation approaches. *Water Resources Research*, 48(5).
- Daniels, D. J. (Ed.). (2004). *Ground penetrating radar* (Vol. 1). Iet.
- Daniels, D. J. (2004). *Ground Penetrating Radar, the Institution of Electrical Engineers*, London, UK.

Day-Lewis, F. D., Lane Jr, J. W., Harris, J. M., & Gorelick, S. M. (2003). Time-lapse imaging of saline-tracer transport in fractured rock using difference-attenuation radar tomography. *Water Resources Research*, 39(10).

Diamanti, N., & Giannopoulos, A. (2009). Implementation of ADI-FDTD subgrids in ground penetrating radar FDTD models. *Journal of Applied Geophysics*, 67(4), 309-317.

Doetsch, J., Linde, N., Coscia, I., Greenhalgh, S. A., & Green, A. G. (2010). Zonation for 3D aquifer characterization based on joint inversions of multimethod crosshole geophysical data. *Geophysics*, 75(6), G53-G64.

Döring, U., 1997. Transport der reaktiven Stoffe Eosin, Uranin und Lithium in einem heterogenen Grundwasserleiter, Ph.D. thesis, Christian Albrecht Universität Kiel.

Dorn, C., Linde, N., Le Borgne, T., Bour, O., & Baron, L. (2011). Single-hole GPR reflection imaging of solute transport in a granitic aquifer. *Geophysical Research Letters*, 38(8).

Eisenberg, D., & Kauzmann, W. (2005). *The structure and properties of water*. OUP Oxford.

Englert, A. (2003). Measurement, estimation and modelling of groundwater flow velocity at Krauthausen test site (Doctoral dissertation, Bibliothek der RWTH Aachen).

Eppstein, M. J., & Dougherty, D. E. (1998). Efficient three-dimensional data inversion: Soil characterization and moisture monitoring from cross-well ground-penetrating radar at a Vermont test site. *Water resources research*, 34(8), 1889-1900.

Ernst, J. R., Maurer, H., Green, A. G., & Holliger, K. (2007a). Full-waveform inversion of crosshole radar data based on 2-D finite-difference time-domain solutions of Maxwell's equations. *IEEE transactions on geoscience and remote sensing*, 45(9), 2807-2828.

Ernst, J. R., Green, A. G., Maurer, H., & Holliger, K. (2007b). Application of a new 2D time-domain full-waveform inversion scheme to crosshole radar data. *Geophysics*, 72(5), J53-J64.

Giannopoulos, A. (2011). Unsplit implementation of higher order PMLs. *IEEE Transactions on Antennas and Propagation*, 60(3), 1479-1485.

Giertzuch, P. L., Doetsch, J., Jalali, M., Shakas, A., Schmelzbach, C., & Maurer, H. (2020). Time-lapse ground penetrating radar difference reflection imaging of saline tracer flow in fractured rock. *Geophysics*, 85(3), H25-H37.

Gilson, E. W., Redman, J. D., Pilon, J., & Annan, A. P. (1996, April). Near surface applications of borehole radar. In *9th EEGS Symposium on the Application of Geophysics to Engineering and Environmental Problems* (pp. cp-205). European Association of Geoscientists & Engineers.

Griffiths, D.J., 1981. Introduction to electrodynamics. Perentice Hall.

Gringarten, E., & Deutsch, C. V. (2001). Teacher's aide variogram interpretation and modeling. *Mathematical Geology*, 33(4), 507-534.

Gueting, N., Klotzsche, A., van der Kruk, J., Vanderborght, J., Vereecken, H., & Englert, A. (2015). Imaging and characterization of facies heterogeneity in an alluvial aquifer using GPR full-waveform inversion and cone penetration tests. *Journal of hydrology*, 524, 680-695.

Gueting, N., Vienken, T., Klotzsche, A., van der Kruk, J., Vanderborght, J., Caers, J., Vereecken, H., Englert, A.. (2017). High resolution aquifer characterization using crosshole GPR full-waveform tomography: Comparison with direct-push and tracer test data. *Water Resources Research*, 53(1), 49-72.

Gueting, N., Klotzsche, A., van der Kruk, J., Vanderborght, J., Vereecken, H., & Englert, A. (2020). Corrigendum to " Imaging and characterization of facies heterogeneity in an alluvial aquifer using GPR full-waveform inversion and cone penetration tests"[J. Hydrol.(2015) 680-695]. *Journal of Hydrology*, 590, 125483.

Hagrey, A. (2000). GPR study of pore water content and salinity in sand. *Geophysical Prospecting*, 48(1), 63-85.

Haruzi, P., Schmäck, J., Zhou, Z., van der Kruk, J., Vereecken, H., Vanderborght, J., & Klotzsche, A. Detection of tracer plumes using full-waveform inversion of time-lapse ground penetrating radar data: a numerical study in a high-resolution aquifer model. *Water Resources Research*, e2021WR030110.

Hermans, T., Vandenbohede, A., Lebbe, L., & Nguyen, F. (2012). A shallow geothermal experiment in a sandy aquifer monitored using electric resistivity tomography. *Geophysics*, 77(1), B11-B21.

Hermans, T. (2014). Integration of near-surface geophysical, geological and hydrogeological data with multiple-point geostatistics in alluvial aquifers.

Hermans, T., Wildemeersch, S., Jamin, P., Orban, P., Brouyère, S., Dassargues, A., & Nguyen, F. (2015a). Quantitative temperature monitoring of a heat tracing experiment using cross-borehole ERT. *Geothermics*, 53, 14-26.

Hermans, T., Nguyen, F., & Caers, J. (2015b). Uncertainty in training image-based inversion of hydraulic head data constrained to ERT data: Workflow and case study. *Water Resources Research*, 51(7), 5332-5352.

Hoffmann, R., Dassargues, A., Goderniaux, P., & Hermans, T. (2019). Heterogeneity and prior uncertainty investigation using a joint heat and solute tracer experiment in alluvial sediments. *Frontiers in Earth Science*, 7, 108.

- Holliger, K., Musil, M., & Maurer, H. R. (2001). Ray-based amplitude tomography for crosshole georadar data: A numerical assessment. *Journal of Applied Geophysics*, 47(3-4), 285-298.
- Huisman, J. A., Hubbard, S. S., Redman, J. D., & Annan, A. P. (2003). Measuring soil water content with ground penetrating radar: A review. *Vadose zone journal*, 2(4), 476-491.
- Irving, J. D., Knoll, M. D., & Knight, R. J. (2007). Improving crosshole radar velocity tomograms: A new approach to incorporating high-angle traveltime data. *Geophysics*, 72(4), J31-J41.
- Jol, H. M. (Ed.). (2008). *Ground penetrating radar theory and applications*. elsevier.
- Keskinen, J., Klotzsche, A., Looms, M. C., Moreau, J., van der Kruk, J., Holliger, K., ... & Nielsen, L. (2017). Full-waveform inversion of crosshole GPR data: Implications for porosity estimation in chalk. *Journal of Applied Geophysics*, 140, 102-116.
- Kelter, M., Huisman, J. A., Zimmermann, E., & Vereecken, H. (2018). Field evaluation of broadband spectral electrical imaging for soil and aquifer characterization. *Journal of applied geophysics*, 159, 484-496.
- Kemna, A., Vanderborght, J., Kulesa, B., & Vereecken, H. (2002). Imaging and characterisation of subsurface solute transport using electrical resistivity tomography (ERT) and equivalent transport models. *Journal of Hydrology*, 267(3-4), 125-146.
- Kitanidis, P. K., & McCarty, P. L. (Eds.). (2012). *Delivery and Mixing in the Subsurface: Processes and Design Principles for in Situ remediation* (Vol. 4). Springer Science & Business Media.
- Klepikova, M., Wildemeersch, S., Hermans, T., Jamin, P., Orban, P., Nguyen, F., ... & Dassargues, A. (2016). Heat tracer test in an alluvial aquifer: Field experiment and inverse modelling. *Journal of Hydrology*, 540, 812-823.
- Klotzsche, A., van der Kruk, J., Meles, G. A., Doetsch, J., Maurer, H., & Linde, N. (2010). Full-waveform inversion of cross-hole ground-penetrating radar data to characterize a gravel aquifer close to the Thur River, Switzerland. *Near surface geophysics*, 8(6), 635-649.
- Klotzsche, A., van der Kruk, J., Meles, G., & Vereecken, H. (2012). Crosshole GPR full-waveform inversion of waveguides acting as preferential flow paths within aquifer systems. *Geophysics*, 77(4), H57-H62.
- Klotzsche, A., van der Kruk, J., Linde, N., Doetsch, J., & Vereecken, H. (2013a). 3-D characterization of high-permeability zones in a gravel aquifer using 2-D crosshole GPR full-waveform inversion and waveguide detection. *Geophysical Journal International*, 195(2), 932-944.
- Klotzsche, A. (2013b). Full-waveform inversion of crosshole GPR data for hydrogeological applications. *Forschungszentrum Jülich, Zentralbibliothek*.

- Klotzsche, A., van der Kruk, J., Bradford, J., & Vereecken, H. (2014). Detection of spatially limited high-porosity layers using crosshole GPR signal analysis and full-waveform inversion. *Water Resources Research*, 50(8), 6966-6985.
- Klotzsche, A., Jonard, F., Looms, M. C., van der Kruk, J., & Huisman, J. A. (2018). Measuring soil water content with ground penetrating radar: A decade of progress. *Vadose Zone Journal*, 17(1), 1-9.
- Klotzsche, A., Vereecken, H., & van der Kruk, J. (2019a). GPR full-waveform inversion of a variably saturated soil-aquifer system. *Journal of Applied Geophysics*, 170, 103823.
- Klotzsche, A., Vereecken, H., & van der Kruk, J. (2019b). Review of crosshole ground-penetrating radar full-waveform inversion of experimental data: Recent developments, challenges, and pitfalls. *Geophysics*, 84(6), H13-H28.
- Klotzsche, A., Lärm, L., Vanderborght, J., Cai, G., Morandage, S., Zörner, Vereecken, H., & van der Kruk, J. (2019c). Monitoring soil water content using time-lapse horizontal borehole GPR data at the field-plot scale. *Vadose zone journal*, 18(1), 190044.
- Knight, R. (2001). Ground penetrating radar for environmental applications. *Annual Review of Earth and Planetary Sciences*, 29(1), 229-255.
- Lavoué, F., Brossier, R., Métivier, L., Garambois, S., & Virieux, J. (2014). Two-dimensional permittivity and conductivity imaging by full waveform inversion of multioffset GPR data: A frequency-domain quasi-Newton approach. *Geophysical Journal International*, 197(1), 248-268.
- Li, W., Englert, A., Cirpka, O. A., Vanderborght, J., & Vereecken, H. (2007). Two-dimensional characterization of hydraulic heterogeneity by multiple pumping tests. *Water Resources Research*, 43(4).
- Liu, L., Lane, J. W., & Quan, Y. (1998). Radar attenuation tomography using the centroid frequency downshift method. *Journal of Applied Geophysics*, 40(1-3), 105-116.
- Looms, M. C., Binley, A., Jensen, K. H., Nielsen, L., & Hansen, T. M. (2008). Identifying unsaturated hydraulic parameters using an integrated data fusion approach on cross-borehole geophysical data. *Vadose Zone Journal*, 7(1), 238-248.
- Maliva, R. G. (2016). *Aquifer characterization techniques* (Vol. 10). Berlin: Springer.
- Meles, G. A., Van der Kruk, J., Greenhalgh, S. A., Ernst, J. R., Maurer, H., & Green, A. G. (2010). A new vector waveform inversion algorithm for simultaneous updating of conductivity and permittivity parameters from combination crosshole/borehole-to-surface GPR data. *IEEE Transactions on geoscience and remote sensing*, 48(9), 3391-3407.

Meles, G. A. (2011). *New developments in full waveform inversion of GPR data* (Doctoral dissertation, ETH Zurich).

Klotzsche, A., Vereecken, H., & van der Kruk, J. (2019b). Review of crosshole ground-penetrating radar full-waveform inversion of experimental data: Recent developments, challenges, and pitfalls. *Geophysics*, 84(6), H13-H28.

Knight, R. (2001). Ground penetrating radar for environmental applications. *Annual Review of Earth and Planetary Sciences*, 29(1), 229-255.

Kowalsky, M. B., Finsterle, S., & Rubin, Y. (2004). Estimating flow parameter distributions using ground-penetrating radar and hydrological measurements during transient flow in the vadose zone. *Advances in Water Resources*, 27(6), 583-599.

Mozaffari, A., Klotzsche, A., Warren, C., He, G., Giannopoulos, A., Vereecken, H., & van der Kruk, J. (2020). 2.5 D crosshole GPR full-waveform inversion with synthetic and measured data. *Geophysics*, 85(4), 1-51.

Mozaffari, A., Klotzsche, A., Zhou, Z., Vereecken, H., & Van der Kruk, J. (2021). 3-D Electromagnetic Modeling Explains Apparent-Velocity Increase in Crosshole GPR Data-Borehole Fluid Effect Correction Method Enables to Incorporating High-Angle Traveltime Data. *IEEE Transactions on Geoscience and Remote Sensing*, 60, 1-10.

Müller, K., Vanderborght, J., Englert, A., Kemna, A., Huisman, J. A., Rings, J., & Vereecken, H. (2010). Imaging and characterization of solute transport during two tracer tests in a shallow aquifer using electrical resistivity tomography and multilevel groundwater samplers. *Water Resources Research*, 46(3).

Oberrohrmann, M., Klotzsche, A., Vereecken, H., & van der Kruk, J. (2013). Optimization of acquisition setup for cross-hole GPR full-waveform inversion using checkerboard analysis. *Near Surface Geophysics*, 11(2), 197-209.

Olhoeft, G. R. (1998, May). Electrical, magnetic and geometric properties that determine ground penetrating radar performance. In *Proceedings of GPR* (Vol. 98, pp. 177-182).

Palacios, A., Ledo, J. J., Linde, N., Luquot, L., Bellmunt, F., Folch, A., Marcuello, A., Queralt, P., Pezard, P.A, Martínez, L., del Val, L., Bosch, D., & Carrera, J. (2020). Time-lapse cross-hole electrical resistivity tomography (CHERT) for monitoring seawater intrusion dynamics in a Mediterranean aquifer. *Hydrology and Earth System Sciences*, 24(4), 2121-2139.

Peterson, Jr, J. E. (2001). Pre-inversion corrections and analysis of radar tomographic data. *Journal of Environmental & Engineering Geophysics*, 6(1), 1-18.

- Polak, E. and Ribiere, G. (1969). *Note on Convergence of Conjugated Direction Methods*, volume 3. Revue Francaise d'Informatique de Recherche Operationnelle.
- Remy, N., Boucher, A., & Wu, J. (2009). *Applied geostatistics with SGeMS: a user's guide*. Cambridge University Press.
- Scheidt, C., Li, L., & Caers, J. (Eds.). (2018). *Quantifying uncertainty in subsurface systems* (Vol. 236). John Wiley & Sons.
- Seyfried, M. S., & Grant, L. E. (2007). Temperature Effects on Soil Dielectric Properties Measured at 50 MHz. All rights reserved. No part of this periodical may be reproduced or transmitted in any form or by any means, electronic or mechanical, including photocopying, recording, or any information storage and retrieval system, without permission in writing from the publisher. *Vadose Zone Journal*, 6(4), 759-765.
- Shakas, A., Linde, N., Baron, L., Bochet, O., Bour, O., & Le Borgne, T. (2016). Hydrogeophysical characterization of transport processes in fractured rock by combining push-pull and single-hole ground penetrating radar experiments. *Water Resources Research*, 52(2), 938-953.
- Sirgue, L., Etgen, J. T., & Albertin, U. (2008, June). 3D frequency domain waveform inversion using time domain finite difference methods. In *70th EAGE Conference and Exhibition incorporating SPE EUROPEC 2008* (pp. cp-40). European Association of Geoscientists & Engineers.
- Slob, E., Sato, M., & Olhoeft, G. (2010). Surface and borehole ground-penetrating-radar developments. *Geophysics*, 75(5), 75A103-75A120.
- Sreenivas, K., Venkatarantan, L., & Rao, P. N. (1995). Dielectric properties of salt-affected soils. *International Journal of Remote Sensing*, 16(4), 641-649.
- Tarantola, A. (2005). Inverse problem theory and methods for model parameter estimation. *Society for industrial and applied mathematics*.
- Tillmann, A., Englert, A., Nyári, Z., Fejes, I., Vanderborght, J., & Vereecken, H. (2008). Characterization of subsoil heterogeneity, estimation of grain size distribution and hydraulic conductivity at the Krauthausen test site using cone penetration test. *Journal of contaminant hydrology*, 95(1-2), 57-75.
- Topp, G. C., Davis, J. L., & Annan, A. P. (1980). Electromagnetic determination of soil water content: Measurements in coaxial transmission lines. *Water resources research*, 16(3), 574-582.
- Tronicke, J., & Hamann, G. (2014). Vertical radar profiling: Combined analysis of traveltimes, amplitudes, and reflections. *Geophysics*, 79(4), H23-H35.

Tsoflias, G. P., Becker, M. W., 2008, Ground-penetrating-radar response to fracture-fluid salinity: Why lower frequencies are favorable for resolving salinity changes. *Geophysics*, 73(5), J25-J30.

van der Kruk, J., Gueting, N., Klotzsche, A., He, G., Rudolph, S., von Hebel, C., Yang, X., Weihermüller, L., Mester, A. & Vereecken, H. (2015). Quantitative multi-layer electromagnetic induction inversion and full-waveform inversion of crosshole ground penetrating radar data. *Journal of Earth Science*, 26(6), 844-850.

Vereecken, H., Döring, U., Hardelauf, H., Jackel, U., Hashagen, U., Neuendorf, O., Schwarze, H. & Seidemann, R. (2000). Analysis of solute transport in a heterogeneous aquifer: the Krauthausen field experiment. *Journal of Contaminant Hydrology*, 45(3-4), 329-358.

Virieux, J., & Operto, S. (2009). An overview of full-waveform inversion in exploration geophysics. *Geophysics*, 74(6), WCC1-WCC26.

Warren, C., Giannopoulos, A., & Giannakis, I. (2016). gprMax: Open source software to simulate electromagnetic wave propagation for Ground Penetrating Radar. *Computer Physics Communications*, 209, 163-170.

Warren, C., Giannopoulos, A., Gray, A., Giannakis, I., Patterson, A., Wetter, L., & Hamrah, A. (2019). A CUDA-based GPU engine for gprMax: Open source FDTD electromagnetic simulation software. *Computer Physics Communications*, 237, 208-218.

Zhou, Z., Klotzsche, A., Hermans, T., Nguyen, F., Schmäck, J., Haruzi, P., Harry Vereecken, and van der Kruk, J. (2020). 3D aquifer characterization of the Hermalle-sous-Argenteau test site using crosshole GPR amplitude analysis and full-waveform inversion. *Geophysics*, 85(6), H133-H148.

Zhou, Z., Klotzsche, A., & Vereecken, H. (2021). Improving crosshole ground-penetrating radar full-waveform inversion results by using progressively expanded bandwidths of the data. *Near Surface Geophysics*.

List of figures

Figure 1.1: Flow in heterogeneities at different scales.	5
Figure 1.2: Acquisition geometries for GPR.	9
Figure 1.3: Difference between ray-based and full-waveform.	11
Figure 2.1: Full-waveform inversion workflow.....	21
Figure 2.2: Source wavelet estimation flow.....	25
Figure 3.1: Overview of the Krauthausen test site.	31
Figure 3.2: Aquifer model hydrological and GPR modelling.	33
Figure 3.3: Transport modelling.	36
Figure 3.4: Tracer distribution in the monitoring plane.	37
Figure 3.5: Flowchart recovery of tracers.	40
Figure 4.1: Background permittivity and electrical conductivity models.	46
Figure 4.2: Spectral density of Background FWI models.	47
Figure 4.3: Porosity and formation factor derived from FWI.	48
Figure 4.4: FWI σ_b results for the salt tracer using different starting model strategies.	50
Figure 4.5: Spectral density of recovered FWI σ_b using different starting model strategies.....	50
Figure 4.6: Electrical conductivity FWI recovery of different tracer scenarios.....	51
Figure 4.7: Observed and FWI data.	52
Figure 4.8: Salt tracer conductivity σ_f recovered on different days.	53
Figure 4.9: FWI model recoveries from the synthetic ethanol tracer.....	55
Figure 4.10: Volumetric concentration of ethanol S_{eth} recovered on different days..	56
Figure 4.11: Tracer distribution changes from permittivity between two sequential days.	56
Figure 4.12: Recovered tracer breakthrough curves at single cells from FWI parameters.	57
Figure 5.1: Setup of the salt tracer test scenario at the Krauthausen test site.	63
Figure 5.2: Electrical conductivity measurements in the injection borehole B29.	65
Figure 5.3: Electrical conductivity logs in monitoring boreholes.	66
Figure 5.4: Example of the procedure of the dewow filter.	69
Figure 5.5: Zero-time calibration.	71
Figure 5.6: Time-zero correction for MOG data based on ZOP and MOG traces cross-correlation.	71
Figure 5.7: Exemplary of geometry of borehole deviation for FWI pre-processing.....	72
Figure 5.8: Exemplary of first arrival time picking.	73
Figure 5.9: Data quality check for the time-lapse crosshole GPR data.....	74
Figure 5.10: Analysis of the time-lapse ZOP relative permittivity data.	76
Figure 5.11: Time-lapse ZOP trace energy data.	78
Figure 5.12: Sketch of the different starting model strategies tested for FWI of time-lapse data.	80
Figure 5.13: FWI background results of plane 3831 of two different acquisitions.	82
Figure 5.14: FWI results from three starting model strategies for plane 3831.	83
Figure 5.15: Source wavelet of three starting model strategies for plane 3831.	84
Figure 5.16: FWI results from three starting model strategies for plane 2938.	86
Figure 5.17: Source wavelet of three starting model strategies for plane 2938.	87
Figure 5.18: Exemplary GPR data for different time-lapse days for plane 2938.....	88

Figure 5.19: High borehole saltwater effect on GPR data in plane 2938.....	89
Figure 5.20: Exemplary GPR data for different time-lapse days for plane 2938.....	90
Figure 5.21: FWI difference models for permittivity and electrical conductivity for plane 2938.	91
Figure 5.22: Difference of conductivity FWI results between time-lapse and background FWI models, from Day 1 until Day 14.	93
Figure 5.23: Effective source wavelets in all the time-lapse FWI for all planes.	97
Figure 5.24: Difference of electrical conductivity between FWI time-lapse and background models at specific locations in plane 3831..	97
Figure 5.25: Comparison of the resolution of plume reconstruction between previous salt tracer test measured with borehole ERT and the salt tracer test.	102
Figure A.1: Realistic noise added to synthetic waveforms.	110
Figure A.2: Observed and inverted FWI data at the depth of major tracer intrusion.....	111
Figure A.3: Fit of FWI traces.....	112
Figure A.4: Noise level in comparison to the traces amplitude.	113
Figure A.5: Observed and modelled FWI traces in ethanol tracer scenario.	114
Figure A.6: Investigation of the tracer's out of plane on the GPR data.	117
Figure B.1: Overview of the Hermalle-sous-Argenteau test site.	125
Figure B.2: Image plots of the measured data.....	128
Figure B.3: Trace energy profiles of the measured data.	129
Figure B.4: Approximate waveguide structures based on the amplitude analysis.....	131
Figure B.5: Velocity and ε comparison over depth based on the ZOP data..	134
Figure B.6: Ray-based starting models and FWI results for cross section Pz10-Pz13.	136
Figure B.7: Image plots of the modeled data based on updated FWI results for the cross section Pz10-Pz13.	137
Figure B.8: Starting model tests for ε	139
Figure B.9: Estimated effective source wavelets for the nine cross-sections.	140
Figure B.10: Ray-based results of ε for all crossections.	142
Figure B.11: Estimated porosity distributions.	146
Figure C.1: Flowchart of different time-lapse inversion strategies.....	149
Figure C.2: Plume reconstruction from independent FWI of a positive electrical tracer.	152
Figure C.3: Plume reconstruction from double-difference FWI of a positive electrical tracer.....	153

List of tables

Table 1.1: Dielectric properties values of subsurface materials..	7
Table 3.1: Aquifer peorproperties.	34
Table 4.1: Evaluation of FWI results..	45
Table 5.1: Overview of the acquisition days.....	67
Table 5.2: Evaluation of the FWI results for the different starting model strategies.	87
Table 5.3: Evaluation of FWI convergence using strategy S2 for all inverted planes..	95
Table 5.4: Input parameters for CDE equation.	99
Table B.1: A comparison of FWI results between the traditional FWI and the updated FWI.....	123
Table B.2: Correlation for the updated FWI permittivity and conductivity.....	144
Table C.1: Starting model strategies for time-lapse GPR Full-waveform inversion.	151

List of abbreviations

BKGD – Background.

BTC – Breakthrough curve.

CDE - Convection-dispersion equation.

CMP - Common-midpoint.

COP - Common-offset profile.

CPT - Cone-penetration test.

CRIM - Complex Refractive Index Model.

EM - Electromagnetic.

ERT - Electrical resistivity tomography.

ESW - Effective source wavelet.

FDTD - Finite-difference time-domain.

FWI - Full-waveform inversion.

GPR - Ground-penetrating radar.

GSD - Grain size distribution.

MOG - Multi-offset gathers.

NRMSE - Normalized root-mean-squared error.

PML - perfectly matched layer.

RM – Real model.

RMSE - Root-mean-squared error.

SGSIM - Stochastic Gaussian simulation.

SW - source wavelet.

VRP - Vertical radar profiling.

WARR - Wide-angle-reflection-refraction.

WC - Water column.

WGT - Waveguide type.

ZOP - Zero-offset profiling.

Peleg Haruzi

Kibbutz Ayelet HaShachar 12200, Israel

☎ +972-3-9683527

☎ +972-51-2110383

✉ peleg@volcani.agri.gov.il

curriculum vitae**Personal details**

Date of birth March 11, 1983

Place of birth Safed, Israel

Nationality Israeli

Education8/2017–07/2022 **Doctoral studies in Geophysics,***Forschungszentrum Jülich and University of Cologne (Germany).*

Doctoral thesis High-resolution imaging of transport processes with GPR full-waveform inversion

Supervisor Prof. Dr. Anja Klotzsche, IBG 3 - Agrosphere, Forschungszentrum Jülich and University of Cologne

10/2014–07/2017 **Master in Marine Geosciences,***University of Haifa*Master thesis Evaluation of micro- and macro-scale petrophysical characteristics of lower cretaceous sandstone with flow modeling in μ -CT imaged geometry

Supervisor Prof. Dr. Regina Katsman, University of Haifa

10/2008–07/2011 **Bachelor in Exact Sciences (emphasis on physics),***The Hebrew University of Jerusalem*

09/1995-06/2001 Abitur,

Emek Hahula High School

Work experience1/2022–Date **The Agricultural Research Organization, Volcani Center, Israel**

Geoscience researcher.

*Using physics-informed neural networks (PINN) code to apply for subsurface transport modeling, by including time-lapse geophysical tomograms and logging data – for the purpose of smart irrigation.*8/2017–12/2020 **Agrosphere - Forschungszentrum Jülich**

Geoscience researcher.

Demonstrating the potential of time-lapse GPR full-waveform inversion (FWI) as a high-resolution imaging method to improve understanding and reconstruction of preferential flow paths in aquifers.

10/2014–07/2017 Agrosphere - Forschungszentrum Jülich

Geoscience researcher.

Characterizing the petrophysical properties and the heterogeneity of a reservoir sandstone in a multi-scale multi-methodological approach.

10/2014–07/2017 **Teaching assistant - University of Haifa**

Delivering teaching sessions on BSc course "Electricity and Magnetism".

Publications

- 2022 **Haruzi, P.**, Schmäck, J., Zhou, Z., van der Kruk, J., Vereecken, H., Vanderborght, J., & Klotzsche, A. (2022). *Detection of tracer plumes using full-waveform inversion of time-lapse ground penetrating radar data: a numerical study in a high-resolution aquifer model.* Water Resources Research, e2021WR030110.
- 2022 Hermans, T., Goderniaux, P., Jougnot, D., Fleckenstein, J., Brunner, P., Nguyen, F., ..., **Haruzi, P.**, ... & Le Borgne, T. (2022). *Advancing measurements and representations of subsurface heterogeneity and dynamic processes: towards 4D hydrogeology.* Hydrology and Earth System Sciences Discussions, 1-55.
- 2021 **Haruzi, P.**, Katsman, R., Halisch, M., Waldmann, N., & Spiro, B. (2021). *Benchmark study using a multi-scale, multi-methodological approach for the petrophysical characterization of reservoir sandstones.* Solid Earth, 12(3), 665-689.
- 2021 Zohar, I., & **Haruzi, P.** (2021). *Image Analysis for Spectroscopic Elemental Dot Maps: P, Al, and Ca Associations in Water Treatment Residuals as a Case Study.* Frontiers in Environmental Chemistry, 12.
- 2020 Zhou, Z., Klotzsche, A., Hermans, T., Nguyen, F., Schmäck, J., **Haruzi, P.**, Vereecken, H., and van der Kruk, J. (2020). *3D aquifer characterization of the Hermalle-sous-Argenteau test site using crosshole ground-penetrating radar*

amplitude analysis and full-waveform inversion GPR amplitude analysis and FWI for 3D imaging. Geophysics, 85(6), H133-H148.

submitted **Haruzi, P.**, Schmäck, J., van der Kruk, J., Vereecken, H., Vanderborght, J., & Klotzsche, A. *GPR full-waveform inversion monitoring of a salt tracer test*.

in preparation **Haruzi, P.**, Haoffmann, R., Schmäck, J., van der Kruk, J., Vereecken, H., Vanderborght, J., & Klotzsche, A. *Reconstruction of a heat plume in alluvial sediments using full-waveform inversion of cross-hole GPR data*

Awards

7/2017-12/2020 PhD program as part of ENIGMA ITN (European training Network for in situ imaGing of dynaMic processes in heterogeneous subsurfAce environments) funded by the European Commission.

9/2018 Travel grant to SEG/Chevron Student Leadership Symposium and SEG International Exposition and 2018 Annual Meeting in Anaheim, California, USA.

09/2015-02/2016 Erasmus scholarship for exchange student prohram.

11/2014 Israel Ministry of Energy Scholarship for research in the Fields of Engineering, Geology and Geophysics of Fossil Fuel.

Conferences and Workshops

06/2022 Haruzi et al., "High resolution imaging of salt tracer using GPR full-waveform inversion", *GPR 2022 19th International Conference*, Golden.

10/2021 Haruzi et al., "Time-lapse GPR Full-Waveform Inversion to Monitor a Salt Tracer Test in a Sand Aquifer", Presentation, Near-Surface Imaging with FWI AGU-SEG: Theory and Applications, Workshop Oct. 2021, online.

12/2020 Haruzi et al., "The potential of time-lapse GPR full-waveform inversion as high-resolution imaging technique for salt, heat, and ethanol transport", extended abstract CMWR Dec. 2020, online.

06/2020 Haruzi, P., Schmäck, J., Zhou, Z., Vanderborght, J., Vereecken, H., van der Kruk, J., and Klotzsche, A. (2020). Numerical study for time-lapse GPR full-waveform inversion for salt and heat tracer tests. That extended abstract was accepted to *18th International Conference on Ground Penetrating Radar*, but eventually was not published because the conference was cancelled due to restrictions of Covid19.

- 10/2018 Haruzi et al., “Time-lapse ground-penetrating radar full-waveform inversion to detect tracer plumes: A numerical study”, SEG Technical Program Expanded Abstracts 2018 (pp. 2486-2490), Anaheim.
- 12/2017 Haruzi et al., “Evaluation of micro- and macro-Scale petrophysical characteristics of Lower Cretaceous sandstone with flow modeling in μ -CT imaged geometry” (poster). AGU Fall Meeting 2017, New Orleans.
- Trainings
- 08/2019 Modeling of Geologic Heterogeneity and Groundwater
- 02/2019 Lifetime Skills
- 06/2018 4th Cargèse Summer School : Flow and Transport in Porous and Fractured Media
- 02/2018 Predictive modelling and upscaling of flow and reactive transport in heterogeneous aquifers
- 02/2018 Advanced inverse modelling and stochastic representations of heterogeneous porous and fractured media
- 10/2017 Multi-scale in situ investigation of fractured media: theory and field practice
- 10/2017 Advanced subsurface characterization methods: theory and field practice
- 07/2015 Pore-Scale Modelling and Upscaling of Reactive Transport in Partially-Saturated Porous Media
- Languages
- Hebrew Mother tongue
- English Fluent (written and spoken)
- Computer skills
- Prog. languages C, C++, python (basic)
- Computer algebra Matlab (advanced)
- Operating systems Windows (advanced), Linux (basic)
- Geophysical tools Geostatistic software, Hydrus, R2, gprMax
- Interests
- Literature Historical novels
- Sports Triathlon training, chess

Erklärung zur Dissertation

"Hiermit versichere ich an Eides statt, dass ich die vorliegende Dissertation selbstständig und ohne die Benutzung anderer als der angegebenen Hilfsmittel und Literatur angefertigt habe. Alle Stellen, die wörtlich oder sinngemäß aus veröffentlichten und nicht veröffentlichten Werken dem Wortlaut oder dem Sinn nach entnommen wurden, sind als solche kenntlich gemacht. Ich versichere an Eides statt, dass diese Dissertation noch keiner anderen Fakultät oder Universität zur Prüfung vorgelegen hat; dass sie - abgesehen von unten angegebenen Teilpublikationen und eingebundenen Artikeln und Manuskripten - noch nicht veröffentlicht worden ist sowie, dass ich eine Veröffentlichung der Dissertation vor Abschluss der Promotion nicht ohne Genehmigung des Promotionsausschusses vornehmen werde. Die Bestimmungen dieser Ordnung sind mir bekannt. Darüber hinaus erkläre ich hiermit, dass ich die Ordnung zur Sicherung guter wissenschaftlicher Praxis und zum Umgang mit wissenschaftlichem Fehlverhalten der Universität zu Köln gelesen und sie bei der Durchführung der Dissertation zugrundeliegenden Arbeiten und der schriftlich verfassten Dissertation beachtet habe und verpflichte mich hiermit, die dort genannten Vorgaben bei allen wissenschaftlichen Tätigkeiten zu beachten und umzusetzen. Ich versichere, dass die eingereichte elektronische Fassung der eingereichten Druckfassung vollständig entspricht."

Israel, August 2022

Peleg
Haruz;

22.8.2022

Band / Volume 590

NiFe Layered Double Hydroxide Catalysts for Oxygen Evolution Reaction in Alkaline Water Electrolysis

W. Jiang (2022), 165 pp

ISBN: 978-3-95806-658-8

Band / Volume 591

Optimizing Cross-linked Infrastructure for Future Energy Systems

L. Welder (2022), xxiii, 360 pp

ISBN: 978-3-95806-659-5

Band / Volume 592

Evaluation von Reaktorkonzepten für die CO₂-basierte Methanolsynthese aus Wasserstoff und Kohlendioxid mithilfe von CFD-Simulationen

S. Weiske (2022), x, 369 pp

ISBN: 978-3-95806-661-8

Band / Volume 593

Spectral Induced Polarization of Biochar in Soil

Z. Gao (2022), XXVI, 155 pp

ISBN: 978-3-95806-662-5

Band / Volume 594

Eignung von nickelhaltigen Katalysatorsystemen in sauren Medien zur Nutzung im Betrieb von Brennstoffzellen

A. Karaca (2022), iv, 249 pp

ISBN: 978-3-95806-663-2

Band / Volume 595

Seasonal Comparison of the Chemical Composition and Source Apportionment of Aerosols during the Year-Long JULIAC Campaign

L. Liu (2022), VIII, 189 pp

ISBN: 978-3-95806-668-7

Band / Volume 596

Nanoscale Understanding and Control of Metal Exsolution in Perovskite Oxides

M. L. Weber (2022), ix, 160 pp

ISBN: 978-3-95806-669-4

Band / Volume 597

Nanostructures of Transition Metal Sulfides for Anion Exchange Membrane Water Electrolysis

L. Xia (2022), 161 pp

ISBN: 978-3-95806-670-0

Band / Volume 598

Recycling- und Defossilisierungsmaßnahmen der Energieintensiven Industrie Deutschlands im Kontext von CO₂-Reduktionsstrategien

F. Kullmann (2022), XII, 237 pp

ISBN: 978-3-95806-672-4

Band / Volume 599

IEK-14 Report 2022

Research contributions for the energy transition and structural change in the Rhineland

B. Emonts (Ed.) (2022), 83 pp

ISBN: 978-3-95806-676-2

Band / Volume 600

Development of Glass-based Sealants for the Joining of Oxygen Transport Membranes

X. Li (2022), IV, 159 pp

ISBN: 978-3-95806-677-9

Band / Volume 601

High-resolution imaging of transport processes with GPR full-waveform inversion

P. Haruzi (2022), iv, 173 pp

ISBN: 978-3-95806-678-6

Weitere **Schriften des Verlags im Forschungszentrum Jülich** unter
<http://wwwzb1.fz-juelich.de/verlagextern1/index.asp>

Energie & Umwelt / Energy & Environment
Band / Volume 601
ISBN 978-3-95806-678-6